University of Cyprus

SCHOOL OF ENGINEERING
DEPARTMENT OF CIVIL AND ENVIRONMENTAL ENGINEERING

Modelling of Fluid Driven Fractures in Cohesive Poroelastoplastic Formations

Ernestos N. Sarris

Diploma of Mineral Resources Engineering, Technical University of Crete, Greece
M.Sc. Environmental Geotechnology, Technical University of Crete, Greece

A THESIS
SUBMITTED TO THE FACULTY OF CIVIL AND ENVIRONMENTAL ENGINEERING OF THE UNIVERSITY OF CYPRUS
IN PARTIAL FULFILLMENT OF THE REQUIREMENTS FOR THE DEGREE OF DOCTOR OF PHILOSOPHY

April 2011

Modelling of Fluid Driven Fractures in Cohesive Poroelastoplastic Formations

Ernestos N. Sarris

EXAMINATION COMMITTEE

Professor Panos Papanastasiou (Advisor)	University of Cyprus
Professor Euripides Papamichos	Aristotle University of Thessaloniki
Professor Jean Sulem	Paris Tech, Ecole des Ponds
Associate Professor Dimos Charmpis (Chair)	University of Cyprus
Lecturer Dimitrios Loukidis	University of Cyprus

Submitted to the Examination Committee on March 25, 2011.

University of Cyprus

SCHOOL OF ENGINEERING
DEPARTMENT OF CIVIL AND ENVIRONMENTAL ENGINEERING

Approval Page

Doctor of Philosophy

Modelling of Fluid Driven Fractures in Cohesive Poroelastoplastic Formations

Ernestos N. Sarris

Research Advisor

ΠΡΟΣΩΠΙΚΑ ΔΕΔΟΜΕΝΑ

Professor Panos Papanastasiou

Committee Member (Chair)

ΠΡΟΣΩΠΙΚΑ ΔΕΔΟΜΕΝΑ

Assistant Professor Dimos Charmpis

Committee Member

ΠΡΟΣΩΠΙΚΑ ΔΕΔΟΜΕΝΑ

Professor Euripides Papamichos

Committee Member

ΠΡΟΣΩΠΙΚΑ ΔΕΔΟΜΕΝΑ

Professor Jean Sulem

Committee Member

Lecturer Dimitrios Loukidis

This research was performed at the University of Cyprus in the Faculty of Engineering at the Department of Civil and Environmental Engineering, Nicosia, Cyprus and it was partially funded by the Research Promotion Foundation (R.P.F).

Abstract

The fluid driven problem arises in hydraulic fracturing, a technique widely used in the petroleum industry to enhance the recovery of hydrocarbons in low permeability underground reservoirs. In practice, attention is focused on the prediction of the propagation pressure at wellbore which is normally measured during the treatment and is usually the only parameter available to evaluate the success of the operation. The main objective of this research is to investigate the discrepancy between classical hydraulic fracturing simulators, which often underestimate the measured down-hole pressures, and field observations by utilizing advanced theories of fluid mechanics, fracture mechanics and poroelastoplasticity.

Based on the analysis of the physical problem a model that governs the fluid driven fracture was build and solved numerically with the finite element code Abaqus. The equations that describe the fluid driven fracture are coupled and highly non-linear. The deformation of the porous continuum is obtained by the derivation of the equilibrium equation for the porous media incorporating the effective stress principle. Fluid flow in the porous domain is governed by a continuity equation and the Darcy law. Fluid flow inside the fracture is modeled with lubrication theory and a diffusion equation for the fluid infiltration from the fracture into the surrounding medium. The inelastic behavior of the porous continuum is described by Mohr-Coulomb yield criterion with an associative flow rule.

The first part of this research is concerned with fracture analysis based on cohesive zone approach. We examined the influence of bilinear and exponential forms constitutive laws on the fracture process zone in impermeable and permeable fluid driven fractures. It is demonstrated that the crack profiles and the propagation pressures are larger in the case of elastic-softening cohesive model compared to the results of the rigid-softening cohesive model for both elastic and poroelastic cohesive solids. It is found that the results are affected by the slope of the loading branch of the cohesive model and they are nearly unaffected from the exact form of the softening branch. Furthermore, the size of the process zone, the fracture geometry and the propagation pressure increase with increasing confining stresses.

In the second part we studied the hydraulic fracturing in a cohesive poroelastic formation. We found that higher pressures are needed to extend a fracture in a

poroelastic medium than in an elastic and the created profiles of poroelastic fracture are wider. We found that grain compressibility plays a minor role and does not result to any significant difference on the fluid pressures and fracture dimensions. Wider fracture profiles are obtained with higher injection rates. The fluid pressures and the fracture apertures are larger in the case of a high permeability formation.

In the last part we studied the hydraulic fracturing in a cohesive poroelastoplastic formation. We propose a scaling of the size of the plastic zones with the most important parameters and examined the validity of the scaling law through a series of computations. We found that size of the process zone which includes plastic zone increase with a) the elastic-softening cohesive fracturing model b) with the stress deviator c) with the injection rate and d) formation pressure. In cases of low injection rates and low formation pressure the fluid filtration creates back stresses which tend to reduce the fracture width in the bulk of the fracture. Summarizing the results obtained in this research, a mathematical model is proposed based on the physical processes that are dominant in a fluid driven fracture propagating in a cohesive poroelastoplastic rock formation for explaining the elevated net pressures observed in field treatments.

Acknowledgements

This work would have never been possible without the support of many people to whom I would like to express my gratitude.

I wish to thank my advisor Professor Panos Papanastasiou for believing in me and giving me the opportunity to work under his guidance and also for being so patient with me all these years. Furthermore, I could not have done this research without his insights and expertise.

I would like to thank all the other Committee members for their valuable time and helpful advice.

I want to express my gratitude to my family for their support and trust they gave me all these years when I was studying.

I express special thanks to my former fellow graduate students and friends, Loizos Papaloizou, Panikos Polycarpou and Antri Kakoniti who helped me in many ways.

"Difficult is what we don't know!
If we know it, it is simple"

Ioannis Vardoulakis.

To Nikos Sarris

Table of Contents

List of Figures

List of Tables

1. Introduction

1.1 Preamble

Hydraulic fracturing is a technique widely used in the petroleum industry to enhance the recovery of hydrocarbons from underground reservoirs. The hydraulic fracturing process involves the pumping of a viscous-fluid from a well into the rock formation under high enough fluid pressure to fracture the reservoir. In general, a fracture will re-orient itself in the complex stress field near the wellbore and will propagate further perpendicular to the minimum compressive stress. The pumping of fluid is maintained at a rate high enough for the fluid pressure to overcome the minimum in-situ stress and hence to propagate the fracture. The fracture propagation is assumed to take place when the stress intensity factor at the tip reaches a critical value equal with the rock fracture toughness. During the pumping process, proppant particles like sand grains are gradually mixed with the fracturing fluid to ensure that the fracture will remain propped open when the pumping stops. A highly permeable channel will hence be formed for oil or gas to flow from the pay zone in the well. Since its introduction, hydraulic fracturing has been one of the primary engineering tools for improving well productivity and these days it covers more than 90% of gas wells and 70% for oil wells worldwide (Economides and Nolte, 2000).

1.2 Applications of Hydraulic Fracturing

The mathematical problem of a fluid driven fracture arises in hydraulic fracturing for enhanced hydrocarbon recovery in the petroleum industry. Some other related applications in geomechanics include the magma-driven fractures (Spence and Turcotte, 1985), the preconditioning of rock masses in mining operations to promote caving (Jeffrey et al., 2001) , the formation of barriers to stop contaminant transport in environmental projects (Murdoch and Slack, 2002), the re-injection of drilling cuttings (Moschovidis et al., 2000), the heat production from geothermal reservoirs (Legarth et al., 2005) and more recently the CO_2 sequestration in deep geological formations (Logan et al., 2001).

Even in its most basic form, hydraulic fracturing is a complex process to model, as it involves the coupling of at least four physical processes: (i) the viscous flow of the fluid in the fracture (ii) the rock deformation of the surrounding medium

induced by the fluid pressure on the fracture surfaces (ii) the fluid diffusion in the porous continuum and (iv) the rock splitting and fracture propagation. Usually the solid deformation is modeled with the elasticity theory, which in analytic form can be represented by an integral equation that determines the non-local relationship between the fracture width and the fluid pressure. The fluid flow is modeled by lubrication theory, represented by a non-linear partial differential equation that relates the fluid flow velocity, the fracture width and the gradient of the pressure. The fluid diffusion is governed by simple expressions that express the loss from the fracture in the surrounding formation (Carter, 1957).

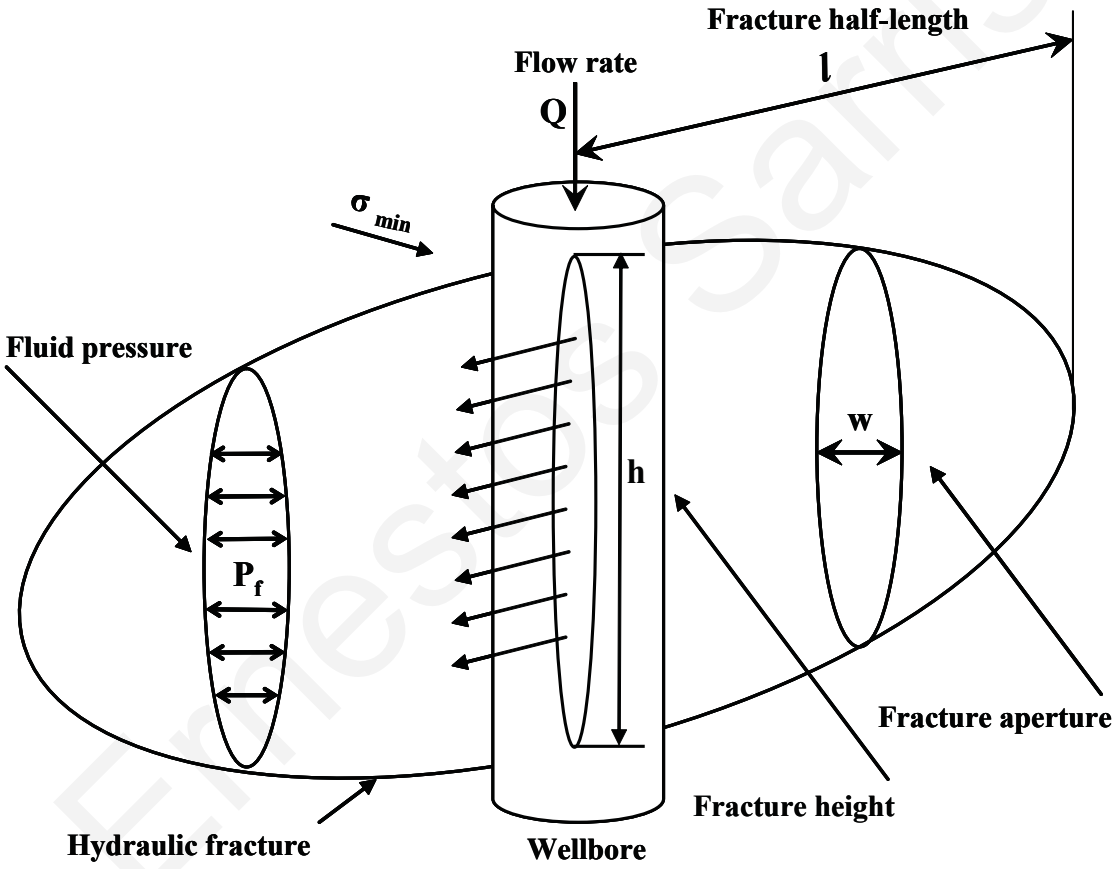

Figure 1.1: Process and parameter representation in hydraulic fracturing

Figure (1.1) presents a simple schematic representation of a hydraulic fracture. The main parameters that affect the fracture propagation are separated into fluid mechanics and fracture mechanics (geometric) parameters. In this figure the fracture propagates perpendicularly to the minimum insitu stress σ_{min}. The viscous fluid which is injected in the wellbore to fracture the formation is controlled by the flow rate Q that is maintaining the fluid net pressures. The net pressure is defined as the fluid

pressure inside the fracture P_f minus the minimum insitu far field stress σ_{min}. Once the fracture is initiated and propagates away from the wellbore it gains fracture height h, fracture length l and fracture width w. In summary all the necessary fluid flow and fracture (geometric) parameters are available to analyze the success of the treatment.

1.3 Problem Statement and Motivation

In field operations, attention is focused on the prediction of the wellbore pressure (P_f) which is normally measured during the treatment and is usually the only parameter available to evaluate the operation. Classical hydraulic fracturing simulators often underestimate the measured down-hole pressures. Research works involving a world wide survey on net pressures, indicated that the net pressures encountered in the field are on average 50-70% higher than the ones predicted by conventional hydraulic fracturing simulators (Van Dam et al., 1997). These observations have triggered a series of dedicated studies which looked into the importance of the net pressure incorporating higher order constitutive theories to explain this observed difference between field operations and numerical simulations (Papanastasiou, 1999; Papanastasiou, 1999b; Van Dam et al., 1997). However all these studies had ignored the pressure diffusion and porous behavior of the rock deformation. According to Adachi (2001), discrepancy also exists between experimental data and numerical simulations. Adachi (2001) demonstrated that the difference between experimental data and simulated data for the length of the fracture can vary as much as a factor of three. The differences in fracture opening are about 20% while the fluid pressures differ by a factor of two. The reasons for these differences are due to the complexity of the solid-fluid interaction at the fracture tip and strong scale effects. Furthermore, although the cohesive model approach has been utilized by many authors in different disciplines, the physical interpretation of the process zone and its influence in hydraulic fracturing is still unexplored.

1.4 Objectives and Methods

The interaction between a pore fluid and the elastic skeleton of a porous material was first developed by Biot (1941) and may be considered to be a special case of the theory of interacting continua or of the theory of mixtures. Since then the theory of poroelasticity was established. The assumption of linear elastic behavior and Darcy

flow behavior of the porous skeleton that will remain unaltered during loading of a poroelastic material is recognized as a limitation of the classical theory. A natural extension of the classical theory is to introduce concepts such as elasto-plasticity to account for irreversible deformation of the porous skeleton. Such an extension is capable to give rise to alterations in the elasticity and fluid flow behavior as a result of micro-cracks and micro-voids generation in the porous continuum.

The use of porous elastic and porous plastic models is common in many disciplines of engineering, especially in geomechanics. In geomechanics, the coupling between the deformation of the solid skeleton and the motion of the pore fluid is thought to be of primary importance. The materials constituting the solid skeleton and the fluid can be different from one application to another. In geomechanics the solid skeleton may consist of sand grains or porous rocks and the fluid that moves through the solid may be any type of rheological fluid such as Newtonian or Power law. The skeleton may exhibit inelastic phenomena, such as permanent strain and damage that may cause failure in advanced states. The comprehension of these non linear mechanisms and associated parameters is of paramount importance in hydraulic fracturing operations as it may explain discrepancies in net-pressures between field measurements and conventional model predictions.

When a fracture is driven in a saturated domain, the newly created surface of the fracture alters the stress field surrounding the body of the fracture and induces a pore pressure gradient which affects the effective stresses and the development of the plastic zones in the near tip area of the fracture. Furthermore, the diffusion of the fracturing fluid through the solid introduces some rate-dependency in the overall solution to be predicted by the numerical model. Thus it is necessary to develop an appropriate numerical model to investigate further the coupling of pore pressure diffusion in a rock governed by non linear damage or failure criterion.

In this research work the cohesive zone approach is incorporated as the fracture propagation criterion to investigate the influence of the surrounding porous deformation on the net pressure and fracture dimensions. The development of analytical solutions for the fluid driven problem in porous inelastic domains is a challenging problem. The numerical solution of this problem poses also special challenges. These difficulties arise from the coupling of the cohesive zone as a fracture criterion with the fluid flow in the fracture and the deformation of the inelastic porous continuum. The coupling includes fluid pressure-traction-separation

relation in the cohesive zone ahead of the pressurized fracture. Furthermore, the fluid driven problem is a moving boundary value problem and the positions of the fluid front and fracture tip and their influence on the overall non local solution is a matter of debate in the hydraulic fracture community. For the numerical solution of the governing equations, the finite element method was utilized. A numerical model dealing with the issues outlined above is expected to be valuable for the scientific community and the industry in general.

1.5 Thesis Outline

The fundamentals and principles for the theory of hydraulic fracturing technique are presented in Chapter 2. It describes a brief review in the most relevant fields of geomechanics, fluid mechanics, fracture mechanics and poromechanics necessary for modelling the fluid driven problem under complex conditions. Chapter 3 introduces the numerical model of the fluid driven fracture in a deformable poroelastoplastic continuum for finite element formulation. The numerical implementation and validation of the numerical model is presented in chapter 4. Chapters 5, 6 and 7 present computational results and major conclusions. Chapter 5, presents a detailed analysis of the influence of the cohesive zone on a fluid driven fracture in elastic and poroelastic domains. Chapter 6 presents an analysis of the influence of the main poroelastic parameters on propagating hydraulic fractures. The influence of the process zone of a poroplastic formation and scaling of the plastic zones are presented in chapter 7. Finally, chapter 8 summarizes the main conclusions obtained from this research work and makes recommendations for future work.

2. Hydraulic Fracturing Fundamentals and Principles

2.1 Preamble

Hydraulic fracturing is a powerful stimulation method which originally was initiated and is still used for increasing the productivity of hydrocarbon in oil and gas wells. The mathematical model for modelling hydraulic fracturing is the so called fluid driven problem. It has special practical applications not only in petroleum engineering but also in other related disciplines of ground engineering. In order to model the fluid driven problem under complex conditions it is important to discuss appropriate fundamentals and principles from the fields of geomechanics, fluid mechanics, fracture mechanics and poromechanics. This chapter contains some of the principles and fundamentals with their relevant assumptions based on previous works. Section 2.2 describes the modelling of a hydraulic fracture for non-porous and porous conditions. An attempt to cite the most significant works dedicated to the inelastic description of the problem is included in section 2.3. It is mentioned here that the review on previous work is by no means exhaustive but only the ones related with the present work are briefly described. Section 2.4 presents an attempt to close the gap between conventional fracture mechanics and cohesive zone mechanics as a basis of the fracture propagation criterion. Finally, section 2.5 presents some of the most basic issues related to hydraulic fracturing.

2.2 Modeling of Hydraulic Fractures in Non-Porous and Porous Formations

The discussion on the modelling of hydraulic fracturing in porous and non porous continua will be restricted to previous work done to understand the parameters affecting the fluid driven problem. This is achieved through the study of energy dissipative mechanisms such as the energy expended to fracture the solid formation in a “toughness dominated” regime and the energy lost in the viscous fracture fluids in a “viscosity dominated” regime. Many other contributions beyond that point are actually based on those two regimes before expanding in more complex analyses by including additional parameters. Furthermore, significant contributions have also been devoted in the explanation of the effect of the fluid lag, the area between fluid front and fracture tip, on the overall solution of the problem (Garagash 1998; 2006).

Extending the research work in hydraulic fracturing other forms of dissipative mechanisms were also examined such as the energy lost due to inelastic effects. Many research works has also been devoted on non linear fracture mechanics by implementing the cohesive zone in a propagating fracture which turns to be another form of dissipative mechanism (Ritchie 1999; Li & Chandra 2003). Furthermore, in the attempt to model this complex behavior, a substantial amount of contributions were also devoted in the numerical development (Papanastasiou 1999; Lecampion & Detournay 2007). All the aforementioned contributions form the basis for answering a key question that in many times is still a matter of open research. Common objective was to explain and minimize the discrepancies in the net-pressures (pressure needed to extend the fracture under confinement) between field measurements and numerical simulators. The first part of this section is devoted in understanding the fracture geometry considered in this problem. The coupling of fluid flow and deformation is introduced next followed by a literature review.

2.2.1 Fracture geometry

Hydraulic fracturing simulators are used in practice for the development of a treatment pump schedule which must take into account many options. The interactive roles of the various major variables such as the fracture height h_f, Elastic modulus E, fluid leak off C_L, fracture toughness $K_{IC\text{-}apparent}$, fracture fluid viscosity μ, and injection rate q_i must be considered on the net pressure p_{net}, fracture width w, fracture length l, proppant transport and fluid loss. In addition, the design must consider the various roles of the pad volume concerning fluid loss and creating the fracture width. For these reasons a final schedule is generally developed for a specific fracture geometry model. The use of a properly calibrated fracture geometry model enables also the efficient consideration of multiple scenarios for designing the optimum treatment for a specific application.

One of the aspects for a successful modelling of the fracture geometry is the correct understanding of the differences between vertical and horizontal stresses within the earth. This understanding is essential for the qualitative and quantitative explanation of the orientation of the fractures. Accurate determination of the stress difference can be used for preventing tortuosity effects of the fracture geometry. A significant contribution on the orientation of the fractures was provided by Hubbert and Willis (1957) who identified the stress difference between the vertical and

horizontal insitu stresses as the main control parameter. Fractures will tend to propagate perpendicular to the minimum insitu stress. Until then, all design considerations were based on the assumption of an isostatic state of stress prevailing everywhere.

The first work on hydraulic fracturing modelling was presented by Khristianovich & Zheltov (1955) and Perkins & Kern (1961). Their models were developed to calculate the fracture geometry and particularly the width, length and fluid pressure for a specified flow rate. Carter (1957) introduced a model to satisfy the volume balance under the assumption of constant and uniform fracture width. Carters work was significant at the time because it was further used in combination with the geometric models to ensure that the fracture width was sufficient for proppant entry and transport. Geertsma and De Klerk (1969) and Nordgren (1972) extended the approach of Khristianovich & Zheltov (1955) and Perkins and Kern (1961), respectively, to create the two basic hydraulic fracture models generally known as the KGD and PKN which were the first models to include both volume balance and solid mechanics.

The KGD and PKN models, both of which are applicable only to fully confined fractures, differ in the way in which they convert a 3D solid and fracture mechanics into 2D problem. Khristianovich & Zheltov (1955) assumed plane strain geometry in the horizontal direction (i.e. all horizontal cross sections act independently or equivalently). This means that the fracture width changes more slowly vertically along the fracture face than horizontally (Figure 2.1 a). In practice this is true if the fracture height is much greater than the length. Perkins & Kern (1961) on the other hand, assumed that each vertical cross section acts independently, which is equivalent to assuming that the pressure is dominated by the height of the section rather than the length of the fracture (Figure 2.1 b). This is true for fractures with length much greater than height. This difference leads to a completely different way of solving the problem. In the PKN model, fracture mechanics and the effect of the fracture tip are ignored and focus is based on the effect of fluid flow in the fracture and to the corresponding pressure gradients. In the KGD model, the tip region is much more important and the fluid gradients can be approximated with significant accuracy.

Another form of fracture geometry is the penny shape fracture (Figure 2.1c). In this type of geometry, fracture propagation takes place within a given plane and symmetrically with respect to a point contained in this plane. The penny shape

fracture was originally studied by Abe et al. (1976) for dry rock mass conditions. In their work they assumed a uniform distribution of fluid pressure and constant fluid injection rate. They also considered the fluid lag concept between the fluid front and the fracture tip. They concluded that in most practical applications, the fracture propagates in a "toughness dominated" regime (i.e most energy is expended in extending the fracture as opposite to the "viscosity dominated" regime, where most energy is expended in viscous fluid dissipation). The concepts of energy dissipation are also applicable to the other two cases of geometric models.

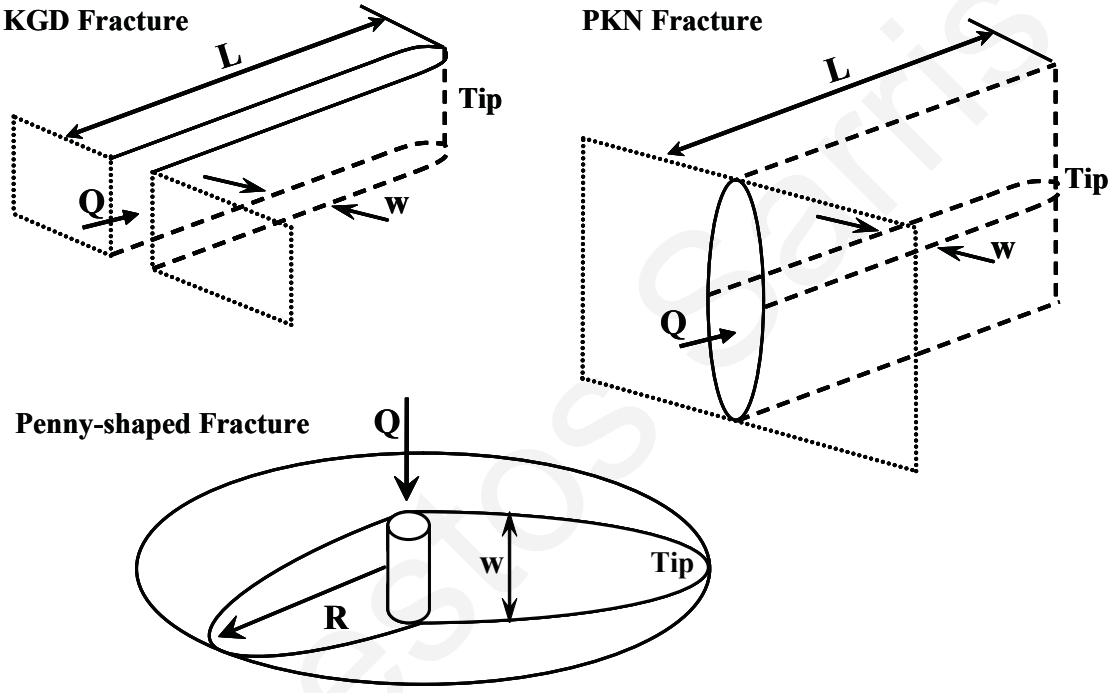

Figure 2.1: Hydraulic fracturing models

A significant amount of research contributions is oriented in the modeling and is usually dedicated to the development of numerical algorithms and simulators. A simulator is a computational implementation of a model. These models which are based on the above geometrical models and their extensions are often used to predict the propagation of hydraulic fractures in the complex and variable geological conditions. Warpinski et al., (1994) performed a detailed comparison of the predictions of some numerical simulators used in practice (Clifton & Abou-Sayed, 1981; Ingraffea & Boone, 1988; Advani et al., 1990; Sousa et al., 1993) and showed difference between numerical simulators and experimental data. The difference in the prediction of the fracture length varies up to three times. The predictions of the

fracture width differed on up to 20%, whereas the predictions of pressure at the wellbore varied by a factor of two. As a result of the discrepancies between the numerical models, significant efforts have also been oriented towards a more rigorous theoretical analysis of the hydraulic fracturing process (Adachi, 2001).

2.2.2 Poroelastic coupling of fluid flow-deformation

Rocks are in most cases porous materials. The pores in these rock materials may contain various fluids also called pore fluids. In complex fluid systems like oil reservoirs, the pore fluids may contain oil, with fractions of natural gas and water. When the fracturing fluid is injected down the borehole in a hydraulic fracturing treatment, the oil is displaced and temporarily replaced by the fracturing fluid. It is possible that the pores may be fully or partially occupied by the complex system of fluids. The transition from partially to fully occupied pores is given by the degree of saturation of the porous materials. It is also mentioned that there is a case where the rock maybe fully dry and that corresponds to the case where only highly compressible gas will be present in the pores. The presence of especially highly incompressible liquids such as oil and water, significantly modifies the mechanical behavior of the porous materials. In the opposite case where the pores are partially filled with compressible fluids, any compressive load acting on the saturated porous material will compress the pore space, and thus the pore fluids (Schmitt & Zoback, 1992).

The analysis of a poro-mechanical system is usually performed under two conditions in the attempt to isolate the time dependency which is introduced in the poroelastic equations. The first condition is the rapid loading, under which the pore fluid has very little time to escape and excess pore pressures are generated which resist the deformation of the porous material. Any condition related with this type of loading is also known as undrained condition. The opposite case is slow compressive loading under which the pore fluid has plenty of time to dissipate or diffuse. Any condition related with this type of loading is also known as drained condition and it does not contribute to an apparent stiffening of the porous materials. Therefore, it is evident that the deformation and pore fluid flows are coupled (Detournay & Cheng, 1988).

The first contribution in the poroelastic analysis was described by Terzaghi (1925) for the time dependent deformation of porous materials which otherwise do not show any sensitivity to the rate of loading. Since then the classical theory of

consolidation was formulated for the gradual settlement of water saturated soil. A further and more consistent theory for cohesive porous materials capturing the time dependence aspect of the problem was first described by the pioneering work of Biot (1941). The relation of the poroelastic behavior and the mechanical behavior of rock was first discussed by Geertsma (1957). Since then, research of the poroelastic behavior of fluid saturated rock has been exponentially increased (Berryman 1992; 1993).

In summary, the creation of excess pore pressures and pore pressure gradients modify the mechanical behavior of saturated porous materials. The problem is further complicated by the fact that the pore pressures and pore fluid flow are in return partly controlled by the deformation of the porous materials. This behavior of saturated porous materials is thus characterized by coupled deformation-flow mechanisms (Detournay et al., 1986; Cheng et al., 1993).

2.2.3 Fluid driven fractures in poromechanical systems

The problem of fluid driven fractures is characterized by both the fluid pressure in the fracture responsible for deforming and splitting the solid formation and by the pore pressures in the saturated poromechanical system. Excess pore pressures counteract the fracture fluid pressure. The fracture fluid pressure can thus be expected to be less efficient in a saturated porous material (Thiercelin et al., 1987). Because of the time dependency which is introduced with the pore pressure in the poromechanical equations, also the hydraulic fracturing process becomes time dependent.

The fluid driven fracturing process is then further complicated when the porous material is permeable to the fracture fluid. The fracture fluid will then leak-off from the fracture into the surrounding material. Adjacent to the fracture, pore pressure will build-up which is equally large as the fracture pressure. Furthermore, if the leak-off is high enough, the fracture pressure may drop when the fluid influx in the fracture is lower than its leak-off in the porous domain. However, it is possible that the fracture pressure for high injection rate will increase even under such of leak-off. This interaction is also known as the back stress effect which results in paradoxical elevated fracturing pressures but small fracture width. At this point it is reasonable to assume that fluid flow in the fracture and from the fracture into the material may introduce another time dependent response. Consequently, the mechanical response of the porous material is coupled with different fluid flows, a) within the fracture, b)

from the fracture into the porous material and c) fluid movement in the porous material characterized by different flow mechanisms when several pore fluids are present.

In summary, fluid driven fractures in porous domains are characterized by the coupling between continuum mechanics, fracture mechanics and fluid mechanics. The continuum mechanics describes the deformation of the material under external and internal loading. The fracture mechanics describes the propagation while the fluid mechanics describes the mechanism of fluid flow inside the fracture and in the porous domain.

2.2.4 Analytical works for impermeable and permeable domains

Among the most important work in impermeable elastic domain was the work of Spence & Sharp, (1985) which presented a self-similar solution for a KGD propagating fracture with finite toughness. They combined the lubrication theory for the fluid flow and elasticity theory for the plane strain geometry to model the fracture opening under a given pressure distribution. They assumed that propagation is controlled by the stress intensity factor and the fracture opening is obtained from a square-root tip asymptote.

Another significant work in which self-similar solutions were presented for the pressure, opening and length derived for a constant flow boundary condition at the fracture inlet, was presented by Biot et al. (1986) for the hydraulic fracture process by applying Lagrange's equations of classical mechanics. Their analysis was focused on an elliptical fracture shape and Newtonian fluid.

One of the first research works based on a poroelastic medium was presented by Advani et al., (1987) in which they approached the problem of a penny-shaped hydraulic fracture. They derived self similar form of solutions separating the spatial and time components for both Newtonian and non-Newtonian fluids using Lagrangian, explicit time-dependent formulation. However, a significant limitation of that work was the inconsistency in the assumed spatially uniform pressure distribution inside the fracture and the fracture propagation in a viscosity-dominated regime.

A significant work in which the fluid lag was originally predicted was presented by Nilson (1988). In this work, the author developed a solution for the plane-strain (KGD) fracture in which a degenerated form of the continuity equation was used in the region of the crack tip, where the value of the crack opening goes to zero. A

constant pressure boundary condition was applied at the fracture inlet. Two of the most important results of this research work were a) for the case of zero toughness the solution predicts the presence of a lag between the fluid front and the fracture tip with a cusp-tip shape b) for the finite toughness case, the solution fails to predict any lag and a rounded shape is observed for the tip. Moreover, the fluid pressure was predicted to be finite which is inconsistent with the Reynolds lubrication equation.

Based on previous research works and a detailed review of the coupled problem of fluid flow and fracture mechanisms, Desroches et al., (1994) redefined the problem by analyzing the near tip area of the fracture for the case of zero toughness in impermeable elastic solid. From their seminal work under the assumption that the fluid flows up to the tip, it was recognized that the strong fluid-solid coupling in the near tip region, actually corresponds to an exact matching singularity at the fracture tip between the lubrication and elasticity equations and hence they revealed the existence of the asymptotic behavior close to the fracture tip. For the purpose of their analysis they utilized complex potential theory (Muskhelishvilly, 1953). Their work was named the "SCR tip asymptote" after their work in Schlumberger Cambridge Research. This work was derived for a semi-infinite fluid-driven propagating fracture under constant velocity.

Another related work based on the approach of Spence & Sharp (1985) and extending the work of Desroches et al., (1994) was the development of a self-similar asymptotic solution for the case of zero toughness and a finite fracture by Carbonell & Detournay (1998). Their work suggested that the global solution, defined as the evolution of fracture length, the fluid pressure and the fracture aperture at the inlet, is hardly influenced by the details of the solution at the tip area under conditions where the energy dissipation in the fluid is much larger than the energy expended in fracturing the solid formation (Detournay, 1998). It was recognized from that point that a key question in hydraulic fracturing is the understanding of the viscosity and toughness dominated regimes. Indeed from the previous analytic works, the zero energy release rate and negative infinite fluid pressure at the tip, leads to the existence of a fluid lag between the fluid front and the tip of the moving fracture. This has lead to the beginning of many dedicated research works to analyze the fluid lag.

Extending the previously explained concepts in poroelastic media, Lenoach (1995) presented expressions for these tip asymptotes for the case of a very permeable rock assuming a pressure independent fluid leak-off rate.

The influence of the fluid lag in the propagation of three-dimensional fractures using a numerical finite-element scheme was studied by Advani et al., (1997). They found that that the fluid lag could be responsible for the presence of abnormal excessive pressures (which is currently the main open question in practice) at the wellbore in real treatments when compared with predictions given by simplified models like the PKN. However, their analysis was performed with constant fluid pressure inside the crack, which essentially requires a large-toughness boundary condition which forces the energy dissipation to move in the toughness dominated regime.

A detailed study of the processes occurring near the tip of a fluid-driven fracture propagating in an elastic medium with arbitrary toughness was presented by Garagash (1998). In particular, he focused on searching for a solution that considers the lag between the fluid front and the fracture tip. Additionally, he contributed to the poroelasticity aspect of the problem by analyzing the tip region of a hydraulic fracture propagating in a permeable saturated rock under certain limiting conditions. The fluid lag was assumed to be filled by pore fluid, and a consistent solution that describes the circulation of pore fluid between the rock and the tip cavity was found. This solution satisfies simultaneously the diffusion equation in the permeable rock, the equations of linear elastic fracture mechanics and the lubrication theory for the flow of pore fluid in the cavity. The condition under which the absolute fluid pressure becomes zero was also predicted.

Applying all the knowledge learned from the plane strain geometry, Savitski (2000) presented a self-similar solution for the problem of a penny-shaped fracture propagating in an impermeable, elastic medium with zero toughness and Newtonian fluid. The solution was based on Spence and Sharp's approach and also makes use of the SCR tip asymptotes (Desroches et al., 1994). His work improved the numerical convergence and accuracy of the solution (Savitski & Detournay 2000; 2001b).

Improving their previous work, Garagash (2000; 2002) introduced an asymptotic self-similar solution for the case of a KGD crack propagating in an impermeable, elastic medium with Newtonian fluid and large toughness, under the assumption of constant fluid injection rate. The range of validity of the asymptotic solution in terms of critical value of toughness is also established in this work. In a similar approach, large-toughness solution for the case of a penny-shaped crack has also been derived by Savitski (2000) and Savitski & Detournay (2001a).

Lecambion & Detournay (2007) presented an implicit moving mesh numerical algorithm to study the propagation of hydraulic fractures in impermeable medium. The fluid front was allowed to lag behind the fracture tip. Their solution, expressed in appropriate scaling, involves a self similar solution characterized by a dimensionless stress which controls the size of the fluid lag. Attention was focused on the efficiency of the numerical algorithm rather than on the understanding of the dissipative mechanism of this dimensionless stress.

Extending the work of Lecambion & Detournay (2007) on the issue of the fluid lag, Adachi & Detournay (2008) presented a numerical solution of the fluid driven fracture problem under plane strain conditions in a permeable elastic medium. Their solution was restricted to the cases where the toughness of the medium and the lag between the fluid front and the fracture tip are both zero. These conditions correspond to the cases where the energy rate dissipated in fracturing the medium is negligible compared to the viscous dissipation (zero toughness) and the far field stress perpendicular to the fracture is large which actually forces the fluid lag to be zero. They introduced two dimensional parameters the first of which controls the gradual disappearance of the lag in the absence of leak-off. The second one tracks the transition under conditions of zero lag from a regime of propagation without leak-off to another where leak-off dominates.

Closing the discussion on the analytical framework devoted mostly in the understanding of the propagation regimes, the fluid lag concept and the fluid losses from the fracture towards the porous domain, it is also worth mentioning the work developed by Zhang et al., (2001) on the study of a penny-shape hydraulic fracture propagating close to a free surface. Their work was motivated by the work of Murdock (1993) who was originally the first contribution to propagate near surface hydraulic fractures in soil like materials. The applicability of their work is oriented to the stimulation of caving of ore bodies in large-scale mining operations and to environmental applications. Regarding the modeling of the fluid leak-off processes, it is important to mention that most of the studies (Williams, 1970; Settari, 1985; Yi & Peden, 1994; Van Damme, 1989) are based on the early contribution of Carter (1957), which is still used in the practical treatments.

2.2.5 Numerical works for impermeable and permeable domains

In the attempt to analyze the complex behavior of fluid driven fractures, a significant amount of contributions were also devoted in the numerical development of models and techniques to optimize the procedure of the analysis. Among the most important contributions, utilizing a finite element formulation was described by Advani et al. (1990) for the analysis of a planar vertical hydraulic fracture of arbitrary shape propagating in a layered medium. They solved simultaneously the elasticity, lubrication and fracture propagation equations. The model is also capable in dealing with power-law fluids with arbitrary injection rates and time-dependent leak-off. However, the numerical model that they proposed does not capture the right tip asymptotes and the pressure at the tip. A numerical model for the case of a PKN hydraulic fracture propagating in a permeable medium taking also into consideration poroelastic effects was proposed by Detournay et al., (1990). The model is based on an explicit finite difference scheme with a moving mesh for the spatial discretization.

In the formulation of the complex behavior of the fluid driven fractures, integro-differential equations arise which accurately describe a certain behavior. This type of equations is extremely notorious for numerical solution. Desroches & Thiercelin (1993) were among the first to present a numerical model based on an integro-variational approach for the elasticity equation, relating the gradient of the fracture aperture to the net fluid pressure in the fracture. Provided that the stress intensity factor is strictly positive, this variational formulation ensures the correct behavior of the fracture opening in the vicinity of the tip.

The analysis of penny-shape fractures has also attracted many contributions in the development of numerical algorithms. Yuan (1997) proposed a pseudo-explicit finite difference scheme to solve the problem of a penny-shaped fracture propagating in an elastic, permeable medium with power-law fluid taking into account poroelastic effects. The fluid leak-off in the numerical scheme is accounted either by a pressure-independent or pressure-dependent law. An implicit finite difference scheme for the case of a penny-shape fracture with zero toughness was proposed by Savitski (2000). The scheme considered the known tip and inlet asymptotes for opening and pressure, thus reducing the computational effort in the analysis.

Recently a new method was introduced in the analysis of fractures known as the displacement discontinuity method (DDM). In a standard fracture mechanics analysis, the stress and strain fields responsible for fracturing the material are obtained with

finite elements or boundary elements. However, the use of FEM and BEM presents limitations in the sense of computational efficiency under certain problems. In finite elements, the accurate numerical solution is based on the domain discretization and powerful remeshing techniques that are incorporated to complete this cumbersome task where heavy computational power is needed. In boundary elements, the discretization of the boundaries is only needed and the limitation arises at the singularity in the algebraic system of equations which is obtained when the upper and lower fracture surfaces are modeled in the same plane. The displacement discontinuity method is based on the concept that is possible to make a discrete approximation to a distribution of displacement discontinuities along a fracture in a body by subdividing the fracture into elements and assuming to vary over the individual elements according a predetermined mode. Among the first contributions utilizing the displacement discontinuity method in hydraulic fracturing in porous materials was a study published by Van Damme et al., (1989). They presented a numerical model for coupling the diffusion and deformation induced by the opening of a hydraulic fracture in a poroelastic medium under rapid loading.

A fully-coupled numerical model for simulating planar three-dimensional hydraulic fractures in layered media was presented by Siebrits & Peirce (2000). The algorithm uses a Fourier-based displacement discontinuity method to generate the layer-dependent influence coefficient matrix. The fluid flow equations are solved using a standard finite difference scheme. The coupling between the equations is performed using a damped quasi-Newton scheme (Siebrits & Peirce, 2001). Since then, many contributions have been published with this method as it is recognized for its rapid convergence. Dong & De Pater (2001) presented a new formulation using collocation points for straight fractures and a standard Cauchy type formulation for curved fractures for two dimensional elastic hydraulic fractures. Their formulation greatly improves the solution time for extending hydraulic fractures.

2.3 Inelastic Processes in Hydraulic Fracturing

The study of the inelastic behaviour in hydraulic fracturing was originally studied in the seminal contribution of Papanastasiou & Thiercelin (1993). Since then a significant number of research works has been based in their work and the analysis of inelasticity in hydraulic fracturing was established. In this section a brief discussion is

performed to analyse the most important aspects of inelastic processes in hydraulic fracturing.

It is generally accepted that due to the fracture loading, significant stress concentration is accumulated near the tip region. This stress concentration is capable to create micro cracks and void coalescence which is primarily occurring in the fracture process zone near the fracture tip. The motivation which triggered the research work based in inelastic processes is the study of the discrepancy in the observed high net pressures needed to extend the fractures (Papanastasiou 1997; 1999).

The incorporation of inelastic yield criteria is also motivated by the fact that fracturing in weak rocks (sandstone) will create plastic zones that are significantly larger than the small ones for which Linear Elastic Fracture Mechanics theory can be applied. According to conventional fracture mechanics, the stress intensity is utilized as a propagation criterion and a main assumption that is required is that the process zone has to be small compared with the dimensions of the fracture. Therefore, the description of the irreversible deformation needs to be included in the analysis. Papanastasiou & Thiercelin (1993) and Papanastasiou (1997; 1999), performed detailed studies based on numerical simulations using incremental plasticity theory and investigated the influences of inelasticity in hydraulic fracturing. Papanastasiou (1997) found for a propagating fracture in an elastoplastic material the plastic zones which are created in the fracturing process unload elastically behind the advancing fracture tip and the new area near the current tip deforms plastically. In other words, the rock mass remote from the fracture may deform elastically, whereas the region near the body of the fracture may deform plastically and finally unloads elastically after the fracture has advanced when the fracture is driven in weak formation. The plastic yielding takes place in the area near the tip, which is characterized by a high stress concentration. The plastic zones have the so-called ‘rabbit ears’ shape. The size of the plastic zones is greatly influenced by the contrast of the magnitude of the far-field insitu stresses, the strength of the rock, the effective Young’s modulus, the viscosity of the fracturing fluid, and the propagation velocity. These parameters will be analyzed in detail latter in this section.

Papanastasiou (1999) showed that the presence of yielded material around the tip has the effect of screening the remote loads which increases significantly the level of the apparent fracture toughness. Therefore, the plastic yielding near the tip of a

propagating fracture provides an effective shielding. Van Dam et al., (2002) performed large scale laboratory experiments and has confirmed the numerical work of Papanastasiou (1999). They noted that the important effect of plasticity was on the shielding of the fluid loading from the fracture tip. A stronger loading close to the tip was observed during fracture extension. This elevated loading of the fracture, had an important influence on the fracture geometry. The fracture width profile that is created is wider and the fracture length is shorter for a certain injection volume. Additionally, another possible influence of high net pressure may be explained by underestimation of the elastic rock modulus. The value in soft rock can be underestimated by a factor of two to three (Van Dam et al., 2002). In field applications other possible reasons could be that rock behaviour may be governed by anisotropy, large-scale heterogeneities and natural fractures as pointed out by De Pater et al. (1994).

Generally, all the aforementioned contributions result in the following mechanism of the appearance of plastic yielding. Soft and hard rocks are characterized by low tensile strength compared to its compressive strength (σ_c = 8 - 10 σ_t). Therefore, tensile fracturing conditions will be created if the rock is loaded to rupture. This is actually the case for fluid-driven fractures in which the high fluid pressures will lead to extensile loading ahead of the fracture tip. Ahead of the fracture and at a certain distance from the tip, stresses tend to reduce to the far field insitu stress field. At a distance offset from the fracture plane, the stress decreases strongly in a direction perpendicular to the fracture plane, whereas the stress along the fracture flanks is nearly unaffected. This stress situation and loading near the fracture induces shearing of the rock. Fluid driven fractures are then expected to create shear plastic deformation around the fracture tip.

There are few contributions that account for the elastic-plastic behaviour of fluid saturated porous media when analysing fracture propagation. Plastic dilatancy effects at the crack tip were also analyzed by Van Den Hoek et al., (1993) with the conduction of laboratory experiments. Near tip asymptotic solutions were reported with a Drucker-Prager yield condition with volumetric associative (Bigoni & Radi 1993) and non-associative flow law (Radi et al., 2002) with isotropic hardening to analyse steady crack growth firstly in plastic dry domains and then extend their work to fluid-saturated porous mechanics. Papanastasiou and Durban (2001) derived the asymptotic singular stress fields for a Drucker-Prager non-associative power law hardening material. However, all these works are restricted to proportional loading

where as in hydraulic fracturing due to elastic unloading the stress field near the fracture tip follows a non-proportional loading and thus an incremental plastic theory must be used.

2.3.1 Scaling of plastic zones

When plastic deformation takes place, it is generally accepted that the influence of dilation and yielding would become important. Due to the material model and loading conditions the problem results in extreme complexity that prevents the determination of the exact location of the plastic zone boundaries. Therefore, instead of determining the exact size of the plastic zones in the poroelastoplastic continuum, an attempt is made to reach conclusions through the scaling on the most important parameters that affect the size of the plastic zones.

Previous research studies (Papanastasiou & Thiercelin 1993; Papanastasiou 1997; Papanastasiou 1999) have showed that in a dry domain the size of the plastic zones l_p, can be a function of the deviator of the insitu stress field.

$$\ell_p \propto \frac{\sigma_1 - \sigma_3}{\sigma_1 + \sigma_2 + \sigma_3} \tag{2.1}$$

where σ_1, σ_2, σ_3 are the insitu principle stresses.

According to equation (2.1) large yielding is not expected to occur when the fracture propagates in a hydrostatic stress field. However, in rock formations a highly non hydrostatic stress field is encountered due to the significant stress difference between vertical and horizontal stresses. It is then clear that with an increase of the insitu stress difference, the plastic zones will increase.

Following the stress analysis, Papanastasiou and Thiercelin (1993) showed that when the fracture propagates in a rock formation with high fracture toughness, the size of the plastic zones developing around the tip is greater. Therefore, the main material parameters that affect the size of the plastic zones are the fracture toughness, K, and the tensile yield strength, σ_T. For a plane strain problem, in an elastic - perfectly plastic material, the approximate distance to the boundary ahead of the fracture tip is given by:

$$\ell_p = \frac{1}{3\pi}\left(\frac{K}{\sigma_T}\right)^2 \tag{2.2}$$

However, equation (2.2) is valid for linear fracture mechanics for a uniformly loaded fracture. Advanced asymptotic analysis by Desroches et al., (1994) found for a fracture propagating in a domain with zero fracture toughness, the singularity that dominates in the near tip region is weaker than the inverse square root singularity of linear elastic fracture mechanics. Following the work of Desroches et al., (1994), Garagash & Detournay (2005) have confirmed that the exact match of this weak singularity between lubrication and elasticity leads to a self similar solution that the singularity can be a function of the fracture toughness of the rock. From the above discussion, the characteristic length of the elastoplastic problem relates the material and the fluid rheology parameters with the size of the plastic zones through:

$$\ell_p \sim \frac{E'^2 \mu v}{\sigma_T^3} \tag{2.3}$$

where E' is the plane strain modulus, μ is the fluid viscosity, v is the propagation velocity and σ_T is the tensile yield strength. According to this characteristic length, high values of elastic modulus, viscosity, propagation velocity and low values of rock strength will lead to higher stress concentrations near the tip and higher plastic zones are expected to develop. Papanastasiou and Thiercelin (1993) found that equation (2.3) dominates in hydraulic fracturing resulting in a characteristic length of an order of magnitude greater than the characteristic length of equation (2.2). This finding is explained by the fact that equation (2.2) is based on LEFM and completely neglects the fluid rheology contribution to the plastic zone development.

2.3.2 Hydraulic fracture initiation in weak formations

Weak formations can be regarded as soils or rocks with low cohesion or cohesionless behaviour. In these types of formations, one of the objectives is to study the prediction of the fracture initiation and propagation pressure. Based on this objective many researchers (Mori & Tamura 1987; Panah & Yanagisawa 1989) have performed experimental and numerical studies to understand the parameters affecting fracture initiation and propagation pressures. They performed borehole injection tests on

cohesive soils at low stress, and found that the laboratory observations of the injection pressure were consistent with the prediction of shear failure. Shear failure as a dominant fracturing mechanism was also observed by Bohloli & de Pater (2006) and recently by Dong (2010) by examining the influence of confining stress on injection pressure in tests on sand (cohesionless formations) under well-defined boundary conditions. They found that a strong influence exists between the confining stress and the injection pressure. At higher confining stress, the ratio of maximum injection pressure to confining stress was lower, because shear failure depends on the confining stress levels.

2.3.3 Inelastic process in the cohesive zone and energy distribution

The various possible mechanisms that dissipate inelastic energy when a fracture is driven in a cohesive material were discussed by Ritchie (1999). These mechanisms can be also considered in the process zone. Fracture growth can be considered a mutual competition between intrinsic microstructural damage mechanisms which promote fracture propagation ahead of the fracture tip and extrinsic fracture tip shielding mechanisms which act primarily behind the fracture tip to retard fracture propagation. This analysis was originally proposed by Ritchie (1999). Intrinsic damage mechanisms typically involve processes which create micro cracks or voids by dislocation pile-ups or interface decohesion in the highly stressed region ahead of the fracture tip leading to classical failure by cleavage, inter-granular cracking or micro-void coalescence. Extrinsic shielding mechanisms, conversely, result from the creation of inelastic zones surrounding the fracture wake or from physical contact between the fracture surfaces through wedging, bridging, sliding or combination of them. Intrinsic mechanisms are inherent property of the material, and thus are active irrespective of the fracture length or the geometry of the numerical model under monotonic loads and they control the driving forces to initiate the fracture (stress intensity). Extrinsic mechanisms, act in the fracture wake and are critically dependent on fracture size and geometry and play a predominant role in the driving forces required to continue fracture growth.

Based on the above discussion the question that remains to be answered is where to locate the position of the cohesive fracture tip. The position of the cohesive fracture tip taken to coincide with the peak traction was discussed by Shet & Chandra (2002). According to their work, this selection facilitates a part of the cohesive energy

to be dissipated in the forward region of the fracture while the rest of the energy is to be dissipated in the wake region. The conditions prevailing in the process zone will vary according to the type of material, geometry and loading conditions. Fracture growth is generally promoted by dissipation resulting from microstructural damage mechanisms in the forward region, both in the bounding material and the cohesive zone, while fracture advancement in impeded by other dissipation mechanisms. However, both physical processes consume energy, part of it being dissipated into the material and the rest into the fracture within the cohesive zone.

The various energy dissipation quantities as discussed above can be studied from the conservation of energy implied by the first law of thermodynamics stating that the time rate of change of kinetic energy and internal energy for a fixed body of material equals the sum of the rate of work done by the surface and body forces given by (e.g. Li and Chandra 2003; Abaqus 2006):

$$\frac{d}{dt}\int_{\mathbf{V}}\left(\frac{1}{2}\rho\mathbf{v}\cdot\mathbf{v}+\rho U\right)dV+\int_{intS}\overline{\mathbf{T}}\,\overline{\delta}\,dS=\int_{extS}\mathbf{t}\cdot\mathbf{v}dS+\int_{V}\mathbf{b}\cdot\mathbf{v}dV \tag{2.4}$$

where ρ is the current density, $\mathbf{v}$ is the velocity field vector, U is the internal energy density, V is the control volume, *intS* is the surface where intrinsic processes are active, *extS* is the surface where extrinsic processes are active, **t** is the exterior surface traction vector, **b** is the body force vector and **T** are the tractions active across the interface. For the present problem, the kinetic energy term is ignored and hence, the internal energy for the system under consideration can be written as

$$\begin{aligned}&E_u=\int_0^t\left(\int_V\boldsymbol{\sigma}:\dot{\boldsymbol{\varepsilon}}^{el}\,dV\right)dt+\int_0^t\left(\int_V\boldsymbol{\sigma}:\dot{\boldsymbol{\varepsilon}}^{pl}\,dV\right)dt+\int_0^t\left(\int_{\text{int}S}\overline{\mathbf{T}}.\overline{\boldsymbol{\delta}}\,dS\right)dt+E_i\Leftrightarrow\\&E_u=E_e+E_p+E_c+E_i\end{aligned} \tag{2.5}$$

where t is the time, E_e is the elastic recoverable energy, E_p is the plastic dissipated energy, E_c is the cohesive energy and E_i is any other inelastic work. The external work due to applied force up to time t is given by

$$E_w=\int_0^t\left(\int_S\mathbf{t}.\mathbf{v}\;dS+\int_V\mathbf{b}.\mathbf{v}\;dV\right)dt \tag{2.6}$$

2.4 Conventional Fracture Mechanics and Cohesive Zone Mechanics-Closing the Gap

In this section, a detailed analysis is performed based on the fracture mechanics theories because often discrepancies arise under which conditions or assumptions they can be applied. The discussion will be based on the most notorious open questions still under debate in the use of the cohesive zone mechanics as a fracture propagation criterion.

2.4.1 Critical stress intensity factor and energy release approaches

There are two alternate approaches to fracture analysis. These are the energy criterion approach and the stress intensity approach. As it will be discussed next, these two approaches are equivalent in certain circumstances. However, it is understood that the critical stress intensity factor does not necessarily emerge from an energy release rate approach as these two different approaches are somehow different.

The above discrepancy can be analyzed with the LEFM theory. The energy approach states that fracture extension occurs when the energy available for growth is sufficient to overcome the resistance of the material. This material resistance may include the surface energy, plastic work or other types of energy dissipation associated with a propagating fracture. Griffith (1920) was the first to propose the energy criterion for fracture, but Irwin (1956) developed the present version of this approach. The energy release rate G, is defined as the rate of change in potential energy with the fracture area for linear elastic materials. At the moment of fracture, the energy release rate equals the critical energy release rate, which is a measure of fracture toughness ($G = G_C$). For a fracture of length $2a$ in an infinite plate subjected to remote tensile stress, the energy release rate is given by:

$$G = \frac{\pi \sigma^2 \alpha}{E} \tag{2.7}$$

where E is the Young's modulus, σ is the remotely applied stress, and α is the half length of the fracture. At fracture ($G = G_C$), equation (2.7) describes the critical combinations of stress and fracture size for failure as:

$$G_C = \frac{\pi \sigma_f^2 \alpha_c}{E} \tag{2.8}$$

where σ_f is the remotely applied stress at failure and α_c is the critical half length of the fracture. Note that for a constant value of G_C the failure stress varies with $1/\sqrt{\alpha}$. The energy release rate G is the driving force for fracture, while G_C is the material's resistance to fracture. This concept is also accepted in the strength of materials. The applied stress can be viewed as the driving force for plastic deformation, while the yield strength is a measure of the material's resistance to deformation.

The stress intensity approach states that in an element near the tip of a fracture in pure tension in an elastic material, the stress and strain fields are proportional to a single constant K_I (mode-I opening). If this constant is known, the entire stress distribution at the fracture tip can be computed through a set of well established equations (e.g. Anderson, 2005). This constant K_I, which is called the stress intensity factor, completely characterizes the fracture tip conditions in a linear elastic material. If the material is assumed that it fails locally, at some critical combination of stress and strain, then it follows that fracture propagation must occur at critical stress intensity K_{IC}. Thus, K_{IC} is an alternate measure of fracture toughness. For a uniformly loading crack in tension of length a, the Stress Intensity Factor is defined as

$$\mathrm{K_I} = \sigma \sqrt{\pi \alpha} \tag{2.9}$$

Failure occurs when $K_I = K_{IC}$. In this case, K_I is the driving force for fracturing the material and K_{IC} is a measure of material resistance. As with G_C, the property of similitude should apply to K_{IC}. That is, K_{IC} is assumed to be a size independent material property. Combining equations (2.7) and (2.9) results in a relationship between K_I and G (Irwin, 1957):

$$G = \frac{\mathrm{K_I^2}}{E} \tag{2.10}$$

where E is the young modulus, $E = E$ for plane stress and $E' = E/(1-\nu^2)$ for plane strain conditions. The same relation obviously holds for G_C and K_{IC}. Thus, the energy release rate and stress intensity approaches are essentially equivalent and uniquely related for linear elastic materials. Hence, the energy release rate quantifies the net

change in potential energy that accompanies an increment of fracture extension and stress intensity factor characterizes the stresses, strains and displacements near the fracture tip. *G* describes a global behavior while *K* is a local parameter.

2.4.2 Equivalence between the cohesive zone model and the Griffith energy approach

The equivalence between the cohesive zone and the energy approach can be easily proved with the non linear theory of the J-integral. The J-contour integral has been successfully applied by researchers as a fracture parameter for non linear materials. Rice (1968) was the first to extent the fracture mechanics methodology well beyond the validity limits of LEFM. He showed that the non linear energy release rate J-integral could be written as a path-independent line integral. Hutchinson (1968) and Rice & Rosengren (1968) also showed that the J-integral uniquely characterizes fracture tip stresses and strains in non-linear materials. Thus J-integral can be viewed as both, an energy parameter and a stress intensity parameter. According to Rice (1968), the J-integral is a more general version of the energy release rate. For the special case of a linear elastic material, $J = G$ and hence

$$J = \frac{K_I^2}{E'} \tag{2.11}$$

For a linear elastic Mode-I fracture, the J-integral is also uniquely related to the difference in energy absorbed by specimens with neighboring fracture sizes. This finding is very important when the fracture grows. It can be demonstrated that there is a relation between the CTOD (Crack Tip Opening Displacement) and the J-integral.
The application of the J-integral methodology can be seen in Figure (2.2). It is assumed that the fracture is under a state of mobile equilibrium. In the strip yield zone model, the zone is modeled by surface tractions along the crack face. The cohesive forces acting on the fracture are given by $\sigma(\delta)$. The separation distance beyond which the cohesive tractions vanish is given by δ^* or by the critical separation sign δ_c.

Consider the closed contour path Γ, is the curve surrounding the fracture tip as shown in Figure (2.2). The boundary and initial conditions on this path are given by

$$\Gamma^{-}\Big|_{dx=ds}^{dy=0} \qquad \Gamma^{+}\Big|_{dx=-ds}^{dy=0}$$
$$T_1 = 0 \tag{2.12}$$
$$T_2 = -\sigma(\delta)$$

where T_i are the tractions acting on the fracture faces defined in an outward normal direction along the contour path Γ and ds is an element of length along path Γ.

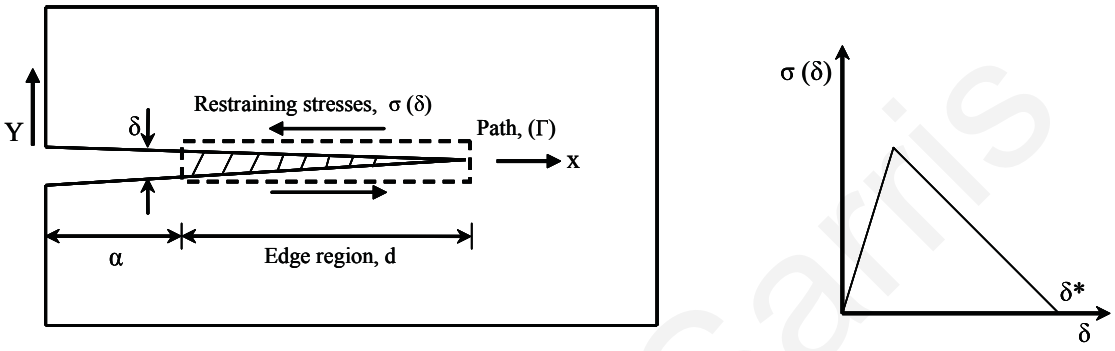

Figure 2.2: Fracture mechanics model

The J-integral is being evaluated in an anticlockwise sense starting from the lower flat surface and yields

$$J = \int_{\Gamma}\left(U_d dy - T_i.\frac{\partial u_i}{\partial x} ds\right) \Leftrightarrow$$
$$J = -\int_{\Gamma^-} -\sigma(\delta)\frac{\partial u_2}{\partial x} ds - \int_{\Gamma^+} -\sigma(\delta)\frac{\partial u_2}{\partial x} ds \Leftrightarrow$$
$$J = -\int_{a}^{a+d} \sigma(\delta)\frac{\partial}{\partial x}(u_2^+ - u_2^-)\, dx \Leftrightarrow \tag{2.13}$$
$$J = -\int_{a}^{a+d} \sigma(\delta)\frac{\partial \delta}{\partial x} dx \Leftrightarrow$$
$$J = \int_{0}^{\delta^*} \sigma(\delta)\, d\delta$$

where U_d is the strain energy density in the edge region d of the fracture, u_i is the displacement vector, u_2 are the vertical displacements, α is the visible fracture length. The value of the J-integral which will cause fracture extension is given by the integral of the cohesive forces (Equation. 2.13).

The fictitious fracture model of Hillerborg et al., (1976) was also called a cohesive zone model and is merely an application of the Dugdale-Barenblatt approach. According to the Hillerborg model, the stress-displacement behavior (σ-δ) observed in the damage zone of a specimen is a material property. At the tip of the traction free fracture, the damage zone reaches a critical displacement δ_C. The traction is equal to the tensile strength σ_t, at the tip of the damage zone. Further assuming that the closure stress and the opening displacement are uniquely related, the critical energy release rate (also termed as cohesive energy density) for the fracture growth is given by

$$G_C = \int_0^{\delta_C} \sigma(\delta) d\delta \tag{2.14}$$

which is virtually identical with equation (2.13) derived via the J-integral approach.

Although the cohesive zone modeling approach has been used by many authors to analyze fracture propagation problems for few decades, the physical interpretation of the cohesive zone is still an issue of debate. The key assumption of this model, that the σ-δ relationship (Figure 2.2) is a unique material property, is not strictly correct. The assumption of the unique material property losses its meaning as in most cases the process zone that is produced is quite large. Furthermore, since the cohesive zone approach states that it has no thickness but has a limiting stress level that affects the stress field in the region surrounding it, the cohesive zone model cannot be considered identical to the conventional continuum fracture mechanics.

2.4.3 Physical meaning of the critical separation distance based on LEFM and cohesive zone mechanics

The separation distance as shown in Figure (2.2) has a special definition based on LEFM and Cohesive zone mechanics. This separation distance can be used as a critical parameter in all the fracture modes. For simplicity we replace the general symbol δ^* with δ_{IC} to discuss the critical separation under mode-I fracture loading and will be only for mode I loading unless stated otherwise.

According to fracture mechanics, Wells (1961), attempted to measure K_{IC} and found that materials were too tough to be characterized by LEFM. He observed that fracture faces had moved apart prior to fracture. He concluded that plastic deformation had blunted an initially sharp fracture. The degree of this fracture

blunting was increasing proportional to the toughness of the material. With this observation Wells (1961) proposed the opening at the crack tip as a measure of fracture toughness also known as the CTOD parameter. The actual relationship between the CTOD, K_I and G depends on the stress state and strain hardening of the material as

$$CTOD = \delta = \frac{G}{m\sigma_Y} \tag{2.15}$$

where δ is the full displacement of the blunted fracture, G is the energy release rate and m is a dimensionless constant with $m = 1$ for plane stress and $m = 2$ for plane strain conditions. There are a number of alternative definitions of CTOD based on fracture mechanics. The two most common definitions are the displacement at the original fracture tip and the 90^0 intercept. The later definition was suggested by Rice (1968) and is commonly used to implement CTOD in finite element measures. Note that these two definitions are equivalent if the fracture blunts in semicircle.

According to cohesive zone mechanics, Chandra & Sigh (1998) identified three specific points on a traction-separation curve which can characterize the position of the fracture tip. The first one corresponds to the case when the displacement reaches δ_{max} and the traction, attaining the cohesive strength, reaches its maximum value on the σ-δ curve. The second point corresponds to the case where the displacement reaches δ_{IC} and the traction has just vanished. The last point is found to be when the material is just about to separate and the cohesive strength and separation are zero on the σ-δ curve. Selection of anyone of these points will have different implications on the physics of the problem. It is generally accepted that the area under the σ–δ curve represents the fracture toughness, $J = G_{IC}$. Selection of the last point implies that the entire cohesive energy will be absorbed by the cohesive zone model (C.Z.M). Such a definition will exclude many inelastic processes, e.g., cavitation damage occurring in the immediate vicinity ahead of a crack tip. On the other hand, if the crack tip is defined at the point of δ_{IC} then the crack has fully separated and has absorbed all the energy required for the decohesion leaving no active wake behind the tip.

2.4.4 Elimination of the fracture tip stress singularity in the cohesive zone mechanics

The cohesive fracture concept, aimed at eliminating the fracture tip stress singularity of the classical linear elastic fracture mechanics (LEFM), was originally proposed by Barenblatt (1962). The strip yield model of Dugdale (1960) which was proposed earlier for estimating the size of the fracture tip plastic zone has also been regarded as a cohesive zone type model with the strip yield zone treated as a cohesive zone.

The physical idea behind the stress singularity cancellation is that fracture growth occurs when the fracture tip reaches a critical value at which the cohesive traction vanishes. Clearly, the cohesive zone modeling approach does not invoke fracture tip stress singularities as in classical fracture mechanics and material failure is controlled by quantities such as displacements and stresses, which are consistent with the usual strength of materials theory.

The mathematical explanation of the stress singularity cancellation which is observed in the near area of a fracture tip is analyzed by Sinclair (1996). Stresses around a fracture tip behave as the inverse of the square root of the distance from the fracture tip according to the LEFM approach. The cohesive stress-separation laws cancel the opening singularity produced by loading remotely from the fracture with the closing singularity produced by cohesive stresses on the fracture flanks near the fracture tip. To further explain this cancelation, we recall that the coefficient of the inverse-square-root singularity in the fracture tip stress field is the stress intensity factor K_I in Cartesian Coordinates x,y where the origin is taken at the fracture tip. The stress intensity factor for mode-I loading is given by

$$K_I = \sigma\sqrt{\pi\alpha} \tag{2.16}$$

where σ is the far field stress and α is the fracture half length (2α for full length fracture).

The cohesive stress σ_c acts on the fracture tip for a small extent $\Delta\alpha$ which is the zone in which the cohesive stresses act. The stress intensity factor at the fracture tip including the small extension is then defined by

$$K_I = -\sqrt{\frac{\alpha}{\pi}}\int_0^{\Delta\alpha}\frac{2\sigma_c(\xi)d\xi}{\sqrt{\xi(2\alpha-\xi)}} \tag{2.17}$$

where $\xi = -x$. By ensuring that the magnitude of the stress intensity factors in both cases is equal, then the singularity cancellation takes place and the fracture tends to have a singularity-free behavior. The main assumption behind the mathematical validity of the above equations is that the length of the cohesive zone is small compared to the fracture length.

2.4.5 Brief review of cohesive zone models

As an alternative approach to the conventional singularity driven fractures, as mentioned above, the cohesive zone concept has evolved as a preferred method to analyze fracture problems in monolithic and composite materials, not only because it avoids the singularity but also because it represents a powerful and efficient technique for computational fracture studies. There are numerous contributions concerning the fracture analysis with cohesive zone models. The following review will be restricted to the most important works with main focus on the shape of the cohesive constitutive laws and the respective problems that they have been used for.

The early conceptual works related to the cohesive zone model, were introduced by Barrenblatt (1959; 1962) who proposed the cohesive zone model to investigate perfectly brittle materials. Dugdale (1960) adopted a fracture process zone to investigate ductile materials exhibiting small scale plasticity. Since then, a series of research work, to mention few (Hillerborg et al., 1976; Needleman and his co-workers, 1987, 1994; Camacho & Ortiz, 1996), have been oriented in the development of the cohesive zone concept in computational fracture mechanics.

Needleman (1987; 1990) was one of the first to use polynomial and exponential types of traction-separation equations to simulate particle debonding in metal matrices. Extending the previous work of Needleman (1987; 1990), Xu & Needleman (1993; 1994) have presented a potential-based cohesive zone model with cohesive elements that are inserted into a finite element mesh in advance and which obey an exponential constitutive law in the normal direction, to study the void nucleation at the interface of particle and matrix material, fast fracture growth in brittle materials under dynamic loading and fracture growth along the interface of bimaterials.

Tvergaard & Hutchinson (1992) used a trapezoidal shape of traction-separation model to calculate the fracture growth resistance in elasto-plastic materials. Another modeling approach which has been proposed by Camacho & Ortiz (1996) was a stress based cohesive zone model where a new surface is adaptively created by duplicating

nodes which were previously bonded. They used linear cohesive fracture models to propagate multiple fractures along arbitrary paths during impact damage in brittle materials.

The work of Xu & Needleman (1994) has been widely used as it is easier to implement into finite element analysis. Some limitations recognized in Xu & Needleman (1994), related to the imposed initial artificial compliance of the utilized cohesive zone law, were addressed by Geubelle & Baylor (1998) and Espinosa & Zavattieri (2003) who have adopted bilinear cohesive zone models by providing an adjustable initial slope in the cohesive law. Geubelle & Baylor (1998) utilized a bilinear cohesive zone model to simulate spontaneous initiation and propagation of transverse matrix fractures and delamination fronts in thin composite plates subjected to low velocity impact.

Shet & Chandra (2002) analyzed the energy balance in a cohesive zone model to simulate the inelastic fracture process. They examined how the external work flows as recoverable elastic strain energy, inelastic strain energy and cohesive energy. The later encompasses the work of fracture and other energy consuming mechanisms within the process zone. They showed that any form of plastic energy in the bounding material surrounding the fracture is not accounted in the cohesive energy. This energy only accounts for cavitation, surface energy and internal grain sliding. Improving their own work Shet & Chandra (2004), have analyzed the effect of the shape of traction-separation curves in inelastic fracture growth and attempt to establish criteria for the selection of appropriate cohesive zone models for fracture analysis.

There are few studies utilizing the cohesive zone model in hydraulic fracturing. Some early studies in this area include the important work of Boone and his co-workers (1986; 1990) in which they used the cohesive zone approach to model the fracture process in impermeable and permeable rocks. Other significant works include the use of the cohesive zone law to propagate fractures in order to investigate the inelastic behavior of rocks in hydraulic fracturing by Papanastasiou & Thiercelin (1993), Papanastasiou (1997; 1999). Improving the research work in hydraulic fracturing Schreffler et al. (2006) proposed a model, with a tip-velocity provided as part of the solution algorithm, and propagated successfully hydraulic fractures in an unknown path that may nucleate everywhere depending only on the stress and pressure fields.

Among the latest contributions using the cohesive zone model for analyzing a hydraulic fracture in non porous and porous domains was the study by Sarris & Papanastasiou (2010). They investigated in detail the influence of the constitutive cohesive zone characteristics (loading and softening part of the constitutive law) on the size of the process zone and consequently on the obtained results in hydraulic fracturing modelling. They further demonstrated that the existence of high confining stresses influences further the size of the process zone both in elastic and poro elastic conditions. Extending their own work, Sarris & Papanastasiou (2011) analyzed the influence of the poroelastic parameters such as the injection rate, formation permeability and rock compressibility in hydraulic fracturing modelling. Furthermore, they included leak-off in their analysis to investigate the effects of the diffusion process.

2.5 Special Issues in Hydraulic Fracturing

This section is concerned with some basic parameters and processes related to poroelasticity and continuum mechanics in hydraulic fracturing. It was considered important to outline them as a special section of this chapter because many contributions have been devoted to the analysis of specialized aspects of the hydraulic fracturing process. These special parameters and processes concerning the poroelastic effects include the influence of leak-off, fluid lag, pore pressure and propagation velocity. The special parameters and processes based on continuum mechanics include the influence of dilatancy in an inelastic analysis, the influence of grain size and finally the influence of the scale which is always a matter of open debate.

2.5.1 Fluid losses or leak-off

Fluid loss or fluid leak-off is defined as the process in which portion of the fracturing fluid infiltrate into the surrounding formation. The fundamentals for analyzing this process were given by Carter (1957), also known as the Carter's leak-off model, which has been successfully used and is widely accepted throughout the industry. Carter's model is based on two major assumptions. The first important assumption is that the fluid loss into the formation can be approximated as one-dimensional flow, perpendicular to the fracture propagation axis. This assumption is actually true and is based on the fact that the zone in which most of the fluid diffusion process takes

place, the filter cake and the invaded zone, is usually a very thin region (mm) compared to the fracture length (m). The second assumption is derived from the nature of the fracturing fluids. These fluids are specifically designed for providing sufficient effective viscosity to open the fracture and create the necessary fracture width to allow for the movement of the proppant particles and minimize the fluid 1osses.

All fracturing fluids possess a cake-building property. This is also called filter cake and helps to control the fluid losses. As the fracturing fluid leaks into the surrounding medium, some of the solid constituents which are gradually mixed with the fracturing fluids start to deploy on the fracture walls forming this filter cake. The filter cake serves as a low permeability barrier that resists fluid losses (Mack & Warpinski 2000). The cake-building mechanism is based on classical theory of particle deposition which obeys three assumptions. The first assumption says that the cake deposition is proportional to the volume of filtrate that has passed through its surface. The second assumption says that the permeability of the cake is independent of its thickness and the last one assumes that the difference of permeabilities between the filter cake and the formation is large enough to consider the latter as a constant pressure fluid boundary.

The assumptions behind Carter's leak-off model indicate that its applicability is restricted by three basic requirements. The first requirement is the presence of a low-permeability filter cake building on top of a relatively pervious rock. The second requirement is the viscosity of both the fracturing fluid and the filtrate to be higher than the viscosity of the natural reservoir fluid, and the third requirement is the thickness of the invaded zone must be relatively small compared to the fracture length. These conditions are met in high-efficiency formations. Discrepancies occur in long-term treatments in which the invaded zone extends deep into the formation or in the case of a treatment with low-viscosity fluids such as water with no cake-building properties (Adachi, 2001).

2.5.2 Fluid lag

The fluid lag is defined as the distance between the front of the fracturing fluid and the propagating-tip of the fracture. In numerical modeling the presence of fluid lag is actually a physical requirement. It has been proved that for a fracture driven by a viscous fluid, the coupling between the equations yields a negative singularity for the

fluid pressure at the fracture tip. It is then understood that the fluid pressure must remain finite, and thus the need for such a non-wetted zone.

In fracture mechanics analysis, a process zone is again a physical requirement to ensure that stresses in the solid ahead of the fracture tip are finite. However, classical singular solutions for stresses near the tip can be used if treated as intermediate asymptotics (solutions that capture the dominant behavior up to a certain small distance from the tip). This approach involves really complex boundary layer analysis that has to be matched and represented by the lag itself. This is a major drawback in the analysis of hydraulic fracturing treatments and even though this type of analysis is useful in the understanding of the process it can only serve as benchmarks.

Based on this drawback, hydraulic fracturing analysis can be considered by ignoring the fluid lag for certain conditions under which this idealization can be used. The fluid lag cannot be neglected in high permeability, low toughness, low confining stress and for analysis at early times close to initiation. The condition under which the lag can be neglected in the case of a plane-strain fluid-driven fracture has been already established by Garagash & Detournay (2000). This condition was supported by laboratory tests reported from Van Dam et al., (2002). For the case of a fracture propagating in a permeable elastic and permeable inelastic medium, however, this is still an open question. It is expected that in very permeable formations, suction and fluid exchange with the reservoir could have an important effect on the sizing of the lag and furthermore the lag itself can have serious implications on the plastic zone development.

2.5.3 Pore pressure

The study on the influence of pore pressure in hydraulic fracture analysis is mainly performed with laboratory experiments. Numerical studies involving the influence of pore pressure are limited. Bruno & Nakagawa (1991) found in experimental studies that tensile failure is determined by the effective stress. Their experiments showed that an effective tensile stress caused by pore pressure increase initiated failure at effective stresses that agreed with uniaxial tensile tests. In addition, they found that a local increase in pore pressure around the fracture tip facilitates fracture extension. From an energy balance, it was inferred that the strain energy release by the pore fluid

contributes to the fracture driving force compared to Griffith's energy balance approach.

Abou-Sayed (1978) performed experiments in which he examined the effect of pore pressure on the toughness of the material. He indicated that tensile fracturing is governed by effective stress. From his experiments he found that the measured fracture toughness stayed equal if the pore pressure was increased with the same amount as the confining stress. Miller (1986) also found that the measured separation energy stayed unaltered when the pore pressure was increased with the same value as the hydrostatic confining stress.

These experiments suggest that the separation energy is independent of the pore pressure. In hydraulic fracturing, the situation is more complicated because of the possibility of flow of pore fluid near the tip. The presence of the fluid lag and the lower pore pressure near the tip as a result of unloading of the stress will cause flow of pore fluid respectively out of and towards the rock near the tip. When the pore pressure is maintained by flow towards the near-tip region, the effective stress will become negative and tensile fracturing can be enhanced. However, the influence of the pore pressure compared with the above observations has never been addressed if the fracture is driven in inelastic porous domain and is still an open question.

2.5.4 Propagation velocity

The usual assumption is that the fracture surface energy is approximately independent of the propagation velocity (Shlyapobersky, 1985). Muller (1986) measured an increase of fracture toughness with increasing COD rate in three-point bending tests. His measurements would suggest an increase in toughness smaller than approximately two times for rates in the laboratory compared with rates in the field. Whittaker et al., (1992) reported laboratory investigations which showed that the loading rate in laboratory experiments did not significantly influence the measured toughness. For high loading rates, in general, lower values of the toughness are measured, which is explained by the process zone having insufficient time to develop completely. Zhang et al., (1999) measured a constant fracture toughness for certain loading rates of interest for hydraulic fracturing. Analysis of the propagation velocity on the plastic zones was originally discussed by Papanastasiou and Thiercelin (1993). According to equation (2.3), it is showed that the velocity of propagation is capable in contributing to the plastic zone development. As presented by the aforementioned observations the

influence of the propagation velocity on the fracture toughness in elastic and inelastic impermeable or permeable domains of a fluid driven fracture is still not fully addressed.

2.5.5 Dilatancy

When a material deforms plastically due to frictional sliding, along particles or in micro cracks, dilation is observed coupled with plastic yielding. Papanastasiou & Thiercelin (1993) systematically studied numerically the dilatancy effect and found that increasing dilation will result in greater plastic zones which in turn will result in wider fracture openings. These plastic wider openings present smaller fluid lag than the elastic fracture. Their observations were confirmed by Van Dam et al., (2002) by performing laboratory tests and found that dilation led to an increased fracture width. However, these findings contradicted the early hypothesis on dilation which assumed that it creates narrower fractures (Cleary et al., 1991). As it was reported, dilation of the rock is associated with plastic yielding which increases the apparent toughness resulting in wider fractures and smaller fluid lag regions (Papanastasiou and Thiercelin, 1993; Dong 2010).

2.5.6 Grain size

Among the special issues based on continuum mechanics that we will investigate in the analysis of hydraulic factures is the influence of the grain size. Wang et al., (1990) showed that the size of the fracture process zone increases with the grain size. This observation was also confirmed experimentally by Schlangen & Van Mier (1992). A possible explanation for this observation is based on the assumption that there are more weaknesses in an area near the fracture plane when the grain size is small. Therefore, micro-cracks grow easier. However, the increase of the process zone size does not necessarily mean an increase in separation energy which is related to the fracture process zone. According to a recent review reported by Whittaker et al., (1992), the separation energy generally decreases with the grain size. This was observed for relatively small grain sizes, smaller than $l0^{-4}$ m.

In situations where confined conditions are present, the size of the tensile zone is smaller than in situations where unconfined conditions exist. Furthermore, significant discrepancies exist between laboratory tests and field observations. These discrepancies concern the fracture width and the process zone length. Results obtained

from experiments show that the fracture width and the process zone is smaller than the ones observed in the field. Due to these reasons, differences in the ratio of the grain size to one of these length scales may occur (Van Dam 1999).

2.5.7 Scale

The issue of the length scale is related to an increase of separation energy with the fracture length for short fractures. However, when the fracture reaches a certain length, the fracture toughness becomes approximately constant (Papanastasiou, 1999). This behavior can be explained by assuming that for fractures smaller than a certain length, the process zone has not developed completely. This observation partially explains the increase in the apparent fracture toughness in hydraulic fracture operations.

Many contributions were devoted in explaining this behavior. There is no real evidence of a fundamental increase of fracture surface energy with fracture size. Assuming that the fracture surface energy depends on scale, the extrapolation of these results to hydraulic fracture field size (100 – 1000 m) would imply extreme values for the fracture surface energy. In recent studies reported by Van Vliet (2000), a decrease in tensile strength with increasing fracture size was observed. This implies that the parameters in the cohesive zone model also depend on fracture size. However, the effect of size on tensile strength is still not fully explained and predictions of a decreasing tensile strength of approximately 2 times for a field scale compared with the lab need to be explained.

2.6 Conclusions

The important fundamentals and principles from the fields of geomechanics, fluid mechanics, fracture mechanics and poromechanics have been presented so as to analyze the fluid driven problem under complex conditions. The main conclusions from this review are summarized as follows:

- The most appropriate geometry to analyze the process zone of a propagating fracture tip is the plane strain KGD.
- Hydraulic fracturing in permeable inelastic domains is not yet fully understood.
- Scaling the plastic zones in porous continua in the presence of pore pressure is an open question.

- The inelastic behavior in the process zone and in the surrounding porous medium must be accounted for in the dissipated energy in the hydraulic fracturing process.
- The most appropriate and robust fracture propagation criterion to analyze the influence of the process zone in hydraulic fracturing is the cohesive zone which under certain conditions is equivalent with the non linear J-integral approach which is widely accepted for fracture analyses.
- The singularities observed in the conventional fracture analysis and which demand complex intermediate asymptotic analyses are completely avoided through the cohesive zone approach.

3. Finite Element Model of a Fluid-Driven Fracture in a Deformable Poroelastoplastic Continuum

3.1 Preamble

In this chapter we introduce the numerical model of the fluid driven fracture in a deformable poroelastoplastic continuum by means of finite elements. The numerical modeling is aiming to investigate the main physical parameters that affect the process zone of a fracture propagating in a porous medium incorporating inelastic behavior. The fluid driven fracture is simulated using the plane strain geometric model (KGD). The analysis for the solid deformation of the porous continuum, involves a) the effective stress principle and the constitutive behavior of the porous continuum as well as their fundamental constitutive assumptions b) the continuity equation that governs the flow of the wetting liquid c) the inelastic behavior which describes the yielding process and d) the derivation of the equilibrium equation for the porous media in a discretized form. The fluid flow in the fracture is derived via the lubrication model which includes a diffusion equation for the fluid infiltration from the fracture into the surrounding medium. The propagation criterion is based on modeling the cohesive zone which is considered to be the most robust criterion for propagating fractures in a non-linear material. The derivation of the set of equations can be found in Vardoulakis & Sulem (1995) and Abaqus (2006). The equations are presented below in the most general form which will allow for future investigations in other cases e.g. hydraulic fracturing in natural gas formations.

3.2 Effective Stress Principle for the Porous Continuum

The conventional approach which is usually adopted to model a multiphase material in a porous medium is based on the effective stress principle to describe the mechanical behavior. The porous medium modeling, with finite elements, considers the presence of two fluids in the medium. One is the “wetting liquid”, which is assumed to be relatively (but not entirely) incompressible. Often the other fluid is a gas, which is relatively compressible. An example of such a system is soil containing ground water and air. When the medium is partially saturated, both fluids exist at a point: when it is fully saturated, the voids are completely filled with the wetting liquid. The elementary volume dV is made up of a volume of grains of solid material

dV_g, a volume of voids dV_u and a volume of wetting liquid $dV_w \leq dV_u$ that is free to move through the medium if driven. The total stress $\boldsymbol{\sigma}$, acting at a point is assumed to be made up of an average pressure in the wetting liquid u_w called the "wetting liquid pressure". An average pressure in the other fluid u_a and an "effective stress" $\bar{\boldsymbol{\sigma}}^*$ which is defined by equation (3.1) for the multiphase material:

$$\bar{\boldsymbol{\sigma}}^* = \boldsymbol{\sigma} + \left(\chi u_w + (1-\chi) u_a \right) \mathbf{I} \tag{3.1}$$

For the sign convention the tensile stress is positive, but u_w and u_a are pressure values. This explains the sign in this equation. The term χ, is a factor that depends both, on saturation and on the surface tension of the liquid/solid system. The usual values of this term is 1.0 when the medium is fully saturated and between 0.0 and 1.0 in unsaturated systems when its value depends on the degree of saturation of the medium. In the numerical model presented herein we simply assume that $\chi = 1$ which corresponds to fully saturated conditions.

To simplify the model, we assume that the pressure applied to the non-wetting fluid is constant throughout the domain being modeled and does not vary with time. Furthermore, it is small enough that its value can be neglected. This requires that the non-wetting fluid can diffuse through the medium sufficiently freely so that its pressure u_a never exceeds the pressure applied to this fluid at the boundaries of the medium, which remains constant throughout the process being modeled. The most common example where this simplification applies is a porous medium that is quite permeable to gas flow, in which the non-wetting fluid is air, exposed to atmospheric pressure. The dimensions of the region modeled must not be large so that the gravitational gradient of atmospheric pressure causes a significant change in the air pressure, and must not be any external event that provides a transient change in the air pressure. This assumption allows u_a to be removed from equation (3.1), provided that the corresponding loading term (i.e., atmospheric pressure on the boundary of the medium) is also omitted from the equilibrium equations and that u_a is small enough that its effect on the deformation of the medium is not important (or that the deformation is measured from the state $\boldsymbol{\sigma} = - u_a \mathbf{I}$). This simplification reduces the effective stress principle to the following

$$\bar{\boldsymbol{\sigma}}^* = \boldsymbol{\sigma} + \chi u_w \mathbf{I} \tag{3.2}$$

The constitutive response of the porous medium is a function of simple bulk elasticity relationships for the liquid and for the soil grains, together with a constitutive theory for the soil skeleton whereby $\bar{\sigma}$ (effective stresses) are defined as a function of the strain history of the domain. These types of constitutive models and their formulation are appropriate for voided materials, such as soils.

The remaining part in completing the analysis of the porous media, involves the discussion of the equilibrium equation, the discretized equilibrium statement for a porous medium, the constitutive behavior of the porous continuum as well as their fundamental constitutive assumptions and the continuity equation that governs the flow of the wetting liquid. Newton's method is then used to solve the governing equations for the implicit time integration procedure.

3.2.1 Preliminary definitions

As preliminaries, the porosity, void ratio, and saturation must be defined as these terms are essential for the porous continuum description. The porosity of the medium *n* is the ratio of the volume of voids to the total volume (Abaqus 2006):

$$n \overset{def}{=} \frac{dV_u}{dV} = 1 - \frac{dV_g}{dV} \tag{3.3}$$

Using the superscript (*o*) to indicate values in some convenient reference configuration allows the porosity in the current configuration to be expressed as

$$\begin{aligned} n &= 1 - \frac{dV_g}{dV_g^0}\frac{dV^0}{dV}\frac{dV_g^0}{dV^0} \Leftrightarrow \\ n &= 1 - J_g J^{-1}\left(1 - n^0\right) \end{aligned} \tag{3.4}$$

So that

$$\frac{1-n}{1-n^0} = \frac{J_g}{J} \tag{3.5}$$

where the term *J* is given by

$$J \overset{def}{=} \left|\frac{dV}{dV^0}\right| \tag{3.6}$$

where the superscript (def) indicates definition. Equation (3.6) is the ratio of the medium's volume in the current configuration to its volume in the reference configuration. Furthermore, the ratio of the current to reference volume for the grains can be given by a similar definition as

$$J_g \overset{def}{=} \left| \frac{dV_g}{dV_g^0} \right| \tag{3.7}$$

Generally, in soil mechanics, the void ratio term is usually used instead of the porosity. The definition of the void ratio is the ratio of the volume of voids to the volume of grains

$$e \overset{def}{=} \frac{dV_u}{dV_g} \tag{3.8}$$

Conversion relationships are readily derived

$$e = \frac{n}{1-n}, \qquad n = \frac{e}{1-e}, \qquad 1-n = \frac{1}{1+e} \tag{3.9}$$

As discussed above, another significant term in the equations which is essential for the description of the porous media is the degree of saturation s. By definition, the saturation is described by the ratio of free wetting liquid volume to voids volume as

$$s \overset{def}{=} \frac{dV_w}{dV_u} \tag{3.10}$$

At a certain point, the volume ratio of free wetting liquid is given by

$$n_w \overset{def}{=} \frac{dV_w}{dV} = sn \tag{3.11}$$

To complete the preliminary definitions, the total volume of wetting liquid (free liquid) per unit of current volume is given by

$$n_f = sn \tag{3.12}$$

It is worth noting that the term n_w is the same with n_f. After the description of the effective stress principle and the preliminary definitions of the terms that are essential in the description of the porous continuum we precede to a more sophisticated analysis which is the description of the equations of the porous continuum.

3.3 Discretization of the Equilibrium Equations for the Porous Continuum

The Equilibrium equations for the porous medium can be expressed by writing the principle of virtual work for the volume with boundary *S*, under consideration in its current configuration at time *t*. The principle of the virtual work for the porous continuum is given by (Abaqus 2006):

$$\int_V \boldsymbol{\sigma} : \delta\boldsymbol{\varepsilon} dV = \int_S \mathbf{t}.\delta\mathbf{v} dS + \int_V \hat{\mathbf{f}}.\delta\mathbf{v} dV \tag{3.13}$$

where, $\delta\mathbf{v}$ is a virtual velocity field, $\boldsymbol{\sigma}$ is the true (Cauchy) stress, $\mathbf{t}$ are surface tractions per unit area. The term $\delta\boldsymbol{\varepsilon}$ is the virtual rate of deformation and is given by

$$\delta\boldsymbol{\varepsilon} \overset{def}{=} sym\left(\frac{\partial\delta\mathbf{v}}{\partial\mathbf{x}}\right) \tag{3.14}$$

Furthermore, the term $\hat{\mathbf{f}}$ in equation (3.13) expresses the body forces per unit volume. For our system $\hat{\mathbf{f}}$ will include the weight of the wetting liquid as

$$\mathbf{f}_w = (sn)\rho_w \mathbf{g} \tag{3.15}$$

where, ρ_w is the density of the wetting liquid which we assume to be constant and $\mathbf{g}$ is the gravitational acceleration. For simplicity we consider this loading explicitly so that any other gravitational term in $\hat{\mathbf{f}}$ is associated only with the weight of the dry porous medium. Thus, we rewrite the virtual work equation (3.13) as

$$\int_V \boldsymbol{\sigma} : \delta\boldsymbol{\varepsilon}\, dV = \int_S \mathbf{t}.\delta\mathbf{v} dS + \int_V \mathbf{f}.\delta\mathbf{v} dV + \int_V (sn)\rho_w \mathbf{g}.\delta\mathbf{v}\, dV \tag{3.16}$$

where $\mathbf{f}$ are all body forces except the weight of the wetting liquid.

In the finite element model, the equilibrium equation (3.16) is approximated as a finite set of algebraic equations by introducing interpolation functions. The notation used here to indicate such discretizations is the uppercase superscripts (i.e, u^N). These uppercase superscripts represent nodal variables, with the summation convention adopted for the superscripts. The interpolation is assumed to be based on material coordinates in the material skeleton also known as "Lagrangian" formulation. For simplicity, we consider only the case where the problem has no internal constraints (such as incompressibility) and the discretization is made entirely by approximating the equilibrium equation (3.16) which will result in the displacement (or stiffness) method.

The virtual velocity field is interpolated according to

$$\delta \mathbf{v} = \mathbf{N}^N \delta u^N \tag{3.17}$$

where $\mathbf{N}^N$ are interpolation functions defined with respect to material coordinates S_i.

The virtual rate of deformation is interpolated according to

$$\delta \boldsymbol{\varepsilon} = \boldsymbol{\beta}^N \delta u^N \tag{3.18}$$

where in the simplest case is valid for the $\boldsymbol{\beta}^N$ term

$$\boldsymbol{\beta}^N = sym\left(\frac{\partial \delta \mathbf{N}^N}{\partial \mathbf{x}} \right) \tag{3.19}$$

Substituting equations (3.17) and (3.18) in the virtual work equation (3.16) we obtain the discretized equation

$$\delta u^N \int_V \boldsymbol{\beta}^N : \boldsymbol{\sigma}\, dV = \delta u^N \left[\int_S \mathbf{N}^N . \mathbf{t}\, dS + \int_V \mathbf{N}^N . \mathbf{f}\, dV + \int_V \left(sn \right) \rho_w \mathbf{N}^N . \mathbf{g}\, dV \right] \tag{3.20}$$

where the terms δu^N are assumed to be independent.

The term conjugate to δu^N on the left-hand side of equation (3.20) is referred to subsequently as the internal force array I^N and we subtract it from equation (3.20) for illustration purposes as

$$I^N \overset{def}{=} \int_V \boldsymbol{\beta}^N : \boldsymbol{\sigma} dV \tag{3.21}$$

Likewise the external force array P^N is taken from the right-hand side and we subtract it from equation (3.20) for illustration purposes again

$$P^N \overset{def}{=} \int_S \mathbf{N}^N . \mathbf{t}\, dS + \int_V \mathbf{N}^N . \mathbf{f}\, dV + \int_V (sn)\, \rho_w \mathbf{N}^N . \mathbf{g}\, dV \tag{3.22}$$

The external force array P^N includes any D'Alembert forces. According to the D'Alembert principle, it is stated that the sum of the differences between the forces acting on a system and the time derivatives of the momentum of the system itself along any virtual displacement consistent with the constraints of the system, is zero. The equilibrium state of the porous continuum as a balance of internal and external forces is expressed by choosing each δu^N to be nonzero

$$I^N - P^N = 0 \tag{3.23}$$

These discretized equilibrium equations, together with the continuity equation which will be discussed in the following, define the state of the porous medium. The equilibrium equations are written at the end of a time increment when implicit integration is used and are in most cases, except some simple ones, nonlinear. Newton's iterative method is used for their solution. These considerations imply the need to establish the Jacobian matrix of the system, which defines the variation of each term in the equations with respect to the basic variables of the discretized problem which in our case are the nodal positions χ^N or equivalently the displacements $\chi^N - X^N$ and the nodal wetting liquid pressure values u_w^N. Symbolically we write such a variation of the term f as df with the following meaning

$$df = \frac{\partial f}{\partial x^N} dx^N + \frac{\partial f}{\partial u_w^P} du^P \tag{3.24}$$

From the variation of the discretized equilibrium equation (3.23), the variance of the external force array dP^N gives rise to the mass matrix for the D'Alembert forces and

the load stiffness matrix in the Jacobian. The load stiffness matrix is derived using standard finite element methodology.

The load stiffness term associated with the weight of the wetting liquid is given by

$$-\int_V \frac{1}{J} d\left[J\left(sn\right)\rho_w\right]\mathbf{N}^N.\mathbf{g}\,dV \tag{3.25}$$

where J is defined in equation (3.6).

The variation in the internal force array dI^N is given as

$$dI^N = d\int_V \boldsymbol{\beta}^N : \boldsymbol{\sigma}\,dV = \int_V \left[\frac{1}{J}\boldsymbol{\beta}^N : d(J\boldsymbol{\sigma}) + \boldsymbol{\sigma} : d\boldsymbol{\beta}^{\mathrm{N}}\right] dV \tag{3.26}$$

The second part of equation (3.26) includes the term $d\,(J\boldsymbol{\sigma})$ which is the variation of stress caused by variations of nodal positions and pore liquid pressure. In a continuum sense, before the spatial discretization of the solution variables, this term is defined by the effective stress principle and by the constitutive assumptions used for the material as it will be discussed in more detail below. The spatial discretization into the second term provides a contribution to the initial stress matrix.

Since the effective stress $\bar{\boldsymbol{\sigma}}$ is generally stored as components associated with spatial directions, the rotation of the material during an increment must be included in the formulation. For the purpose of the present development we assume that the variation of stress $d\,(J\boldsymbol{\sigma})$ is given by

$$d(J\boldsymbol{\sigma}) = d^{\nabla}(J\bar{\boldsymbol{\sigma}}) - d(J\,\bar{p}_l\mathbf{I}) + J(d\boldsymbol{\Omega}.\boldsymbol{\sigma} + \boldsymbol{\sigma}.d\boldsymbol{\Omega}^T) - d(J\chi u_w)\mathbf{I} \tag{3.27}$$

where $d^{\nabla}(J\bar{\boldsymbol{\sigma}})$ is the variation in effective stress associated with constitutive response in the material that is caused by variations in strain. The term $d\Omega$ is defined by

$$d\boldsymbol{\Omega} \overset{def}{=} asym\left(\frac{\partial d\mathbf{x}}{\partial \mathbf{x}}\right) \tag{3.28}$$

Equation (3.28) is the spin of the material. Using this assumption, the Jacobian contribution from stress in the porous medium arises in the variation of the internal force array and is given by

$$dI^N = \int_V \left[\frac{1}{J} \boldsymbol{\beta}^N : \left\{ d^{\nabla}(J\bar{\boldsymbol{\sigma}}) \right\} \right] dV + \int_V \left[\boldsymbol{\sigma} : \left(d\boldsymbol{\beta}^{\mathrm{N}} + 2\boldsymbol{\beta}^{\mathrm{N}} . d\boldsymbol{\Omega} \right) \right] dV$$
$$- \int_V \left[\boldsymbol{\beta}^{\mathrm{N}} : \mathbf{I}(\chi + u_w \frac{d\chi}{du_w}) du_w \right] dV - \int_V \left[\boldsymbol{\beta}^{\mathrm{N}} : \mathbf{I}\chi u_w \mathbf{I} : d\boldsymbol{\varepsilon} \right] dV \tag{3.29}$$

where $d\boldsymbol{\varepsilon}$ is the strain rate defined by

$$d\boldsymbol{\varepsilon} \overset{def}{=} sym\left(\frac{\partial d\mathbf{x}}{\partial \mathbf{x}} \right) \tag{3.30}$$

This rate of deformation is such that the following equation must be valid:

$$\frac{dJ}{J} = trace(d\boldsymbol{\varepsilon}) = \mathbf{I} : d\boldsymbol{\varepsilon} \tag{3.31}$$

In the above analysis we described in detail the equilibrium state in a porous continuum.

3.4 Constitutive Behavior of the Porous Continuum

The porous medium is considered to consist of a mixture of solid matter and voids that contain liquid or gas or both. The constitutive behavior of the porous media discussed here is concerned with the mechanical aspect of the porous medium which consists of the responses of the liquid and solid matter to local pressure and of the response of the overall material based on the effective stress principle as discussed earlier. The assumptions made for these responses are discussed in this section.

3.4.1 Liquid response

In a porous system in which the liquid is free to move in the voids of the porous matrix, the liquid response is given by (Abaqus 2006):

$$\frac{\rho_w}{\rho_w^o} \approx 1 + \frac{u_w}{K_w} \tag{3.32}$$

where ρ_w is the density of the liquid ρ_w^o is the density of the liquid in the reference configuration, K_w is the liquid's bulk modulus which is temperature θ, dependent. The

ratio of the average pressure stress in the wetting liquid to the liquid bulk modulus u_w/K_w is assumed to be small.

3.4.2 Grains response

In a porous system in which the solid matter in the porous matrix has local mechanical response under pressure, the grains response is given by (Abaqus 2006):

$$\frac{\rho_g}{\rho_g^o} \approx 1 + \frac{1}{K_g}\left(su_w + \frac{\overline{p}}{1-n} \right) \tag{3.33}$$

where $K_g(\theta)$ is the bulk modulus of this solid matter which is temperature dependent, s is the saturation in the wetting fluid. The absolute ratio of the grain density to the grain density in the current configuration $\left|1-\rho_g/\rho_g^O\right|$ is assumed to be small.

It is important to distinguish K_g as a property of the solid grains of the material. The porous medium as a whole will exhibit a much softer (and generally non-recoverable) bulk behavior.

3.4.3 Effective strain

A more detail examination of equation (3.33) shows that the volumetric strain which is given from the ratio of the average pressure stress in the wetting liquid to the grains bulk modulus $-u_w/K_g$ represents that part of the total volumetric strain caused by pore pressure acting on the solid matter in the porous medium. The strain caused by the term $-u_w/K_g$ in the porous medium is given from (Abaqus 2006):

$$\overline{\boldsymbol{\varepsilon}} \overset{def}{=} \boldsymbol{\varepsilon} + \left(\frac{1}{3}\frac{su_w}{K_g} \right)\mathbf{I} \tag{3.34}$$

The above equation (3.34) represents the strain that is assumed to modify the effective stress in the porous continuum. Therefore, the effective stress is a function of the effective strain. Many constitutive equations are given in rate forms as the relation between a stress rate and a strain rate (or the rate of deformation). The constitutive equations must be frame indifferent. If the stress and strain measures are material quantities then objectivity is automatically satisfied. From this assumption, we can

adopt the Jaumann rate which expresses the change of the effective stress in terms of the rate of change of the kinematic and pore liquid pressure variables. At this point it is considered important to mention that the Jaumann rate leads to symmetric tangent modulus which is of paramount importance for numerical convergence. This rate is given by

$$d^{\nabla}\left(J\bar{\boldsymbol{\sigma}}\right)=\left(J\bar{\mathbf{D}}\right):\left(d\boldsymbol{\varepsilon}+\left(\frac{s}{3K_g}+\frac{u_w}{3K_g}\frac{ds}{du_w}+\frac{1}{K_w}\right)\mathbf{I}\,du_w\right) \tag{3.35}$$

where $\bar{\mathbf{D}}$ is the tangent stiffness matrix, given in general form and it is defined for each particular material model. The discussion of inelastic effects is included in this tangent stiffness matrix and it will be discussed in detail later in this chapter. Combining equations (3.33), (3.34), (3.35) and (3.29), we obtain the variation of the internal force array which is caused by the effective strain in the porous medium as

$$\begin{aligned} dI^N &= \int_V \left[\boldsymbol{\beta}^N : \bar{\mathbf{D}} : d\boldsymbol{\varepsilon}\right] dV - \\ &\int_V \left[\boldsymbol{\beta}^{\mathrm{N}} : \left((\chi + u_w \frac{d\chi}{du_w})\mathbf{I} - \left(\frac{s}{3K_g}+\frac{u_w}{3K_g}\frac{ds}{du_w}+\frac{1}{K_w}\right)\bar{\mathbf{D}} : \mathbf{I} + \left(\frac{ds}{du_w}\bar{\mathbf{D}}\right)\right) du_w\right] dV \\ &+\int_V \left[\boldsymbol{\sigma} : \left(d\boldsymbol{\beta}^{\mathrm{N}} + 2\boldsymbol{\beta}^{\mathrm{N}}.d\boldsymbol{\Omega}\right) - \boldsymbol{\beta}^{\mathrm{N}} : \mathbf{I}\chi u_w \mathbf{I} : d\boldsymbol{\varepsilon}\right] dV \end{aligned} \tag{3.36}$$

Equation (3.36) is essential for the solution of the equilibrium equation (3.23) of the porous continuum which is the balance of internal and external forces. With the discussion of the internal force array variance we have defined the constitutive behavior of the solid matter in the porous matrix.

3.5 Mass Continuity Equation for the Wetting liquid in a Porous Continuum

Problems involving fluid flow can be separated into particular cases of fluid flow through a porous medium. These cases are associated with a relatively incompressible wetting liquid present in the porous medium. The medium may be wholly or partially saturated, with this liquid.

A porous medium is modeled approximately, by attaching the finite element mesh to the solid phase. Liquid can flow through this mesh. A continuity equation is

therefore required for the liquid. The continuity equation says that the rate of increase in liquid mass stored at a point is equal to the rate of mass of liquid flowing into the point within the time increment. In this section, the continuity state will be defined in a variational form needed for finite element approximation. Liquid flow is described by Darcy's law. The continuity equation is satisfied approximately in the finite element model by using excess wetting liquid pressure as the nodal variable (degree of freedom), interpolated over the elements. The equation is integrated in time by using the *backward Euler* approximation. The total derivative of this integrated variational statement of continuity with respect to the nodal variables is required for the *Newton iterations* used to solve the nonlinear and coupled, equilibrium and continuity equations.

In order to establish the mass continuity for the wetting fluid in the porous continuum we need to consider a control volume which contains a fixed amount of solid matter. The current volume configuration occupies space V with surface S. In the reference configuration it occupies space V^0. The wetting liquid now can flow freely through this volume and at any time the volume of such free liquid can be written as V_w. Such description of the physical process allows the modeling of fluid flow driven by pressure which is essential for poro-mechanical problems.

The *total mass of wetting liquid* in the control volume is given by (Abaqus 2006):

$$\int_V \rho_w dV_w = \int_V \rho_w n_w dV \tag{3.37}$$

where ρ_w is the mass density of the liquid. The change in the mass of the wetting liquid involves a time rate, therefore, equation (3.37) is reformulated to account for the time variable as

$$\frac{d}{dt}\left(\int_V \rho_w n_w dV\right) = \int_V \frac{1}{J}\frac{d}{dt}\left(J\rho_w n_w\right) dV \tag{3.38}$$

The mass of the wetting liquid crossing the surface and entering the volume per unit time is

$$-\int_S \rho_w n_w \mathbf{n} \,.\mathbf{v}_w ds \tag{3.39}$$

where $\mathbf{v}_w$ is the average velocity vector of the wetting liquid relative to the solid phase (seepage velocity) and is the vector with the outward direction and normal to the surface *S*. The condition that the liquid mass across the surface S is equal to the rate of change of this liquid mass within the control volume *V* gives the wetting liquid mass continuity equation

$$\int_V \frac{1}{J}\frac{d}{dt}\left(J\rho_w n_w\right) dV = -\int_S \rho_w n_w \,\mathbf{n}.\mathbf{v}_w ds \tag{3.40}$$

Using the divergence theorem for an arbitrary volume, provides the pointwise equation

$$\frac{1}{J}\frac{d}{dt}\left(J\rho_w n_w\right) + \frac{\partial}{\partial \mathbf{x}}.\left(\rho_w n_w \mathbf{v}_w\right) = 0 \tag{3.41}$$

in which the equivalent *weak form* of equation (3.41) is given by

$$\int_V \delta u_w \frac{1}{J}\frac{d}{dt}\left(J\rho_w n_w\right) dV + \int_V \delta u_w \frac{\partial}{\partial \mathbf{x}}.\left(\rho_w n_w \mathbf{v}_w\right) dV = 0 \tag{3.42}$$

where δu_w is an arbitrary but continuous variational field. This equation can also be written on the reference volume as

$$\int_{V^0} \delta u_w \frac{d}{dt}\left(J\rho_w n_w\right) dV^0 + \int_{V^0} \delta u_w J\frac{\partial}{\partial \mathbf{x}}.\left(\rho_w n_w \mathbf{v}_w\right) dV^0 = 0 \tag{3.43}$$

This mass continuity equation is integrated approximately in time by the backward Euler formula and the descritized equation (3.43) takes the form

$$\int_{V^0} \delta u_w \left[\left(J\rho_w n_w\right)_{t+\Delta t} - \left(J\rho_w n_w\right)_t\right] dV^0 + \Delta t \int_{V^0} \delta u_w \left[J\frac{\partial}{\partial \mathbf{x}}.\left(\rho_w n_w \mathbf{v}_w\right)\right]_{t+\Delta t} dV^0 = 0 \tag{3.44}$$

which over the current control volume takes the form

$$\int_V \delta u_w \left[\left(\rho_w n_w\right)_{t+\Delta t} - \frac{1}{J_{t+\Delta t}} \left(J \rho_w n_w\right)_t \right] dV + \Delta t \int_V \delta u_w \left[\frac{\partial}{\partial \mathbf{x}} . \left(\rho_w n_w \mathbf{v}_w\right) \right]_{t+\Delta t} dV = 0 \qquad (3.45)$$

If we drop the subscript $t+\Delta t$ by adopting the convention that any quantity that is not explicitly associated with a point in time is taken at $t+\Delta t$, the divergence theorem allows equation (3.45) to be rewritten as

$$\int_V \left[\delta u_w \left(\frac{\rho_w}{\rho_w^0} n_w - \frac{1}{J} \left(\frac{\rho_w}{\rho_w^0} \left(J n_w\right) \right)_t \right) - \Delta t \frac{\rho_w}{\rho_w^0} n_w \frac{\partial \delta u_w}{\partial \mathbf{x}} \mathbf{v}_w \right] dV + \Delta t \int_S \delta u_w \frac{\rho_w}{\rho_w^0} n_w \mathbf{n}.\mathbf{v}_w dS = 0 \qquad (3.46)$$

It is convenient to normalize equation (3.46) by the density of the liquid in the reference configuration ρ_w^0 and to substitute

$$\int_V \left[\delta u_w \left(\frac{\rho_w}{\rho_w^0} \left(sn\right) - \frac{1}{J} \left(\frac{\rho_w}{\rho_w^0} \left(J \left(sn\right)\right) \right)_t \right) - \Delta t \frac{\rho_w}{\rho_w^0} sn \frac{\partial \delta u_w}{\partial \mathbf{x}} \mathbf{v}_w \right] dV + \Delta t \int_S \delta u_w \frac{\rho_w}{\rho_w^0} sn \mathbf{n}.\mathbf{v}_w dS = 0 \qquad (3.47)$$

3.5.1 Constitutive behavior

The constitutive behavior for pore fluid flow is governed by the Darcy law. This hydraulic law is generally applicable to low fluid flow velocities.

Darcy's law states that under uniform conditions the volumetric flow rate of the wetting liquid through a unit area of the medium, ($s\, n\, \mathbf{v}_w$) is proportional to the negative of the gradient of the piezometric head (Bear, 1972):

$$s\, n\, \mathbf{v}_w = -\hat{\mathbf{k}} . \frac{\partial \phi}{\partial x} \qquad (3.48)$$

where $\hat{\mathbf{k}}$ is the permeability of the porous medium and Φ is the piezometric head defined as

$$\phi \overset{def}{=} z + \frac{u_w}{g \rho_w} \qquad (3.49)$$

where z is the elevation above some datum and g is the gravitational acceleration, which acts in the direction opposite to z. The permeability of the porous continuum $\hat{\mathbf{k}}$ can be anisotropic and it is a function of the saturation and void ratio of the material. It is reminded that the permeability has velocity dimensionality (length/time). Some authors refer to as the *hydraulic conductivity* (Bear, 1972). If we assume that g is constant in magnitude and direction, then the piezometric head Φ in any direction (i.e. x-direction) can be given by

$$\frac{\partial \phi}{\partial \mathbf{x}} = \frac{1}{g\rho_w}\left(\frac{\partial u_w}{\partial \mathbf{x}} - \rho_w \mathbf{g}\right) \tag{3.50}$$

where $\mathbf{g} = -g\,\partial z/\partial \mathbf{x}$ is the gravitational acceleration (we assume that ρ_w varies slowly with position). Introducing the flow constitutive law as stated above in the mass continuity equation (3.47) results in

$$\begin{aligned}&\int_V \left[\delta u_w \left(\frac{\rho_w}{\rho_w^0}(sn) - \frac{1}{J}\left(\frac{\rho_w}{\rho_w^0} J(sn)\right)_t\right)\right] dV + \int_V \left[\Delta t \frac{k_s}{\rho_w^0 g}\frac{\partial \delta u_w}{\partial \mathbf{x}}.\mathbf{k}.\frac{\partial u_w}{\partial \mathbf{x}} - \rho_w \mathbf{g}\right] dV + \\ &\Delta t \int_S \left[\delta u_w \frac{\rho_w}{\rho_w^0} sn\mathbf{n}.\mathbf{v}_w\right] dS = 0\end{aligned} \tag{3.51}$$

3.5.2 Volumetric strain in the liquid and grains

The bulk behavior of the grains was discussed earlier in Section (3.4). We will investigate the contribution of the volumetric strain caused by the solid grains of the porous matrix in equation (3.33). Combining equation (3.33) with equation (3.5) and neglecting all but first-order terms in small quantities we obtain (Abaqus 2006):

$$n \approx 1 + \frac{\overline{p}}{K_g} + \frac{1}{J}\left(1 - n^0\right)\left(\frac{u_w}{K_g} - 1\right) \tag{3.52}$$

Using equation (3.52) together with the equation (3.32) which accounts for the liquid response in the porous matrix and again neglecting second-order terms in small quantities, we obtain the following equation which is the contribution of both the solid grains and liquid response in the porous continuum

$$\frac{\rho_w}{\rho_w^o} n \approx 1 - \frac{1}{J}\left(1 - n^0\right) + \frac{\bar{p}}{K_g} + u_w \left(\frac{1}{K_w} + \frac{\left(1 - n^0\right)}{J} \left(\frac{1}{K_g} - \frac{1}{K_w} \right) \right) \tag{3.53}$$

With the end of this discussion we have reached the detailed description of the porous continuum involving the mechanical behavior of the solid skeleton and the fluid flow in the porous matrix. Furthermore, we have analyzed in detail the constitutive behavior that governs the material failure. In the next part of this analysis we will define the fluid flow within the fracture that is responsible for splitting the formation. This process is modeled via the Lubrication theory (Bachelor, 1967) which we will describe next.

3.6 Fracture Fluid Flow - Lubrication Theory

The fluid flow in the fracture and the exchanges of the fracturing fluid and the porous continuum can be approximated with a reasonable degree of accuracy with the Lubrication theory. According to Batchelor (1967), Reynolds set the fundamentals of this theory by examining the simple case of one solid body with plane surface gliding steadily over another. Since then, Lubrication theory has been used to analyze many fluid-solid interaction engineering problems. One of these engineering problems is the fluid driven fracture.

Lubrication theory accepts that two solid bodies can slide over one another very easily when there is a thin layer of fluid between them and that under certain conditions a high positive pressure is set up in the fluid layer. The existence of this high pressure in the fluid layer between the surfaces offers great resistance when being squeezed and remains as a "lubricating" film between the two surfaces. As a result of the thickness of the fluid layer between the two surfaces (boundaries) being so small, the rate of strain and stress due to viscosity of the fluid is very large. This large stress is then used with a suitable choice of configuration of the fluid layer to develop large pressure, thus making this theory most suitable to examine the fluid driven problem.

Lubrication theory in not always applicable and for this reason we examine next the requirements in order for the theory to be valid. If the distance of motion is large, then the flow can be considered as "plane two-dimensional" (i.e. tangential and normal flow takes place in the plane under consideration). Furthermore, if this

thickness is even larger then the lubrication model looses its meaning and cannot be applied. In order to apply the theory, the following mathematical requirement must be satisfied Batchelor (1967):

$$\alpha \frac{\rho dU}{\mu} \ll 1 \tag{3.54}$$

where α is the inclination of the sliding surface in relative motion, ρ is the fluid density, d is the thickness of the fluid layer, U is the fluid speed and μ is the fluid viscosity. In the fluid driven fracture problem, this requirement is usually satisfied under practical conditions and therefore we can proceed to the definition of the equations governing this theory.

The flow of an incompressible, Newtonian fluid is described by the Navier-Stokes equations. These equations which describe the motion of fluids arise from Newton's second law to fluid motion, together with the assumption that the fluid stress is the sum of a diffusing viscous term (proportional to the gradient of velocity), plus a pressure term. These equations are given in a concise form as

$$\rho \frac{D\mathbf{v}}{Dt} = -\nabla p_f + \mu \nabla^2 \mathbf{v} \tag{3.55}$$

where $\mathbf{v}$ is the fluid velocity vector, p_f is the fluid pressure, ρ is the density of the fluid and μ is the dynamic viscosity. Additionally, the first and third term in equation (3.55) are further analyzed as:

$$\begin{aligned} &\frac{D\mathbf{v}}{Dt} = \frac{\partial \mathbf{v}}{\partial t} + \nabla . \mathbf{v} \\ &\nabla^2 . \mathbf{v} = \nabla \nabla . \mathbf{v} - \nabla \times \left(\nabla \times \mathbf{v} \right) \end{aligned} \tag{3.56}$$

If the fluid flow velocity is small enough to neglect inertial effects (i.e. small Reynolds number) then the fluid is under the Stokes flow condition and equation (3.55) is simplified to

$$\nabla p_f = \mu \nabla^2 \mathbf{v} \tag{3.57}$$

Equation (3.57) can be used for modeling fluid flow within the fracture. Additionally, if the fracture shape ratio $w(x,t)/l(t)$ is small, where *w(x,t)* is the fracture opening and *l(t)* the fracture half length, then the fluid velocity can be considered unidirectional. This condition simplifies further the Stokes equation (3.57) to the normal flow as:

$$\frac{\partial p_f}{\partial x} = \mu \frac{\partial^2 u_x}{\partial y^2} \tag{3.58}$$

However, as mentioned before if the fracture shape ratio is large then normal flow must be considered. The solution of equation (3.58) yields the velocity profile

$$u_x = -\frac{1}{2\mu}\frac{\partial p_f}{\partial x}\left(\frac{w^2}{4} - y^2\right) \tag{3.59}$$

Integration of equation (3.59) yields the Poiseuille equation which for tangential and normal flow gives

$$\mathbf{q} = -\frac{w^3}{12\mu}\nabla p_f \tag{3.60}$$

where **q** is the fluid flow rate or flux. For the general case of a fracture propagating in a permeable medium, the condition of fluid mass conservation for an incompressible fluid is given

$$\frac{\partial w}{\partial t} + \nabla.\mathbf{q} + (q_t + q_b) = Q(t)\delta(x,t) \tag{3.61}$$

where **q***(x,y,t)* is the fluid flux of the tangential flow, and *Q(t)* is the injection rate. The terms $q_t(x,y,t)$ and $q_b(x,y,t)$ reflect the leak-off through the fracture into the adjacent material. If the fracture is impermeable, these terms are zero. The leak-off terms are defined by

$$\begin{aligned} q_t &= c_t(p_f - p_t) \\ q_b &= c_b(p_f - p_b) \end{aligned} \tag{3.62}$$

where p_t and p_b are the pore pressures in the adjacent porous material at the top and bottom surfaces of the fracture. The terms c_t and c_b define the corresponding fluid leak-off coefficients in units of [m/(Pa.sec)]. Substituting equations (3.60) and (3.62) into equation (3.61) yields the final Reynolds lubrication equation (Abaqus 2006):

$$\frac{\partial w}{\partial t} + c_t(p_f - p_t) + c_b(p_f - p_b) = \frac{1}{12\mu}\nabla.(w^3\,\nabla p_f) + Q(t)\delta(x,t) \tag{3.63}$$

The fluid pressure p_f is considered as traction acting on the open surfaces of the fracture. As complete separation eventually occurs in the material, there will be no contribution from the cohesive tractions in the open part of the fracture. The fluid pressure which is responsible for opening the fracture is balanced by the far-field stress acting across the process zone and by the cohesive tractions acting across that zone. Therefore, there exists a coupled relationship between the fluid pressure and the traction-separation in the process zone which can be described by an appropriate cohesive zone constitutive law. The only constrain in equation (3.63), which fully describes the fluid flow in the fracture as well as the fluid leak-off process on the adjacent porous continuum, is the requirement for all tractions acting on the entire fracture and the process zone to be in equilibrium.

3.7 Solution of the Coupled Diffusion-Deformation Equations

The numerical solution of the governing equations of pore fluid diffusion-deformation is briefly described in this section. These governing equations describe the equilibrium and the pore fluid flow as we discussed in detail in previous sections. The Equilibrium of the system is given by (Abaqus 2006):

$$\mathbf{K}^{MN}\overline{c}_{\delta}^{\mathrm{N}} - \mathbf{L}^{MP}\overline{c}_{u}^{P} = \mathbf{P}^{M} - \mathbf{I}^{M} \tag{3.64}$$

and the pore fluid flow is given by

$$\left(\hat{\mathbf{B}}^{MQ}\right)^{\mathrm{T}}\overline{u}^{M} + \hat{\mathbf{H}}^{QP}\overline{u}^{P} = \mathbf{Q}^{Q} \tag{3.65}$$

where **K** is the stiffness matrix, **L** is the coupling matrix, **P** is the external force array, **I** is the internal force array, **B** is the compressibility matrix, **H** is the flow matrix and **Q** is the nodal flow matrix. c_{δ}, c_u , u^M, u^P are nodal displacements and pressures with

their associated shape functions. The superscripts *M*, *N*, *P*, *Q* represent the matrices dimensions.

There are two common approaches to solving these coupled equations. One approach is to solve one set of equations first and then use the results obtained to solve the second set of equations. These results in turn are fed back into the first set of equations to see what changes (if any) result in the solution. This process continues until succeeding iterations produce negligible changes in the solutions obtained. This is the so called staggered approach to the solution of coupled systems of equations. The second approach is to solve the coupled systems directly. This direct approach is the approach that we have used because of its rapid convergence even in highly nonlinear cases.

We first introduce a time integration operator in the pore fluid flow equation. The operator chosen is the simple one-step method:

$$\overline{\delta}_{t+\Delta t}^{N} = \overline{\delta}_{t}^{N} + \Delta t\left[\left(1-\zeta\right)\overline{u}_{t}^{N} + \zeta\overline{u}_{t+\Delta t}\right] \tag{3.66}$$

where $0 \le \zeta \le 1$. In fact, to ensure numerical stability, we choose $\zeta = 1$ (backward difference/Euler) so that:

$$\overline{u}_{t+\Delta t} = \frac{1}{\Delta t}\left(\overline{\delta}_{t+\Delta t}^{N} - \overline{\delta}_{t}\right) \tag{3.67}$$

With this operator the pore fluid flow equation at time $t+\Delta t$ can be rewritten as:

$$\left(\hat{\mathbf{B}}^{MQ}\right)^{\mathrm{T}}\overline{\delta}_{t+\Delta t}^{M} + \Delta t\hat{\mathbf{H}}^{QP}\overline{u}_{t+\Delta t}^{P} = \Delta t\mathbf{Q}_{t+\Delta t}^{Q} + \left(\hat{\mathbf{B}}^{MQ}\right)^{\mathrm{T}}\overline{\delta}_{t}^{M} \tag{3.68}$$

Using the Newton linearization, the flow equation becomes:

$$\left(\mathbf{B}^{MQ}\right)^{\mathrm{T}}\overline{c}_{\delta}^{\mathrm{M}} - \Delta t\mathbf{H}^{QP}\overline{c}_{u}^{P} = \Delta t\left[-\mathbf{Q}_{t+\Delta t}^{Q} + \left(\hat{\mathbf{B}}^{MQ}\right)^{\mathrm{T}}\overline{u}_{t+\Delta t}^{M} + \hat{\mathbf{H}}^{QP}\overline{u}_{t+\Delta t}^{P}\right] \tag{3.69}$$

Then the coupled system of equations to be solved is:

$$\begin{aligned}\mathbf{K}^{MN}\overline{c}_{\delta}^{N} - \mathbf{L}^{MP}\overline{c}_{u}^{P} &= \mathbf{P}^{M} - \mathbf{I}^{M}\\ -\left(\mathbf{B}^{MQ}\right)^{\mathrm{T}}\overline{c}_{\delta}^{\mathrm{M}} - \Delta t\mathbf{H}^{QP}\overline{c}_{u}^{P} &= \mathbf{R}^{Q}\end{aligned} \tag{3.70}$$

where

$$\mathbf{R}^{Q} = \Delta t\left[-\mathbf{Q}^{Q}_{t+\Delta t} + \left(\hat{\mathbf{B}}^{MQ}\right)^{\mathrm{T}} \overline{u}^{M}_{t+\Delta t} + \hat{\mathbf{H}}^{QP}\overline{u}^{P}_{t+\Delta t} \right] \tag{3.71}$$

These equations form the basis of the iterative solution for a time step in a coupled flow deformation solution. They are, in general, non-symmetric. The lack of symmetry may be due to a number of effects, such as, changes in geometry, dependence of permeability on void ratio and inclusion of fluid gravity load terms in total pore pressure analyses. The steady-state version of the coupled problem is also non-symmetric.

3.8 Inelastic Behavior

Incremental plasticity theory is based on fundamental postulates, which means that all of the elastic-plastic responses have the same general form. In this section we will define the basic equations in their general form. Plasticity models are written as rate-independent or as rate-dependent models. A rate-independent model is one in which the constitutive response does not depend on the rate of deformation. In a rate-dependent model the response does depend on the rate at which the material is strained. Because these models have similar forms, their numerical treatment is based on the same technique.

A basic assumption of elastic-plastic models is that the deformation can be divided into an elastic part and an inelastic part. In its most general form this statement is written as:

$$\mathbf{F} = \mathbf{F}^{\mathrm{el}} \cdot \mathbf{F}^{\mathrm{pl}} \tag{3.72}$$

where $\mathbf{F}$ is the total deformation gradient, $\mathbf{F}^{\mathrm{el}}$ is the fully recoverable part of the deformation at the point under consideration, $[\mathbf{F}^{\mathrm{el}}]^{-1}$ is the deformation that would occur if after the deformation F, the inelastic response were somehow prevented but at the same time the stress at the point is reduced to zero. $\mathbf{F}^{\mathrm{pl}}$ is defined by

$$\mathbf{F}^{\mathrm{pl}} = \left[\mathbf{F}^{\mathrm{el}}\right]^{-1} \cdot \mathbf{F} \tag{3.73}$$

The rigid body rotation at the point can be included in the definition of either $\mathbf{F}^{el}$ or $\mathbf{F}^{pl}$ or can be considered separately before or after either part of the decomposition. This makes no difference except in the convenience of the basis for writing the parts of the deformation. This decomposition can be used directly to formulate the plasticity model by writing the additive strain rate decomposition as

$$\dot{\boldsymbol{\varepsilon}} = \dot{\boldsymbol{\varepsilon}}^{el} + \dot{\boldsymbol{\varepsilon}}^{pl} \tag{3.74}$$

Here, $\dot{\boldsymbol{\varepsilon}}$ is the total (mechanical) strain rate, $\dot{\boldsymbol{\varepsilon}}^{el}$ is the elastic strain rate, and $\dot{\boldsymbol{\varepsilon}}^{pl}$ is the plastic strain rate. It can be shown that equation (3.74) can be a consistent approximation to equation (3.72) when the elastic strains are infinitesimal (negligible compared to unity) and when the strain rate measure used in equation (3.74) is the rate of deformation

$$\dot{\boldsymbol{\varepsilon}} = \mathrm{sym}\left[\frac{\partial \mathbf{v}}{\partial \mathbf{x}}\right] \tag{3.75}$$

Equation (3.74), with the rate of deformation equation (3.75) used as the definition of total strain rate, is used in the plasticity models. Rice's argument implies that the elastic response must always be small in problems in which these equations are used. In practice this is the case.

The elastic part of the response is assumed to be derivable from an elastic strain energy density potential, as

$$\boldsymbol{\sigma} = \frac{\partial \mathrm{U}}{\partial \boldsymbol{\varepsilon}^{el}} \tag{3.76}$$

where, U is the strain energy density potential. Since we assume that, in the absence of plastic straining, the variation of elastic strain is the same as the variation in the rate of deformation, conjugacy arguments define the stress measure $\boldsymbol{\sigma}$ as the true Cauchy stress.

In some materials the elastic response is essentially incompressible. But this is not usually the case for the materials whose inelastic deformation is considered, so equation (3.76) can be taken to define the stress completely. However, the inelastic response is often assumed to be approximately incompressible, so care must be taken

to ensure that the elements chosen can accommodate incompressible response without exhibiting "locking" problems when the model is plane strain or axisymmetric. The strain energy density potential has a simple form as the elasticity is considered to be linear.

The rate-independent plasticity models have a region of purely elastic response. The yield function, *f*, defines the limit to this region of purely elastic response and is written so that the following inequality is satisfied for purely elastic response

$$f(\boldsymbol{\sigma}, H_\alpha) < 0 \tag{3.77}$$

Here H_α is a set of hardening parameters. The subscript α is introduced simply to indicate that there may be several hardening parameters. The range of α is not specified until we define a particular plasticity model. The hardening parameters are state variables that are introduced to allow the models to describe some of the complexity of the inelastic response of real materials. In the simplest plasticity model (perfect plasticity) the yield surface acts as a limit surface and there are no hardening parameters at all (i.e. no part of the model evolves during the deformation). Complex plasticity models usually include a large number of hardening parameters.

The yield behavior can be modeled with several independent inelastic flow systems and for this case, equation (3.77) is generalized for purely elastic response in system *i*, as:

$$f_i(\boldsymbol{\sigma}, H_{i,a}) < 0 \tag{3.78}$$

where, f_i is one of the yield functions and $H_{i,\alpha}$ are the hardening parameters for the i^{th} system. For generality in this discussion we assume the model uses such a system of independent yield functions. In the simple system with a single yield function, *i* take the value of unity.

Stress states that cause the yield function to have a positive value cannot occur in rate-independent plasticity models, although this is possible in rate-dependent models. Thus, in the rate-independent models we have the yield constraints during inelastic flow also known as the *consistency condition* given by

$$f_i = 0 \tag{3.79}$$

when the material is flowing inelastically the inelastic part of the deformation is defined by the flow rule,

$$d\boldsymbol{\varepsilon}^{pl} = \sum_i d\lambda_i \frac{\partial g_i}{\partial \boldsymbol{\sigma}} \tag{3.80}$$

where $g_i(\boldsymbol{\sigma}, H_{i,\alpha})$ is the flow potential for the i^{th} system and $d\lambda_i$ is a scalar measuring of the amount of the plastic flow rate on the i^{th} system, whose value is determined by the requirement to satisfy the consistency condition, for plastic flow of a rate-independent model. The summation is over only the active yielding systems: $d\lambda_i = 0$ for those systems for which equation (3.78) is valid.

The form in which the flow rule is written in equation (3.80) assumes that there is a single flow potential, g_i, in the i^{th} system. More general plasticity models might have several active flow potentials at a point. For some rate-independent plasticity models the direction of flow is the same as the direction of the outward normal to the yield surface given by

$$\frac{\partial g_i}{\partial \boldsymbol{\sigma}} = c_i \frac{\partial f_i}{\partial \boldsymbol{\sigma}} \tag{3.81}$$

where c_i is a scalar. Such models are said to obey an associated flow rule. Associated flow models are useful for materials in which dislocation motion provides the fundamental mechanisms of plastic flow when there are no sudden changes in the direction of the plastic strain rate at a point. The rate form of the flow rule is essential to incremental plasticity theory because it allows the history dependence of the response to be modeled.

The final ingredient in plasticity models is the set of evolution equations for the hardening parameters. We write these equations as:

$$dH_{i,\alpha} = d\lambda_i \, h_{i,\alpha}(\boldsymbol{\sigma}, H_{i,\beta}) \tag{3.82}$$

where $h_{i,\alpha}$ is the (rate form) hardening law for $H_{i,\alpha}$. In complex plasticity models these evolution laws have complicated forms, since such complexity is required to reach accurate conclusions. The independence of the yield systems, designated by the subscript *i,* is implicit in the assumption of equation (3.82) that the evolution of the $H_{i,\alpha}$ depends only on other hardening parameters $H_{i,\beta}$, in the same i^{th} system.

Equations (3.72) to (3.82) define the general structure of all plasticity models. Since the flow rule and the hardening evolution rules are written in rate form, they must be integrated. The general technique of integration is discussed in the following.

3.8.1 Integration of inelastic behavior

The equations describing the plasticity models have been discussed in detail in the last section. The only rate equations are the evolutionary rule for the hardening, the flow rule, and the strain rate decomposition. The simplest operator that provides unconditional stability for integration of rate equations is the backward Euler method. Applying this method to the flow rule equation (3.80) can be rewritten as:

$$\Delta\boldsymbol{\varepsilon}^{pl} = \sum_i \Delta\lambda_i \frac{\partial g_i}{\partial \boldsymbol{\sigma}} \tag{3.83}$$

Applying this method to the hardening evolution equations (3.82), gives:

$$\Delta H_{i,\alpha} = \Delta\lambda_i h_{i,\alpha} \tag{3.84}$$

In these equations any quantity not specifically associated with a time point is taken at the end of the increment (at time t+Δt). The strain rate decomposition equation (3.74) is integrated over a time increment as:

$$\Delta\boldsymbol{\varepsilon} = \Delta\boldsymbol{\varepsilon}^{el} + \Delta\boldsymbol{\varepsilon}^{pl} \tag{3.85}$$

where $\Delta\varepsilon$ is defined by the central difference operator as:

$$\Delta\boldsymbol{\varepsilon} = sym\left[\frac{\partial\Delta\mathbf{x}}{\partial(\mathbf{x}_t + \frac{1}{2}\Delta\mathbf{x})}\right] \tag{3.86}$$

We integrate the total values of each strain measure as the sum of the value of that strain at the start of the increment, rotated to account for rigid body motion during the increment, and the strain increment. The rotation to account for rigid body motion during the increment is defined approximately using the algorithm of Hughes and

Winget (1980). This integration allows the strain rate decomposition to be integrated into

$$\boldsymbol{\varepsilon} = \boldsymbol{\varepsilon}^{\mathrm{el}} + \boldsymbol{\varepsilon}^{\mathrm{pl}} \tag{3.87}$$

From a computational viewpoint the problem is now algebraic. We must solve the integrated equations of the constitutive model for the state at the end of the increment. The set of equations that define the algebraic problem are the strain decomposition equation (3.87), the elasticity equation (3.76), the integrated flow rule equation (3.83), the integrated hardening law equation (3.84) and for rate independent models, the consistency condition.

We assume that the flow surface is sufficiently smooth so that its second derivatives with respect to stress and the hardening parameters are well-defined. This is generally true with exceptions occurring at corners or vertices of the surfaces. For some plasticity models the algebraic problem can be solved in closed form. For other models it is possible to reduce the problem to a one variable or a two variable problem that can then be solved to give the entire solution.

For other rate-independent models with a single yield system the algebraic problem is considered to be a problem in the components of $\Delta\boldsymbol{\varepsilon}^{\mathrm{pl}}$. Once these have been found, the elasticity together with the integrated strain rate decomposition defines the stress. The consistency condition defines $\Delta\lambda$ and the hardening laws define the increments in the hardening variables.

We now derive the equations for the Newton solution of the integrated problem for the case of rate-independent plasticity with a single yield system. The rate-dependent problem with a single yield system is solved in a similar way. During the solution, the elasticity relationship and the integrated strain rate decomposition are satisfied exactly, so that:

$$\mathbf{c}_{\sigma} = -\mathbf{D}^{el} : \mathbf{c}_{\varepsilon} \tag{3.88}$$

Where $\mathbf{c}_{\sigma}$ is the correction to the stress, $\mathbf{c}_{\varepsilon}$ is the correction to the plastic strain increments. The tangent elasticity matrix is given by

$$\mathbf{D}^{el} = \frac{\partial^2 U}{\partial \boldsymbol{\varepsilon}^{el} \partial \boldsymbol{\varepsilon}^{el}} \tag{3.89}$$

The hardening laws are also satisfied exactly (because the increments of the hardening parameters are defined from these laws) so that:

$$c_\alpha = h_\alpha c_\lambda + \Delta\lambda \left(\frac{\partial h_a}{\partial \boldsymbol{\sigma}} : \mathbf{c}_\sigma + \frac{\partial h_a}{\partial H_\beta} c_\beta \right) \tag{3.90}$$

where c_α is the correction to ΔH_α and c_λ is the correction to $\Delta\lambda$.

This set of equations can be rewritten as:

$$c_\alpha = H_\alpha c_\lambda + \hat{\mathbf{w}}_\alpha : \mathbf{c}_\sigma \tag{3.91}$$

where

$$\hat{H}_\alpha = \left[\delta_{\alpha\beta} - \Delta\lambda \frac{\partial h_\beta}{\partial H_\alpha} \right]^{-1} h_\beta \tag{3.92}$$

and

$$\hat{\mathbf{w}}_\alpha = \Delta\lambda \left[\delta_{\alpha\beta} - \Delta\lambda \frac{\partial h_\beta}{\partial H_\alpha} \right]^{-1} \frac{\partial h_\beta}{\partial \boldsymbol{\sigma}} \tag{3.93}$$

The flow rule is not satisfied exactly until the solution has been found, so it gives rise to the Newton equations:

$$\mathbf{c}_\varepsilon - c_\lambda \frac{\partial g}{\partial \boldsymbol{\sigma}} - \Delta\lambda \left(\frac{\partial^2 g}{\partial \boldsymbol{\sigma} \partial \boldsymbol{\sigma}} : \mathbf{c}_\sigma + \frac{\partial^2 g}{\partial \boldsymbol{\sigma} \partial \mathrm{H}_\alpha} c_\alpha \right) = \Delta\lambda \frac{\partial g}{\partial \boldsymbol{\sigma}} - \Delta\boldsymbol{\varepsilon}^{pl} \tag{3.94}$$

Substituting equation (3.88) and equation (3.91) into equations (3.94) allows these equations to be rewritten as:

$$\left[\mathbf{I} + \Delta\lambda \hat{\mathbf{N}} : \mathbf{D}^{el} \right] : \mathbf{c}_\varepsilon - \hat{\mathbf{n}} c_\lambda = \Delta\lambda \frac{\partial g}{\partial \boldsymbol{\sigma}} - \Delta\boldsymbol{\varepsilon}^{pl} \tag{3.95}$$

where

$$\hat{\mathbf{N}} = \frac{\partial^2 g}{\partial \boldsymbol{\sigma} \partial \boldsymbol{\sigma}} + \frac{\partial^2 g}{\partial \boldsymbol{\sigma} \partial H_a} \hat{\mathbf{w}}_a \tag{3.96}$$

and

$$\hat{\mathbf{n}} = \frac{\partial g}{\partial \boldsymbol{\sigma}} + \Delta\lambda \frac{\partial^2 g}{\partial \boldsymbol{\sigma} \partial H_a} \hat{\mathrm{H}}_a \tag{3.97}$$

Likewise, the yield condition is not satisfied exactly during the Newton iteration, so

$$\frac{\partial f}{\partial \boldsymbol{\sigma}} : \mathbf{c}_\sigma + \frac{\partial f}{\partial H_\alpha} c_\alpha = -f \tag{3.98}$$

Substituting equation (3.88) and equation (3.91) into equation (3.98) allows this equation to be rewritten as:

$$\hat{\mathbf{m}} : \mathbf{D}^{el} : \mathbf{c}_\varepsilon - \frac{\partial f}{\partial H_a} \hat{H}_a c_\lambda = f \tag{3.99}$$

where

$$\hat{\mathbf{m}} = \frac{\partial f}{\partial \boldsymbol{\sigma}} + \frac{\partial f}{\partial H_\alpha} \hat{\mathbf{w}}_a \tag{3.100}$$

We now eliminate c_λ between equation (3.95) and equation (3.99). Taking equation (3.95) along $\hat{\mathbf{m}} : \mathbf{D}^{el}$ and using equation (3.99) gives equation (3.101):

$$c_\lambda = \frac{1}{d} \Delta\lambda \, \hat{\mathbf{m}} : \mathbf{D}^{el} : \hat{\mathbf{N}} : \mathbf{D}^{el} : \mathbf{c}_\varepsilon - \frac{1}{d} \hat{\mathbf{m}} : \mathbf{D}^{el} : (\Delta\lambda \frac{\partial g}{\partial \boldsymbol{\sigma}} - \Delta\varepsilon^{pl}) + \frac{1}{d} f \tag{3.101}$$

where

$$d = \hat{\mathbf{m}} : \mathbf{D}^{el} : \hat{\mathbf{n}} - \frac{\partial f}{\partial H_a} \hat{H}_a \tag{3.102}$$

Using equation (3.102) in equation (3.95) then gives:

$$\left[\mathbf{I} + \Delta\lambda \mathbf{Z} : \hat{\mathbf{N}} : \mathbf{D}^{el} \right] : \mathbf{c}_\varepsilon = \mathbf{Z} : \left(\Delta\lambda \frac{\partial g}{\partial \boldsymbol{\sigma}} - \Delta\varepsilon^{pl} \right) + \frac{1}{d} f \hat{\mathbf{n}} \tag{3.103}$$

where

$$\mathbf{Z} = \mathbf{I} - \frac{1}{d}\hat{\mathbf{n}}\,\hat{\mathbf{m}} : \mathbf{D}^{el} \tag{3.104}$$

which is a set of linear equations solved for the $\mathbf{c}_\varepsilon$. The solution is then updated and the Newton loop continued until the flow equation and yield constraint are satisfied (Abaqus 2006).

3.8.2 Inelastic tangent matrix

The tangent matrix for the material, $\partial\boldsymbol{\sigma}/\partial\varepsilon$, is required for the implicit time integration and the Newton's method is being used to solve the equilibrium equations. The matrix is obtained directly by taking variations of the integrated equations with respect to all solution parameters and then solving for the relationship between $\boldsymbol{\sigma}$ and $\boldsymbol{\varepsilon}$. The procedure closely follows the derivation used above for the Newton solution. The result is the elastoplastic tangent matrix (Abaqus 2006):

$$\boldsymbol{\sigma} = \mathbf{D}^{ep} : \boldsymbol{\varepsilon} \tag{3.105}$$

where

$$\mathbf{D}^{ep} = \left[\mathbf{I} + \Delta\lambda \mathbf{D}^{el} : \mathbf{Z} : \hat{\mathbf{N}}\right]^{-1} : \mathbf{D}^{el} : \mathbf{Z} \tag{3.106}$$

Equation (3.106) expresses the elastoplastic tangent stiffness matrix of the material which in turn is inserted in equation (3.36) that expresses the variation of the internal force array and therefore the behavior of the poroelastoplastic continuum is completely defined.

3.9 Propagation Criterion

The propagation criterion that was used in the fluid driven fracture was the cohesive zone. Cohesive zone has proved to be a useful tool in modelling among others, rock fractures that can be envisioned as bonded interfaces. The constitutive response of these interfaces depends on the specific application and is based on certain assumptions about the deformation and stress states that are appropriate for each application area. For rock fracture the most appropriate constitutive behaviour is the traction-separation description of an interface.

The modelling of fractures by means of interfaces, often involves situations where the intermediate glue material is thin and for practical purposes may be considered to be of zero thickness. This allows the use of concepts derived from fracture mechanics (i.e. such as the amount of energy required to create new surfaces). The cohesive zone is able to model the initial loading, the initiation of damage and the propagation of damage, leading to eventual failure at the bonded interface. This means that it can be used to model situations where fractures are expected to develop. The precise locations where fractures initiate, as well as the evolution characteristics of such fractures, are determined as part of the solution. The fractures are restricted to propagate along the predefined layer of the cohesive zone and will not deflect into the surrounding material. In two dimensional problems the traction separation based model assumes two components of separation, one normal to the interface and the other parallel to it. The corresponding stress components are assumed to be active at a material point.

The constitutive behaviour of traction-separation which is described in this section is most suitable for bonded interfaces where the interface thickness is negligibly small. In such cases it may be straightforward to define the constitutive response of the cohesive layer directly in terms of traction versus separation. This behaviour in the cohesive zone is defined directly and can be used to model the linear elastic traction-separation law prior to damage and assume that failure of the cohesive zone is characterized by progressive degradation of the material stiffness, which is driven by a damage process.

3.9.1 Linear elastic traction-separation behavior

The traction-separation model assumes initially linear elastic behaviour followed by the initiation and evolution of damage. The elastic behaviour is written in terms of an elastic constitutive matrix that relates the nominal stresses to the nominal strains across the interface. The nominal stresses are the force components divided by the original area at each integration point, while the nominal strains are the separations divided by the original thickness at each integration point. Assuming a value of constitutive thickness 1.0 ensures that the nominal strain is equal to the separation. The constitutive thickness used for traction-separation response is typically different from the geometric thickness (which is typically close or equal to zero).

The nominal traction stress vector **t**, consists of three components (two in 2D problems): $\mathbf{t_n}$, $\mathbf{t_s}$, and (in 3D problems) $\mathbf{t_t}$, which represent the normal and two shear tractions respectively. The corresponding separations are denoted by δ_n, δ_s and δ_t. Denoting by T_o the original thickness of the cohesive element, the nominal strains can be defined as (Abaqus 2006):

$$\varepsilon_n = \frac{\delta_n}{\mathrm{T}_o}, \quad \varepsilon_s = \frac{\delta_s}{\mathrm{T}_o}, \quad \varepsilon_t = \frac{\delta_t}{\mathrm{T}_o} \tag{3.107}$$

The elastic behaviour can then be written according to

$$\mathbf{t} = \mathbf{K}.\varepsilon \Rightarrow$$
$$\begin{Bmatrix} t_n \\ t_s \\ t_t \end{Bmatrix} = \begin{bmatrix} K_{nn} & K_{ns} & K_{nt} \\ K_{ns} & K_{ss} & K_{st} \\ K_{nt} & K_{st} & K_{tt} \end{bmatrix} . \begin{Bmatrix} \varepsilon_n \\ \varepsilon_s \\ \varepsilon_t \end{Bmatrix} \tag{3.108}$$

The elasticity matrix provides fully coupled behaviour between all components of the traction vector and separation vector and can depend on temperature. If the off-diagonal terms in the elasticity matrix are zero then the uncoupled behaviour between the normal and shear components is modelled.

3.9.2 Damage modelling

Progressive damage and failure is usually modelled in the cohesive zone layers whose response is defined in terms of traction-separation. Damage of the traction-separation response is defined within the same general framework used for conventional materials. This general framework allows the combination of several damage mechanisms acting simultaneously on the same material. Each failure mechanism consists of three ingredients: a damage initiation criterion, a damage evolution law and a choice of element removal (or deletion) upon reaching a completely damaged state. While this general framework is the same for traction-separation response and conventional materials, many details of how the various ingredients are defined are different. Therefore, the details of damage modelling for traction-separation response are presented below. The initial response of the cohesive zone is assumed to be linear as discussed above. However, once a damage initiation criterion is met, material damage can occur according to a damage evolution law. At this point it is considered

important to mention that the cohesive zone layer does not undergo damage under pure compression.

3.9.3 Damage initiation

Damage initiation refers to the beginning of degradation of the response of a material point. The process of degradation begins when the stresses or the strains satisfy certain damage initiation criteria. Several damage initiation criteria are available in the literature. Each damage initiation criterion has an output variable associated with it to indicate whether the criterion is met. A value of 1 usually indicates that the initiation criterion has been met.

In the discussion below, $\mathbf{t_n^o}$, $\mathbf{t_s^o}$, and $\mathbf{t_t^o}$ represent the peak values of the nominal stress when the deformation is either purely normal to the interface or purely in the first or the second shear direction, respectively. Likewise, ε_n^o, ε_s^o and ε_t^o represent the peak values of the nominal strain when the deformation is either purely normal to the interface or purely in the first or the second shear direction, respectively. With the initial constitutive thickness $T_o = 1$, the nominal strain components are equal to the respective components of the relative displacements δ_n, δ_s, and δ_t between the top and bottom of the cohesive zone layer.

3.9.3.1 Maximum nominal stress criterion

Damage is assumed to initiate when the maximum nominal stress ratio reaches a value of one. This criterion can be represented as (Abaqus 2006):

$$\max\left\{\frac{\langle t_n\rangle}{t_n^o}, \frac{t_s}{t_s^o}, \frac{t_t}{t_t^o}\right\} = 1 \tag{3.109}$$

The symbol $\langle\ \rangle$ used in the discussion below represents the Macaulay brackets with the usual interpretation. The Macaulay brackets are used to signify that a pure compressive stress state does not initiate damage.

3.9.3.2 Maximum nominal strain criterion

Damage is assumed to initiate when the maximum nominal strain ratio reaches a value of one. This criterion can be represented as (Abaqus 2006):

$$\max\left\{\frac{\langle \varepsilon_n \rangle}{\varepsilon_n^o}, \frac{\varepsilon_s}{\varepsilon_s^o}, \frac{\varepsilon_t}{\varepsilon_t^o}\right\} = 1 \tag{3.100}$$

Selection of either of the damage initiation criteria (max nominal stress/ max nominal strain), will make no difference and the result will be the same.

3.9.4 Damage evolution

The damage evolution law describes the rate at which the material stiffness is degraded once the corresponding initiation criterion is reached. A scalar damage variable *D*, represents the overall damage in the material and captures the combined effects of all active mechanisms. The damage variable *D*, initially has a value of 0. If damage evolution is desired, *D* monotonically evolves from 0 to 1 upon further loading after the initiation of damage. The stress components of the traction-separation model are affected by the damage as (Abaqus 2006):

$$\begin{aligned} \mathbf{t_n} &= \begin{cases} (1-D)\,\bar{\mathbf{t}}_\mathbf{n}, & \bar{\mathbf{t}}_\mathbf{n} \geq 0 \\ \bar{\mathbf{t}}_n, & otherwise \end{cases} \\ \mathbf{t_s} &= (1-D)\,\bar{\mathbf{t}}_\mathbf{s} \\ \mathbf{t_t} &= (1-D)\,\bar{\mathbf{t}}_\mathbf{t} \end{aligned} \tag{3.111}$$

where $\bar{\mathbf{t}}_\mathbf{n}$, $\bar{\mathbf{t}}_\mathbf{s}$ and $\bar{\mathbf{t}}_\mathbf{t}$ are the stress components predicted by the elastic traction-separation behavior for the current strains without damage. For a deformation in the normal direction, the values for the two shear tractions (shear and transverse direction) are zero.

There are two components to the definition of the evolution of damage. The first component involves specifying either the effective displacement at complete failure δ_m^f, relative to the effective displacement at the initiation of damage δ_m^f or the energy G_C dissipated due to failure. The second component to the definition of damage evolution is the specification of the nature of the evolution of the damage variable *D*, between initiation of damage and final failure. This can be done by either defining linear or exponential softening laws or specifying *D* directly as a tabular function of the effective displacement relative to the effective displacement at damage initiation.

3.9.4.1 Evolution based on effective displacement

When the evolution of damage is based on the effective displacement, the quantity $\delta_m^f - \delta_m^o$ can be specified. This quantity can specify the effective displacement at complete failure δ_m^f, relative to the effective displacement at damage initiation δ_m^o. In addition, this quantity can be modeled to account for either a linear or an exponential softening law that defines the detailed evolution (between initiation and complete failure) of the damage variable *D* as a function of the effective displacement beyond damage initiation.

3.9.4.2 Evolution based on energy

Damage evolution can be defined based on the energy that is dissipated as a result of the damage process, also called the fracture energy. The fracture energy is equal to the area under the traction-separation curve. This quantity can be specified as a material property and modify it to account either a linear or an exponential softening behavior. The area under the linear or the exponential damage response curve is then integrated and is taken to be equal to the fracture energy and no fracture propagation takes place until all the amount of fracture energy is expended.

3.10 Conclusions

In this chapter we presented the equations that govern the fluid driven problem in a deformable poroelastoplastic continuum to formulate and solve the numerical model with the finite element method. The equations are coupled and non linear. The main assumptions upon the model is based, are summarized in the following:

- The deformation of the porous continuum is obtained from the equilibrium equation for the porous media in the descritized weak form.
- The constitutive behavior of the porous continuum is incorporated in the effective stress principle.
- The fluid flow in the porous domain is governed by a continuity equation that describes the flow of the wetting fluid and incorporates the Darcy's law.
- The Fluid flow inside the fracture is derived via the lubrication model which is represented by a diffusion equation that includes fluid infiltration from the fracture into the surrounding medium.

- The inelastic behavior of the porous continuum is described by the tangent stiffness matrix of the material which is required in the equilibrium equations. The tangent stiffness matrix is obtained directly by taking variations of the integrated flow rule and the hardening evolution rule with respect to the solution parameters.
- The propagation criterion used for extending the fracture is the cohesive zone which can be easily implemented in a finite element model.
- The coupled equations can be solved numerically by utilizing the finite element method.

4. Numerical Implementation

4.1 Preamble

In this chapter the fully coupled numerical model for a fluid driven fracture in a dry rock is described. It will be modified and used later to study the importance of the cohesive zone characteristics in hydraulic fracturing under poroelastic and poroelastoplastic conditions. The models were developed for plane strain geometry taking into consideration both upper quarter symmetry conditions and half symmetric fracture. This geometry is appropriate for modelling short fractures with fracture height relatively greater than the fracture length. Furthermore, this geometry is also appropriate for examining tip effects since the deformation of any arbitrary fracture shape is approximately planar near the tip. The fracture propagates perpendicular to the minimum in situ stress and remains planar. This predefined path for the propagation is also convenient with the cohesive zone numerical approach. Section 4.2 describes the methodology that has been used to setup the numerical models. The complete numerical solution and the necessary checks to validate the numerical model are presented in section 4.3, while in section 4.4 the numerical model is verified by comparing with analytical solutions and other related numerical results. Finally, section 4.5 summarizes the conclusions obtained from these comparisons.

4.2 Numerical Modelling Methodology

The physical process of the fluid driven fracture involves the pumping of a viscous fluid that pressurizes the fracture surfaces which deform. Increasing the pressurization, critical loading conditions will be reached ahead of the tip splitting the rock and driving hydraulically the fracture. Thus, this process reveals that there is a strong coupling between the moving fluid, rock deformation and fracture propagation. Depending on the formation properties, in-situ stresses and pumping parameters, the fracture may propagate for more than hundred meters. In this study the fracture will propagate few meters, enough to extrapolate and reach correct conclusions for long-fractures. The propagation of a short fracture can also be used to interpret the results of the mini-frac, a calibration test that is carried out first in-situ for determining parameters such as the formation permeability and the closure stress that are further used for modelling the long hydraulic fractures.

4.2.1 Fracturing fluids and rock failure

The fluids that are used in hydraulic fracturing are normally power-law with shear-thinning behavior which means that the viscosity decreases with increasing shear rate. In order to avoid this complex fluid behavior, a simple appropriate model for fluid flow in a fracture is embodied in lubrication theory. It assumes laminar flow (uniformly viscous Newtonian), the fluid is incompressible and it accounts for the time dependent rate of fracture opening. This behavior is described by equation (3.64) that has been presented in chapter 3. The mechanical failure of the rock is assumed to follow the effective stress principle as described by equation (3.2) that has been presented in chapter 3. Here it is just repeated for the purpose of complete description of the numerical model.

4.2.2 Propagation criterion parameters

The most robust criterion for non-linear mechanics is described by the cohesive zone constitutive model. The cohesive zone is a region ahead of the crack tip that is characterized by micro-cracking along the crack path. The main fracture is formed by inter connection of these micro cracks. The cohesive zone model implies that normal stress continues to be transferred across a discontinuity which may or may not be visible as shown in Figure (4.1):

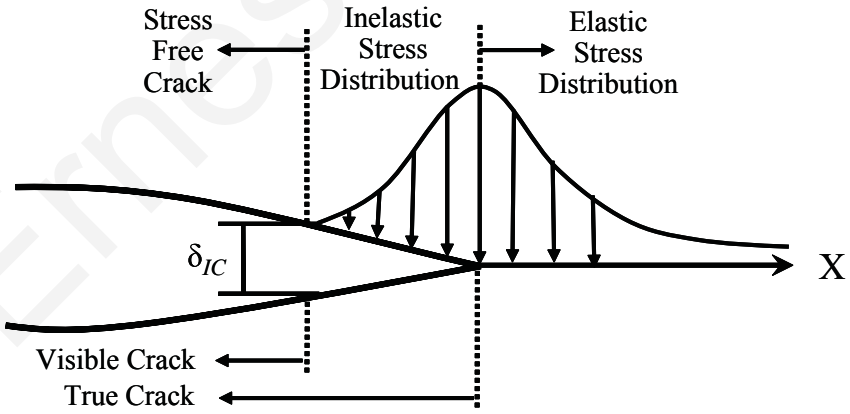

Figure 4.1: Representation of the fracture process

This stress is determined from the softening stress-strain relation that various rocks exhibit in calibrations tests. This transferred normal stress is a function of the separation and falls to zero at a critical opening and then the fracture propagates. The evolution of the crack is governed by energy balance between the work of the external loads and the sum of the bulk energy of the uncracked part and the energy dissipated

in the fracture process. The main mathematical difficulty is given by the fact that the fracture energy depends on the opening of the distributed micro-cracks. To simplify the mathematical difficulties, it is assumed that the cohesive zone localizes, due to its softening behavior, into a narrow band ahead of the visible fracture. The upper and lower surfaces of the narrow band are termed as the cohesive surfaces or interfaces and are linked by the cohesive tractions which follow a cohesive constitutive law that relates the cohesive traction to the separation displacement of the cohesive surfaces.

The constitutive behavior of the cohesive zone is defined by the traction-separation relation which is derived from laboratory tests. The traction-separation constitutive relation for the surface is such that with increasing separation, the traction across this cohesive surface reaches a peak value and then decreases and eventually vanishes, permitting for a complete separation. Simple cohesive zone models (figure 4.2) can be described by two independent parameters which are usually, for mode-I plane strain, the normal work of separation or the fracture energy G_{IC} and either the tensile strength σ_t or the complete separation length δ_{IC}. An additional parameter in these models is the slope of the initial loading which may define a range from rigid-softening to elastic-softening response under tensile stress-state.

The area under the traction-separation curve equals the fracture energy G_{IC} which is the work needed to create a unit area of fully developed fracture. For elastic solids this energy is related to the rock fracture toughness K_{IC} as (Rice 1968; Kanninen & Popelar 1985):

$$K_{IC}^2 = \frac{G_{IC} E}{1-\nu^2} \tag{4.1}$$

where E is the young modulus and ν is the Poisson ratio. The rock fracture toughness can be calculated from laboratory tests. For the case of the rigid-softening behavior the traction-separation relation is uniquely determined by

$$\sigma = \sigma_t (1 - \frac{\delta}{\delta_{IC}}) \tag{4.2}$$

where σ_t is the uniaxial tensile strength of the rock and δ_{IC} is the critical opening displacement at which σ falls to zero. The value of δ_{IC} is given by

$$\delta_{IC} = \frac{2K_{IC}^2(1-\nu^2)}{\mathrm{E}\sigma_t} \tag{4.3}$$

For the case of the elastic loading the cohesive constitutive relations were augmented and modified to take into account the initial part of the curve as follows

$$\sigma = \sigma_t \left(\frac{\delta}{\delta_{el}} \right) \tag{4.4}$$

with the limit of elastic deformation given by

$$\delta_{el} = \frac{\sigma_t}{k_n} \tag{4.5}$$

where k_n is the stiffness of the traction-separation relation in the loading regime with units of [MPa/m]. In the post-peak softening regime the cohesive constitutive relation is given by

$$\sigma = \sigma_t \left[1 - \frac{(\delta - \delta_{el})}{(\delta_{IC} - \delta_{el})} \right] \tag{4.6}$$

Therefore, the traction-separation equation yields:

$$\sigma = \sigma_t (1 - D) \tag{4.7}$$

The critical value of the fracture opening displacement is uniquely determined from the above equation (4.7).

Figure (4.2) shows the graphical representation of the cohesive zone laws for rigid-softening and elastic-softening behavior. The material parameters used are shown in Table (4.1). Two different cases K_n (x1) and K_n (x20) are assumed to represent the cases of soft rock formation and hard rock formation respectively and will be analyzed in detail later in this chapter. For the objectives of this chapter, the hard rock formation K_n (x20) will be utilized so as to compare with analytic solutions readily available from the literature.

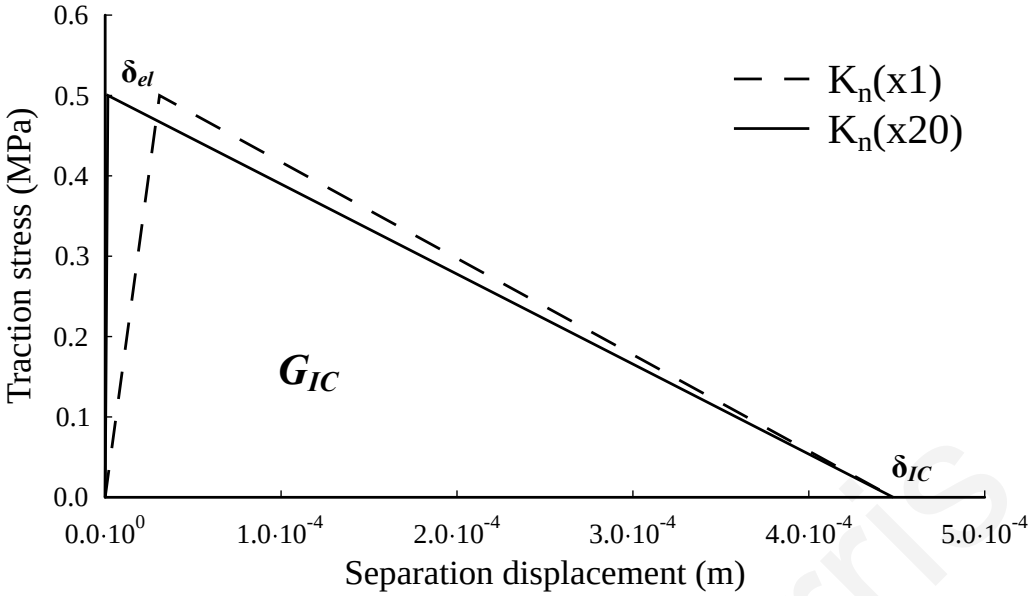

Figure 4.2: Constitutive cohesive zone law

Figure (4.2) shows the tractions stress vs the separation distance. The critical separation δ_{IC} is the point that describes the visible fracture opening (complete separation-fracture propagation). The inelastic stress distribution is described when the separation distance is between the peak value δ_{el} and the critical separation δ_{IC}. The peak value of δ_{el} describes the position of the actual fracture tip which is the point that the fracture is initiated. Finally, the separation distance from 0 to the peak value δ_{el} is the regime that the material obeys elastic stress distribution.

4.2.3 Domain discretization for fracture analysis

As described before, the major advantage of the cohesive zone is the ability to predict both onset and propagation of fracturing without the need of complex analysis as it is widely accepted that the fracture tip location analysis is a moving boundary problem which poses special numerical difficulties. Furthermore, it does not require the topological information for the fracture front (or the exact fracture shape) in finite element implementation. However, the softening part of the cohesive law in certain instances can give rise to difficulties leading to mesh sensitivity, lack of convergence, computing inefficiency, sensitivity to element aspect ratio. These issues are summarized in the work of De Borst (2001; 2003).

Currently there are two major approaches in implementing a cohesive zone model. The smeared cohesive element and the interface cohesive element. In the first

approach, the cohesive zone is applied as a part of the stress vs. strain relation like a conventional continuum element. This approach is not suitable for analyzing interfacial fracture growth. When the cohesive elements are placed between the two surfaces of initial zero separation that need to be decohered, a very thin layer must be inserted between the two surfaces to accommodate the smeared cohesive elements. This leads to large aspect ratio elements that may prevent the finite element analysis even to proceed. Furthermore, severe convergence difficulties may also encountered. Depending on the formulation, the stiffness matrix of these smeared elements may contain off-diagonal terms and will lead to a fully populated stiffness matrix as analyzed by Schellekens & De Borst (1993). These limitations were overcome by a number of researchers, to mention few, Benzeggagh & Kenane (1996); Mi et al. (1998), Alfano & Crisfield (2001) and Camanho & Davila (2002). The interface cohesive element approach is developed in a similar manner to the smeared cohesive approach except that the formulation is based on the stress vs. displacement separation. This approach eliminates the undesired spurious oscillation of the traction field when large traction gradients are present over an element.

The descritized domain area was considered to be a 30 m x 30 m and the predefined path of the fracture (interface cohesive elements) was defined to be 11 m. If a longer fracture is required, it can be easily implemented by extending the interface cohesive elements to the desired fracture length. The placement in the first 11 m only was considered to save computational time. In order to guarantee numerical convergence and to properly capture the details of the deformation field in the vicinity of the fracture tip and the traction distribution within the cohesive zone, the element size constrain must be smaller than the cohesive zone length. The cohesive zone length is an inherent length scale determined by the material properties and for mode-I fracture loading under plane strain conditions this length d_z, is given from (Rice 1980; Zuorong et al., 2009):

$$dz = \frac{9\pi}{32}\frac{K_{IC}^2}{\sigma_t^2} = \frac{9\pi}{32}\frac{E}{(1-\nu^2)}\frac{G_{IC}}{\sigma_t^2} \tag{4.8}$$

This element size constrain has been used as a criterion to build the cohesive elements in domain meshing. This was performed by placing 100 elements per 1 meter of fracture propagation which is more than sufficient to capture the cohesive zone length.

No special re-meshing scheme was used as the mesh was defined to be sufficiently fine along the fracture path. The finite element mesh was generated using the front advancement algorithm. The geometry and the resulting discretization are shown in Figure (4.3).

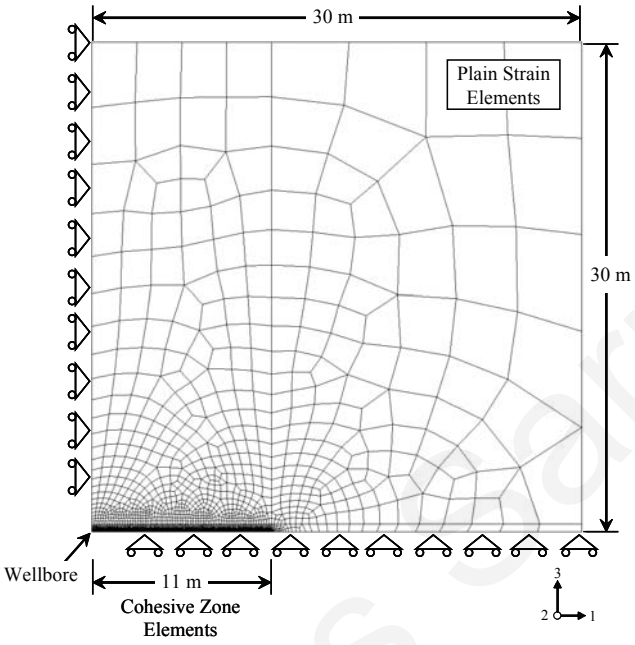

Figure 4.3: Geometry, boundary conditions and discretized domain

Plane strain isoparametric elements with 4-nodes were used to model the domain. The 4-node elements were chosen to obtain one to one correspondence between the nodes of the flow and the domain elements. In this way the fluid mass is conserved across the boundary. For the fluid flow, 6-node cohesive elements were used to model the viscous flow in the fracture and the fracturing process. The cohesive elements were enhanced with two additional nodes for the modeling of the fluid flow. The type of flow constitutive response comprises a tangential and a normal flow along the fracture walls as shown in Figure (4.4). The numerical model for the fluid flow is constructed for the complete length of the predetermined fracture path. There is one to one correspondence between the plane strain "flow" and "domain" elements at the corner nodes along the fracture path, ensuring that the fluid mass is conserved across their interface.

There are two types of coupling that can occur along the fracture depending on whether the fracture walls are assumed permeable or impermeable. For impermeable walls, the fluid pressures in the fracture are converted to equivalent nodal loads and

applied appropriately. For permeable walls, the fluid pressure in the fracture must be applied as a pore pressure and a total stress boundary condition. This is also known as the Cauchy boundary condition for the pressure in flow problems. In the case under consideration in this chapter, we assume impermeable domain, therefore the plane strain isoparametric elements with 4-nodes do not have a pore pressure d.o.f and will contribute only in a mechanical manner (u,v translation d.o.f). In later chapters where the porous behavior will be analyzed, pore pressure d.o.f's will be assigned in the domain and diffusion will be modeled. The numerical approximation of this behaviour is presented in figure (4.4) which expresses the type of flow pattern along the fracture utilizing the cohesive zone elements.

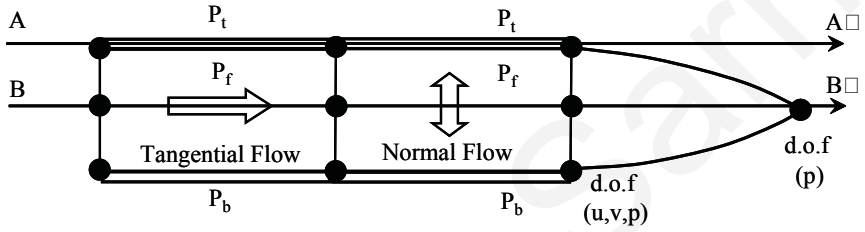

Figure 4.4: Cohesive zone element

where P_f is the fluid pressure inside the fracture, P_t and P_b are the fluid pressures outside the fracture in the adjacent continuum on top and the bottom of the created fracture.

Lines A-A' and B-B' represent the paths that are followed to analyze the obtained results after the numerical simulation. Sampling the unique nodal vertical translation (u_y) along line A-A' will give the fracture opening vs. distance from wellbore. Sampling the unique nodal pore pressure (p) along line B-B' will give the fracture fluid pressure vs. distance from wellbore. Furthermore, sampling at the fracture mouth only (initial node) at the beginning of line B-B' will yield the pressure at wellbore according to the pumping schedule. Sampling at the node above the fracture mouth at the beginning of line A-A' will give the fracture opening at wellbore.

4.2.4 Boundary and initial conditions

The wellbore location is at the left-lower corner and the fracture is assumed to grow in both directions along the axis-1 (figure 4.3). For a long fracture the size of the wellbore is negligible and is usually ignored in the modeling. This remark, along with

the condition that the wellbore is cased, cemented and fully bonded with the rock formation, justifies the use of symmetry conditions within a reasonable accuracy (Figure 4.3). In order to simulate the growth in both directions and under upper quarter symmetry conditions, all the left boundary nodes were imposed with a symmetry condition ($d_x = 0$, fixed displacements). Furthermore, all the lower end nodes are imposed with symmetry conditions ($d_y = 0$, fixed displacements) as well as zero flow condition necessary due to symmetry requirements. The in-situ stresses were inserted as initial stresses and by applying the equilibrium load at the far right and top edges. At the top edge a value of $\sigma_3 = 3.7$ MPa was applied parallel to axis-3 as the minimum in situ stress or closure stress perpendicular to the fracture surfaces. The fracture will propagate along the axis-1 which is parallel to the maximum in situ stress $\sigma_1 = 14$ MPa. An initial condition is also required for defining an initial fracture length for the flow. This length was considered 0.1 m, approximately equals with the perforation length from where the fractures initiate. The in-situ stresses and the initial conditions are applied in the first step to achieve system equilibrium before the injection of the fracturing fluid and after that, in the second step, the fracture propagation is modeled. The fracturing fluid is assumed to be incompressible and the flow boundary condition is imposed at the fracture mouth to meet the specific injection flow rate (Neumann boundary condition).

4.3 Numerical Model Validation

In this section the results from the analysis of the fluid driven problem in an elastic and impermeable domain are presented to demonstrate the fully coupled solution. Furthermore, the numerical solution is compared with analytic solutions and other related numerical results for validating the numerical model. According to Valko & Economides (1995), a fully coupled numerical elastic solution of a fluid driven fracture is defined with the illustration of five plots described as follows:

- The first plot gives the displacement of the fracture walls (or in other words the fracture half-width) which will have an ellipsoid shape.
- The second plot gives the pressure distribution acting along the fracture walls as a result of the numerical solution.
- The third plot gives the fracture aperture at wellbore vs. injection time.

- The fourth plot gives the pressure profile at the wellbore vs. injection time which in field operations is of paramount importance as it is the only available parameter to evaluate the treatment operation.
- The last and fifth plot gives the tensile traction stress distribution ahead of the fracture tip.

From the above plots it is possible to calculate the solution of a) the fracture width *w (x,t)* b) the fracture length *l (t)* c) the fluid pressure *p (x,t)* and d) the tensile traction stress distribution ahead of the fracture tip where the three first are the main parameters needed to evaluate a hydraulic fracture treatment. Accurate conclusions can also be reached by examining the figure of pressure vs. distance from wellbore and the fracture half width vs. distance from wellbore.

The governing equations were discretized in space with the finite element method and in time with the finite difference method. Linear interpolations were used for both, the approximation of displacements and for the pore pressure degrees of freedom. The sharp changes that are expected in the geometry of the propagating tip, is dealt with placing a sufficient fine mesh around the predefined fracture path so as to ensure numerical accuracy. The calculations were carried out in Abaqus a nonlinear, state of the art finite element analysis software.

The parameters upon which the numerical computations were based are given in Table 4.1. For the constitutive cohesive law the rigid-softening curve was used. Results with elastic-softening will be reported in a later chapter. The main characteristic of the cohesive zone law which is the area under the curve G_{IC}, is calculated to be equivalent with fracture toughness K_{IC} = 1 MPa.m $^{0.5}$. In the pumping parameters, the fluid pressures are generated with the injection rate, Q which can be expressed as the fluid loading inside the fracture. The results presented in this chapter for the purposes of comparison with analytic solutions are obtained with an injection rate of 500e-06 (m^3/m.sec). For convergence reasons, the injection rate was set to climb its final flow rate value at the first 0.05 seconds of the injection time. The effect of the ramping slope to the final value is considered negligible. Generally, the solution of the fracture propagation length, width, fracturing pressures and cohesive stresses are a natural outcome of the numerical solution.

Table 4.1: Input parameters for the computational examples

Variable	Value
Elastic Rock Properties	
Young modulus, $\boldsymbol{E}$ (MPa)	16200
Poisson ratio, $\boldsymbol{v}$	0.3
Cohesive zone properties	
Constitutive thickness	1
Maximum Traction, $\boldsymbol{\sigma_t}$ (MPa)	0.5
Cohesive stiffness, $\boldsymbol{K_n}$ (MPa)	16200/324000
Cohesive energy, $\boldsymbol{J_{IC}} = \boldsymbol{G_{IC}}$ (kPa.m)	0.112
Permeability coefficients $\boldsymbol{qt}/\boldsymbol{qb}$ (m/sec)	2.421E-10
Pumping Parameters	
Viscosity, $\boldsymbol{\mu}$ (kPa.sec)	0.0001
Injection rate, $\boldsymbol{q}$ (m3/sec.m)	500.E-6
In-Situ Stress Field (Effective stresses)	
σ_1 (MPa)	14
σ_2 (MPa)	9
σ_3 (MPa)	3.7
Initial Conditions	
Void ratio, $\boldsymbol{e}$	0.333
Initial gap (perforation) - (m)	0.1
Pore pressure, $\boldsymbol{p}$ (MPa)	0

At this point, it is considered important to summarize the assumptions made for these particular simulations used for the comparison with analytic solutions:

- The solid is considered to be impermeable, isotropic linear elastic and homogeneous. This behavior is successfully described by the Young modulus E, and the Poisson ratio v.
- The fluid used to fracture the formation was considered to be viscous and incompressible with Newtonian Rheology. This behavior is successfully described by the fluid viscosity μ.
- The fracture is always in mobile equilibrium at all time frames and propagates only when it has dissipated all the cohesive energy described from the constitutive cohesive zone law (Figure 4.2).
- Fracturing is assumed to obey mode-I conditions.
- The fracture is assumed to be completely filled up with the injected fracturing fluid (i.e. fluid front coincides with the fracture visible tip), no fluid lag is attempted to be captured in the numerical models.
- Fluid flow is modeled according to lubrication theory.
- The analyses that are performed are quasi-static.

4.3.1 Numerical solution of a fluid driven fracture in an impermeable domain

In this section the results of the fully coupled elastic numerical solution are demonstrated for model verification. All the results correspond to fractures at the state of propagation. The fractures were propagated from an initial length of 0.1 m to reach 9 m long. Figure (4.5) shows the fracture half profile of a propagating fracture at different lengths every 1m interval for clarity reasons. In the area of the tip a small cusping exists as a result of the non linear distribution of the cohesive stresses that act on the fracture and tend to close it. As a result of the non local nature of the solution this behavior is transferred along the fracture and the resulting profile is not as blunted as an elastic fracture.

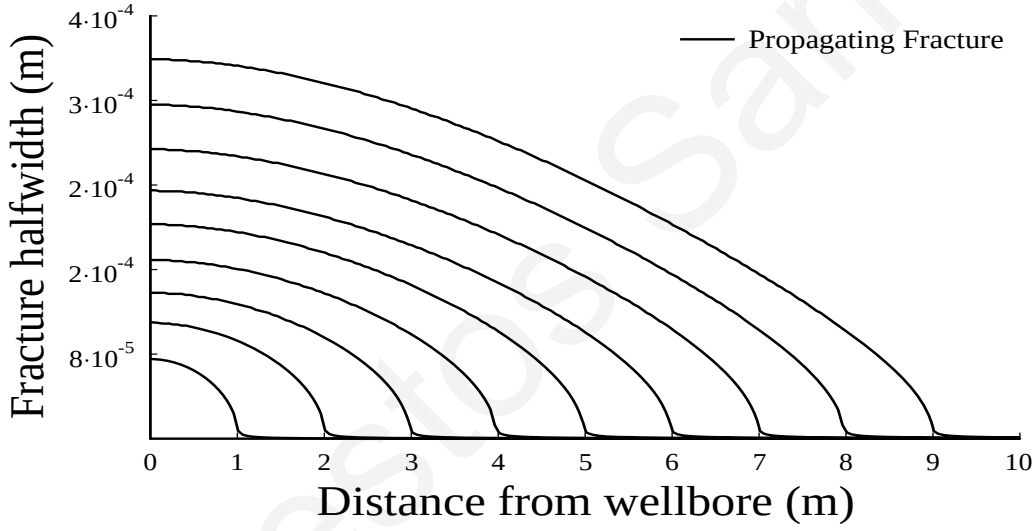

Figure 4.5: Fracture profiles of a propagating fracture

Figure (4.6) shows the corresponding fluid pressure profile in the fracture at different lengths, every 1m interval. The fluid front position is found at the point where the profile falls to zero. As it was mentioned the domain was considered to be impermeable and this assumption was also considered for the case of the cohesive elements. Therefore, the pressure drop takes place mainly at the visual tip for these specific parameters. Another important feature of Figure (4.6) is the large pressure drop is in the area near the tip.

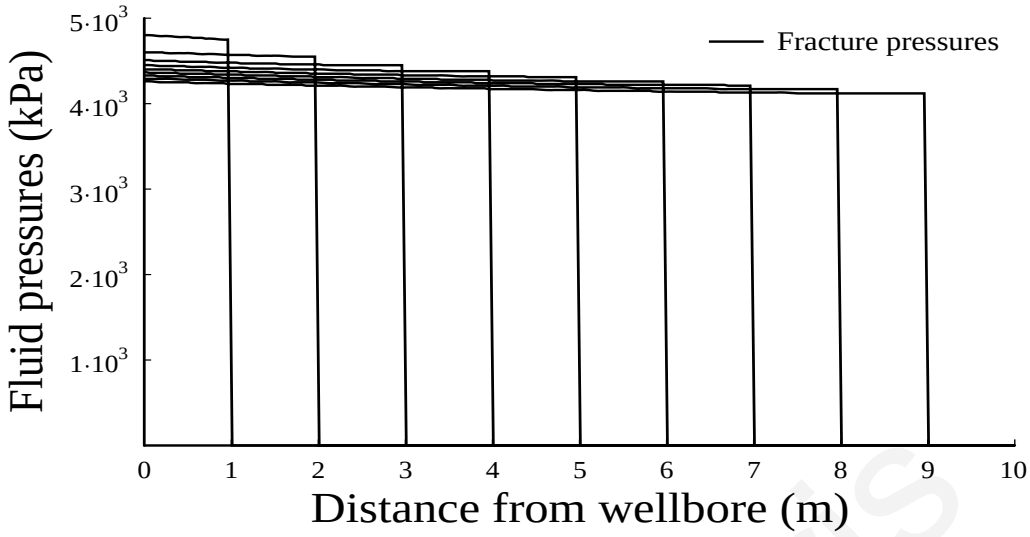

Figure 4.6: Fluid pressures of a propagating fracture

As mentioned earlier, the pressure is the only available parameter to evaluate the hydraulic fracture operation. The proper engineering approach to hydraulic fracturing design is to maximize the post-treatment performance and ensuing benefits with the lowest treatment costs. Net Present Value (NPV) Investment models.

Figure (4.7) presents the value of net pressure versus distance from wellbore. A significant pressure drop takes place when the fracture is shorter than 4 m. For longer propagation the net pressure tends to zero.

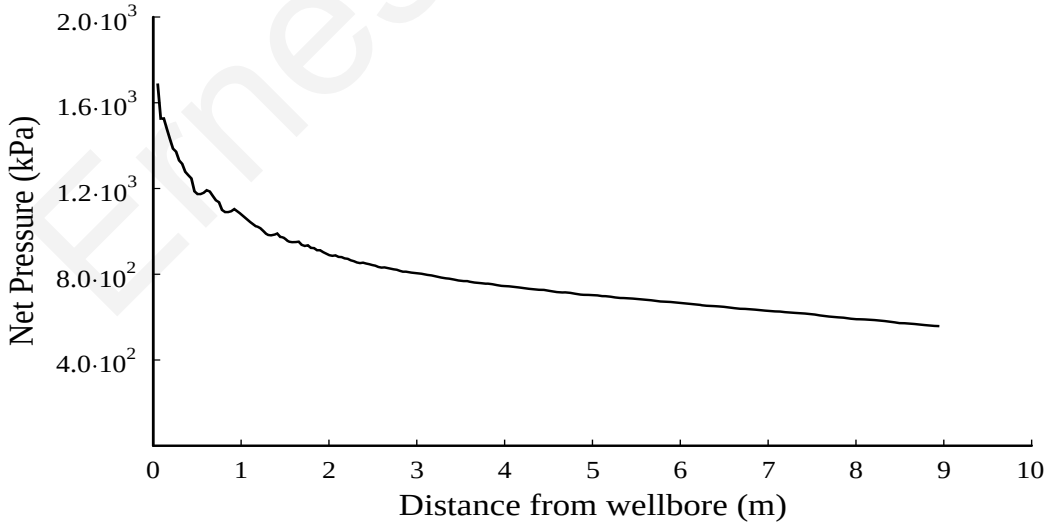

Figure 4.7: Net pressure of a propagating fracture

This outlines the importance of the net pressure as a part of the numerical solution. Predicting the net pressure with numerical models will result in significant cost effectiveness of the design operation as such fracturing fluids with peculiar rheological behavior must be designed and pumped into the fracture and formations. This is done with the study of similar plots as shown in figure (4.7).

All the results in figures (4.5)-(4.7) are depicted vs fracture length or distance from wellbore. However, for the complete evaluation of a hydraulic fracture model, information vs. time is also needed. Figure (4.8) shows the fracture opening at the wellbore versus time. The fracture propagated up to 3 m. For fracture analysis this plot is significant because any geomechanical problems associated within the area near the wellbore will be shown in this plot. Furthermore, any problems associated with early time injection will also be visible in this plot. As it can be seen the fracture curve presents an ascending trend. A check for this figure (4.8) verifies that the peak value of the width coincides with the peak value of the 3 m fracture profile of Figure (4.5). Therefore the time required for the fracture to reach the required lengths can be taken from this plot which is particularly useful for calculation of the fracture volume.

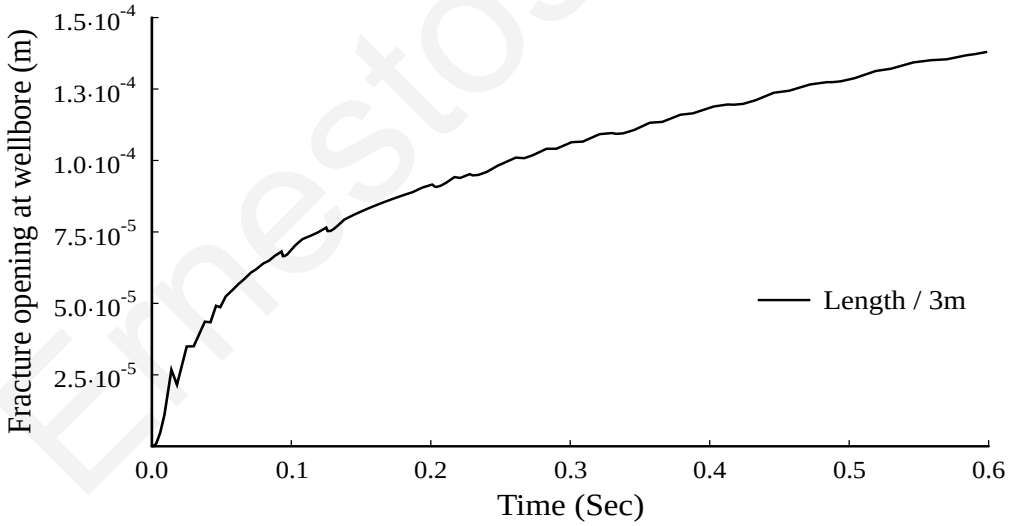

Figure 4.8: Fracture opening at wellbore

The other type of plot associated with the time parameter is the pressure at wellbore versus time. Figure (4.9) shows the pressure at wellbore versus time. Again this means that the curve path has the same form for all fracture lengths and will continue its path for large times. For fracture analysis this plot is significant because any type of problem will have a direct impact on the pressure history from early to

large times. Figure (4.9) presents the pressure needed to propagate the fracture to reach a length of 3 m as in figure (4.8). As it can be seen the pressure history curve gives us two important informations. The first is the significant pressure elevation at early times that is observed which is associated with the formation breakdown and fracture initiation. The second is the pressure history behavior for propagating a long fracture. As it can be seen, about 37.5% above the closure stress is needed to fracture the formation and then to propagate the fracture. This result is obtained for elastic analysis which it is known that underestimates significantly the net pressure in weak formations (Papanastasiou 1999). This has a direct implication on the fluid rheology design. If the "pad" fluid is not designed to undertake such pressures, failure of the hydraulic fracture treatment is eminent. This outlines the importance of analyzing this type of plots. A validation check for figure (4.9) confirms that lowest value must coincide with the nearly uniform value of the 3 m pressure profile of figure (4.6).

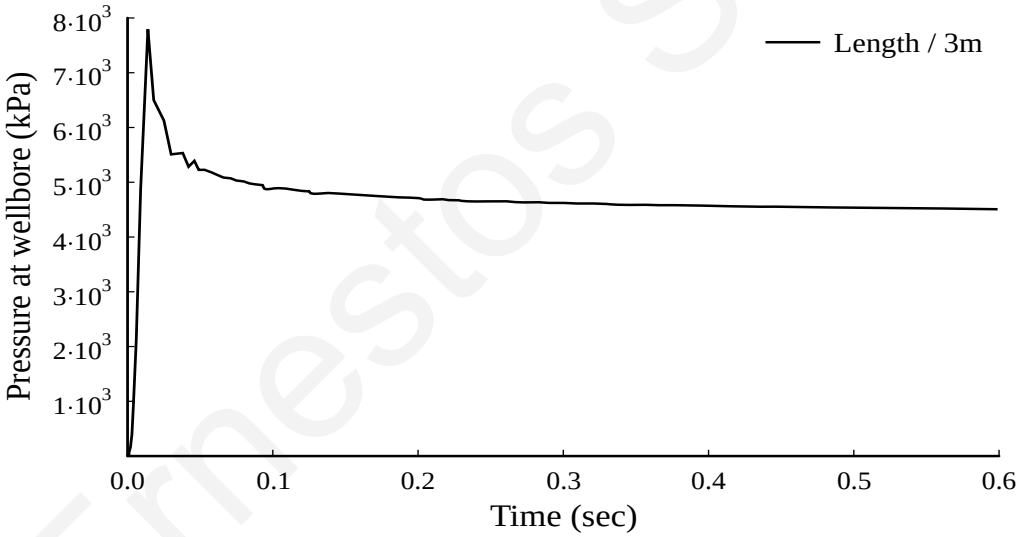

Figure 4.9: Pressure at wellbore

The next step for completing the analysis of a hydraulic fracture is the stress profile around the area of the tip. As it was mentioned earlier, the fracture propagates perpendicular to the minimum insitu stress. Therefore, a study is needed for the minimum insitu stress as this stress significantly influences the net pressure needed to extend the fracture (net pressure = the fluid pressure - the minimum insitu stress).

Figure (4.10) shows the stress perpendicular to the fracture plane along the fracture direction. It is seen that this stress profile gives three important informations. The first is the significant stress concentration which is observed in the area of the

fracture tip. The second information comes from the right side of the curve which tends to the numerical value of the minimum insitu stress that is has been imposed as a boundary condition. This is a preliminary check to confirm that the boundary conditions have been imposed correctly. The left side of the stress corresponds to the fluid pressure profile in the fracture (Figure 4.6) due to mobile equilibrium requirement ($\sigma_{22}^{3m} = p_f^{3m}$).

Small differences of the value of this stress from the imposed boundary conditions are due to the sampling procedure in the numerical model. For example, the pressure profile at 3 m in figure (4.6) and the stress profile of figure (4.10) appear to have a discrepancy of 0.3 MPa. This is attributed to the sampling of data that has been done. Due to the assumed impermeable fracture condition, sampling along the line path A-A' shown in figure 4.4 (at the exact boundary of the fracture wall) will result in a curve with spurious oscillations. In order to overcome this irregularity, sampling was taken as closest as possible to the boundary. Therefore, this small discrepancy is justified and the mobile equilibrium check is confirmed.

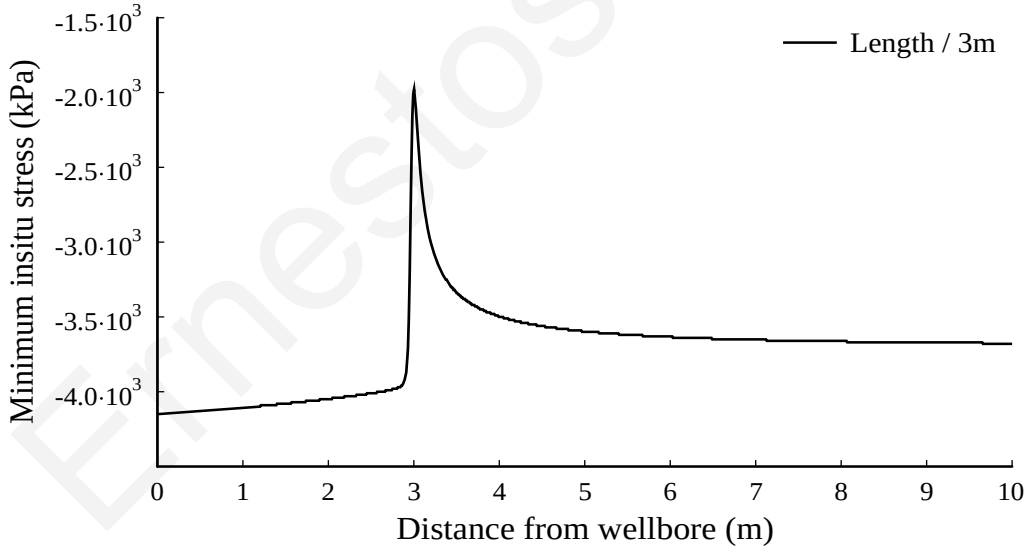

Figure 4.10: Minimum insitu stress profile

In order to double check the mobile equilibrium requirement, the contours of the fluid pressure inside the fracture at 3 m length is plotted in figure (4.11) and is compared with the minimum insitu stress field surrounding the fracture which is plotted in figure (4.12).

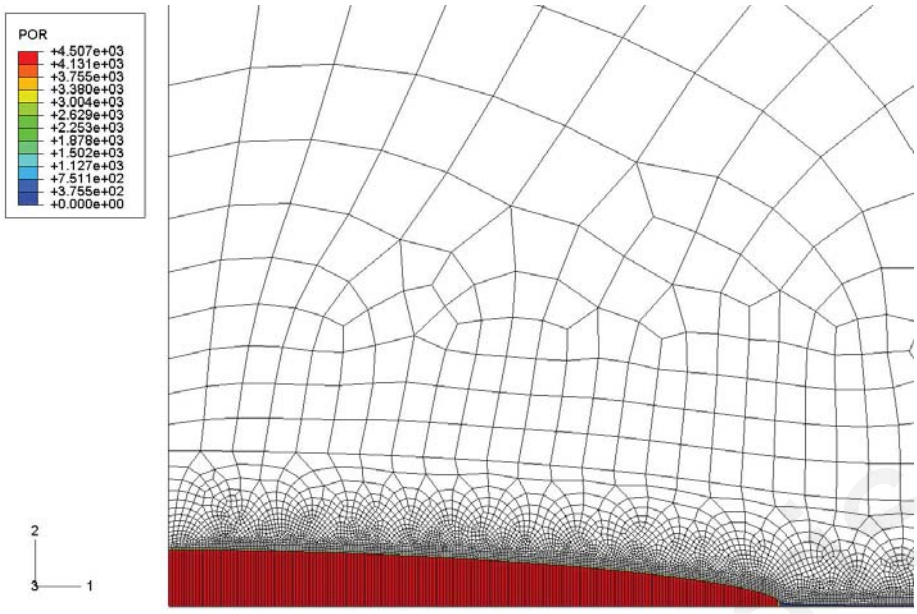

Figure 4.11: Pressure inside the fracture (length 3m)

Both figures (4.11) and (4.12) were plotted for deformation magnified by 1000 times for illustration purposes.

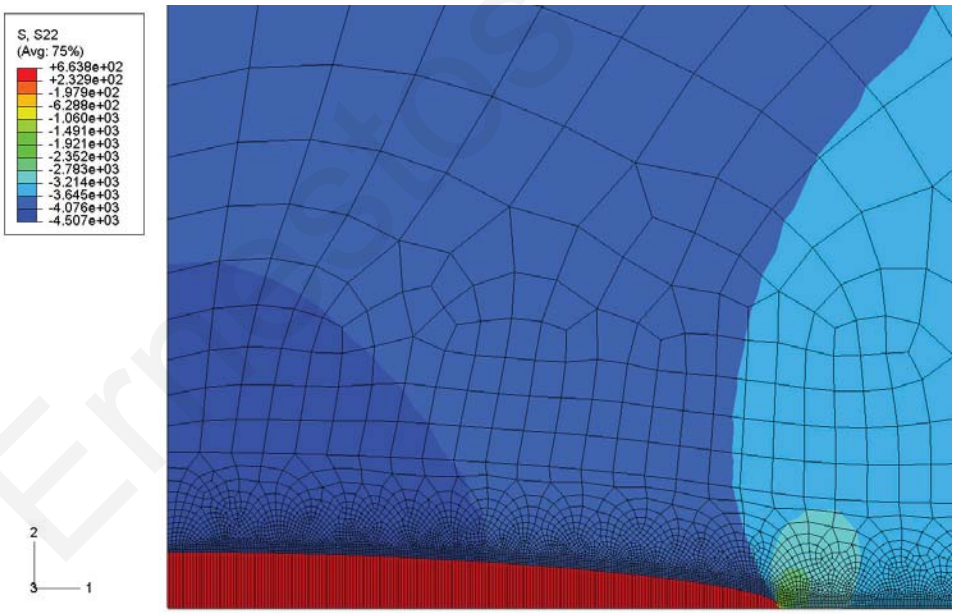

Figure 4.12: Distribution of the stress normal to the fracture plane

An examination of figures (4.11) and (4.12) it appears that the mobile equilibrium requirement is verified.

An extension of the stress analysis is the calculation of the cohesive stresses ahead of the visual fracture tip. The stresses obtained from the numerical model in the process zone are not sufficiently smooth. This drawback can be resolved by a simple

subroutine which determines the cohesive stresses in front of the visual fracture tip from the separation displacement and the cohesive constitutive law. This subroutine is described next and is illustrated in figure (4.13).

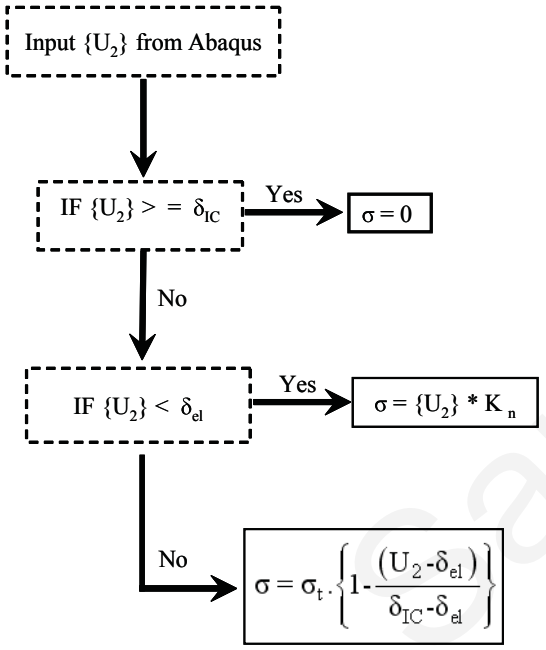

Figure 4.13: Calculation of cohesive stress distribution in the process zone

The first step is to obtain the fracture profile (U-displacements in 2-direction). Then these displacements are compared with the critical displacement δ_{IC} which has been calculated analytically and is material dependent. If the fracture profile displacements are greater or equal with the critical displacement δ_{IC} then the fracture is open and it's a stress free fracture (no stresses are acted in the fracture). However, if the profile displacements are not greater or equal with the critical displacement δ_{IC} then are compared with the peak value δ_{el} (limit of elastic deformation) which is also calculated analytically. Then if the fracture profile displacements are smaller than the peak value δ_{el} then the fracture profile displacements are multiplied with the stiffness k_n of the traction-separation relation in the loading regime of the cohesive constitutive relation. If the profile displacements are not smaller than the peak value δ_{el} (limit of elastic deformation) then the uniaxial tensile strength of the rock σ_t is multiplied with the post-peak softening regime of the cohesive constitutive relation as shown in figure (4.13).

Figure (4.14) shows the result obtained by applying the described subroutine to calculate the cohesive stress distribution ahead of the visual fracture tip. The results

are for a fracture of 3 m long. Behind the visual fracture tip (0-3 m) the cohesive stresses are zero thus confirming the stress free condition for open fractures. In front of the visual fracture tip, the cohesive stresses increase to the tensile strength of the rock and from that point and further, the cohesive stresses follow the elastic stress distribution tending asymptotically to the imposed boundary condition of the minimum insitu stress.

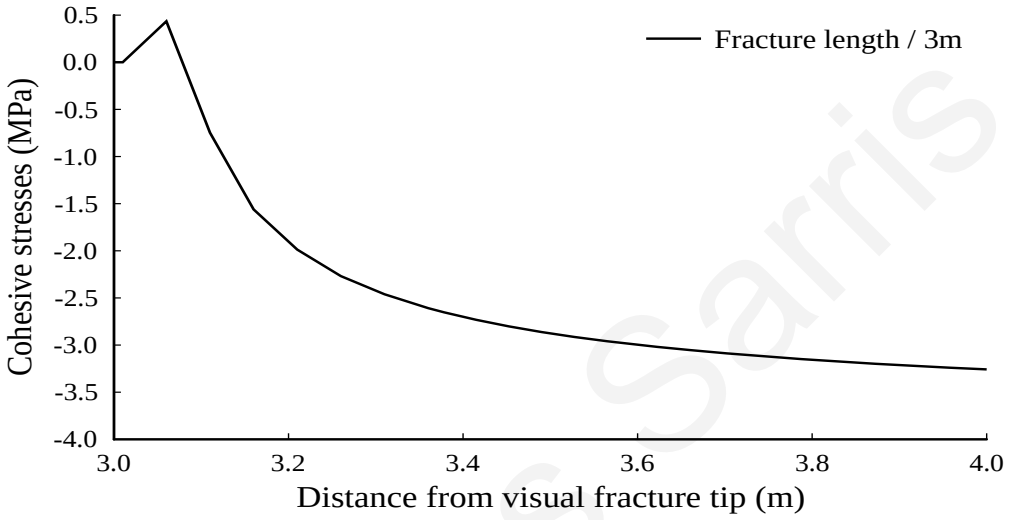

Figure 4.14: Cohesive stress distribution

The result obtained from figure (4.14) is of paramount importance as the size of the process zone can be calculated graphically from this curve. The limits of the X-axis are set from 3 m up to 4 m for illustration purposes. The size of the *process zone is 10 cm* long for this particular set of data that has been used for this simulation.

4.3.2 Comparison with a fully grown fracture

In the previous section, the complete numerical analysis of a fluid driven fracture was performed in a domain with upper quarter symmetry conditions. It is understood that some questions may arise at this point. For example, how the cohesive interface element behaves with symmetry conditions? Furthermore, is the predefined path of the cohesive interface elements of 11 m sufficient to avoid boundary effects? These questions were the motivation for the next analysis. In order to answer these questions a new model was designed with a significantly larger geometric domain. This large geometric domain, with the boundary conditions and the finite element mesh is shown in figure (4.15).

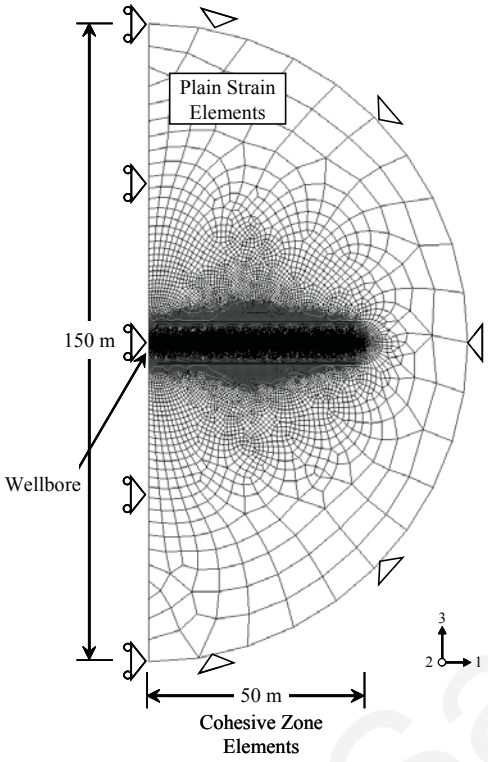

Figure 4.15: Complete geometry, boundary conditions and discretized domain

The descritized domain was considered to be a semi circle with a diameter of 150 m and the predefined path of the fracture (interface cohesive elements) was defined to be 50 m long. For numerical convergence and to properly capture the details of the deformation field in the vicinity of the fracture tip and the traction distribution within the cohesive zone, the element size constrain which is given from equation (4.8) was again considered to satisfy the element size condition in this model. Interface elements were generated for the desired length of 50 m which is more than sufficient to capture the cohesive zone length. The fracture was created for plane strain analysis. Once again the fracture was assumed to grow under mode-I loading conditions. Furthermore, this type of large scale geometry (far from wellbore) allows the application of fixed displacements in both directional translations (i.e $d_x = d_y = 0$) at the semi circle boundaries. Assuming that the fracture grows in both directions along axis-1 (figure 4.15), the wellbore location is located at the left side and at the middle of the geometric diameter. Symmetry conditions are imposed at the left end (diameter) of the semi-circle. Additionally, the symmetry condition for the flow was removed as no symmetry requirements are present in this case. The in-situ stresses were created as initial stresses keeping the same numerical values with the previous simulation (Table 4.1). The fracture will propagate along the axis-1 which is

parallel to the maximum and perpendicular to the minimum insitu stress. The initial condition which is required for defining an initial fracture length for the flow was considered 0.1 m, approximately equals with the perforation length from where the fracture initiates. The fracturing fluid rheology was assumed to be for an incompressible and Newtonian fluid, identical with the previous simulation.

Figure (4.16) presents the comparison of the fracture profiles versus distance from wellbore after the fractures propagated up to 3 m long. At this distance, no boundary effects are present and as it can be seen, the convergence is satisfactory. The small difference that is observed it can be attributed to the finite element density over the propagation path. For the upper quarter symmetric model it is reminded that ten times finer mesh was created along the propagation path.

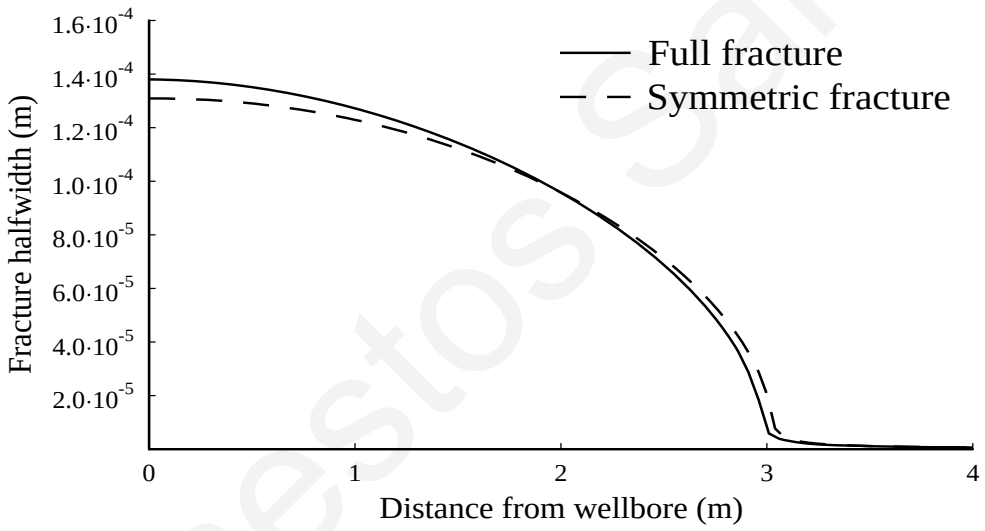

Figure 4.16: Fracture profile comparison between a fully grown and a symmetric fracture

The fluid pressure profiles needed to extend the fractures at the length of 3 m, are almost identical (Figure 4.17). This accuracy is desired because the main focus of the fluid driven fractures is mainly dedicated to the fracture dimensions and propagation pressures.

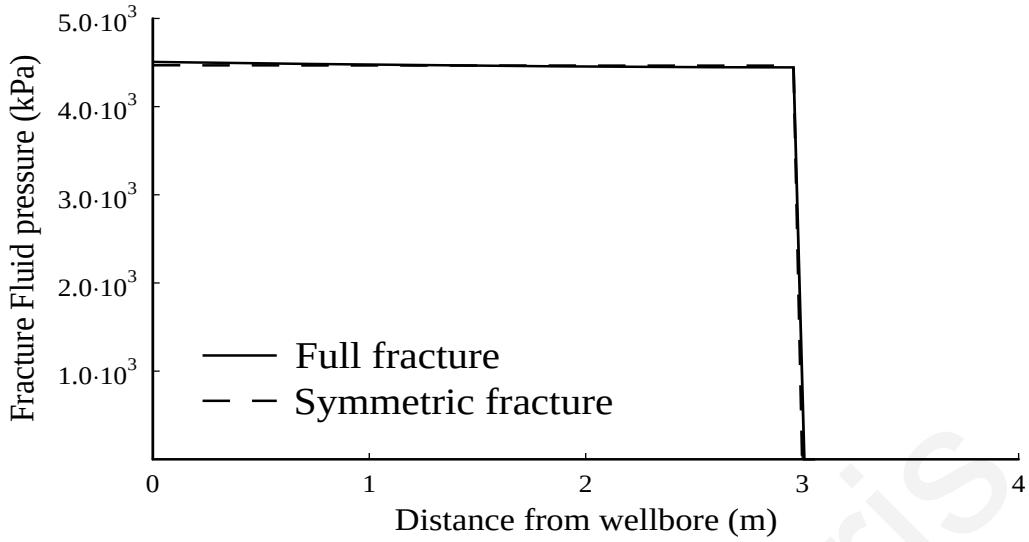

Figure 4.17: Fluid pressure profile comparison between a fully grown and a symmetric fracture

Furthermore, the mobile equilibrium requirement is also checked in the case of a fully grown fracture in a contour form. The contours for the fluid pressure inside the fracture at 3 m length are plotted in figure (4.18) and are compared with the field of the normal stress to the fracture plane which is plotted in figure (4.19). Both figures (4.18) and (4.19) were scaled in deformation 1000 times clearly for illustration purposes only and the fractures are not to width scale.

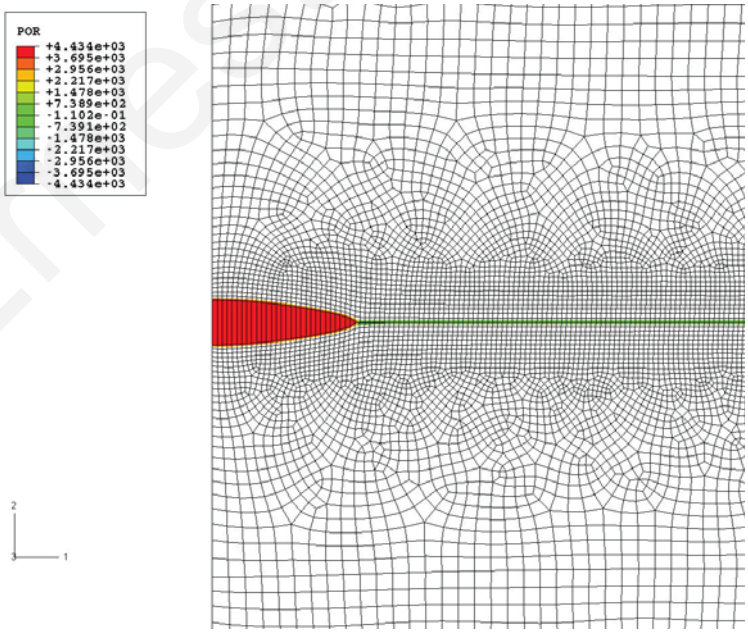

Figure 4.18: Pressure inside the fracture (length 3m) for a fully grown fracture

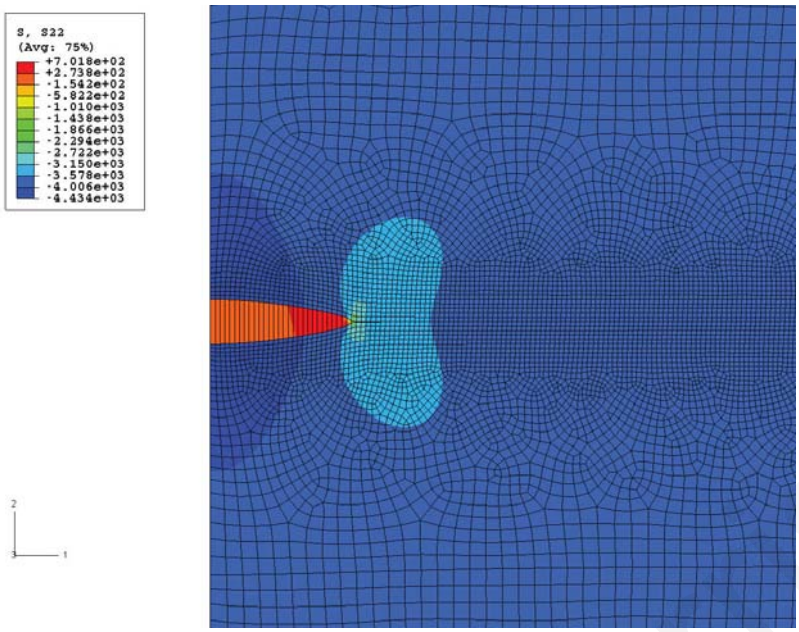

Figure 4.19: σ_{yy} stress field surrounding the fracture for a fully grown fracture (length 3m)

A comparison of figures (4.18) and (4.17) verifies that the mobile equilibrium is satisfied.

A more detailed analysis of the two models was obtained by comparing the fracture volumes. This can be trivially obtained by determining the time needed for the fracture to reach a desired length and then multiplying it with the flow rate. In this case the comparison was made for a fracture at 9 m length. Since the fluid front is assumed to coincide with the fracture tip and the fracture is impermeable (i.e. no fluid losses are modeled) then the fluid volume will be equal with the fracture volume.

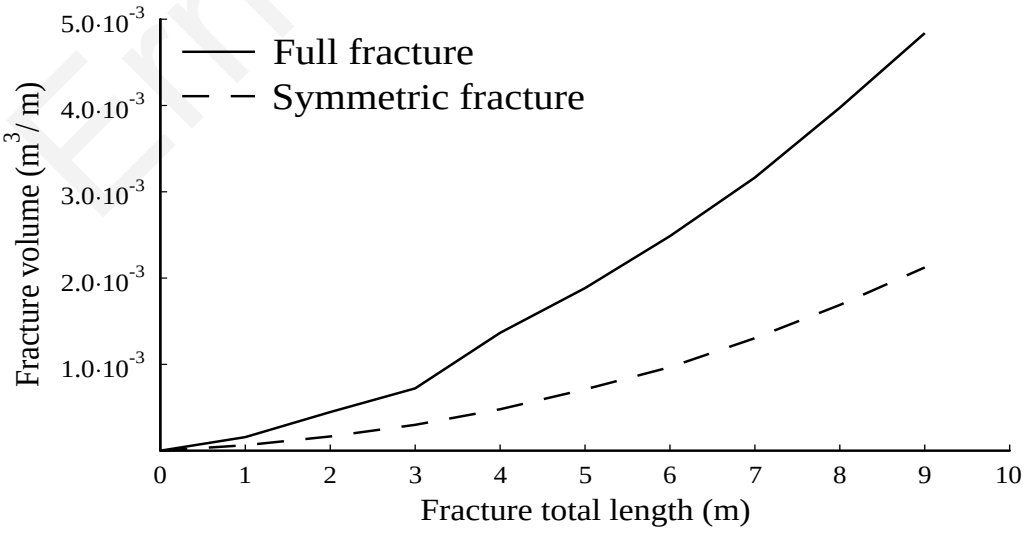

Figure 4.20: Fracture volumes versus length

Figure (4.20) shows the variation of fracture volume versus distance from the wellbore for the two cases examined. As it was expected, the full fracture occupies a double volume compared to the symmetric fracture. Both fracture volumes appear to grow in an exponential manner due to the elliptic shape of the fracture profiles. Figure (4.21) is very similar with figure (4.20) but it presents the variation of the fracture volume versus time needed to reach the desired length of 9 m. Again as it was expected, double time is needed to propagate the fracture to the desired length as the fracture volume that is created in the case of a full fracture is double the half-symmetric fracture.

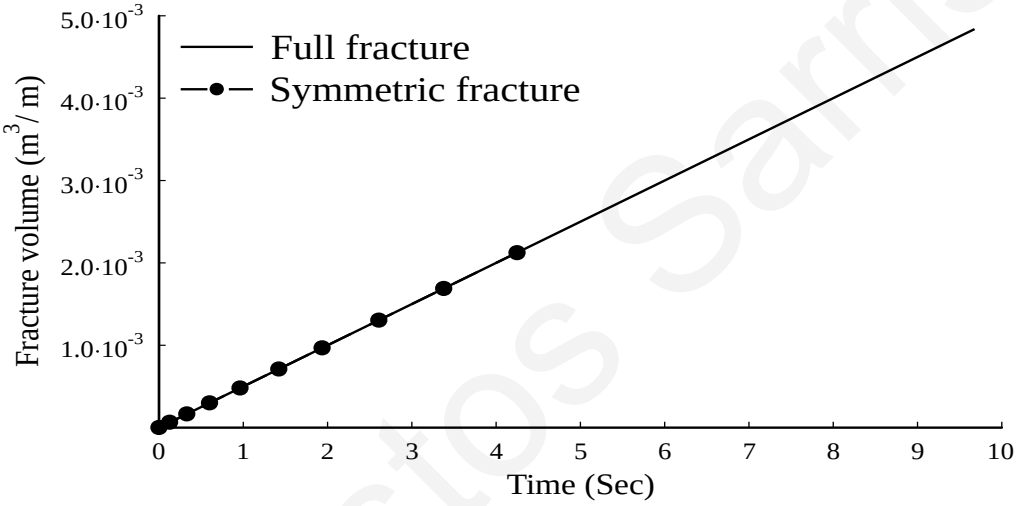

Figure 4.21: Fracture volumes versus time

At this point it is concluded that the cohesive interface element presents identical behavior if designed to model a fully grown fracture compared to a symmetric fracture. Furthermore, no boundary effects were observed in both cases and it is safe to conclude that the modelling with the symmetric fracture will present the benefit of computational efficiency in later simulations. Therefore the upper quarter symmetry model is promoted and will be used throughout the rest of the analyses in this work.

4.4 Comparison with Analytic Solutions and Numerical Results

This section presents the comparison of the numerical model with closed form analytic solutions and other related numerical results. The comparison with the analytic solutions is made progressively. First, a comparison is made from the field of

fracture mechanics with the analytic solution of the integral elasticity equation that determines the non-local relationship between the fracture width and the fluid pressure. The closed form solution of the integral elasticity equation was first given by Sneddon & Lowengrub (1969). The numerical solution is then compared with a fluid driven equilibrium fracture which analytical solutions exist for the fracture width, fluid pressure and length under plane strain conditions. These analytic solutions were originally discussed by Geertsma & De Klerk (1969) and Spence & Sharp (1985). A closest analytical solution to the numerical cohesive fluid driven fracture was proposed by Mokryakov (2011). This analytic solution is derived for a plane strain fracture with the Barenblatt cohesive tip zone which is the most appropriate analytic solution to compare the numerical model. Finally, the numerical solution is compared with the numerical results presented by Papanastasiou (1999).

4.4.1 Comparison with analytic solution from fracture mechanics

The first equation that determines the non-local relationship between the fracture width and the fluid pressure is give by the integral elasticity equation. Sneddon & Lowengrub (1969) were among the first to discuss the analytical solution of the integral equation for a Griffith crack. The closed form analytic solution for a stationary fluid filled fracture is given by

$$w(x)=\frac{4}{\pi E'}\int_0^L p(s)\ln\left|\frac{\sqrt{L^2-x^2}+\sqrt{L^2-s^2}}{\sqrt{L^2-x^2}-\sqrt{L^2-s^2}}\right|ds \quad \Rightarrow \quad w(x)=\frac{4p}{E'}\sqrt{L^2-x^2} \qquad (4.9)$$

where w is the fracture width, p is internal fracture pressure, L is the complete fracture length, x is the distance at a specific point, E' is the plane strain modulus and s an integration constant. Earlier, Muskhelishvilli & Kolossov (1953) have applied a completely different methodology and solved the same problem with the complex potential method for a stationary Griffith fracture with traction loads. Their analytical solution is identical with the Sneddon & Lowengrub (1969).

Figure (4.22) presents the comparison of the numerical solution with the analytic solution of Sneddon & Lowengrub (1969). The comparison was made for the fracture length of 3 m. The value of pressure needed to plot the analytical solution was assumed to be constant. As it can be seen, the elastic solution presents a perfect elliptic shape (continuous line) and the fracture tip vanishes exactly at 3 m. The

fracture profile obtained from the numerical solution (dashed line) is not as blunted as the elastic analytic fracture due to the cohesive forces that are acting in the vicinity of the fracture tip and tend to alter the elliptic fracture profile.

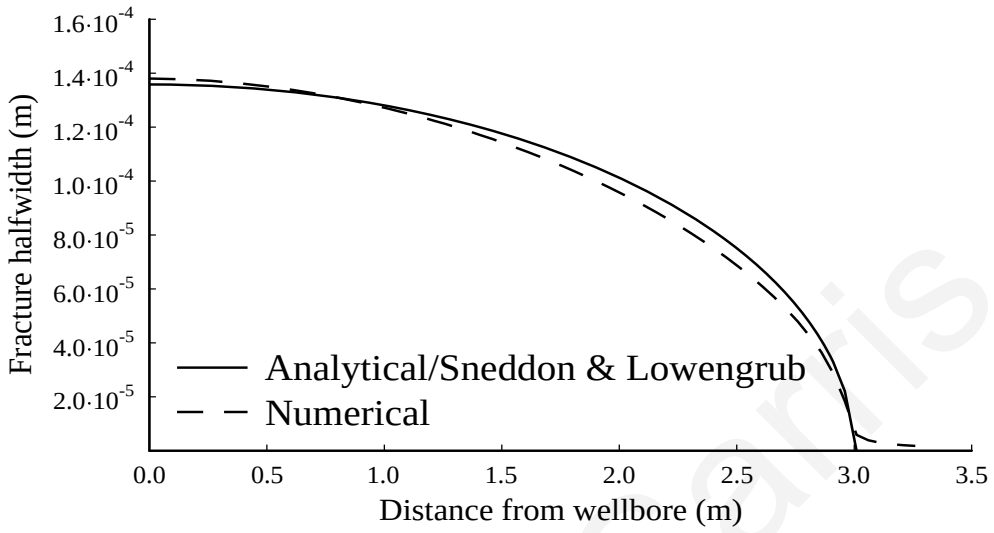

Figure 4.22: Numerical solution vs. analytical of Sneddon & Lowengrub (1969)

Furthermore, a discrepancy is observed in the fracture tip but this is attributed to the cohesive nature of the numerical fracture profile which is distinctive of the Dugdale-Barenblatt model. Therefore, it is concluded that the numerical solution is in excellent agreement with the analytic solution of Sneddon & Lowengrub (1969).

4.4.2 Comparison with hydraulic fracturing analytic solutions

The second comparison of the numerical solution is with a hydraulically fluid driven equilibrium fracture which has been originally discussed by Geertsma & De Klerk (1969) and Spence & Sharp (1985). The Fluid driven fracture in their analytical solution is driven in an impermeable medium under constant flow rate. The fracturing fluid was considered to be incompressible, and the fracture was considered to grow in linear porous elastic formation. In order to simulate the tangential flow in the cohesive interface element, an effective channel permeability is defined as

$$k_t = \frac{d^3}{12\mu} \tag{4.10}$$

where k_t is the cohesive interface element permeability for the tangential flow, d is the cohesive element opening and μ is the fluid viscosity. Equation (4.10) is actually a

measure of resistance to flow. Hence a certain disagreement in the results can be expected mainly related to the process zone.

The fluid is pumped in the borehole at a constant flow rate Q causing the fracture to pressurize and advance after the energy needed to extend the fracture has been reached. The comparison is performed in terms of the fracture opening at wellbore (equation 4.11) and the fluid pressure at wellbore (equation 4.12). In order to calculate the analytic pressure needed to propagate the fracture, the solution of the length is also needed (equation 4.13). The dimensionless quantities are given as function of time in the following expressions

$$W = A\left(\frac{\mu(1-\nu)Q^3}{G}\right)^{1/6}.t^{1/3} \tag{4.11}$$

$$P = B\left(\frac{G^3 Q\mu}{(1-\nu)^3 L^2}\right)^{1/4} + \sigma_{\min} \tag{4.12}$$

$$L = C\left(\frac{GQ^3}{\mu(1-\nu)}\right)^{1/6}.t^{2/3} \tag{4.13}$$

where W is the fracture opening at wellbore, P is the fluid pressure at wellbore, L is the fracture length, σ_{min} is the minimum insitu stress acting perpendicular to the fracture face, Q is the flow rate at the fracture inlet, t is time, G is the shear modulus, v is the Poisson ratio, μ is the fluid viscosity. A, B, C are constants which for the solution of Geertsma & De Klerk (1969) are 1.87, 1.38, 0.68 respectively and for the Spence & Sharp (1985) model are 2.14, 1.97, 0.65 respectively.

Figure (4.23) shows the numerical solution of the fracture opening at wellbore vs. time compared with the analytic solutions of Geertsma & De Klerk (1969) and Spence & Sharp (1985). The comparison is made for a fracture left to propagate up to 3 m long. As it can be seen the numerical solution for early times underestimates the fracture opening at wellbore compared to the analytic solutions. This can be attributed to two reasons. The first reason is that for numerical convergence requirements, the final value to the flow rate is ramped at the first 0.05 seconds and not imposed immediately.

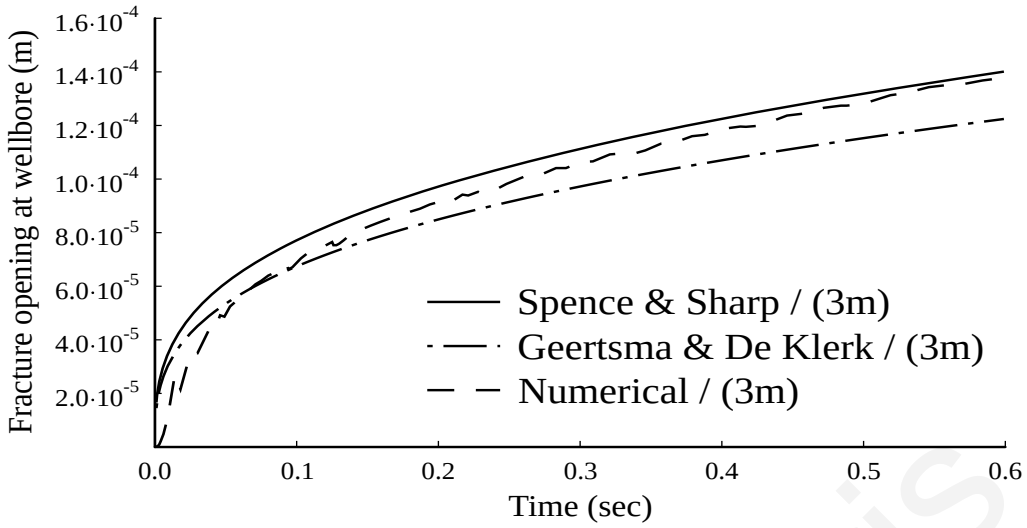

Figure 4.23: Numerical fracture opening at wellbore vs. analytical of Geertsma & De Klerk (1969) and Spence & Sharp (1985)

This may have an effect to the resulting fracture opening at early times. The second reason may be attributed to the permeability of the cohesive interface element as some fluid may have penetrated in the process zone and, as a direct result, the fluid pressure for opening the fracture is lower at early times. This behavior has been also observed by Zuorong et al. (2009). However, after the 0.1 second of injection, the numerical solution approaches the analytical solution of Spence & Sharp (1985). Such behavior is also reported in Boone & Ingraffea (1990).

Figure (4.24) shows the numerical solution of the fluid pressure at wellbore vs. time in comparison with the analytic solutions of Geertsma & De Klerk (1969) and Spence & Sharp (1985). The comparison is made for a fracture left to propagate up to 3 m long. As it was expected and analyzed in the previous figure (4.23), the pressure is lower at early times compared to the analytic solutions. The small difference in pressure values could be caused by the descritization error which does not capture the steep increase and descent in the numerical model. This may result in underestimating the fracture opening at wellbore. The numerical solution is able to predict the fracture onset compared to the analytic solutions which cannot. After the 0.1 second of injection, the numerical solution converges to the analytical solution of Geertsma & De Klerk (1969) and appears to approach the Spence & Sharp (1985) analytic solution for longer fractures and large times of injection.

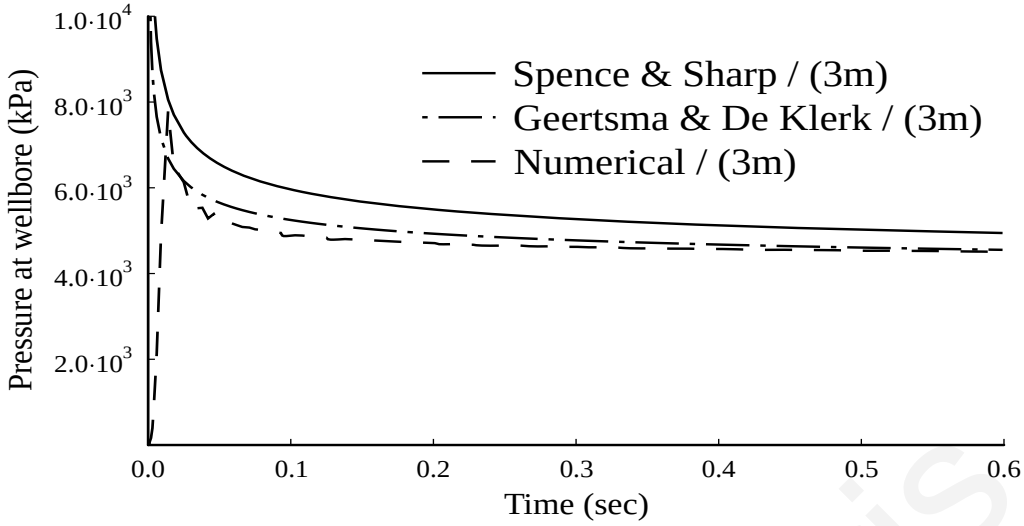

Figure 4.24: Numerical fluid pressure at wellbore vs. analytical of Geertsma & De Klerk (1969) and Spence & Sharp (1985)

From the comparison performed it is concluded that the numerical solution is in satisfactory agreement with the analytic solutions of Geertsma & De Klerk (1969) and Spence & Sharp (1985). The small discrepancies which exist are considered acceptable.

4.4.3 Comparison with hydraulic fracturing analytic solution with cohesive zone

A recent analytical research work performed by Mokryakov (2011), has studied the fluid driven fracture with a tip cohesive zone according to Barenblatt's approach. In this analytical work, the fluid driven fracture is studied under plane strain conditions. The rock is impermeable and no fluid leak off is allowed. The fracturing fluid is incompressible and inviscid. Furthermore the length of the fracture and the cohesive stresses acting on the tip, are assumed to be fixed, hence reducing the problem to conditional case where the stress intensity factor is zero ($K_I = 0$) which simplifies the mathematical manipulations in the equations. These hypotheses can be reproduced by the numerical model except with the one with the inviscid fluid and the zero stress intensity factor for mode-I loading conditions. Hence, a certain disagreement in the results can be expected related both to the nature of the fluid and the zero stress intensity factor condition because these are the two primary energy dissipation mechanisms in hydraulic fracture modeling. However, despite the simplifying

assumptions behind the construction of the analytic solution, it provides the closest approximation to compare the numerical solution.

The fluid is pumped in the borehole at a constant flow rate Q causing the fracture to pressurize and advance. The comparison is performed in terms of the fracture opening at wellbore vs. time and the fluid pressure at wellbore vs. time. The analytic solution from the fracture length, the fluid pressure at wellbore and the fracture opening at wellbore are presented from equations (4.14) to (4.16) as proposed by Mokryakov (2011):

$$L = \left(\frac{E'^2 Q^2}{4\pi K_{IC}^2} \right)^{1/3} . t^{2/3} \tag{4.14}$$

$$P = \left(\frac{2K_{IC}^4}{\pi E' Q} \right)^{1/3} . t^{-1/3} + \sigma_{\min} \tag{4.15}$$

$$W = \left(\frac{32 Q K_{IC}^2}{\pi^2 E'^2} \right)^{1/3} . t^{1/3} \tag{4.16}$$

where W is the fracture opening at wellbore, P is the fluid pressure at wellbore, L is the fracture length, σ_{min} is the minimum insitu stress acting perpendicular to the fracture face, Q is the flow rate at the fracture inlet, t is time, K_{IC} is the fracture toughness of the rock. As it can be seen the fluid viscosity is absent in the analytical solution as a result of the inviscid fluid assumption.

Figure (4.25) presents the fracture opening at wellbore vs. time. The numerical solution is compared to the analytical solution with cohesive tip zone of Mokryakov (2011). The comparison is made for a fracture propagated to reach 3 m long. As it can be seen the numerical solution follows the same form as the analytical solution with a cohesive tip zone. However, the fracture opening obtained with the analytic solution is underestimated by 5 %. This was expected and it can be explained by the fact that the analytical solution was constructed with the zero stress intensity factor (zero singularity) condition. This means that any tip effects are ignored in the analytic solution.

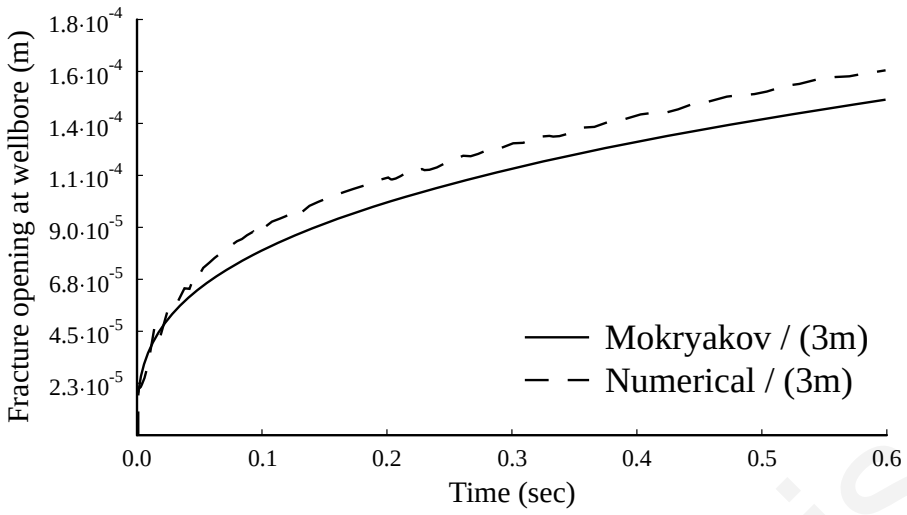

Figure 4.25: Numerical fracture opening at wellbore vs. analytical of Mokryakov (2011) with Barenblatt cohesive tip zone

Figure (4.26) presents the fluid pressure at wellbore vs. time. These pressures are the respective ones for the fracture openings presented in figure (4.25). The comparison is made for a fracture left to reach 3 m long. As it can be seen the numerical solution presents a similar form as the analytical solution for the pressure at wellbore. Furthermore, the pressure needed to initiate the fracture is identical. However the fluid pressure needed to propagate the fracture is overestimated by 5 %.

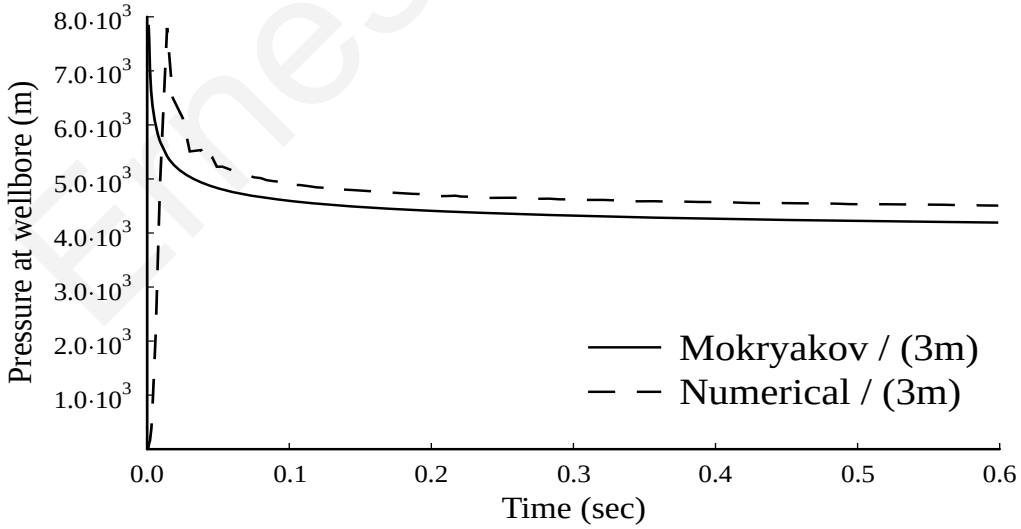

Figure 4.26: Numerical fluid pressure at wellbore vs. analytical of Mokryakov (2011) with Barenblatt cohesive tip zone

This was again expected and it can be explained by the fact that the analytical solution was constructed with no viscosity (inviscid fluid) condition. This means that the loading inside the fracture is partly ignored. This outlines the importance of the viscous fracture fluid (viscosity dominated regime) which cannot be ignored in hydraulic fracture simulations as it may partly explain the elevated fluid pressures needed to extend the fracture. Nevertheless, the comparison between the numerical and the analytical solutions appears to be in good agreement and the small discrepancy of underestimation in fracture opening and the overestimation in pressure is within acceptable limits.

4.4.4 Comparison with numerical results

In this investigation, a comparison is made with the numerical results of a fluid driven fracture in a non porous cohesive formation as presented by Papanastasiou (1999).

Figure (4.27) presents the comparison of the numerical results of Papanastasiou (1999), with the analytic solution of Sneddon & Lowengrub (1969) from fracture mechanics and with the results from the proposed numerical model. The comparison was made for a fracture length of 2 m. The value of pressure needed to plot the analytical solution was assumed to be constant and was taken from the net pressure versus distance from wellbore plot presented by Papanastasiou (1999).

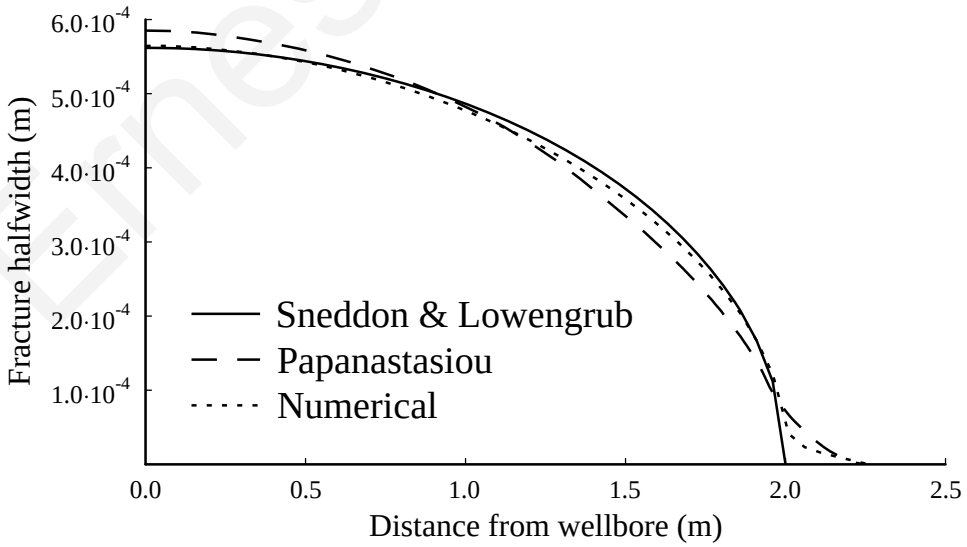

Figure 4.27: Comparison of fracture profiles with numerical results

As it can be seen, the elastic solution presents a perfect elliptic shape (continuous line) and the fracture tip vanishes exactly at 2 m. The fracture profile presented by Papanastasiou (1999) presents different shape from the analytic solution (discontinuous line) and this is due to the cohesive forces that are acting in the vicinity of the fracture tip and tend to change the elliptic fracture profile. The fracture profile obtained from the numerical solution (dashed line) is in good convergence with the analytical and presents small differences from the numerical results of Papanastasiou (1999). However, this small difference is considered to be within acceptable limits.

4.5 Conclusions

In this chapter, the fluid driven fracture was modeled in impermeable elastic rock to demonstrate the efficiency of the fully coupled numerical solution. The models were developed for plane strain geometry which is appropriate for modelling short fractures and examining tip effects. The simulation results were presented and discussed in detail within the context of the numerical model validation. The work presented in this chapter is also compared with analytic solutions readily available for the literature and other related numerical results. The conclusions obtained from these simulations are summarized as follows:

- The constitutive cohesive zone law was constructed analytically and implemented in the numerical simulations as a propagation criterion. This is important in the investigation of the cohesive zone characteristics (i.e. softening part) and its implications in the fluid driven fracture modelling.
- The fully coupled numerical solution was verified with the construction and testing of the five fundamental plots according to Valko & Economides (1995).
- The distribution of the cohesive stresses ahead of the visual fracture tip is calculated through the construction of a simple subroutine and presented in graphical form. From this graphical representation of the cohesive stress distribution, the length of the process zone is exactly calculated.
- Two types of geometric domains were constructed to investigate the behavior of the interface cohesive elements and possible boundary effects influencing the numerical results of a symmetric and a full fracture. Results for the fracture profile and fluid pressures showed that both fractures behave essentially the same. Therefore, the symmetric domain is used for further analyses. Additionally, the

numerical results for the symmetric model are not influenced by any boundary effects.

- The numerical solution was verified with three different analytical solutions and with the numerical results of Papanastasiou (1999). The first comparison was made with the fracture mechanics solution of Sneddon & Lowengrub (1969). The second comparison was made with the Spence & Sharp (1985) and Geertsma & De Klerk (1969) for impermeable elastic fluid driven fracture. The third comparison was made with Makryakov (2011) for impermeable elastic fluid driven fracture with cohesive tip zone. The results presented form these comparisons suggest that the numerical coupled solution is in excellent agreement and within acceptable limits with both, the analytic solutions and other related numerical results.

5. The Influence of the Cohesive Process Zone

5.1 Preamble

The fragmentation process is one of the main problems in fracture mechanics research. Cohesive zone models are increasingly being used to simulate the fracture and fragmentation processes in weak or strong rocks. A key feature of this approach is to represent the micromechanics of the fracture processes through a unique load-displacement relation. Dedicated research works (Papanastasiou 1999; Papanastasiou & Thiercelin 1993) incorporating the cohesive zone approach in hydraulic fracturing has considered the magnitude of energy, in addition to one of the two parameters (cohesive strength or critical displacement), to define the cohesive constitutive law characteristics. However in their works, they completely ignored any influence of the shape (loading or softening) of the constitutive law in the process zone which in its turn may affect the overall numerical results. Cohesive zone represents the embodiment of different inelastic micro-mechanisms active in the fracture process zone. The form of the cohesive zone model represents the effect of the fracture processes and it is material dependent (brittle or ductile). The two most commonly used cohesive zone models to analyze fracture problems is the bilinear model and the exponential. In this chapter, these two models are incorporated to analyze in detail their influence on the fracture process zone of a fluid driven fracture. There is no previous work found in literature, to the author's knowledge, that utilize these two different shapes of the cohesive constitutive laws (bilinear / exponential) in the fluid driven fracture problem. These two cohesive constitutive models (bilinear and exponential) are used to compute numerically the fracture profile, the fluid pressures, the net pressure as well as the length and shape of the process zone in the fluid driven fracture problem.

5.2 Investigation of the Constitutive Cohesive Zone Law (Loading and Softening)

The prediction of fracture propagation and consequent failure in weak rocks still remain one of the daunting problems in hydraulic fracturing mechanics. Rock fracture mechanics can predict the load carrying capacity of a rock mass with the assumed existence of a fracture under the most unfavorable conditions concurrent with small

scale yielding at the fracture tip. Further prediction is restricted mostly to initiation of the fracture under certain idealized rock behavior and fracture geometry. A Significant limitation of the fracture mechanics well established concepts can be attributed to the fact that rocks are assumed to be homogeneous with predominantly elastic strain fields for well defined loading conditions however being adequate for most applications. Phenomenologically, the micro-mechanisms inherent in the fracture process zone is unable to be described by conventional fracture mechanics and the prediction of fracture in complex rock systems under complicated loading conditions such as non proportional loading as in hydraulic fracturing is really poor. This type of fracture problems (fluid driven fracturing) is difficult both in the aspect of mechanics and physics as the fracturing occurs at disparate length scales, e.g., the type of fracturing is brittle or ductile and is governed by the ability of the fracture tip to emit dislocations.

Cohesive zone based formulation has the interesting capability of not only modeling the initiation of the fracture but also the propagation of the fractures. Furthermore cohesive zone modeling has the ability to retain mathematically the continuity conditions despite the physical separation therefore it can be used to simulate fracture under real loading conditions. However, caution must be taken in the parameters that represent the cohesive zone model and should be identified and evaluated carefully and properly.

In all cohesive constitutive laws representing fracture propagation, the traction-separation relations for the interfaces are such that with increasing interfacial separation, the traction across the interface reaches a maximum the decreases and eventually vanishes permitting complete separation. The main difference lies in the shape and the constants that describe that shape. The term “shape” is a loose sense to describe the form of the normal traction versus the normal response of a cohesive constitutive law used to describe the fracture process in a rock mass.

There is a common belief that cohesive zone models can be described by two independent parameters (Shet & Chandra 2004; Hutchinson & Evans 2000). These two parameters can be any of the following three parameters, namely the cohesive energy, cohesive strength or separation length as described earlier in chapter 4. Recent work of Roy & Dodds (2001) showed that the choice of exponential cohesive model was based on the non-linear shape of the cohesive constitutive law. Amrutharaj et al., (1995) demonstrated that a trapezoidal constitutive model better fits some

experimental data that a bilinear model does. Recent work of Chandra et al. (2002) has showed that these two parameters used to describe the fracture process zone are not sufficient. They concluded that the form of the cohesive constitutive law comprising the rise (loading), the peak, and the fall characteristics (softening) should be explicitly accounted to truly represent the material dependent fracture behavior under the state of propagation.

Given a cohesive zone model (e.g. exponential), while is capable for representing the fracture process in a problem (i.e. delamination), it may cannot model the process in another type of problem (i.e. fluid driven fracture). The concept of this chapter is to examine the influence of the "shape" of the constitutive law on the fracture process zone in hydraulic fracturing. The analysis has been divided into two different parts. First, the loading of the cohesive constitutive law is detailed analyzed using simplified heuristic mathematical arguments to relate the physical behavior of brittle to ductile failure in hydraulic fracturing under non porous and porous conditions. Second, the softening part is analyzed by incorporating an equation from damage mechanics to address the transition from linear to exponential unloading (softening) of the cohesive constitutive law to study its influence on the fluid driven problem.

As described in chapter 4, the area under the traction-separation curve equals with fracture energy G_{IC} which is the work needed to create a unit area of fully developed fracture. The cases of the rigid-softening and the elastic-softening cohesive constitutive relations of the traction-separation relations are uniquely determined by equations (4.1) - (4.5). The post-peak softening regime of the linear cohesive constitutive relation is given by equation (4.6) and therefore, the traction-separation, as described by equation (4.7) which yields that the critical value of the fracture opening displacement, can be uniquely determined.

Figure (5.1) presents the elastic loading of the constitutive cohesive zone laws which describe the transition from brittle to ductile behavior. Brittle corresponds to the case where the stiffness k_n of the traction-separation relation in the loading regime with units [MPa/m] is high (i.e k_n x 20) and in rock mechanics this reflects fracturing of a strong rock formation. Likewise, the ductile behavior corresponds to the case where the stiffness k_n of the traction-separation relation in the loading regime is low (i.e k_n x 1) and in rock mechanics this reflects fracturing of a weak rock formation. The other two cases (k_n x 15) and (k_n x 5) represent intermediate states of semi-brittle

(semi-weak) and semi-ductile (semi-strong) material behaviors. Figure (5.1) is exactly the same as figure (4.2) except that only the initial part of the curves are plotted while the post-peak softening regime was not included for illustration purposes. The peak values of these lines represent the limit of elastic deformation. In all cases presented in figure (5.1) the area under all the complete curves (fracture energy G_{IC}) was maintained the same and equal to a rock fracture toughness K_{IC} of 2 MPa.m $^{0.5}$. This constrain would ensure that only the initial slope (loading) will change and not peak values and the critical separation opening δ_{IC}.

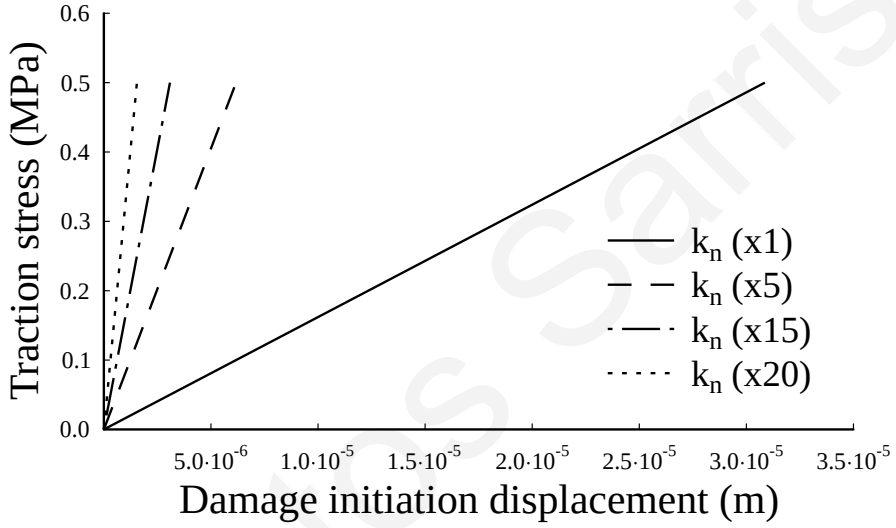

Figure 5.1: Elastic loading of the cohesive constitutive laws

To further investigate the characteristics of the cohesive zone law and their influence in the fluid driven problem, different forms of softening behavior were also studied. For this purpose an exponential softening equation from damage mechanics is proposed to modify the post peak softening regime and is described by

$$D^{\text{Exponential}} = \left\{ \frac{1 - e^{-\alpha\left(\frac{\delta - \delta_{IC}}{\delta_{IC} - \delta_{max}}\right)}}{1 - e^{-\alpha}} \right\} \tag{5.1}$$

The parameter $D^{exponential}$ is controlled by the exponential coefficient α. A similar equation with the proposed (equation 5.1) exists in the numerical code Abaqus.

In order to understand the influence of this parameter in the post peak softening regime in the cohesive zone law, the plots of this exponential damage variable is shown for the two extreme cases examined, brittle (k_n x 20) and ductile (k_n x 1) in

figures (5.2) and (5.3) respectively. Damage mechanics are in agreement with this case, as degradation of the material takes place before complete failure. Figure (5.2) and (5.3) presents the damage variable for four different values of exponential coefficients α. The fifth value represents the linear softening case. It is worth mentioning that equation (5.1) can be reduced from exponential to linear damage variable for low values of exponential coefficient α.

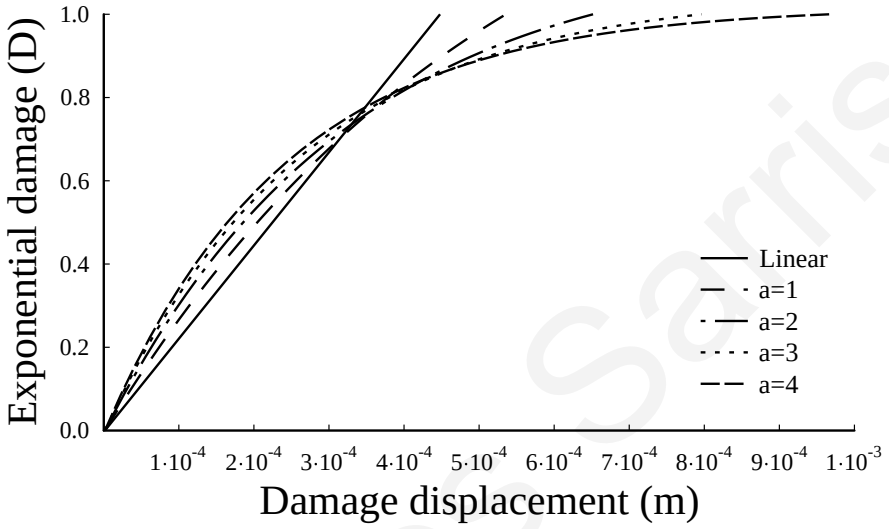

Figure 5.2: Exponential damage variable for brittle material behavior (kn x 20)

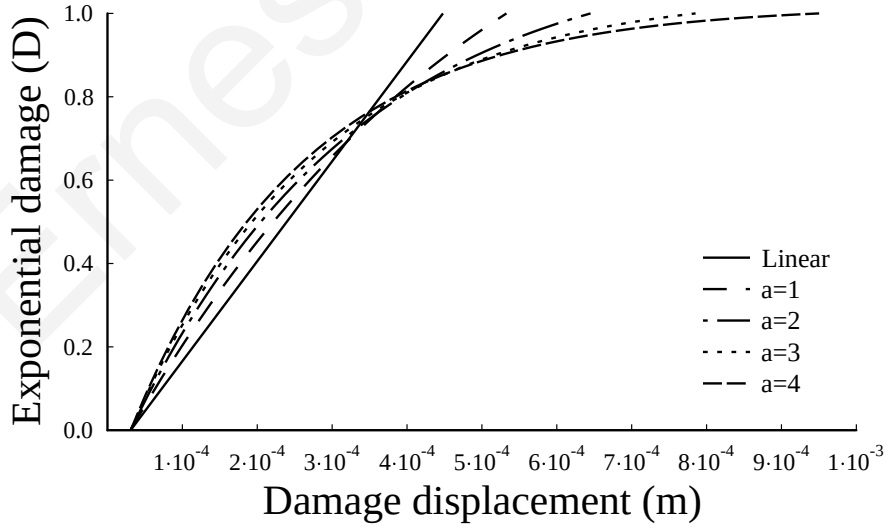

Figure 5.3: Exponential damage variable for ductile material behavior (kn x 1)

The value of the exponent α in figures (5.2) and (5.3) gives a measure of the curvature of the exponential damage parameter in equation (5.1). It is worth

mentioning that the limit of elastic deformation in the exponential damage variable curves, in the case of the ductile behavior (k_n x 1), is accounted in equation (5.1) and is shown in figure (5.3).

Inserting the exponential damage equation (5.1) in the traction-separation constitutive relation will yield the final traction-separation constitutive law with exponential softening as

$$\sigma = \left(1 - D^{Exponential}\right)\sigma_t \tag{5.2}$$

The critical value of the fracture opening displacement with the exponential softening is then uniquely determined from equation (5.2). The shape of the new constitutive behavior for different exponent values for the two extreme cases examined, brittle (k_n x 20) and ductile (k_n x 1) are shown for comparison in figures (5.4) and (5.5) respectively.

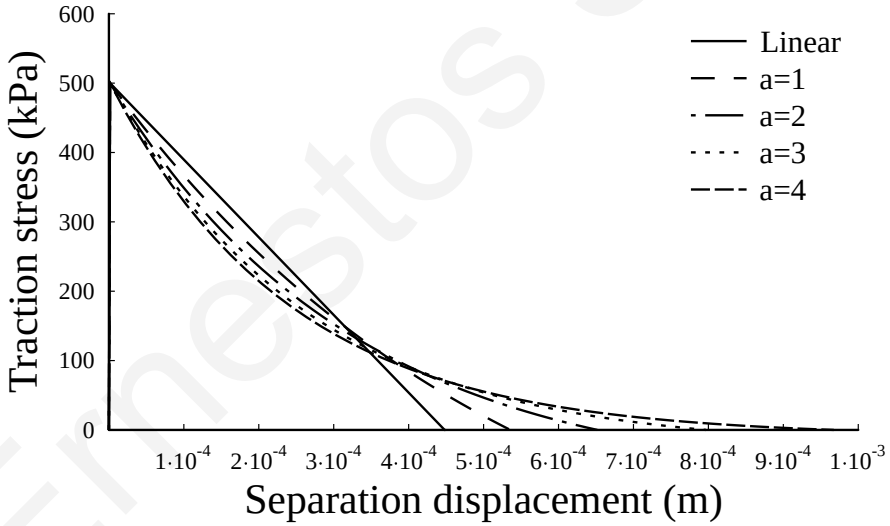

Figure 5.4: Rigid-softening cohesive constitutive zone law

The loading part of the cohesive constitutive law was kept the same and the softening part was parametrically investigated. The peak values of the cohesive constitutive laws represent the limit of elastic deformation as discussed earlier in figure (5.1).

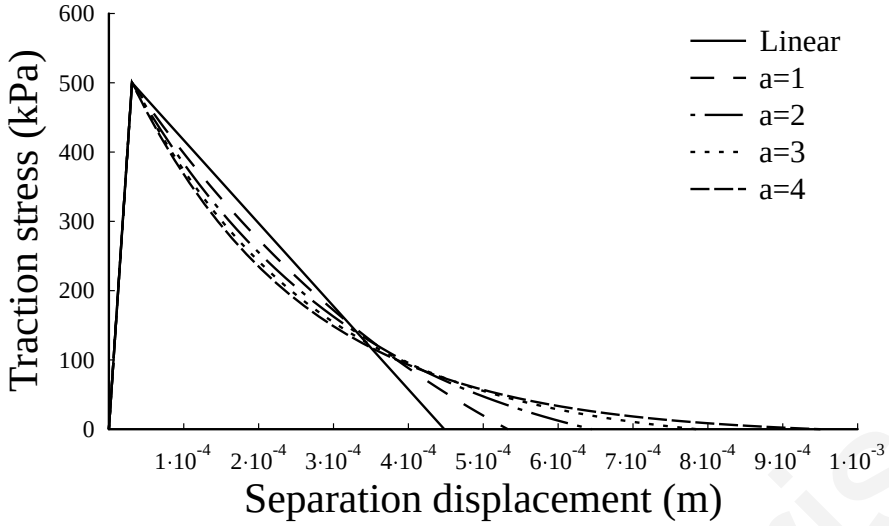

Figure 5.5: Elastic-softening cohesive constitutive zone law

In all cases presented in figures (5.4) and (5.5) the area under all the curves (fracture energy G_{IC}) was maintained the same and equal to a rock fracture toughness K_{IC} of 2 MPa.m $^{0.5}$. The constraints of constant initial loading (i.e. same limit of elastic deformation) and of the same area under the curves will result in different critical separation opening δ_{IC} according to the exponential coefficient α. It is evident from both figures (5.4) and (5.5) that, due to energy balance requirement, the area that is subtracted from the left side of the linear softening curve is added in the right side of the linear softening curve causing the increase of the critical separation opening δ_{IC}.

5.3 Influence of the Loading Part of the Constitutive law on the Process Zone in Hydraulic Fracturing Modelling

In this section we present results to demonstrate the importance of the loading part of the cohesive zone constitutive law in the modeling of the fluid driven fracture in both elastic and porous elastic solids. The parameters which were used in the numerical computations are given in Table (5.1). These parameters include the rock properties, the pumping parameters, the in-situ stress field and the initial conditions. The only extra parameter that is needed to consider poroelastic deformation and propagation of the poroelastic fracture is the pore pressure of the porous domain which requires an extra degree of freedom at the nodes of the plane strain elements. For comparison of the results, the total stress field was applied in the poroelastic analysis whereas for the non-porous models the corresponding effective stress field was applied.

Table 5.1: Input parameters for the computational examples

Variable	Value
Rock Properties	
Young modulus, **E** (MPa)	16200
Poisson ratio, **ν**	0.3
Pumping parameters	
Viscosity, **μ** (kPa.sec)	0.0001
Injection rate, **q** (m^3/sec.m)	5.00E-06
Domain permeability, **k** (m/sec)	5.88E-10
In situ stress field (effective)	
Maximum, σ_1 (MPa)	14
Intermediate, σ_2 (MPa)	9
Minimum, σ_3 (MPa)	3.7
Initial conditions	
Void ratio, **e**	0.333
Pore pressure (MPa)	1.85
Initial gap (perforation) - (m)	0.1

The objective of these simulations of the fluid driven fracture in non-porous and porous rock formations is to examine the influence of the cohesive zone on the overall numerical solution of the fluid driven problem. However, the problem is coupled and complex, therefore some actions were taken to ensure that the analysis will not deviate from the intension of this investigation. The value of the injection rate was set in a pumping schedule to continuously increase (i.e. not constant). This feature together with the low permeability value that was imposed both in the domain and in the predefined fracture will present the benefit of excluding any significant leak-off and diffusion, as well as any fracture fluid storage effects. In this manner the associated leak-off, diffusion and storage effects are isolated and will be discussed in the next chapter. According to this physical explanation and with the fact that the fluid viscosity is kept at intermediate values it ensures that the solution will be restricted to the physical scaling of the fracture toughness dominated regime. From the energy point of view this will guide the analysis to dissipate most of the energy of the physical model in the creation of the new fracture surfaces rather in the dissipation of the energy in the fluid flow in the fracture or in the dissipation of energy in the fluid losses and storage. Ensuring that the scaling will be in the fracture toughness

dominated regime, any irrelevant mechanisms affecting the fracture process zone will be isolated and will be discussed in the next chapter.

As discussed earlier, in order to investigate the main characteristics of the cohesive zone law, a parametric analysis was to simulate the changes from rigid-softening to elastic-softening constitutive behavior. The constitutive response of the rigid-softening corresponds to a strong rock formation whereas the elastic-softening corresponds to a soft rock formation. For simplicity the aforementioned four cases of cohesive stiffness were renamed as k_n = 1, 5, 10, 20 to correspond the times that the slope of the loading branch has been multiplied to meet the constitutive behavior that we have mentioned.

The properties of the cohesive zone are summarized in Table (5.2). These properties include the uniaxial tensile strength, the fracture energy which is the area under the traction-separation curve calculated to meet an equivalent fracture toughness of 2 MPa.m$^{1/2}$, the permeability of the elements and the parametrically investigated loading slope of the first branch of the cohesive constitutive law.

Table 5.2: Cohesive zone properties

Cohesive zone properties	
Uniaxial tensile strength, $\boldsymbol{\sigma_t}$ (MPa)	0.5
Loading stiffness $\boldsymbol{k_n}$ (MPa/m)	16200 / 81000/ 162000/ 324000
Fracture energy, $\boldsymbol{G_{IC}}$ (kPa.m)	0.224
Cohesive zone permeability $\boldsymbol{q_{b,t}}$ (m/sec)	0 / 5.879E-10

All the results presented next correspond to fractures at the state of propagation. The fractures were propagated from an initial length of 0.1 m to reach 9 m long. Figure (5.6) shows the half profile of a propagating fracture versus distance from wellbore in a non-porous domain at different lengths for every 1m interval, for clarity reasons. We observe in figure (5.6) that the fracture tip cusping is really small leading to the result that the cohesive stresses acting in the area near the fracture tip are small. Furthermore, near wellbore, the short fractures appear to have a blunted shape while after a few meters of propagation this bluntness is lost. This is firstly explained by the non-local character of the solution. Any influence at the fracture tip is transferred accumulated and maintained in the overall shape of the fracture. Near wellbore this

non-local character is less significant therefore, for short rigid cohesive fractures the shape approaches the elastic solutions for these reasons the comparison between the elastic analytic solution and the numerical presented in chapter 4 was possible. This means that when the cohesive constitutive law is rigid-softening (k_n x 20) the cohesive zone is suppressed and the solutions resembles the elastic.

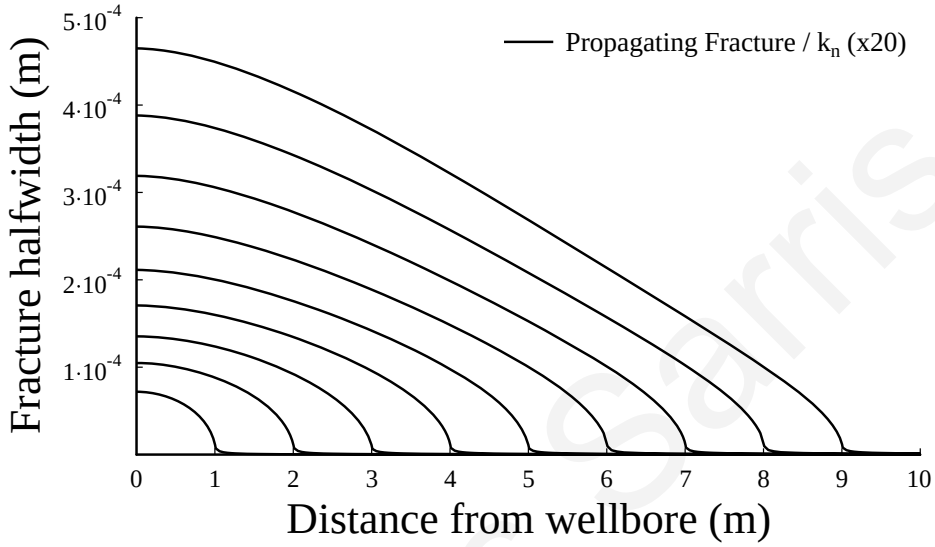

Figure 5.6: Fracture profiles of a propagating fracture

Figure (5.7) shows the obtained half-width of a fracture versus distance from wellbore in an elastic non porous solid, after the fracture has reached a length of 5 m, for cases of different loading slopes of the cohesive constitutive relation (figure 5.1). The calculated width of the propagating elastic-softening, which corresponds to k_n (x1), is much larger than the calculated width of the rigid-softening which corresponds to k_n (x20). The cusping of the fracture profiles is larger for the case of elastic-softening indicating a ductile behavior.

The results of the rigid-softening as discussed earlier are similar to a brittle behavior or to a pure elastic fracture without or with an insignificant process zone. The differences in the results are the outcome of the initial part of the cohesive zone models which were incorporated as the fracture propagation criterion.

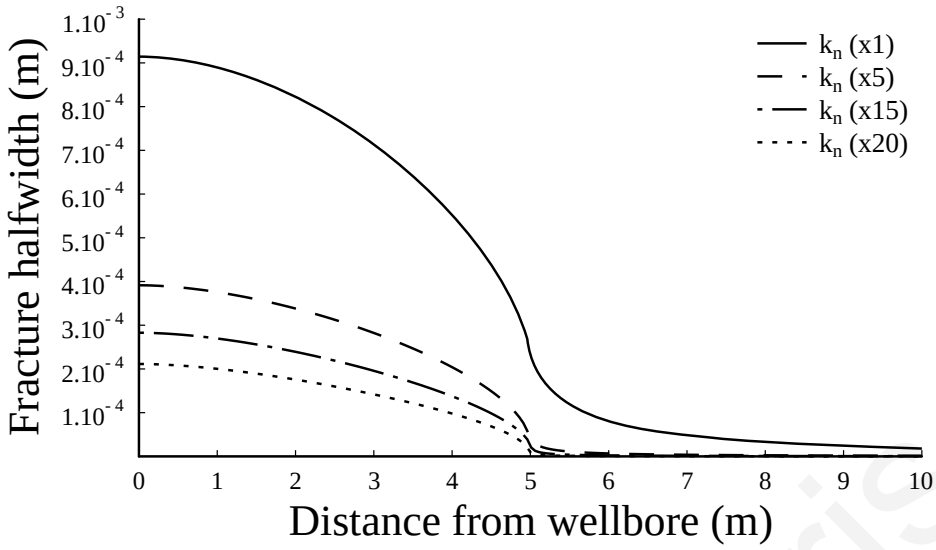

Figure 5.7: Fracture apertures for different values of the loading slope of the constitutive cohesive law

Figure (5.8) shows the corresponding pressure profile versus in the fractures when the visual tip has reached a distance of 5 m. The fluid front position is found to be at the point where the fluid pressure changes sign or falls to zero. It was assumed in these computations that the formation domain is impermeable and the fluid reaches up the fracture tip. This would imply that there is no fluid lag and the pressure drop takes place mainly at the visual tip for these specific parameters. From the curves of figure (5.8), a small negative inclination is observed in the fluid pressures profile inside the fracture. This small non linear behavior is attributed to the value of the fluid viscosity that was imposed. If an inviscid fluid was to be modeled, the shape of these curves would appear to be linear at a constant value above the minimum in-situ stress value. The pressure in the fracture will overcome the closure stress, caused by the far field stress that forces the fracture to close, and propagate the fracture.

According to cohesive zone mechanics the above behavior of the fluid driven fracture is explained from the loading slope of the cohesive constitutive laws. It is obvious that with decreasing the loading slope (i.e. from k_n x 20 to k_n x 1) the value of the limit of elastic deformation δ_{max} is increased therefore permitting more elastic deformation. This elevated value of limit elastic deformation results in an increase of the fluid pressures. Furthermore, the cohesive tractions that are preventing the fracture growth are effective in resisting the fracture propagation due to the artificial elastic

nature of the parameter δ_{max} which in its turn, causes the resulting fracture profile to be significantly larger than the other cases examined.

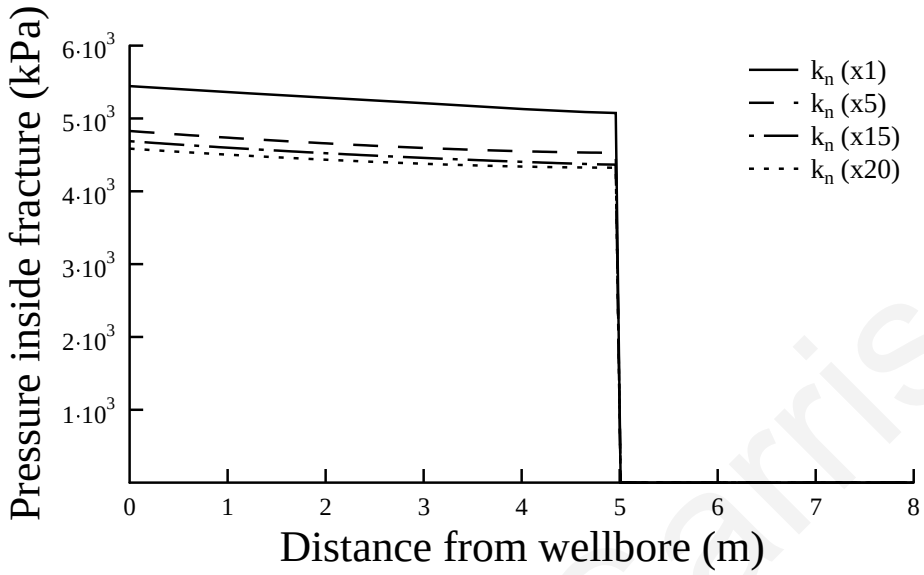

Figure 5.8: Fluid-pressures in the fractures for different values of the loading slope of the constitutive cohesive law.

In this work, small deviations from the actual behavior of a brittle material are investigated in order to have a physical meaning. At this point it is considered important to mention that there is a value of limit elastic deformation δ_{max}^{limit} where the area under the curve in the cohesive zone constitutive law which represents the fracture cohesive energy needed to propagate the fracture is shared into two equal parts. The shape of this cohesive constitutive zone law would result an isosceles triangle. The area of the first part of this isosceles triangle would correspond to the cohesive energy needed to initiate the fracture growth allowing large amounts of elastic energy to be stored up to the damage initiation point. The area of the other part of this isosceles triangle pass the limit elastic damage initiation point would correspond to the case where the rest of the cohesive energy is expended in the damage evolution up to complete failure. However, if this limit point δ_{max}^{limit} surpasses the value under which the cohesive energy needed to initiate the damage would become larger than the energy needed in the damage evolution and as a result the amount of elastic energy storage would have significant implications in the mechanical behavior of the system. The fluid under such limit conditions and according to the material parameters would be capable for penetrating the cohesive

zone because higher fluid pressures would be permitted and the tractions would be resisting the fracture propagation in a large portion of the fracture profile. This is also discussed in the work of Zuorong et al., (2009) however their work is focused in fluid driven fractures mapped in the viscosity dominated regime (highly viscous fluids).

Continuing the analysis, figure (5.9) shows the net-pressure (pressure in the fracture minus the remote confining stress) versus distance from wellbore during fracture propagation. The analysis of the net breakdown pressure is not included and will be discussed in a later figure. Higher propagation net pressure is needed to extend the fracture with elastic-softening cohesive behavior. The pressure drop is more pronounced in the case of the elastic-softening behavior compared to the pressure drop in the case of the rigid-softening behavior. However, as figure (5.7) suggests, for very long fractures is expected that the net-pressure for all cases will tend to a constant value as the length of the process zone diminishes compared to the fracture length and dimensions.

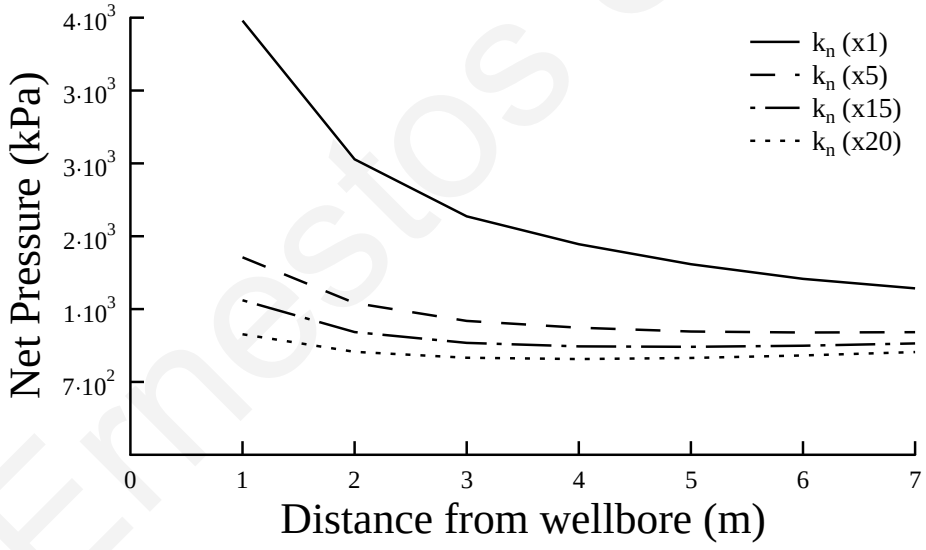

Figure 5.9: Net-propagation pressures vs. fracture length for different values of the loading slope of the constitutive cohesive law

Figure (5.10) shows the distribution of the cohesive stress (stress transferred normal to the propagation direction) versus distance in front of the fractures for the different values of the loading slope of the constitutive cohesive zone models. This stress analysis refers to the calculation of the cohesive stresses ahead of the visual

fracture tip. The methodology followed to plot the corresponding curves was described in detail in section (4.3.1) of chapter 4.

The results reveal that the tensile stress field is contained in a small region near the tip with its maximum value equal to the assumed tensile strength of the rock. During the fracturing process there is a relief of the compressive stresses ahead of the fracture tip followed by a complete separation when the fracture-opening reaches the critical value defined in the propagation criterion. The elastic-softening model which represents fracturing in soft rock formations generates much longer process zone compared to the rigid-softening model which represents fracturing in hard rock formations. The short process zone generated by the rigid-softening model suggests that its results can be compared for validation with the results of an elastic fracture loaded with a uniform internal pressure as discussed earlier. It seems that the loading slope of the constitutive cohesive model influences to a large extent the size of the generated process zone in hydraulic fracturing and as a result wider fractures are generated and higher pressures are needed for propagating an elastic-softening cohesive fracture or a soft rock formation.

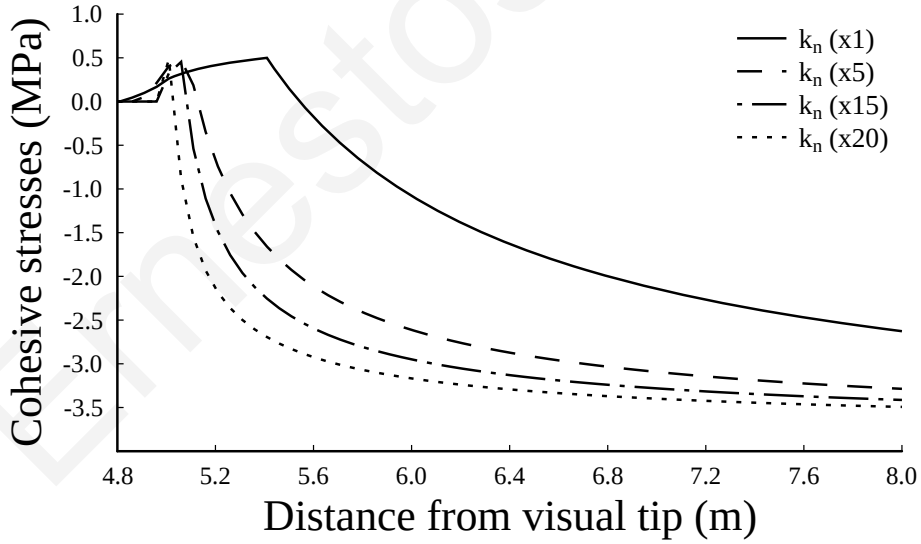

Figure 5.10: Distribution of cohesive stress (normal to propagation direction) in front of the fracture for different values of the loading slope of the cohesive law

Figure (5.11) presents the fracture opening at wellbore versus propagation time for all cohesive constitutive models used in these simulations. The obtained results correspond to a fracture where it has been left to propagate up to 3 m long. Results obtained from this figure (5.11) suggest that significantly larger fracture apertures are

created and as expected more time is needed to propagate the fracture which corresponds to the elastic-softening constitutive law than the other three cases examined. At this point it is considered important to mention that the time observed in x-axis is abnormally large for propagating a fracture up to 3m. This is explained by the extremely slow fracture velocity of propagation which is a direct result of the low initial flow rate that it has been imposed as a boundary condition for a quasi static fracture propagation simulation. From this figure (5.11) the influence of the increasing flow rate is also observed for early times of injection. Initially the fracture pressurization results in exponential volume increase and after the fracture initiates propagation of all fractures follows a linear increasing behavior.

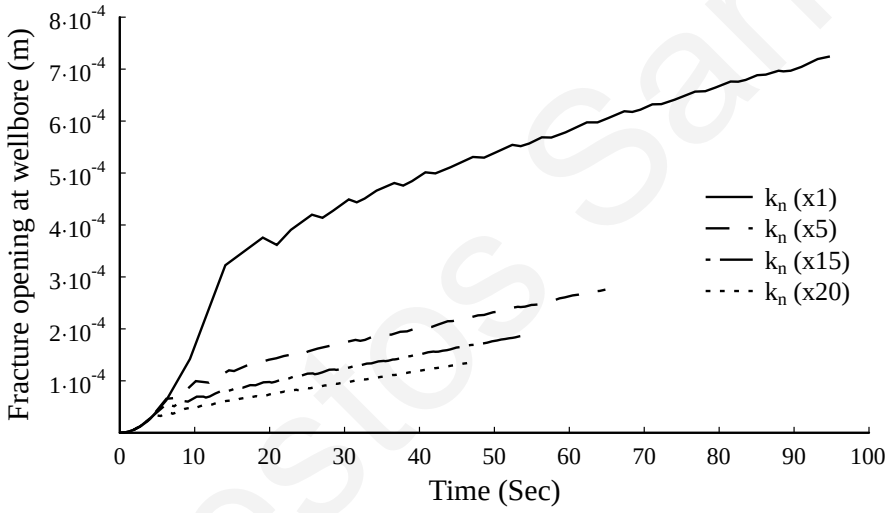

Figure 5.11: Fracture opening at wellbore for different values of cohesive stiffness

Figure (5.12) presents the corresponding fluid pressures at wellbore versus time. In this figure the breakdown pressure needed to initiate the fracture as well as to propagate it to the desired length is clearly shown. Significantly larger breakdown and propagation pressure is observed in the case of elastic-softening constitutive zone law. This is again explained by the elastic limit deformation δ_{max} which is increased with the reduction of the loading cohesive slope, therefore, permitting more elastic deformation. This in its turn results in an increase of the fluid pressures.

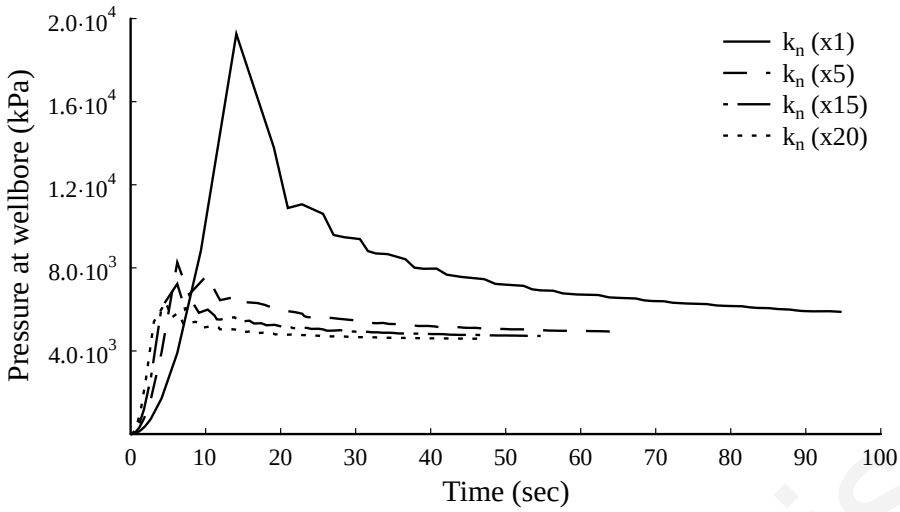

Figure 5.12: Pressure at wellbore for different values of cohesive stiffness

Furthermore, the cohesive tractions that are responsible for the fracture growth are effective in resisting the fracture propagation due to the artificial elastic nature of the parameter δ_{max} which in its turn, causes the resulting breakdown and propagation fluid pressures and the respective fracture profile to be significantly larger than the other cases examined.

5.4 Influence of the Confining Stresses on the Process Zone in Hydraulic Fracturing Modelling

Recent work of Garagash (2006) has outlined the influence of the confining stresses on the size of the fluid lag which is a dry region near the tip of the. In fact it is now understood that one of the factors controlling the size of the fluid lag is the magnitude of the far-field stress. Small confining stress field promotes larger lag due to the viscous nature of the fluid and large confining stress field causes the fracture tip to resist propagation and the fluid front is able to reach the fracture tip thus generating large pressure gradients causing the fluid front to reach the fracture tip. Based on the previously mentioned work of Garagash (2006), the question that may arise is what happens with the fracture process zone if the fluid front coincides with fracture tip? This is exactly the main focus of this section, the analysis of the influence of the insitu confining stress on the cohesive process zone in an impermeable elastic fracture. However, it is considered important to note that it is not claimed that the fluid lag is replaced by the cohesive fracture process zone. These two processes are entirely different and should not be confused between them. Physically these two processes

can be related. When the viscosity of the fracturing fluid is practically zero (inviscid fluid) and the confining stress field is large the fluid is able to reach the fracture tip (lag vanishes) and thus most of the energy that is dissipated in the system is expended to fracture the formation. Similarly if the domain is permeable, the fluid may coincide with the fracture tip. Consistently with the above, the lag is a decreasing function the toughness which in turn influences the size of the process zone.

It is expected that the existence of the confining stresses in field conditions may increase the resistance of rock to fracturing leading to an apparent increase of the fracture toughness (Papanastasiou, 1999). In order to investigate the influence of the confining stresses on the fracture process zone, the calculations of the two extreme cases, for rigid-softening and elastic-softening were repeated for a stress field where the confining stresses were doubled.

Figure (5.13) shows the fracture profile versus distance from wellbore after the fracture was left to reach 2 m long for the two extreme cases of rigid-softening (R-S) and elastic-softening (E-S) for different value of the insitu stress field. The indication that the curves are created with the double insitu stress field is noted with (x2) and with the normal insitu stress field with (x1).

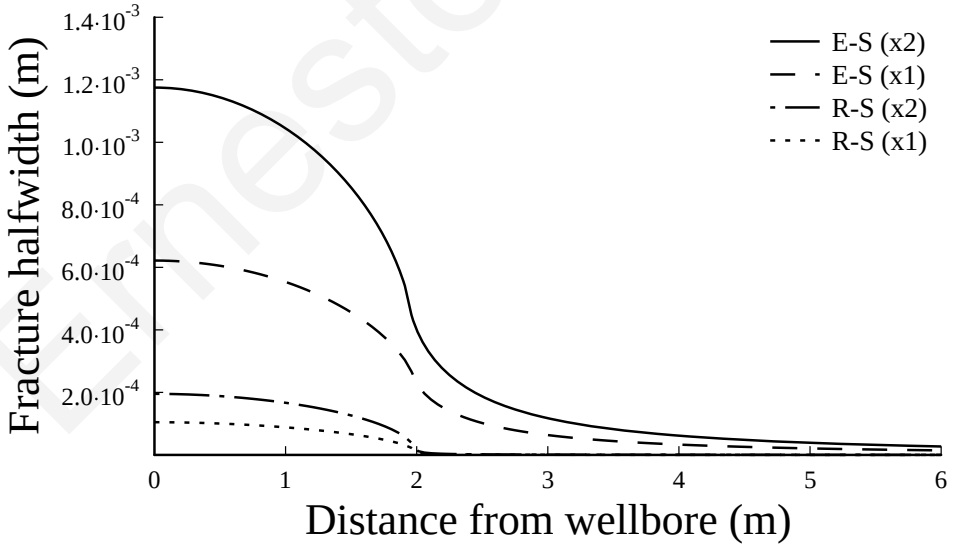

Figure 5.13: Influence of the in-situ stress field on the fracture apertures for elastic-softening (E-S) and rigid-softening (R-S) cohesive laws. The cases marked with X2 correspond to a double value of the confining stresses.

We see that the fracture width profiles were almost doubled when the confining stresses were doubled for both rigid-softening and elastic-softening models. This is

consistent with Papanastasiou (1999) observations that the apparent fracture toughness is significantly increase with the magnitude of the insitu confining stress field. Figure (5.14) shows the corresponding pressure profiles inside the fractures for the two respective cohesive material models and for the different confining stress field.

Figure (5.14) shows that the fluid pressures needed to propagate the fractures in the two extreme cases of rigid-softening (R-S) and elastic-softening (E-S) before and after the doubling the insitu stress field is nearly doubled. This is trivially explained by the minimum insitu stress component that was imposed as a confining stress boundary condition.

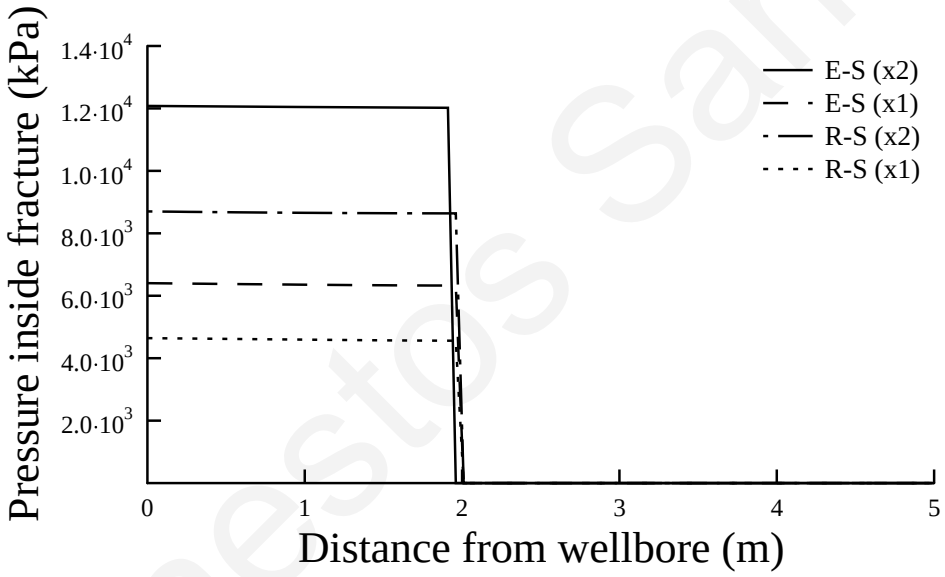

Figure 5.14: Influence of the in-situ stress field on the pressure distributions for elastic-softening (E-S) and rigid-softening (R-S) cohesive laws

In order to propagate the fracture, the fluid pressures must rise such pressure gradients to overcome the minimum insitu stress field which confines and tends to retard the fracture from propagating.

These results are better compared in figure (5.15) where the net-pressures versus distance from wellbore are plotted. Apparently, in a field with high confining stresses, higher net-pressure is needed for propagating a hydraulic fracture and a wider fracture is created as a result of the different size of the process zone.

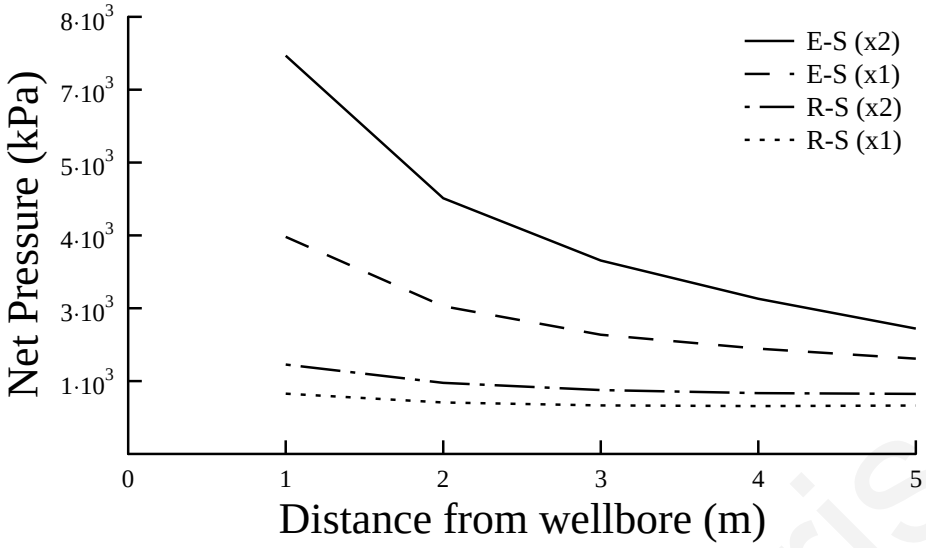

Figure 5.15: Influence of the in-situ stress field on the elastic net pressures for elastic-softening (E-S) and rigid-softening (R-S) cohesive laws

Figure (5.16) shows the detailed plot of the cohesive stresses acting in a direction normal to the fracture path starting from the position of the visual tip and extending some distance from that visual fracture tip. It includes the results obtained according to the methodology described in section (4.3.1) for the two extreme cases of rigid-softening (R-S) and elastic-softening (E-S) and for different values of the insitu stress field.

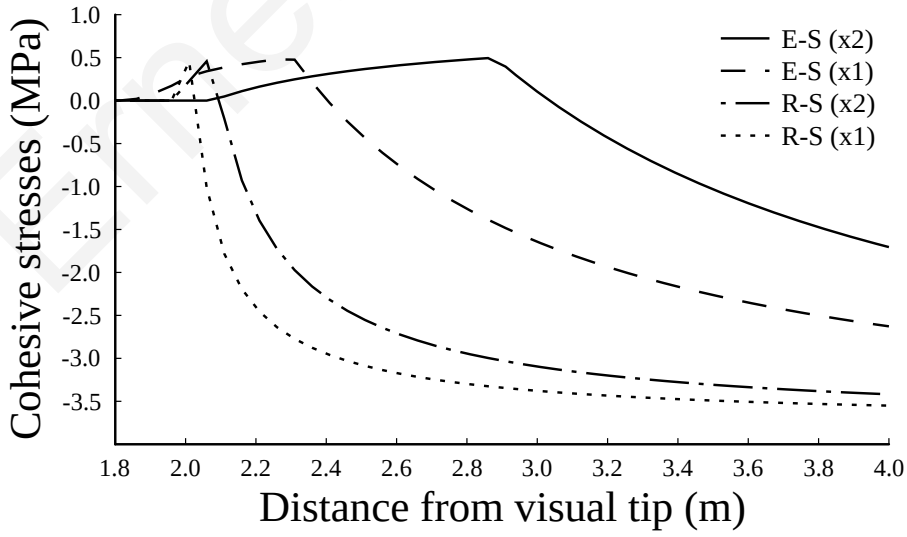

Figure 5.16: Influence of the in-situ confining stresses on the cohesive stresses in front of the fractures for elastic-softening (E-S) and rigid-softening (R-S) cohesive laws.

Figure (5.16) shows that the size of the fracture process zone is proportional to the magnitude of the stress field. Another important result in figure (5.16) is that the fracture process zone in both cases of rigid-softening (R-S) and elastic-softening (E-S) appears to translate a small distance from the visual fracture tip before it begins to completely develop. This is possibly attributed to the magnitude of the highly confined stress field that was applied causing the fracture to close at that point thus demanding higher net pressures to extend the fracture.

It is emphasized that the differences in the results of figures (5.13) to (5.15) are due to the longer process zone which is created under higher confining stresses as clearly shown in figure (5.16). However, examining the results of figure (5.15), it appears that this difference tends to diminish with increasing fracture length and dimensions. The last remark should not be used to underestimate the above findings because there are many applications where short hydraulic fractures are created in weak rock formations.

At this point it is safe to conclude that for short fractures which are confined by a compressive stress field, the size of the process zone L_{FPZ} is directly proportional the magnitude of the minimum insitu stress σ_{min} as

$$L_{FPZ} \propto \sigma_{min} \tag{5.3}$$

5.5 The Influence of the Loading Part of the Constitutive law on the Process Zone in Hydraulic Fracturing under Poroelastic conditions

Computations were also carried out for hydraulic fracturing in a porous material taking into account the fluid diffusion in the surrounding formation. The results were compared with the results from the non-porous material where fluid diffusion and leak-off in the formation were ignored. The objective of these calculations was to further investigate how the results of the cohesive models will be affected by the existence and the changes of the pore pressure in the porous formation.

Figure (5.17) shows the half-width of a propagating fracture versus distance from wellbore in the poroelastic solids for the cases of different loading slope of the cohesive constitutive relation (figure 5.1) after the fracture has reached a length of 3 m. The computed width of the poroelastic propagating fracture utilizing the elastic-softening model (i.e. fracturing in weak rock formation), which corresponds to

k_n (x1), is much larger than the computed width of the poroelastic fracture using the rigid-softening model (i.e. fracturing in hard rock formation) which corresponds to k_n (x20).

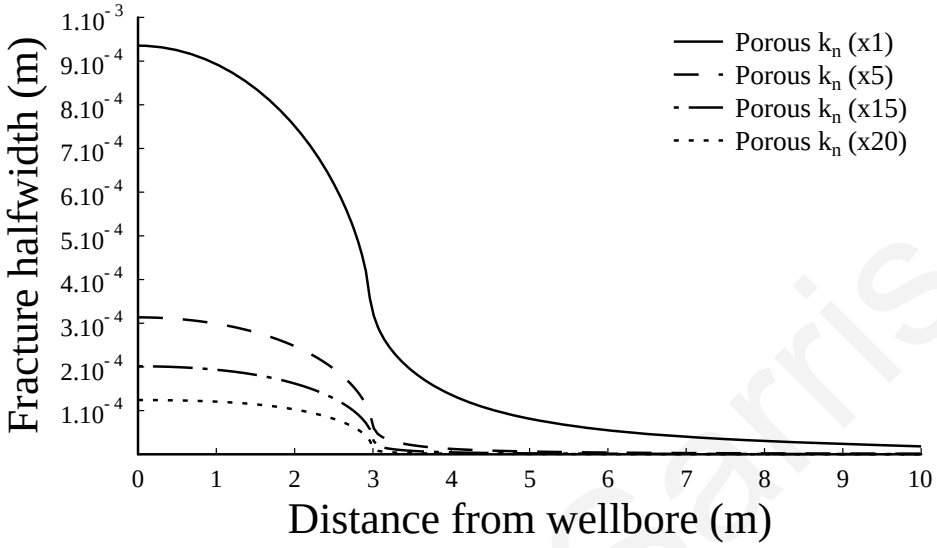

Figure 5.17: Aperture of porous-elastic fractures for different values of the loading slope of the cohesive laws

Comparing the results of figure (5.7) for the non-porous fracture, with the results of figure (5.17) for the porous fracture it is evident that the porous fracture profiles are wider especially for the case of the elastic-softening (weak rock) cohesive model whereas for the case of the rigid-softening behavior (hard rock) the difference appears to be negligible. The porous fractures reached about the same width at a shorter length (3m) compared to a longer length (5m) for the non-porous fractures.

Figure (5.18) shows the pressure profile along the predefined fracture path which is inside the fracture and process zone during propagation when the visual tip reached a distance of 3 m. Figure (5.18) shows that the fluid-pressure drops abruptly near the visual tip when the fracture has reached 3 m in length. From the curves of figure (5.18), the influence of the fluid viscosity is observed through a small negative inclination which is observed in the fluid pressures profile inside the fracture. The pressure ahead of the fracture tip decreases to values below the initial formation pressure and far away from the tips tends asymptotically to its initial undisturbed value of pore pressure that has been incorporated as initial condition (1.85 MPa). This is in agreement with the poroelastic theory.

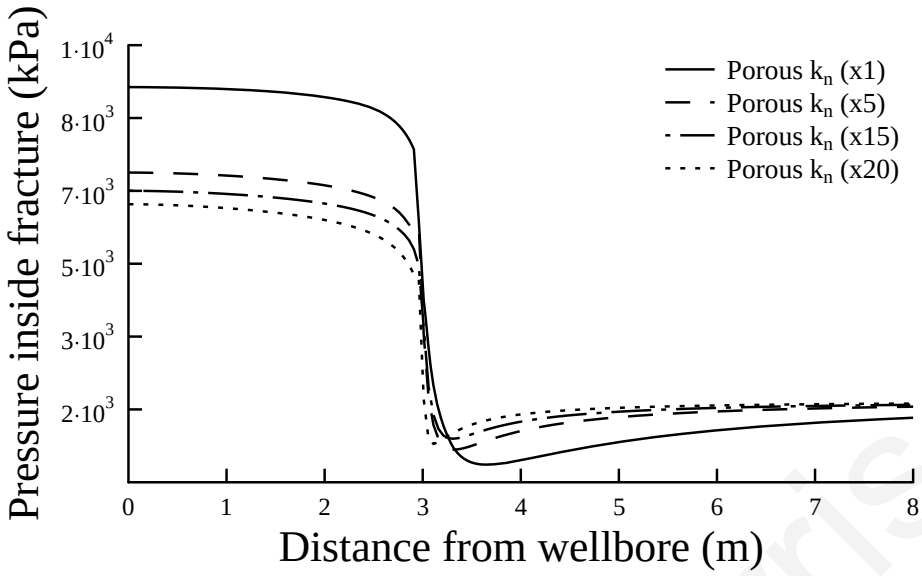

Figure 5.18: Pressure profile in the porous-elastic fractures for different loading slope of the cohesive law

However, in the area near tip, the fluid pressures present significantly different behavior. This behavior can be explained by the local mechanical response of a porous system in which the solid matter in that porous matrix is under pressure. The grains response of the porous medium under high pressure gradients is expected to exhibit a softer bulk behavior even if it is assumed incompressible. This soft response is significantly affected by the voids of the assumed created process zone thus this disturbance can be attributed to the fracture process zone. This behavior is explained by equation (3.34) and it is observed that the volumetric strain which is given from the ratio of the average pressure stress caused by the wetting liquid to the grains bulk modulus actually represents that part of the total volumetric strain caused by the pore pressure acting on the solid matter in the porous medium. The strain caused by the ratio of the average pressure stress in the wetting liquid to the grains bulk modulus in the porous medium represents the strain that is assumed to modify the effective stress in the porous continuum and in its turn the generated fracture process zone.

Figure (5.19) shows the net-pressure (pressure in the fracture minus the remote confining stress) during fracture propagation as a function of the fracture length for all the porous models. In comparison with figure (5.9), the required net-pressure that is needed for propagating the porous fracture is higher than the net-pressure required for propagating the non-porous fracture, especially for short propagations. This result seems to back up the previously discussed assumption that the size of the fracture

process zone is significant near wellbore as the fracture length and dimensions are comparable with the length of the process zone near wellbore.

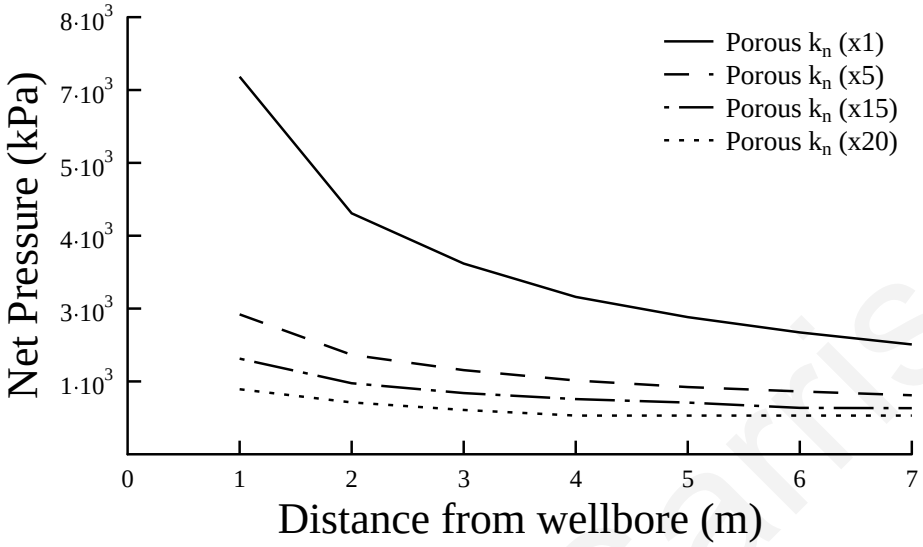

Figure 5.19: Net-pressures for porous-elastic fractures for different loading slope of the cohesive law

In order to estimate the size of the cohesive zone in the porous models, figure (5.20) was constructed which is the profile of the cohesive stress normal to the propagation direction ahead of the visual fracture tip. It is observed once again that the size of the process zone is much larger in the case of the elastic-softening (weak rock) behavior, especially in the case of the porous model, suggesting that the pore pressure in the formation has a strong interaction with the stress concentration near the fracture tip. The local mechanical response of the porous continuum in which the solid matter under highly pressure gradients exhibits a softer bulk behavior and the volumetric strain modifies the effective stress in the porous continuum creating larger process zones.

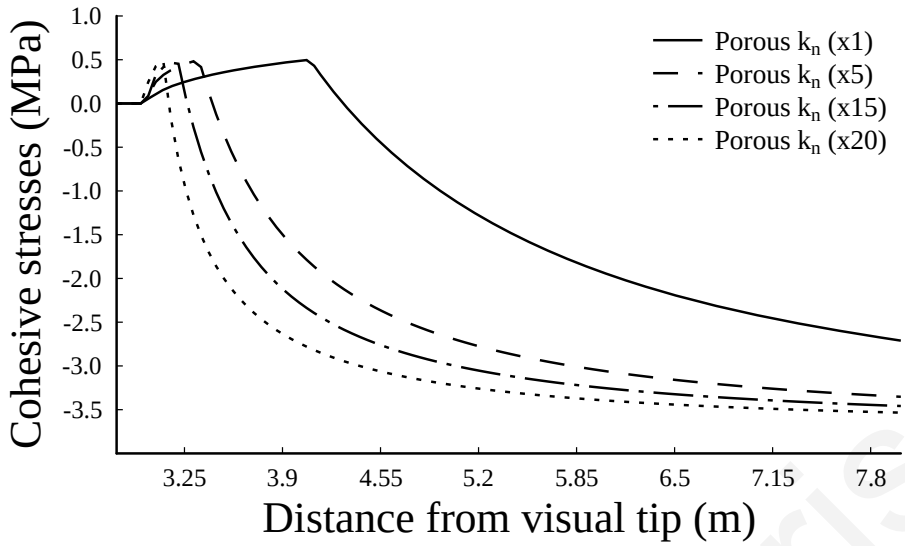

Figure 5.20: Distribution of stress normal to the propagation direction for porous models.

At this point it should be noted that that although a linear softening behavior in the cohesive models was implemented, the calculated stress profiles from the resulting separations are sufficient non-linear. This outlines the adequacy of simple softening relations in capturing the non-linear stress distribution ahead of the fracture tip.

5.6 Influence of the Softening Part of the Constitutive law on the Process Zone in Hydraulic Fracturing Modelling

In the previous sections, the influence of the initial slope of the cohesive constitutive law on the fracture process zone was analyzed in detail. The obtained results of the fracture opening, the fracture length and the pressures needed to drive the fractures were discussed in the context of the process zone in both non porous and porous conditions. The next step to complete the analysis of the influence of the cohesive zone in hydraulic fracturing is to extend the investigation in the softening part of the constitutive cohesive zone law. This is done by the modification of the linear softening behavior of the constitutive behavior as analyzed in section (5.2).

In the following computations, the influence of the exponential softening form described by equations (5.1) and (5.2) is investigated. The modification of the linear softening form to the exponential softening form is given by the damage variable according to equation (5.1) and is depicted in figures (5.2) and (5.3) for the elastic-softening (weak formation) and rigid-softening (hard formation) cases respectively. This is done by introducing an exponential coefficient which gives a measure of the

exponential curvature. After obtaining analytically the exponential damage variables are inserted in equation (5.2) which describes the traction – separation curve and to yield the critical value of fracture opening displacement (figures 5.4, 5.5). Incorporating the exponential constitutive laws, the required propagation pressures and fracture dimensions of the created fractures are computed numerically. Furthermore, the size of the fracture process zone is constructed according to the methodology which it will be described next.

Figure (5.21) shows the half-width profile of a propagating fracture in poroelastic solids for cases of different exponential softening compared to the linear softening for the elastic-softening cohesive zone law.

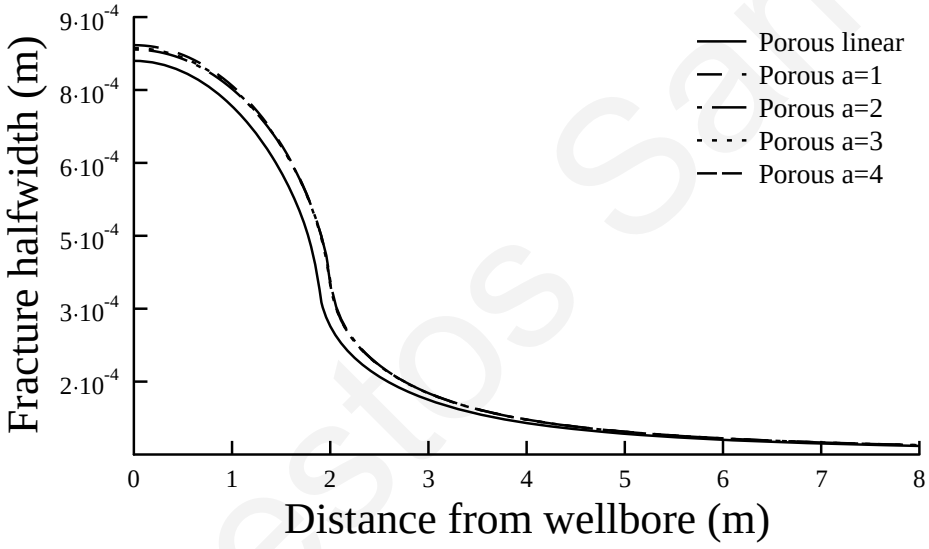

Figure 5.21: Width-profiles for porous elastic fractures with different form of exponential softening

Figure (5.21) shows that the fracture apertures that are created from the exponential softening cohesive zone laws, compared to the linear softening law, does not influence to a great degree the fracture profiles.

Figure (5.22) presents the corresponding pressure profiles for cases of different exponential softening compared to the linear softening for the elastic-softening cohesive zone law.

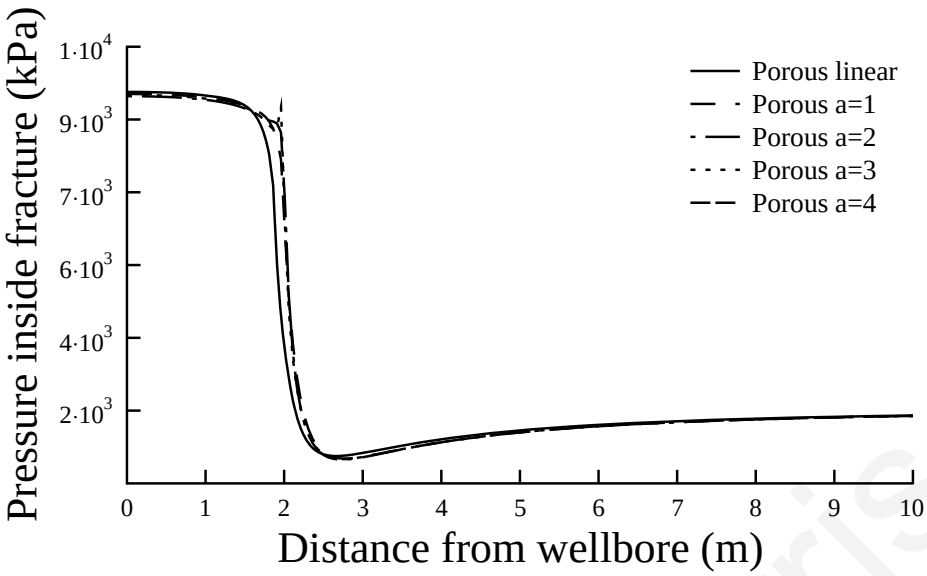

Figure 5.22: Pressure distributions in the porous-elastic fractures for different form of exponential softening

Figure (5.22) confirms also that the pressure that are needed to extend the fractures created from the different exponential softening cohesive zone laws do not deviate from the pressure of the linear softening model.

Figure (5.23) presents the fracture apertures and figure (5.24) shows the respective fracture fluid pressures needed to propagate the fracture for the extreme exponential softening case ($\alpha = 4$) and under non porous conditions. Both cases of cohesive constitutive zone laws of elastic-softening and rigid-softening were considered. These two figures (5.23) and (5.24) are better compared with the two figures (5.25) and (5.26) which represent the fracture profiles and the fluid pressures for the porous continuum.

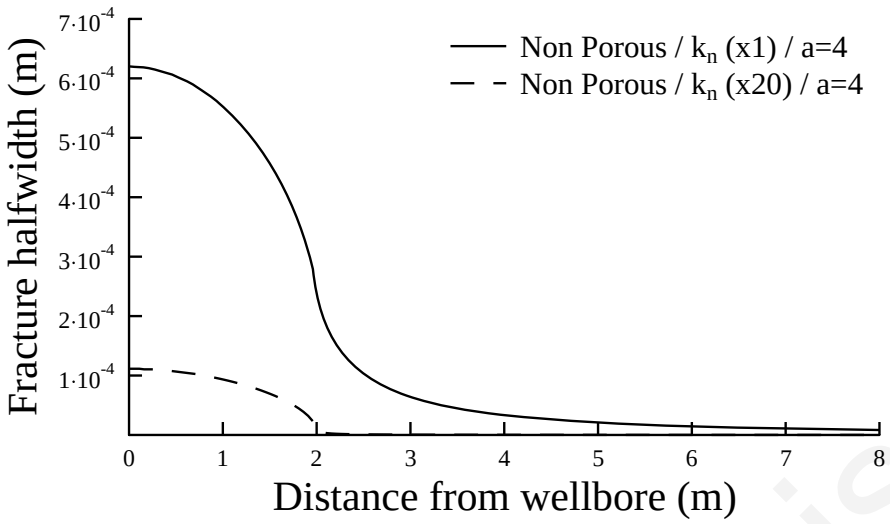

Figure 5.23: Non porous fractures for the extreme case of exponential softening (α = 4)

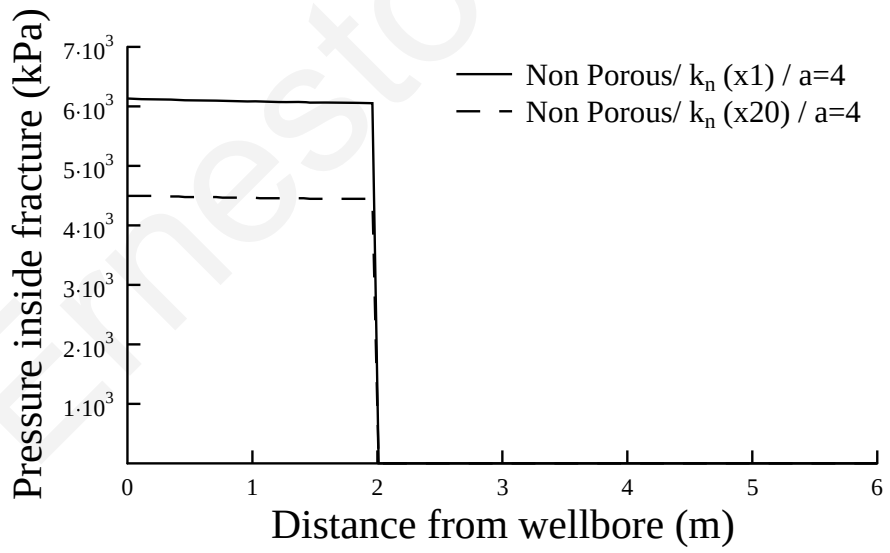

Figure 5.24: Non porous fluid pressures for the extreme case of exponential softening (α = 4)

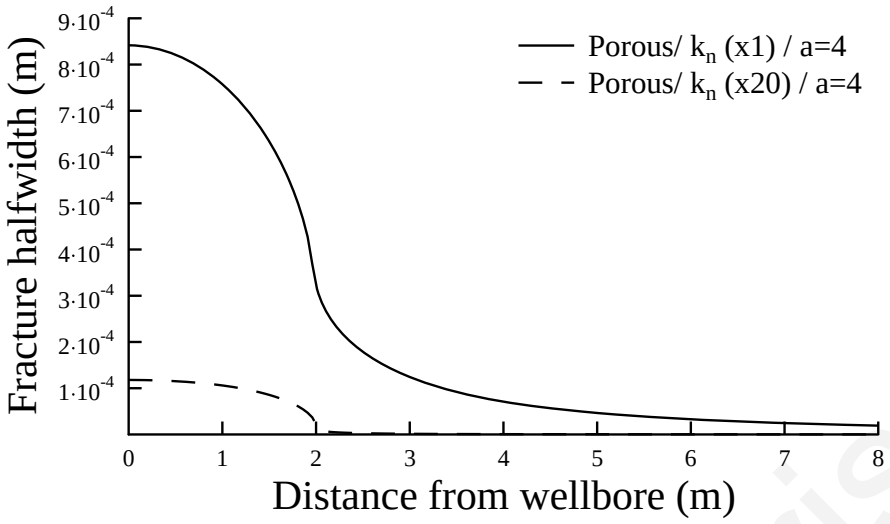

Figure 5.25: Porous fractures for the extreme case of exponential softening (α = 4)

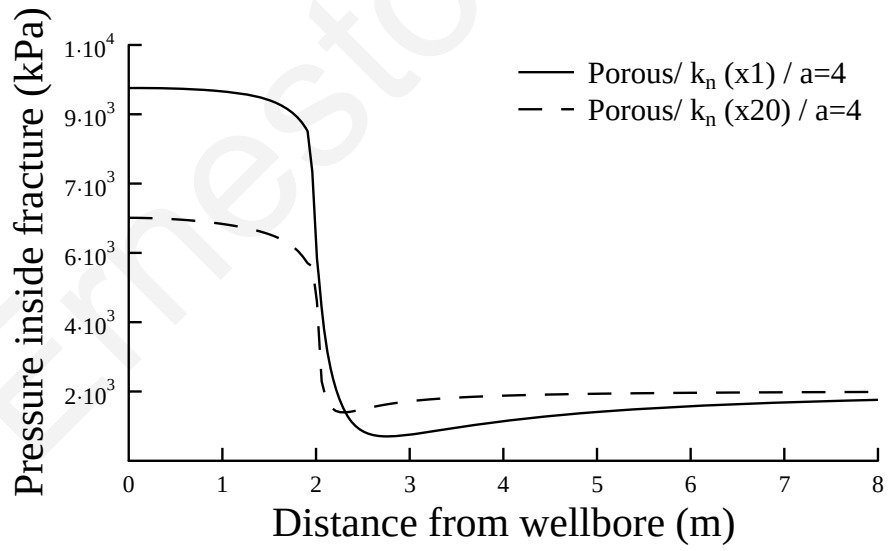

Figure 5.26: Porous fluid pressures for the extreme case of exponential softening (α = 4)

Figures (5.23) to (5.26), confirm that the difference seen in the fracture profiles and the fluid pressures is due to the porous and non porous behavior and more importantly to the different elastic-softening and rigid-softening constitutive laws that have been used and not in the exact shape of the softening branch. The area under the

curve in the cohesive constitutive law which represents the fracture elastic cohesive energy needed to initiate the fracture growth is given by the limit elastic deformation value δ_{max}. The rest of the cohesive energy is expended in the damage evolution up to complete failure. The energy that is removed from the left side of the linear softening curve is added in the right side of the linear softening curve causing the increase of the critical separation opening δ_{IC} (figures 5.4 & 5.5). The result is the modification from linear softening to exponential due to energy balance requirements. However, the amount of energy that is responsible for modifying the softening curve from linear to exponential is small and the results appear to present negligible difference. This is mainly the reason for the similarity in the obtained results.

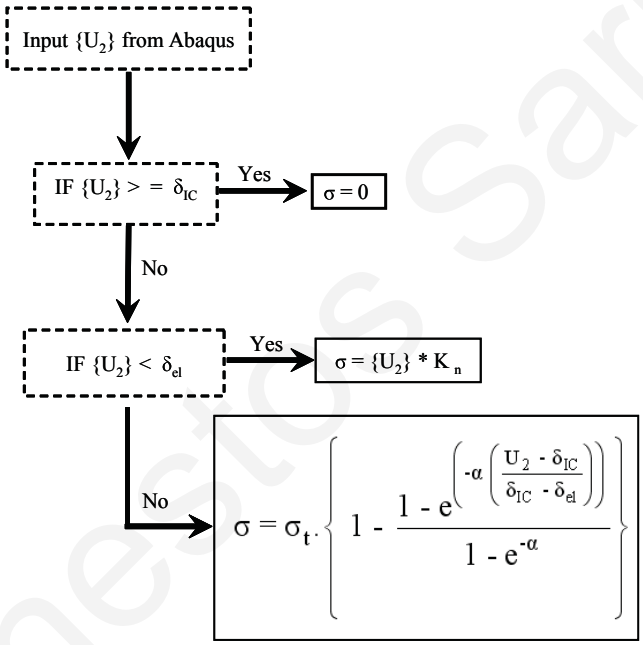

Figure 5.27: Calculation of cohesive stresses in the process zone using exponential softening

In order to construct the cohesive stresses acting in a direction normal to the propagation path, the simple subroutine which has been detailed analyzed in section (4.3.1) for a linear softening is modified to account the exponential softening in figure (5.27). The cohesive stresses were determined from the displacements that represent the fracture profile.

Figure (5.28) an (5.29) presents the cohesive stress distribution along the fracture path for cases of different exponential softening compared to the linear softening for the elastic-softening cohesive zone law (weak formation) in both impermeable and permeable domains.

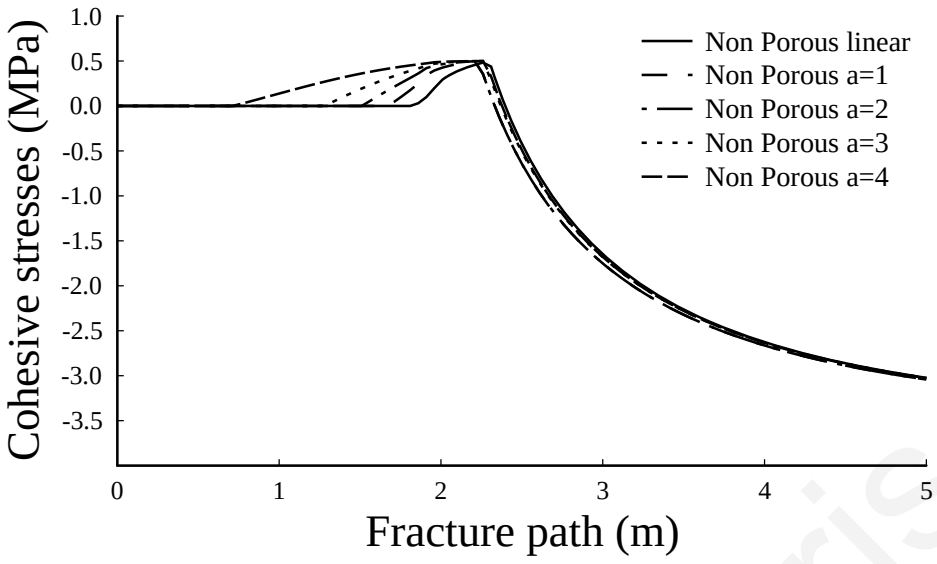

Figure 5.28: Distribution of stress normal to the propagation direction for non porous models and different forms of exponential softening

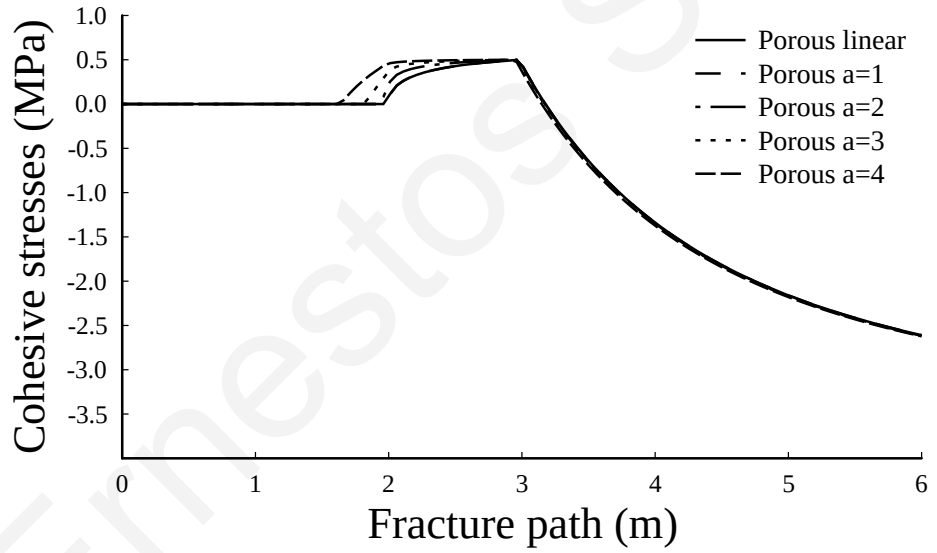

Figure 5.29: Distribution of stress normal to the propagation direction for porous models and different forms of exponential softening

Figures (5.28) and (5.29) show that the distribution of the cohesive stress (stress transferred normal to the propagation direction) in front of the fractures for the different values of the exponential softening is nearly unaffected with the softening branch of in the constitutive cohesive model. As expected, the size of the fracture process zone is significantly larger in the porous models compared to the non porous. However, the significant result illustrated in figures (5.28) and (5.29) is in the exact shape of the fracture process zone. It is evident that the shape of the process zone is

more blunted in the porous than in the non porous case. This observation leads to the conclusion that the shape of the fracture process zone is affected by the diffusion process when the incorporated softening is exponential. This result is supported by the explanation given earlier that the form of the softening is able to influence the mechanical behavior of the continuum and the fracture fluid. Figures (5.28) and (5.29) were plotted for a fracture reaching 2 m length. However, for extreme values (α = 3, 4) of the exponential softening the fracture process zone extends backwards some distance from the actual fracture length and position of the fluid front. This is a direct result of the fluid that has penetrated in the fracture process zone. This effect is more pronounced in the case of the impermeable fracture since the diffusion process is absent and the fluid appears to penetrate in the process zone at larger distance for the extreme case of softening. The fluid penetration in the porous models is smaller because of the fluid losses in the surrounding domain. This explanation is better understood if a comparison is made for the critical separation openings δ_{IC}, for all the softening exponent values α. According to energy balance requirements, increasing the softening exponent value will result in an increase of the critical separation opening thus permitting the fluid to penetrate inside the process zone.

5.7 Conclusions

In this chapter the two most commonly used cohesive zone models to study fracture problems, bilinear and exponential where utilized to analyze their influence on the fracture process zone in impermeable and permeable fluid driven fractures. These two cohesive constitutive models (bilinear and exponential) were used to compute numerically the fracture profile, the fluid pressures, the net pressure as well as the length and shape of the process zone to study the influence of the cohesive zone characteristics on the modeling of hydraulic fracturing technique. The objective was to explain, at least partially, the elevated pressures that are needed to propagate the fractures in the field and are not predicted correctly by the conventional models. In order to keep the model parameters to a minimum, rigid-softening and elastic-softening with both linear and exponential softening cohesive relations were considered to represent the splitting process of the rock near the fracture tip. A set of fully coupled models for the fluid-flow in the fracture, the rock deformation and the

fracturing process were presented and solved numerically with the finite element method.

The results obtained from the analysis conducted are summarized:

- To propagate a fracture with an elastic-softening cohesive model (weak formation) higher breakdown and propagation pressure is needed to drive the fracture and the created fracture is wider compared to the case of a rigid-softening cohesive model (hard formation). These results are due to the larger process zone obtained with the elastic-softening model.
- The existence of high confining stresses increases the size of the process zone and results in wider fractures and higher propagation pressures. It has been shown that for short fractures which are confined by a compressive stress field the size of the fracture process zone is directly proportional to the minimum insitu stress.
- The changes in the pore pressure during fracturing (permeable fracture), increase further the size of the process zone which in turn increase the propagation pressures and the dimensions of the created fractures.
- An exponential damage variable has been proposed and incorporated to deal with damage evolution to complete failure with exponential softening in the constitutive cohesive zone laws.
- It has been shown that the exact form of the softening branch of the cohesive model has no significant influence on the obtained results and although a linear softening behavior in the cohesive models was implemented, the calculated stress profiles from the resulting separations are sufficient non-linear. This outlines the adequacy of simple softening relations in capturing the non-linear stress distribution ahead of the fracture tip.

6. Fracturing in Poroelastic Cohesive Formations

6.1 Preamble

This chapter investigates the parameters affecting the propagation of a fluid driven fracture in a non porous and porous elastic continuum under plane strain conditions. These parameters include the fluid viscosity, the formation permeability, propagation velocity obtained through the injection rate and finally the formation compressibility. The fracture is driven by pumping of an incompressible Newtonian viscous fluid at the fracture inlet and fluid leak-off in the host rock is considered to account diffusion effects in the surrounding formation. Rock deformation is the porous model is assumed as linear elastic. Fluid flow in the fracture is modelled by lubrication theory. The propagation criterion is of the cohesive type which seems to be more appropriate for representing the mechanical behaviour of rocks with computational efficiency. Finite element analysis was performed to compute the solution of the fluid fracturing pressure, the fracture opening and the fracture length as a function of the time and distance from the wellbore.

This chapter aims in understanding the behavior of the fluid driven fractures in poroelastic solids. The analysis is expected to be complex mainly due to the inherent fluid-solid coupling of the fluid driven fracture problem. Fracture propagation in fluid saturated poroelastic media has been initially analyzed for quasi static conditions under shear loading by Rice & Cleary (1976) and later for tensile loading by Atkinson & Craster (1991). Under these circumstances, the region close to the fracture tip is practically drained, even for rapid fracture propagation. However, fracture propagation in poroelastic materials is constrained to computational and asymptotic analysis without a process zone and an extension is attempt in this study with the presence of a cohesive zone.

6.2 Plane Strain Fracture in Poroelastic Media

Simulation of plane strain fractures in poroelastic media is not a trivial task, as it involves the coupling of four physical mechanisms: (i) the flow of the fluid within the fracture, (ii) the mechanical deformation of the surrounding medium induced by the fluid pressure on the fracture surfaces, (iii) the fracture propagation and (iv) the leak-

off process of the fracturing fluid in the permeable medium which is a time dependent process.

The classical Biot theory of poroelasticity attempts to model the mechanical response of a porous material which has a solid elastic skeleton with the pore space filled with a viscous fluid. In the fluid driven problem, the pore fluid flow and the elastic deformations are coupled and the usual assumption made is that the porous materials are saturated with either incompressible or compressible pore fluids. Furthermore, the grains of the solid phase can also be considered either incompressible or compressible. The equations derived by Biot (1941) exhibit an explicit coupling between the dilation of the elastic skeleton and the pressure of the diffusing pore fluid. The theory of poroelasticity has been successfully applied to examine time dependent phenomena in natural and synthetic geomaterials. The governing equations can be derived by using Darcy flow equation to model the diffusion process, a mass conservation equation for the pore fluid and the equilibrium equation for the stresses. Hence, the fundamental basis of the equations is well founded. However, the assumption of linear elastic behavior of the porous skeleton is a significant limitation in the application of the theory to brittle materials which could exhibit stiffness changes. The poroelastic materials differ from the corresponding quasi-static elastic solids as a time dependence is introduced in the otherwise time independent elasticity equations. Furthermore, non-linear behavior can be observed due to development of micro cracks and micro voids in the porous fabric which essentially retains its elastic nature. Another possible reason for non linear response is that the diffusing pore fluid can have a large effect under relatively rapid loading as in hydraulic fracturing operations compared to that of a natural diffusion time scale; hence the material response is stiffer than for slower loadings as the fluid has less time to diffuse away (Atkinson and Craster 1991).

The poroelastic theory is also relevant to the fracture of rocks. Such problems of rock fracturing, where there is pore fluid interaction is believed to be important in enhancing the recovery of hydrocarbons via hydraulic fracturing. The numerical simulations involved in this work are aimed to the understanding of the physical processes that occur in hydraulic fracturing operations in porous materials such as rocks. It is easily understood that during the initiation of the fracture, when the fracture is internally pressurized by pumping viscous fluid, the fluid may leak into the formation depending on the formation permeability. This causes a volume expansion

of the material around the fracture tending to close the fracture. There are also external stresses and pore pressure fields which may affect the hydraulic fracture as the parameters, for as accurate as possible estimation, may deviate. Therefore, there is a complicated interaction between the diffusing pore fluid and applied loading which must be computed numerically as such analytical solutions is difficult to obtain. Furthermore, numerical simulations are a powerful tool for obtaining first results to help reach and extrapolate accurate parameters to calibrate field operations (Craster and Atkinson 1994).

The basic theory of poroelasticity is commonly applied to soil mechanics problems especially for consolidation problems. The elastic response of the porous medium is given by the elastic strain rate and the elastic fluid mass content. These two parameters are related to the rates of total stress $\dot{\sigma}$ and pore pressure $\dot{p}$ through isotropic constitutive equations that involve four material coefficients, namely: (a) the drained young's modulus $\left(E \succ 0\right)$, (b) the drained Poisson ratio $\left(v \in \left[-1/0.5\right]\right)$, (c) the undrained Poisson ratio $\left(v_u \in \left[v/0.5\right]\right)$ and (d) the Skempton coefficient $\left(B \succ 0\right)$. Restrictions on these material parameters according to Rice and Cleary (1976) ensure positive definiteness of the elastic constitutive equations in terms of the strain and stress pairs, $\left(\varepsilon, \zeta\right)$ and $\left(\sigma, p\right)$. By definition the total stresses are related to the effective stresses through the effective stress principle as described in chapter 3. The effective stresses are assumed to govern the failure of the rock. The poroelastic Biot-Willis constant a, is independent of the fluid properties and it is defined as

$$\alpha = \frac{3(v_u - v)}{B(1-2v)(1+v_u)} = 1 - \frac{K}{K_g} \tag{6.1}$$

As it has been mentioned before, this theory is commonly applied in soils and an important distinction when applying the formulation to rocks is that the compressibility of the constitutive materials must be considered. For Soils B and α are equal to unity but in some rocks are significantly less than one.

6.2.1 Plane strain poroelastic scaling

The scaling laws of a fluid driven fracture in a permeable formation were originally studied by Adachi (2001). In his work the fluid front is assumed to coincide with the

fracture tip. This is in good agreement with the numerical model presented herein except that in this case the fracture propagation is of the cohesive type. Adachi identified three energy dissipative processes a) The viscous flow in the fracturing fluid {M}, b) Fracturing of the rock {K} and c) diffusion of fluid into the formation {C}. These dissipative processes define a propagation regime in which one particular process accounts for most of the dissipative energy. Scaling laws obtained by Adachi (2001), can be represented as a triangular parametric space (MKC-triangle) with each vertex corresponding to an ideal situation with only one dissipative process dominates. A fluid driven fracture is evolving in this parametric space moving with time from one propagation regime to another. These scaling laws are particularly useful in explaining the fracture behavior in numerical simulations. The ideal situation where the fracture is driven in an impermeable medium with zero toughness is represented by the M-vertex solution. The paradoxical case where a zero volume fracture is driven in a permeable medium at infinite time scale is represented by the C-vertex solution. Finally, the fracture driven in an impermeable medium with an inviscid fracture fluid is represented by the K-vertex solution and actually corresponds to the case of the classical problem of a uniformly pressurized fracture. At this point it is noted that the leak-off dominated propagation regime (C-vertex) will never be reached in actual hydraulic fracturing treatments as it represents a theoretical aspect of the problem to assist in the construction of complex analytical solutions. However, a numerical model, like the present, is capable for simulating a fluid driven fracture in permeable domain incorporating all the previous dissipative mechanisms as the solution is bounded in the MKC-triangular parametric space.

6.2.2 Poroelastic fracture propagation assumptions

Solution of the fluid driven problem in a permeable formation requires simultaneous considerations from fracture mechanics for the fracture propagation and fracture dimensions, diffusion theory for the porous fluid movement and viscous fluid flow inside the fracture (Garagash 1998). Construction of analytical solutions within this framework is cumbersome to obtain and the problem is treated numerically to reach accurate conclusions.

The numerical models of the fluid driven fracture propagating in a permeable rock present some special limitations and the analysis is performed under the following assumptions:

- The fracture propagates in a permeable linear elastic solid.
- The fracture fluid front coincides with the fracture tip (i.e. no fluid lag is modeled).
- The propagation velocity is adjusted with the injection rate applied as boundary condition.
- The fluid driven fracture is treated as two dimensional under plane strain conditions.
- Variation (evolution) of the pore pressure field in the permeable rock is governed by the homogeneous diffusion equation (i.e. the poroelastic coupling between solid deformation and pore fluid diffusion is such as it is accounted for in the theory of poroelasticity.
- Pore pressure associated with leak-off from the fracturing fluid, behind the fracture walls is able to influence the circulation of pore fluid (i.e. the fracture wall behind the process zone is treated as permeable).
- Even though the cake building property has been assigned, it was set to correspond to the porous domain permeability so as to reach accurate conclusions about the influence of the diffusion process on the fracture analysis. Generally, the viscosity of the fracture fluid is typically two orders of magnitude larger than the pore fluid in the context of the stimulation of oil wells.
- The flow of fluid within the fracture is treated with the lubrication theory and the exchange of pore fluids between the fracture and the porous continuum is allowed.
- The fracture fluid and pore fluid are of the same nature, incompressible and Newtonian.
- The movement of pore fluids in the porous medium (continuity) is treated within the framework of Darcy law.

The main objective is to calculate the fracture dimensions, the fluid pressures as a function of the parameters characterizing the fluid and the rock and to establish the fracture mechanism in poroelastic continuum. These parameters include the fluid viscosity, the formation permeability, propagation velocity obtained through the injection rate and finally the formation compressibility.

6.3 Fluid-Driven Fractures in Impermeable and Permeable Cohesive Formations

The detailed investigation of the main characteristics of the cohesive zone curve and the computations carried out for different initial slopes to simulate a brittle to ductile behavior or more strictly defined a rigid-softening to elastic-softening behavior were presented in chapter 5.

Researchers usually choose to ignore such ductile behaviour due to the usual instability that numerical codes present when they have to deal with fracture extensions which results in non-proportional loading as in the case of hydraulic fracture operations. For the case of the ductile behavior the above relations can be augmented and modified to take into account the initial part of the curve which corresponds to linear elastic deformation.

Table 6.1: Input parameters for poroelastic computations

Variable	Value
Rock Properties	
Young modulus, **E** (MPa)	16200
Poisson ratio, **ν**	0.3
Compressibility, $\mathbf{K_s}$ (PA)	2.5E-10 / 5E-10
Pumping parameters	
Viscosity, **μ (**kPa.sec)	0.1 / 0.01 / 0.001 / 0.0001
Injection rate, **q (**m^3/sec.m)	50E-06 / 500E-06 / 5000E-06
Domain permeability, **k** (m/sec)	5.88E-08 / 5.88E-10 / 5.88E-12
In situ stress field (effective)	
Maximum, $\boldsymbol{\sigma_1}$ (MPa)	14
Intermediate, $\boldsymbol{\sigma_2}$ (MPa)	9
Minimum, $\boldsymbol{\sigma_3}$ (MPa)	3.7
Initial conditions	
Void ratio, **e**	0.333
Pore pressure (MPa)	1.85
Initial gap (perforation) - (m)	0.1

In this section the results to demonstrate the importance of the cohesive zone in modeling hydraulic fracturing in porous elastic continuum are presented. Furthermore, we will investigate the parameters that affect the numerical solutions

which include the fluid viscosity, the formation permeability, the formation compressibility and the injection rate. The numerical values of the input data upon which the numerical computations were all based are summarized in table (6.1). These parameters include the rock properties, the pumping parameters, the in-situ stress field and the initial conditions. In order to investigate the main characteristics of the cohesive zone law in the poroelastic models, a small parametric analysis has been conducted by changing the constitutive behavior of the cohesive zone to simulate the change from brittle to ductile behavior. The constitutive response of the rigid-softening corresponds to strong rock formations and the elastic-softening corresponds to soft rock formations. The value of the injection rate in these simulations was set in a constant pumping schedule. This feature will present the benefit of including any significant leak-off and diffusion, as well as any fracture fluid storage effects. In this manner the associated leak-off, diffusion and storage effects are incorporated and analyzed in detail in this chapter.

The properties of the cohesive zone are summarized in Table (6.2). These properties include the uniaxial tensile strength, the fracture energy which is the area under the traction-separation curve calculated to meet an equivalent fracture toughness of 2 MPa.m$^{1/2}$, the permeability of the elements and the parametrically investigated loading slope of the first branch of the cohesive constitutive law.

Table 6.2: Cohesive zone properties for the poroelastic models

Cohesive zone properties	
Uniaxial tensile strength, $\boldsymbol{\sigma_t}$ (MPa)	0.5
Loading stiffness $\boldsymbol{k_n}$ (MPa/m)	16200 / 81000/ 162000/ 324000
Fracture energy, $\boldsymbol{G_{IC}}$ (kPa.m)	0.224
Cohesive zone permeability $\boldsymbol{q_t}$ (m/sec)	5.88E-08 / 5.88E-10 / 5.88E-12

All the results presented next correspond to fractures at the state of propagation. The fractures were propagated from an initial length of 0.1 m to reach 9 m long. Figure (6.1) shows the half-width of a propagating fracture versus distance from wellbore in elastic (dashed line) and poroelastic (solid line) solids. The k_n (x5) mark in the figure means that the initial loading slope of the cohesive model was five times the one given in table (6.1). The fracture profiles were plotted for the first seven meters at different lengths for every 1m interval for clarity reasons. Each fracture profile corresponds to different pumping time. In figure (6.1) longer fractures and wider

profiles correspond to greater pumping times since the same injection rate was used for comparison of the results. It is evident that the poroelastic fracture is much wider than the elastic fracture. Furthermore, the fracture tip cusping in the poroelastic fracture is larger. What also appears from in figure (6.1) is that for short fractures (near wellbore) the cohesive zone is highly important to the overall hydraulic fracture solution while for long fractures this effect becomes less significant permitting the elastic solution to approximate the poroelastic.

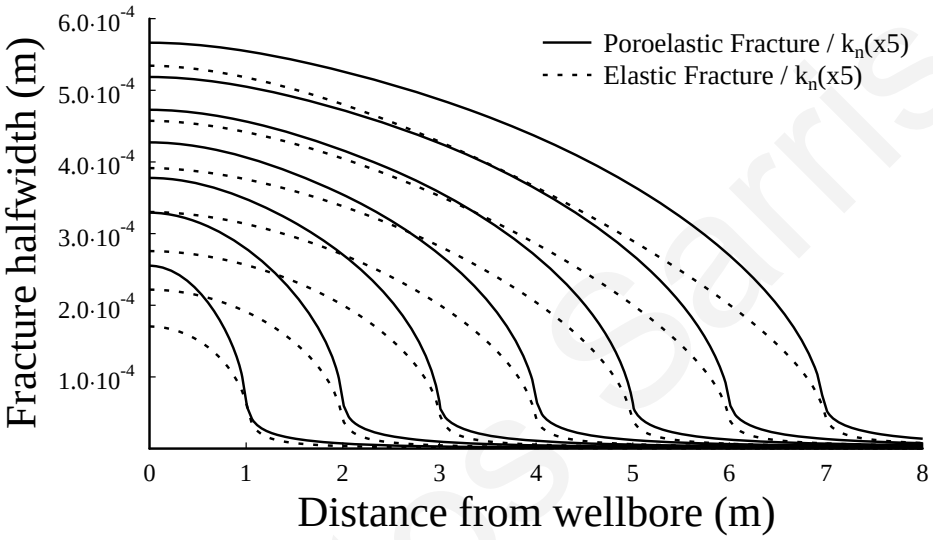

Figure 6.1: Comparison of elastic and poroelastic propagating fractures

Figure (6.2) shows the fluid pressures for propagating the above poroelastic fracture. The fluid pressures that drive the fracture are highly positive along the visible fracture. In the area far-ahead of the propagating tip, the fluid pressure approaches the value of the imposed initial pore-pressure condition. This is a direct result of the cohesive zone that is generated in front of the propagating fracture.

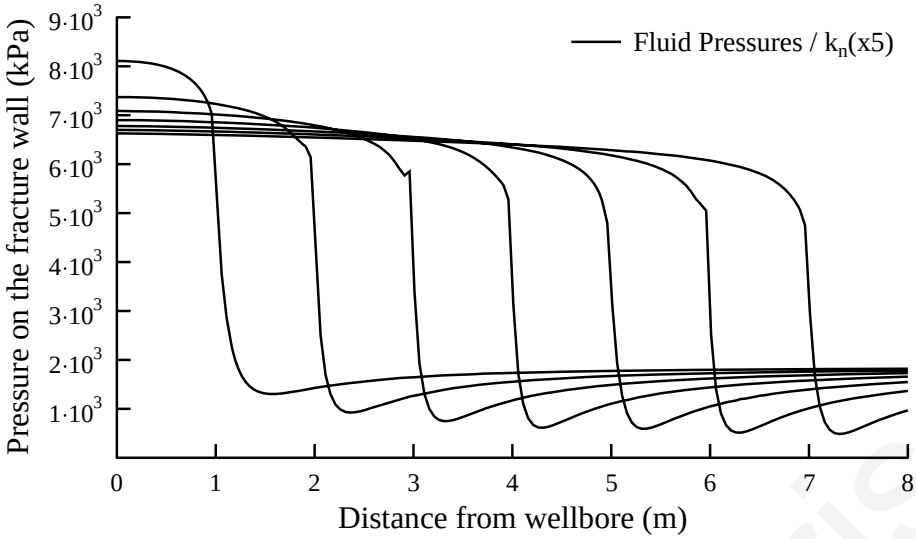

Figure 6.2: Fluid pressures for the poroelastic case

Figure (6.3) shows the net pressures that are needed to propagate the fractures for the elastic and porous-elastic media as the fracture grows. The net pressure is descending as the fracture propagates away from the wellbore and reaches almost a steady value few meters away from the wellbore. Higher pressures are needed to propagate the porous elastic than the elastic fractures. This difference is more pronounced in the area near the wellbore for short fractures. For short fractures the cohesive process zone is significant compared to the fracture length while as the fracture grows the process zone becomes insignificant to the fracture length.

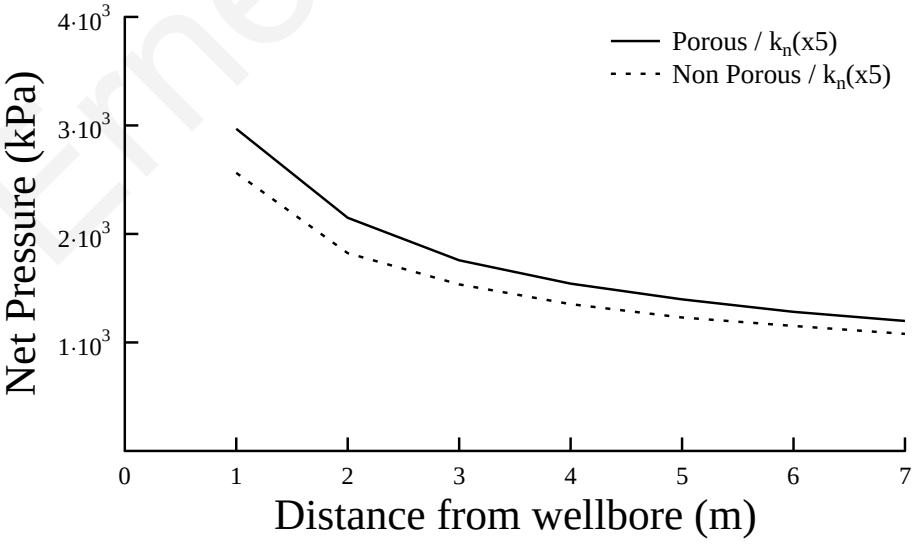

Figure 6.3: Comparison of porous and non porous net pressures

Figure (6.4) shows that the size of the cohesive zone that is created ahead of the visual fracture for the case of elastic-softening behaviour k_n (x5) for porous and non porous domains. The cohesive stresses where chosen to be plotted near wellbore so the choice for the 2m from wellbore is justified. The cohesive zone is larger in the poroelastic fracture which is also consistent with the difference in the fracture apertures (Figure 6.1). The large process zone that is observed in the poroelastic case is also consistent with the elevated net pressures that are observed in (Figure 6.3). Therefore, it is concluded that the net pressures needed to propagate fractures in cohesive mediums are proportional to the size of the created cohesive zone. When the size of the cohesive zone is relatively small the net pressure that is needed to propagate the fracture is comparable to the elastic case, even in the case of the poroelastic fracture.

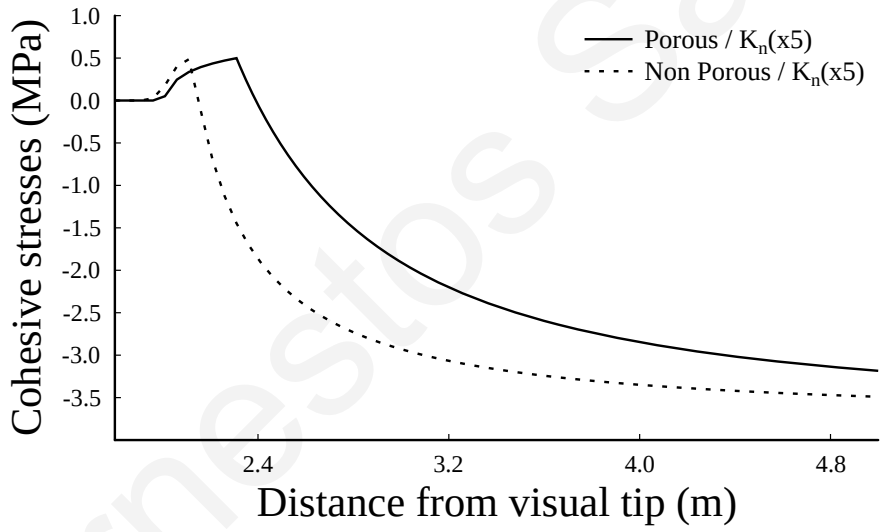

Figure 6.4: Comparison of porous and non porous cohesive stresses

Furthermore, when the cohesive medium that is considered obeys the elastic-softening constitutive behaviour k_n (x5), then the size of the created cohesive zone is consistently larger in the case of the poroelastic medium and the resulting net pressures that are needed to propagate the fracture in permeable medium are significantly larger compared to the impermeable medium.

6.4 Viscosity Dominated Regime Fluid-Driven Fractures in Impermeable and Permeable Cohesive Formations

In real hydraulic fracturing treatments significant energy is dissipated in the viscous fluid flow inside the fracture. It is then said that the hydraulic fracturing treatment falls in the viscosity-dominated regime. Hence, fracture growth in this regime does not depend only on the rock toughness and the leak off and it can be shown that the fracture aperture near the fracture front, when viewed at the scale of the whole fracture, is not characterized by the classical square root behavior predicted by linear elastic fracture mechanics. Furthermore, the dominance of viscous dissipation created conditions of small fluid lag (Bunger et al. 2007). The purpose of this analysis is to investigate the fracture profile, the fluid pressures and the resulting cohesive zones in the viscosity dominated regime and to reach a connection between the porous and non porous elastic fractures. In this analysis both fractures were driven with the same pumping schedule (constant injection rate) to correspond to an intermediate propagation velocity and for the same numerical value of built cake and domain permeability. The fractures were driven in an intermediate state of the rigid-softening and elastic-softening cohesive formation that corresponds to k_n(x10). The computations were initially carried out for a non porous fracture (named as D-dry) and later for a porous fracture (named as P-porous). The guidance of the numerical results in the viscosity dominated regime is succeeded by altering the value of the viscosity in the fluid rheology from 0.0001 to 0.1 kPa.sec.

Figure (6.5) presents the fracture profiles for the non porous fractures with different viscosities after reaching 1 m length. We found that a wider fracture profile is created when the impermeable fracture is driven with highly viscous fluid. We observed that the bulk fracture shape of highly viscous fluids is mainly different compared to the other cases examined. This is explained by the physical scaling of the problem in which the fracture propagation falls in the viscosity dominated regime. In this computation it appears that the toughness which affects the near tip area presents almost negligible influence on the fracture profile.

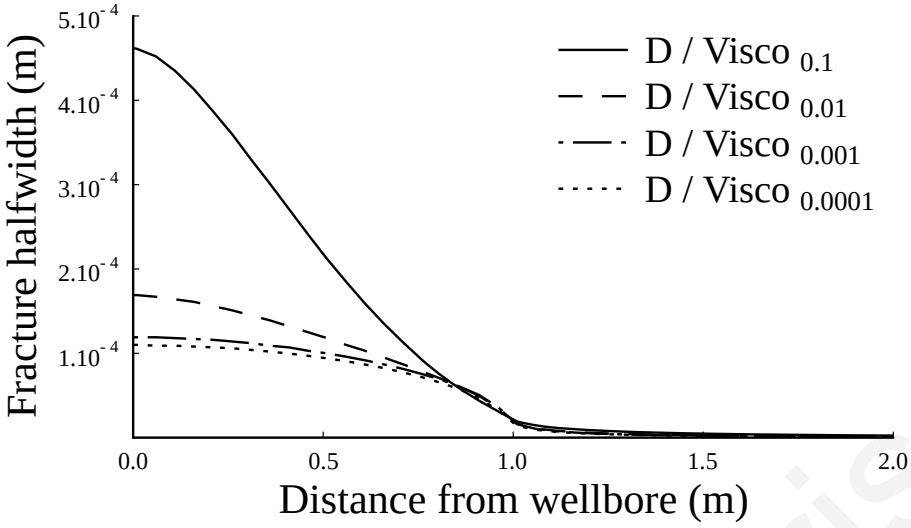

Figure 6.5: Comparison of impermeable fractures driven with different values of viscosity

Figure (6.6) presents the fluid pressures profile inside the fractures for the respective cases of figure (6.5). It is evident that the fluid pressure gradients that are created with the highly viscous fluids are much greater. This can be explained by the viscous nature of the fluid that was assigned. As the viscosity value of the viscous fluid becomes bigger, extreme non linear behavior is observed as a result of the fluid friction on the fracture walls that is resisting the fluid flow.

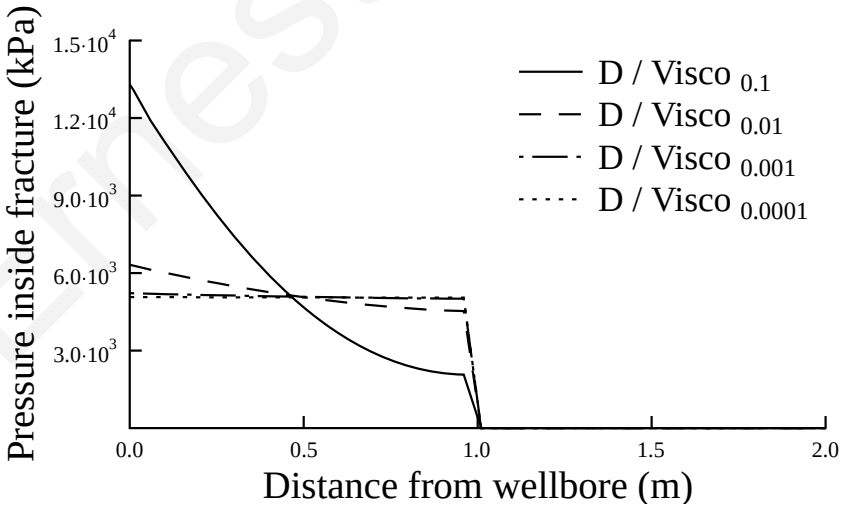

Figure 6.6: Comparison of fluid pressures for impermeable fractures driven with different values of viscosity

This non linear behavior of the fluid pressure profile is reduced as the value of the viscous fluid becomes smaller to reach the limit of constant pressure distribution in the fracture.

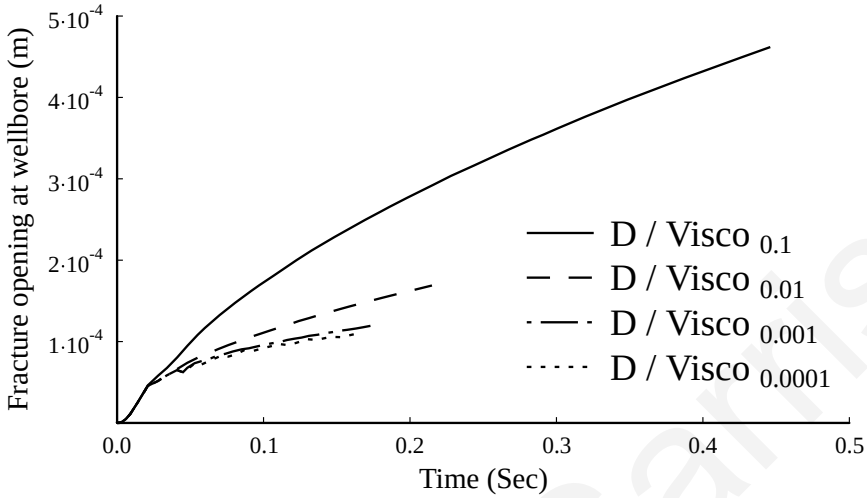

Figure 6.7: Comparison of impermeable fractures apertures at wellbore driven with different values of viscosity

Figure (6.7) presents the fracture opening at wellbore versus time for the impermeable fractures after reached 1 m from wellbore. The fracture openings at wellbore are in complete agreement with the fracture profiles presented in figure (6.5). Larger times are needed to extent the fractures at the same length with the highly viscous fluids. Particularly, for the same fracture length, double time is needed to extent the fracture when driven with highly viscous compared to the low viscous fracture fluids.

Figure (6.8) presents the comparison of net pressures at wellbore versus time for the impermeable fractures driven with different values of fluid viscosity. It is evident that larger net pressures are created when the fracture is driven with high viscous fluids. It is also seen that the net pressure behavior for the highly viscous fluids are completely different from the other cases examined. The usual behavior is that an increasing value of net pressure is build up to the point where the formation breaks down followed by a descending net pressure to a constant value where it represents the net pressure needed for fracture propagation. It is shown that the net pressures needed to breakdown the formation is almost the same for all fluid rheology examined, however the net pressure to extend the fractures appears to depend on the fluid viscosity.

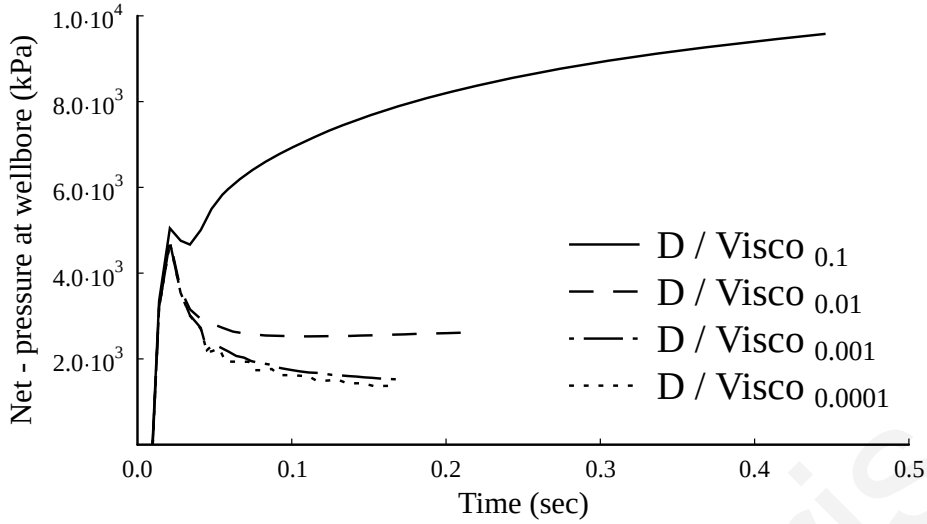

Figure 6.8: Comparison of net pressures at wellbore for impermeable fractures driven with different values of viscosity

Figure (6.9) shows the cohesive stresses created ahead of the visual fracture tip. It appears that significant larger fracture process zone is created when the fracture is propagated with a high viscous fluid.

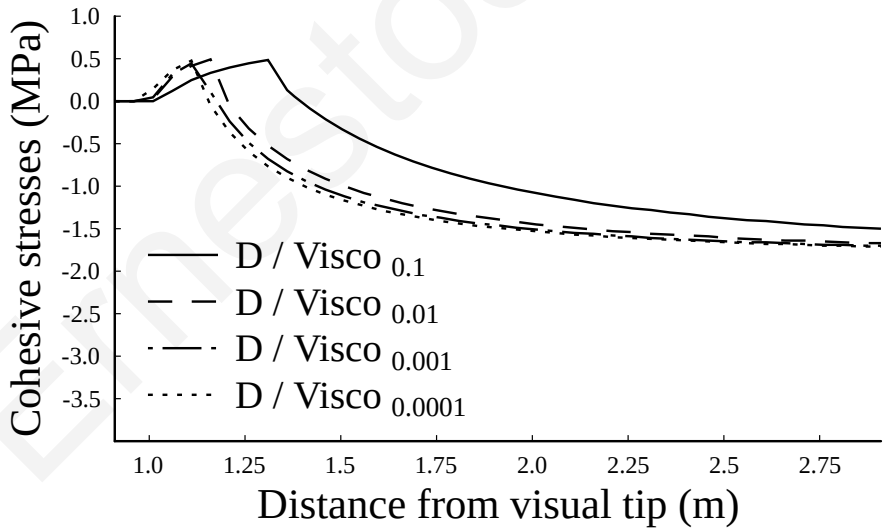

Figure 6.9: Comparison of cohesive zones in impermeable fractures driven with different values of viscosity

The results presented in figure (6.6) suggest that change in the viscosity of the fracturing fluid modifies the load distribution in the fracture walls. Therefore, load redistribution in the fracture results in different cohesive zone sizes. With high viscosity the bulk of the fracture is loaded more than the tip so wider fractures are

created and significant larger pressure is required to extend the fracture. From an energy point of view, when examining fluid driven fractures in impermeable formations, most of the energy is dissipated in viscous fluid flow and the numerical solution falls in the viscosity dominated regime, suggesting the increase of loading inside the fracture thus creating larger fracture process zones. Likewise, with reducing the viscosity in the fluid rheology, the numerical computations suggest that the fracture toughness regime dominates in the HF problem.

To investigate further the viscosity dominated regime in hydraulic fracture treatments, it is natural to extend the previous analysis of impermeable fractures to the case where the fracture is driven in permeable formation within the context of poroelasticity. This introduces an extra dissipative mechanism which is the fluid losses or the leak off regime (the process where energy is dissipated in the fluid losses).

Figure (6.10) presents the fracture profiles for the fractures driven with different viscosities in permeable medium. Figure (6.10) shows that wider fracture profile is created when the permeable fracture is driven with high viscous fluid. If this fracture width is compared to the one which was created in the impermeable case we observed that the profile is even wider when the fracture is driven in the permeable medium. We observe again that mainly the bulk of the fracture shape with high viscous fluids is different compared to the other cases examined. It is also observed that the fracture created with the two lower values of fluid rheology (low viscous fluids) present very similar behavior. This is explained by the constant pressure distribution in the fracture and the diffusion process. For these lower values of viscosity, the fracture fluid is able to diffuse in the surrounding domain and the created fractures are almost identical.

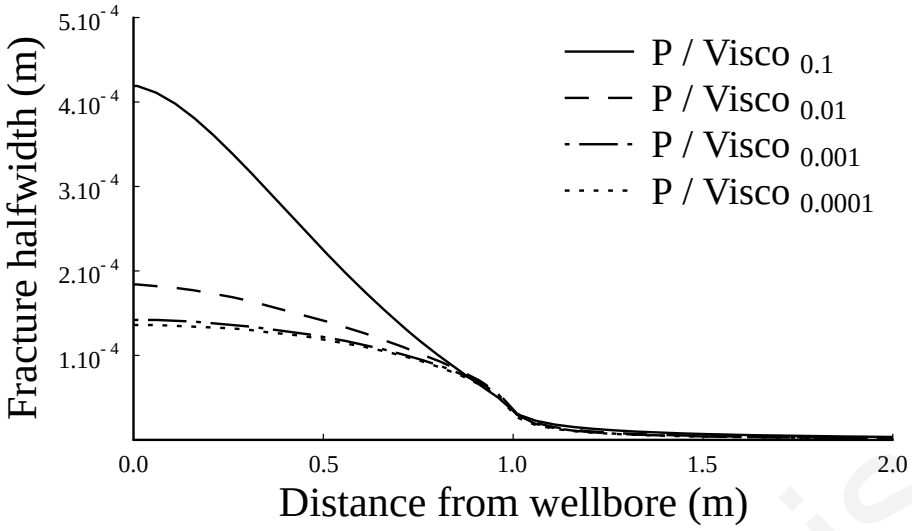

Figure 6.10: Comparison of permeable fractures driven with different values of viscosity

Figure (6.11) presents the fluid pressures profile inside the fractures for the respective cases of figure (6.10). It is evident that behind the fracture tip, the fluid pressure gradients that are created with the highly viscous fluids present a highly non uniform pressure distribution. At the position of the tip, severe under pressure is created suggesting that suction may take place from the formation. Ahead of the position of the fracture tip, the pressure reaches the value of the pore pressure that has been assign as initial condition. This behavior of the pressure profile can be explained by the viscous nature of the fluid.

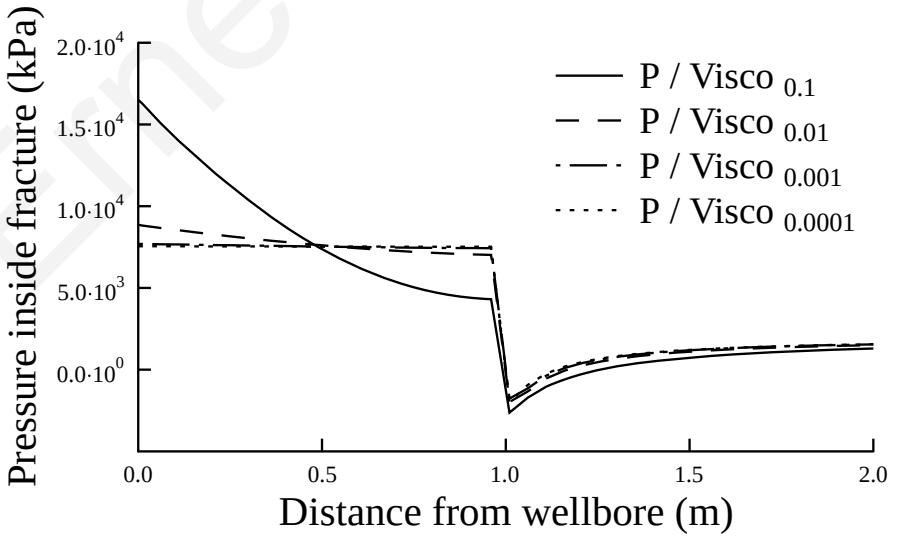

Figure 6.11: Comparison of fluid pressures for permeable fractures driven with different values of viscosity

As the viscosity value becomes bigger, extreme non uniform pressure distribution is observed as a result of the fluid friction on the fracture walls that is resisting the fluid flow. As the viscosity is reduced the fluid pressure becomes constant along the fracture. This is explained by the fact that most of the energy is dissipated in the viscous fluid flow and the fracture toughness becomes less significant in the numerical computations when the viscosity is large. For the two lower values of the fluid rheology (low viscous fluids) the fluid is able to diffuse in the surrounding domain and the behavior of the pressure profiles is almost identical. From the energy point of view, this means that for these cases, some of the internal energy of the system is dissipated in the leak off process and it is concluded that the leak off dominated regime becomes significant for low values of fluid viscosity as the diffusion process becomes important to the poroelastic problem.

Figure (6.12) presents the fracture opening at wellbore versus time for the permeable fractures after reaching 1 m length from wellbore. The fracture openings at wellbore are in complete agreement with the fracture profiles presented in figure (6.10). It is seen that wider profiles are created when the fracture is driven with the highly viscous fluids. Furthermore, the fracture openings at wellbore that are created with the low values of fluid rheology present identical behavior. What is also observed, as with the impermeable cases, is that larger times are needed to extent the fractures at the same length with the highly viscous fluids.

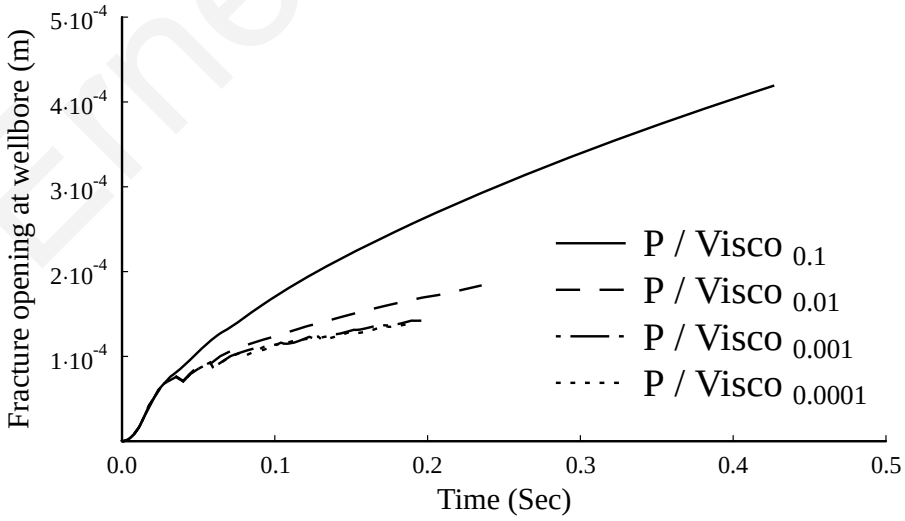

Figure 6.12: Comparison of permeable fractures apertures at wellbore driven with different values of viscosity

Particularly, for the same fracture length, double time is needed to extent the fracture when driven with highly viscous compared to the low viscous fracture fluids even in the permeable case.

Figure (6.13) presents the comparison of net pressures at wellbore versus time for the permeable fractures driven with different values of fluid rheology. It is evident that larger net pressures are needed when the fracture is driven with high viscous fluids. It is also seen that the net pressure behavior for the highly viscous fluids are completely different from the other cases examined. In hydraulic fracturing treatments in permeable formations the usual behavior is that an increasing value of net pressure is build up to the point where the formation breaks down followed by a descending net pressure to a constant value where it represents the net pressure needed for long fracture propagation. It is shown that the net pressures needed to breakdown the formation is almost the same for all fluid rheology examined, however the net pressure presents an increasing non linear behavior to a constant value after the formation breakdown. We note here that the used model does not really models the formation breakdown process as it assumed that pressurization and propagation starts from a short fracture with length approximately equal with the perforation length.

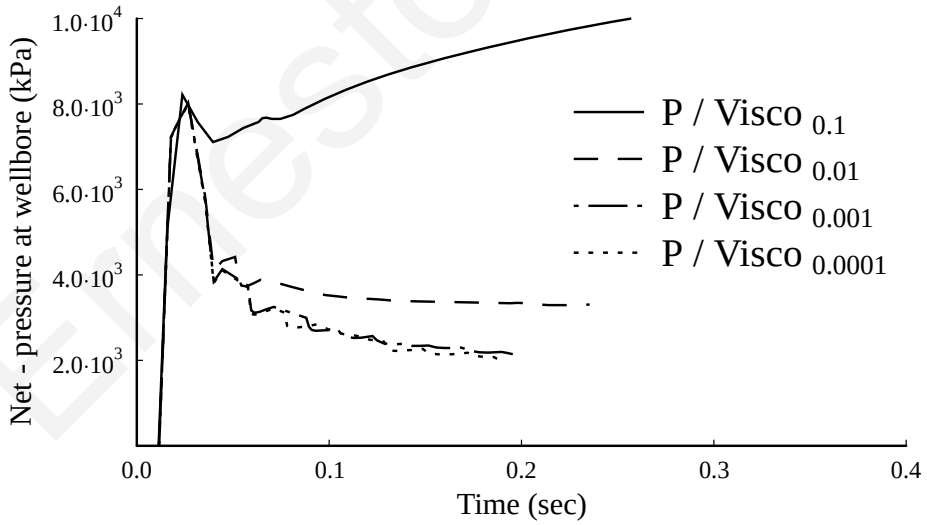

Figure 6.13: Comparison of net pressures at wellbore for impermeable fractures driven with different values of viscosity

The conclusion outlined here is that behavior of the net pressures needed to breakdown the formation and propagate the fracture in the permeable case is identical with the impermeable case. With increasing viscosity in the fluid rheology of the

fracturing fluid, the net pressures needed to extend the fracture are highly non uniform in the fracture and elevated at the wellbore and as a result the fracture profiles that are created are significantly larger mainly at the bulk of the fracture.

Figure (6.14) shows the cohesive stresses created ahead of the visual fracture tip for the fractures driven in permeable formations. It is seen that significantly larger fracture process zone is created when the fracture is propagated with the high viscous fluids. When compared to the impermeable process zone, the cohesive zone that is created in the permeable case is even larger. Examining the internal energy of the system, when driving fractures with highly viscous fluids in permeable formations, most of the energy is dissipated in viscous fluid flow and the numerical solution falls in the viscosity dominated regime, suggesting the increase of loading on the bulk of the fracture thus creating larger fracture process zones at the state of propagation. Likewise, with reducing the viscosity in the fluid rheology, the numerical computations suggest that fluid losses become important and the energy is dissipated in the leak off (diffusion) process which changes the obtained numerical results of the fracture width and shape, the net pressures, the opening at wellbore and pressure at wellbore as a function of both distance from wellbore and time.

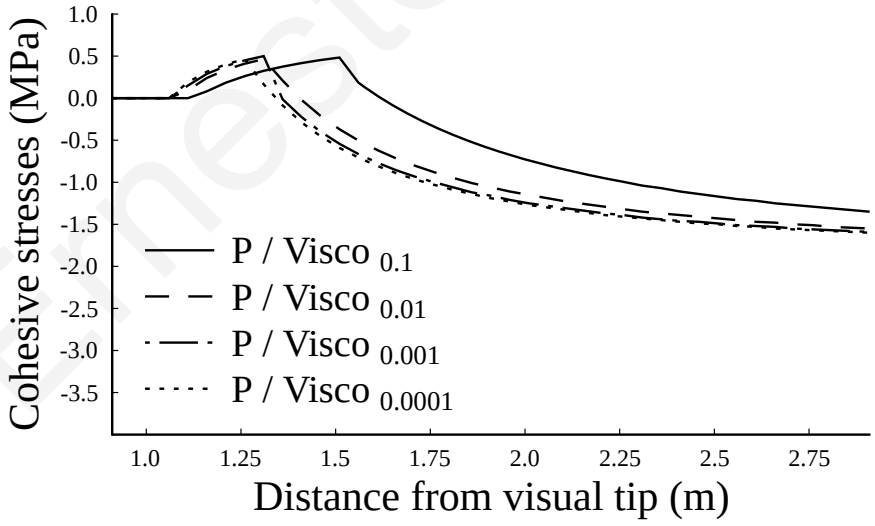

Figure 6.14: Comparison of cohesive zones in permeable fractures driven with different values of viscosity

The conclusions found by this analysis is of paramount importance in hydraulic fracture treatments as the diffusion process and the fluid losses in highly permeable rock formations are completely cancelled with appropriate selection of highly viscous

fluids to fracture the reservoir. The fracture profiles are wider, the fluid pressure profiles are larger and no fluid losses are observed in these cases. Furthermore, the cohesive fracture process zone that is created is significantly larger as a direct result of the equivalent fluid loading which is obtained with the increase of the fluid viscosity. However, the numerical simulators for predicting the net pressure needed to breakdown and extend the fracture must be capable in dealing with severe non uniform pressures to reach accurate conclusions.

6.5 The Influence of Formation Permeability

Previous research works have outlined the importance of hydraulic fracturing in porous and fluid saturated domains. In these research works, the numerical solution was governed by the formation permeability and the propagation velocity (Detournay and Garagash 2003). However, their research work was focus on the fluid lag and a near tip area. In this work, numerical simulations have been performed to investigate the influence of permeability on the pressure gradients and the created cohesive zone size. For this reason, two extreme numerical values which correspond in a highly permeable and a low permeable rock formation have been chosen (table 6.1). The rock formation was considered to be incompressible and in order to keep the parameters affecting the solution to a minimum a pumping schedule with increasing constant rate was selected.

Figure (6.15) presents the fracture apertures of a propagating fracture in a poroelastic medium. The fracture was left to propagate up to 5m so as to avoid any boundary effect problems. The fracture apertures were calculated for the elastic-softening k_n (x1) constitutive laws .As it can be seen the fracture aperture is wider in the case where the formation is highly permeable.

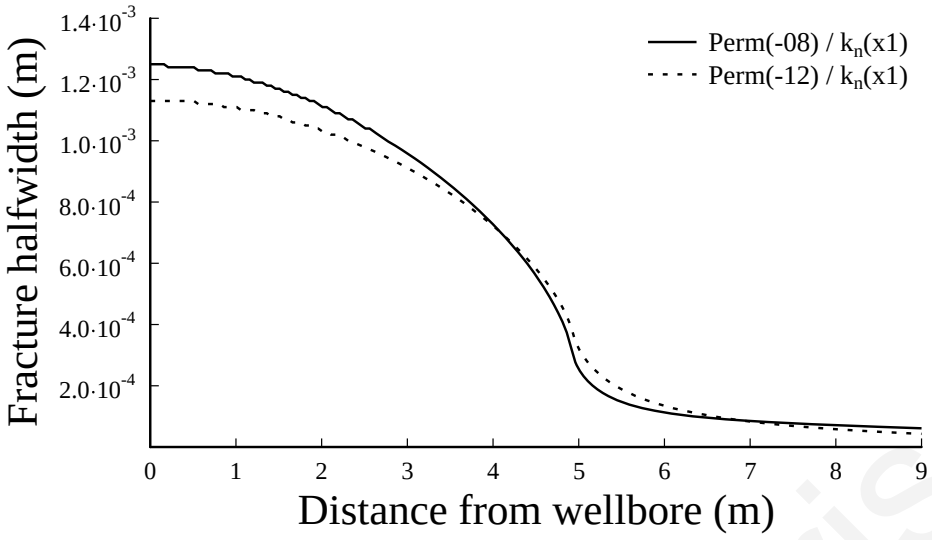

Figure 6.15: Comparison of porous fractures with different permeabilities kn (x1)

Figure (6.16), presents the fluid pressures needed to propagate the fracture for the respective fracture apertures of figure (6.15). It appears that the fluid pressures are larger in the case of the highly permeable rock formation. We observe in the area in front of the tip of the propagating fracture that the redistribution of the pore pressure field descends abruptly and it tends to the far field initial condition of pore pressure that was considered in the simulations.

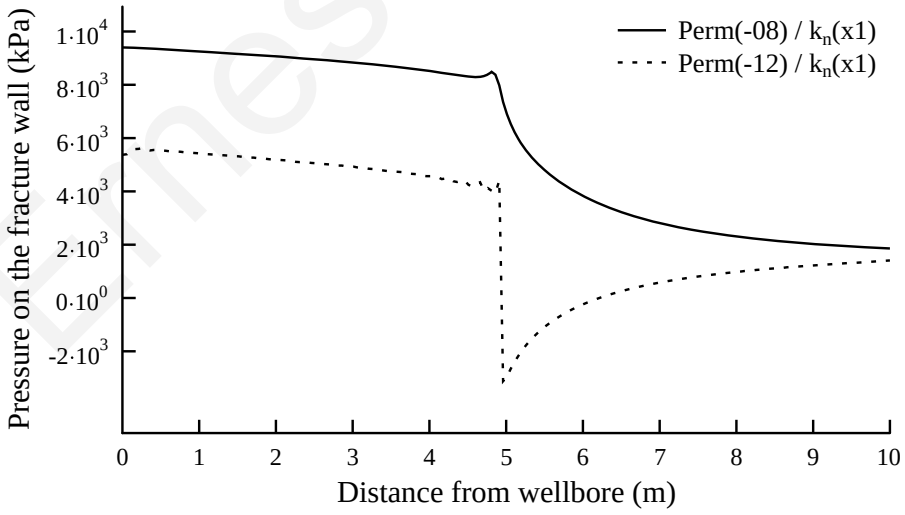

Figure 6.16: Comparison of porous fluid pressures with different permeabilities kn (x1)

For the case of highly permeable rock formations the fracture fluid has intruded significantly in the cohesive zone and due to both, the slow increasing injection rate and the highly permeable rock formation, the fluid had enough time to diffuse

(invade) in the formation hence increasing the pressure formation and creating in its turn the wider fracture apertures.

A further examination of the fluid pressures shows that for the case of low permeable rock formation in the area in front of the tip of the propagating fracture, the redistribution of the pore pressure field presents, a highly negative sign where the fluid front is found to be. From that point it ascends to the far field initial condition of pore pressure that was considered in the simulations. In this case even the low injection rate that was imposed to correspond to slow fracture propagation did not provide the time for the fluid to invade in the rock formation that was practically impermeable thus creating negative pore pressure at the fluid front position. This is of course responsible for the creation of larger cohesive zone sizes. Furthermore, such highly negative signs in the fluid pressures may also imply that suction takes place in the near tip area of the propagating fracture.

Figure (6.17) presents the cohesive stresses in front of the visual fracture tip for the constitutive behaviour examined for both types of rock formations (highly permeable and low permeable). Larger cohesive zones are created in the case where the rock formation is considered with low permeability.

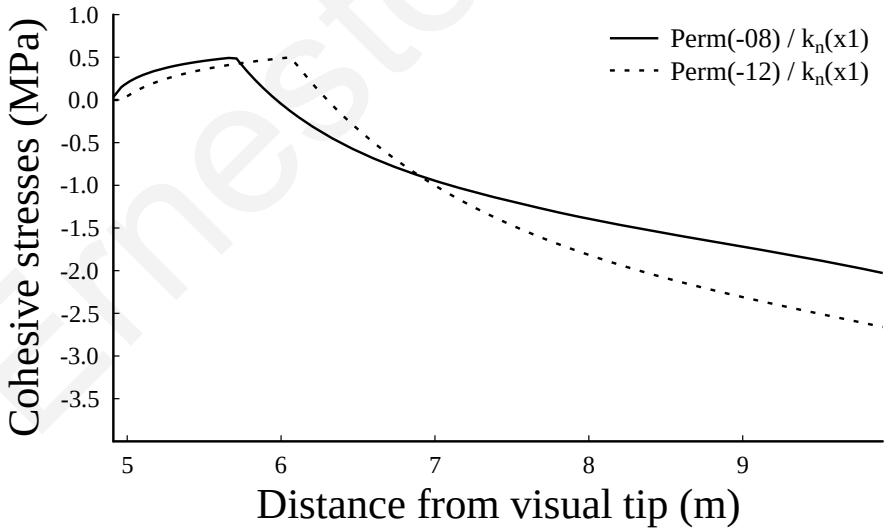

Figure 6.17: Comparison of cohesive stresses with different permeabilities kn (x1)

From the above analysis it is found that when propagating in highly permeable and soft rock formations, the fracture fluid invades the process zone and as a result, wider fracture apertures are created and larger fluid pressures are needed to extend the fractures, however, smaller process zone is created as a direct result of the fluid

invasion in the process zone. Likewise, when fluid driving a fracture in low permeable and soft rock formations, the fracture fluid does not invade the process zone and as a result, narrow fracture apertures are created and smaller fluid pressures are needed to extend the fractures, however, larger process zone is created as a result of the fracture process in the rock formation. From the energy point of view, when a fracture is driven in highly permeable and soft rock formation, energy is dissipated in the leak off dominated regime thus explaining the elevated fracture pressures that are observed and the resulting wider fractures. However, the rest of the energy available to dissipate from the system is to fracture the formation (fracture toughness dominated regime) and the fracture process zone that is created is smaller. Additionally, when a fracture is driven in low permeable and soft rock formation, significantly lower amount of energy is dissipated in the leak of dominated regime because the fluid is not allowed to diffuse in the formation or in the cohesive zone thus the fracture pressure that is needed to extend the fracture is lower and the resulting fracture aperture is narrower. In this case, the rest of the energy available to dissipate into fracturing the formation (fracture toughness dominated regime) creates larger fracture process zone.

To further analyze the influence of the formation permeability numerical simulations have also been performed to investigate the influence of permeability on hard rock formations. As in the previous analysis, two extreme numerical values to correspond in a highly permeable and a low permeable rock formation have been chosen (table 6.1). The rock formation was considered to be incompressible with a constantly increasing pumping schedule. The following results regard the fluid driven fracture in highly permeable and low permeable hard formations.

Figure (6.18) presents the fracture apertures of a propagating fracture in a poroelastic medium. The fracture was left to propagate up to 5m. The resulting fracture apertures are from the constitutive laws of rigid-softening k_n (x20). As it can be seen the fracture aperture for this constitutive behaviour of rigid – softening is significantly wider in the case where the formation is highly permeable. Figure (6.19), presents the fluid pressures needed to propagate the fracture for the respective fracture apertures of figure (6.18).

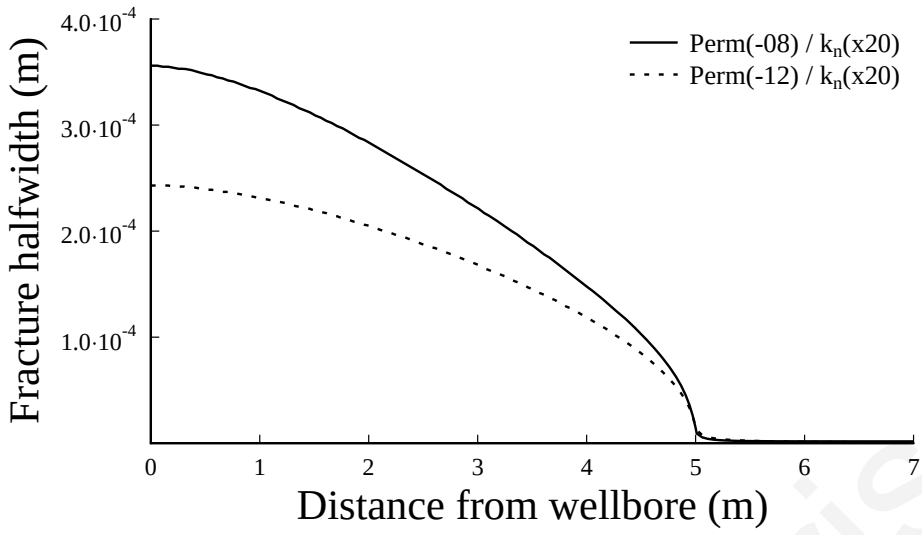

Figure 6.18: Comparison of porous fractures with different permeabilities kn (x1)

It appears that the fluid pressures for the constitutive behaviour examined (rigid-softening), are larger in the case of the highly permeable rock formation. Observing the near tip area in front of the propagating fracture it is seen that the redistribution of the pore pressure field, in both constitutive cases presents, a smooth descending trend to the initial condition of pore pressure that was considered in the simulations. This, as in the previous analysis, has the meaning that that the fracture fluid has intruded significantly in the cohesive zone and due to both, the slow increasing injection rate and the highly permeable rock formation, the fluid had enough time to diffuse (invade) in the formation hence increasing the formation pressure and creating in its turn the wider fracture apertures for the case of highly permeable rock formations.

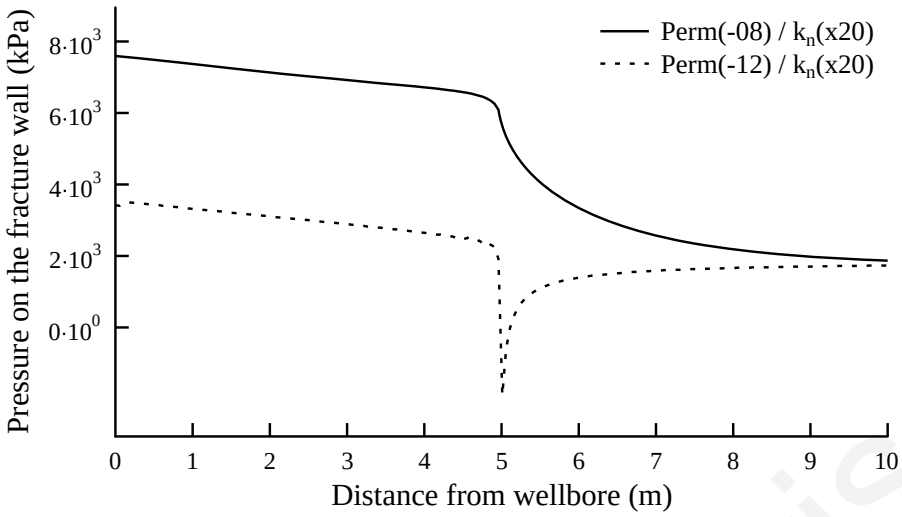

Figure 6.19: Comparison of porous fluid pressures with different permeabilities kn (x20)

Further examination of the fluid pressures reveals that for the case of low permeable rock formation the redistribution of the pore pressure field presents, a highly negative sign where the fluid front is found to be. From that point it ascends to the initial condition of pore pressure that was considered in the simulations. As in the previous analysis, even the low injection rate that was imposed to correspond to slow fracture propagation did not provided the time for the fluid to invade in the rock formation that was practically impermeable resulting in negative pore pressure at the fluid front position. Such highly negative signs in the fluid pressures also imply that suction takes place in the near tip area of the propagating fracture. This suction is of course related to the creation of larger cohesive zones.

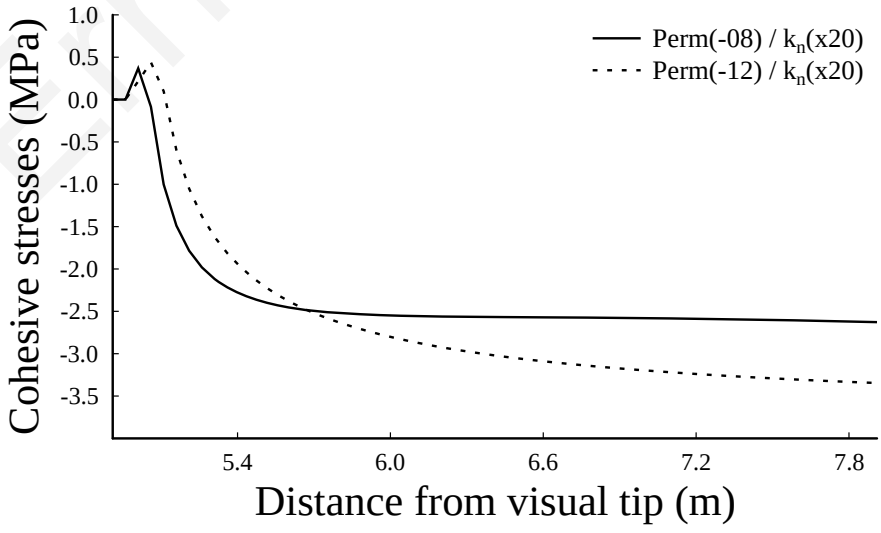

Figure 6.20: Comparison of cohesive stresses with different permeabilities kn (x20)

Figure (6.20) presents the cohesive stresses in front of the visual fracture tip for the constitutive behaviour examined (rigid-softening) for both types of rock formations (highly permeable and low permeable). Figure (6.20) shows that larger cohesive zones are created in the case where the rock formation has lower permeability. However, in both cases examined as in the dry cases the rigid softening behaviour results in smaller process zones.

Continuing the analysis in the energy dissipation, a small comparison is made between the soft and hard formations. When driving a fracture in soft rock formation k_n (x1), the difference in the fracture profiles between a highly permeable and low permeable formation is 13.18 % while in the fluid pressures the difference is 39.79 %. Likewise, when driving a fracture in hard rock formation k_n (x20), the difference in the fracture profiles between a highly permeable and low permeable formation is 28.57 % while in the fluid pressures the difference is 51.28 %. At this point it is considered important to mention that these percentages are material dependent. They are used only in the interpretation of the computational results. From the above numerical percentages it is concluded that when driving the fracture in hard rock formations, the fracture toughness mechanism dominates and most of the available energy of the system is expended in creating new fracture surfaces. In the opposite case of a fracture driven in a soft formation, the leak-off mechanism dominates and significant energy is dissipated in the fluid losses. This leads to the conclusion that higher pressures are needed to breakdown and propagate the fractures when the diffusion process is dominant in a hydraulic fracture treatment. Furthermore, the energy that is dissipated in the leak-off process when propagating in the soft rock formation is transferred in the viscosity dominated regime (fluid loading) when propagating in the hard rock formation thus explaining the observed elevated fluid pressures to propagate the fracture.

The above analysis is based in the energy that is dissipated in all the processes in the fluid driven fracture propagating in a permeable formation. These processes include the fracture toughness energy dissipation, the viscosity energy dissipation and the leak off energy dissipation. The energy that is required to create the fracture process zone (cohesive energy) appears to be another form of dissipative energy that contributes in the obtained results. This rises from the examination of equation (2.5) which describes the internal energy of the system in the conservation of the energy law.

6.6 Influence of the Propagation Velocity of Fluid-Driven Fractures in Poroelastic Cohesive Formations

For the complete investigation of the parameters that affect the fluid driven fracture in porous continuum, a parametric simulation has been conducted to investigate the influence of the propagation velocity in the numerical solution. As mentioned before the fracture propagation in poroelastic media is governed by the formation permeability and the propagation velocity (Detournay and Garagash, 2003). In the previous analysis we presented a study on the influence of the permeability on the pressure gradients and the created cohesive zone size. In trying to isolate the mathematical problem from other parameters affecting the numerical solution the analysis regarding the propagation velocity is restricted to the case of rigid-elastic k_n (x20) constitutive cohesive law. As shown before this constitutive behaviour creates small size of process zone. By obtaining a relatively small process zone size (i.e. negligible) this enables the analysis of the influence of propagation velocity on both fracture dimensions and pressure profiles. For an impermeable formation it is expected that the propagation velocity is directly linked to the injection rate. The numerical value of the permeability was changed to correspond to a relatively permeable rock formation. Three different values of injection rates to correspond to slow, intermediate and fast fracture propagation were chosen to investigate the influence on the fracture dimensions and net pressures.

Figure (6.21) presents the fracture aperture of a propagating fracture with different injection rates which correspond to slow, intermediate and fast propagation velocity in a poroelastic medium. The fracture was left to propagate up to 4m so as to allow the fracture and the fluid pressures to evolve in time (no early time solution) and space. As it can be seen the resulting fracture aperture is wider for the fast propagation followed by the fracture that was propagated with intermediate velocity and finally the fracture that was propagated with slow velocity.

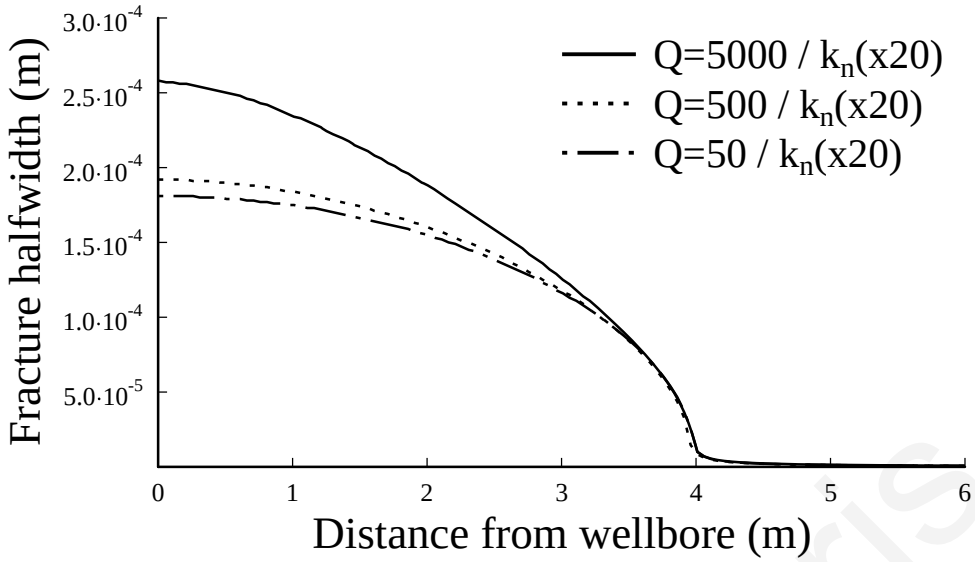

Figure 6.21: Comparison of porous fractures for different injection rates

Figure (6.22) presents the fluid pressures needed to propagate the fractures with the different velocities for the respective fracture apertures of figure (6.21). The fluid front is found to be where the fluid pressures changes sign. It is observed that in front of the propagating fracture in a near tip area there is a highly negative value of fluid pressure for all propagation velocities. This has the physical meaning of pore fluid suction that takes place during the fracture propagation. It appears that the fluid pressures are slightly larger in the area near the wellbore in the case of the fast propagation velocity.

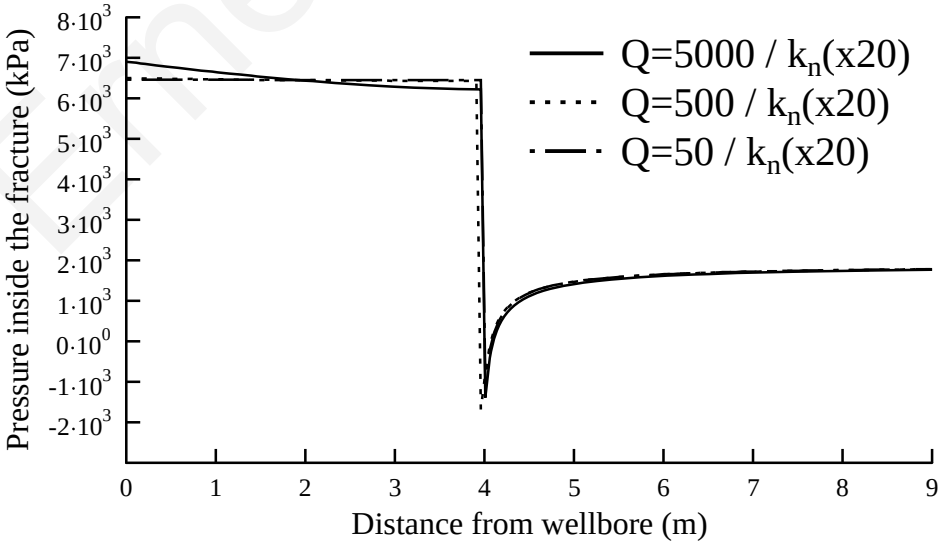

Figure 6.22: Comparison of porous fluid pressures for different injection rates

Despite the small differences in the propagation pressures the obtained width profile for the slow propagation case is narrower mainly due to the developed back stresses in the body of the fracture.

Figure (6.23) shows the fracture apertures at wellbore versus time. The fractures were propagated up to 4 m long. The fracture that is driven with fast propagation velocity results in significantly wider apertures at wellbore, followed by the by the fracture that was propagated with intermediate velocity and finally the fracture that was propagated with slow velocity.

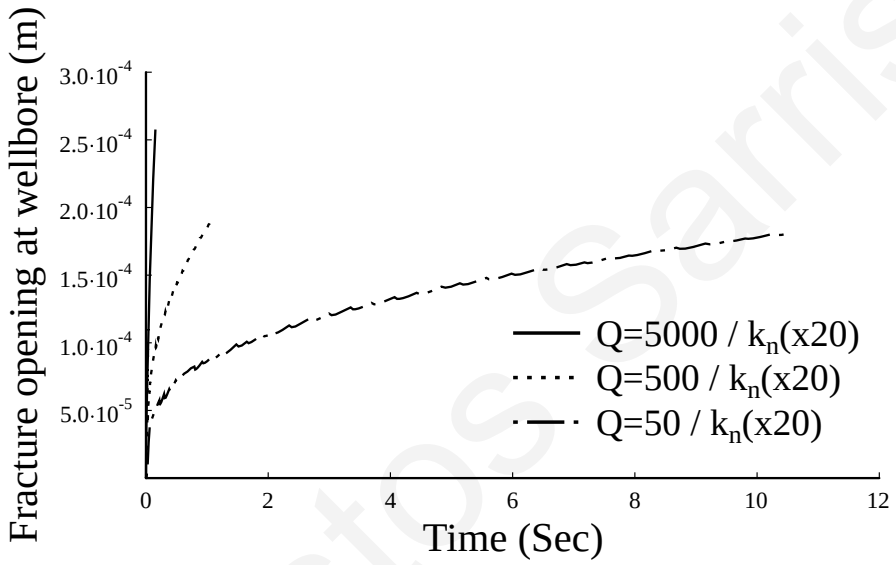

Figure 6.23: Comparison of porous fracture apertures at wellbore for different injection rates

What is interesting in figure (6.23) is the time that is needed for the fracture to reach the desired distance of 4 m in length. It is evident that the fracture that is driven with slow propagation velocity needs more time to reach the desired fracture length. Despite the greater fracture volume in the case of high injection rate, the injection rate is more dominant resulting in much smaller time to reach the same fracture length as in the other two cases. Furthermore, significant amounts of fracture fluids are leaking off in the formation in the case of low injection rate.

Figure (6.24) presents the cohesive stresses that are created ahead of the visual fracture tip. It is evident that the cohesive zones when the fractures are driven with different velocities in hard rock formations remain unaffected. For the constitutive case of elastic-softening it is expected that a small difference will exist for all types of propagation velocities.

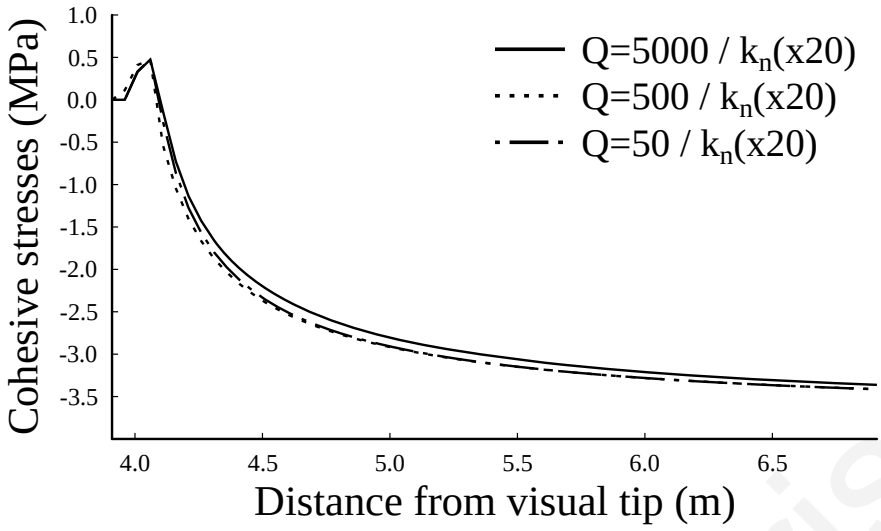

Figure 6.24: Comparison of cohesive stresses for different injection rates

The conclusion that is found here is that for early times of injection, the plane strain fracture in poroelastic and hard rock formation dissipates most of the internal energy of the system in fracturing the formation therefore the fracture toughness scaling dominates for all propagation velocities. When the fracture is driven with fast propagation velocity (negligible fluid losses) and the propagation time evolves to large, energy dissipation is observed in the viscous fluid flow thus explaining the non uniform behavior of the fluid pressure inside the fracture for fast propagation. For slow propagation velocity, as the propagation time evolves, significant energy is dissipated in the fluid losses thus the leak off scaling and diffusion dominates and as a result the fracture fluid invades the formation and is stored in the surrounding medium increasing the pressure. The fluid diffusion results in back stresses on the fracture walls thus it should be expected that the fluid pressures at wellbore will be elevated when the fracture is driven slowly and the fracture profile will be narrower.

Summarizing all the above results obtained with the analysis of the parameters that affect the poroelastic problem, the following physical model is proposed to partly explain the discrepancies between the net pressures encountered in the field and conventional numerical simulators. The initial work of Garagash (1998), later extended by Adachi (2001) are further extended in this work with the numerical solution of the fluid driven problem in permeable formations with cohesive type fracture tip and permeable fracture walls. Figure (6.25) presents the numerical solution of the pressure field of a plane strain fluid driven fracture propagating in

permeable formation. It is seen that a large fan of negative values is observed above the propagating fracture tip suggesting pore fluid flux and suction from the fracture process zone. This fluid is returned to the porous formation behind fracture which is stored in the invasion zone together with the fluid that is leaking off from the fracture into the formation. In this manner the diffusion process is enhanced over the fracture walls. This fracture and pore fluid accumulation has a negative effect in the hydraulic fracturing treatment as back stresses are created above the fracture walls which result in elevated net pressures to propagate the fracture to large lengths and to obtain the desired fracture dimensions.

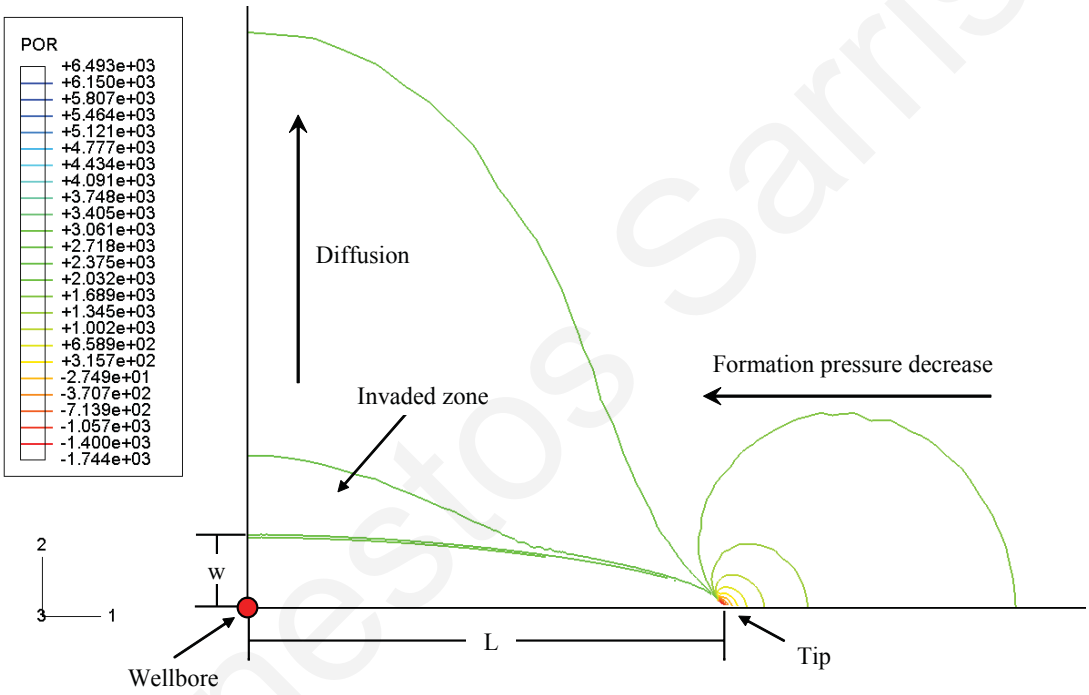

Figure 6.25: Numerical solution of the pressure field of a plane strain fracture driven in permeable formation

According to the above analysis based on the numerical solution, the following stages for explaining the physical processes for a fluid driven fracture propagating in a permeable formation (figure 6.26) are proposed for explaining the elevated net pressures. After creating large pressure gradients at wellbore, the formation breaks down and significant under pressure is generated as a result of the fracture process zone that is created. In this process, energy is dissipated for creating new surface area and the fracture toughness dominates in the physical model (element 1). When the fracture is driven in permeable fully saturated continuum, this under pressure triggers pore fluid flux towards the fracture tip and suction takes place in the fracture process

zone. The fluid flux is circulated from the near area of the tip and is expelled immediately behind the fracture tip where the fluid front coincides with the visual tip. Pore fluid must necessarily be returning to the porous rock as it would otherwise cause an increase of the process zone and this would cause the propagating fracture to retard. With the immediate returning of the pore fluid to the porous continuum it is diffusing behind the advancing fracture and it is stored above the fracture walls (element 2). As the fracture propagation evolves, fracture fluid losses become significant and the fluid is largely invading the formation (element 3) and together with the pore fluid storage (element 2) are enhancing the diffusion process in the porous formation causing significant back stresses on the fracture walls. These two mechanisms are causing the net pressures to increase in order to overcome both the confining insitu stress and the fluid storage that is created from the suction and the leak off process.

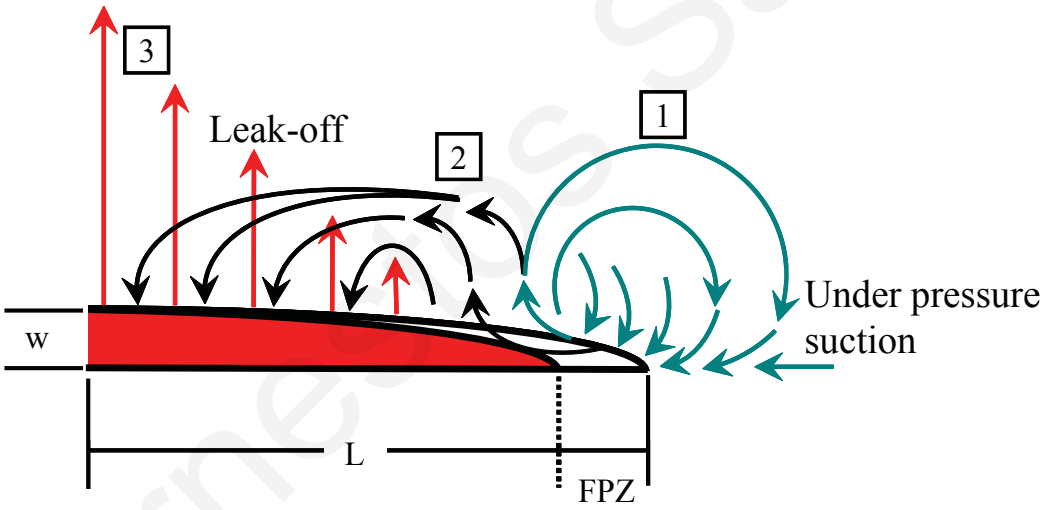

Figure 6.26: Different stages of the processes affecting the net pressure for propagating a fluid driven fracture in permeable formation

These three stages of the physical model described here explain at some extend the discrepancy between the highly elevated net pressures that are encountered in the field and conventional numerical simulators.

6.7 Influence of the Bulk Modulus or Compressibility in Poroelastic Cohesive Formations

For a further analysis of the porous continuum, a parametric analysis has been conducted on the influence of the compressibility of the rock formation. The grain compressibility is defined as the ratio of a fractional volume change with respect to a pressure change. According to Zimmerman et al., (1986) any volume change (i.e. bulk volume, pore volume, fluid volume or solid grain volume) with respect to a pressure change can result in an extra volumetric strain in the poromechanical system of equations. This has been the motivation behind this parametric analysis. The description of the volumetric response of the porous solid is given by the volume of the solid phase and the formation porosity. These two parameters describe effectively the volumetric deformation of the solid phase which can be considered the local relative deformation of the pore grains in this phase. By changing the values of the bulk modulus of the solid grains, only in a small range of values according to Detournay and Cheng (1993), an extra volumetric strain is then induced by the term $-\left(p_f / K_g\right)$ which rises in equation (3.34). This volumetric strain represents the part of the total volumetric strain caused by pore pressure acting on the solid matter in the porous continuum. At this point it is worth noting that the additional volume change ratio caused by the entrapment of liquid and fluid compressibility was not considered as attention was focused in the grains compressibility.

In the simulations described hereafter, the compressibility of the solid grains is considered only and the numerical values were selected from the literature (Detournay and Cheng 1993) to correspond in soft rock, hard rock and incompressible rock. At this point it is noted that the fluid rheology was considered incompressible with Newtonian rheology. The influence of the fluid compressibility it is considered that it would not influence significantly the pressure gradients.

Figure (6.27) presents the comparison of poroelastic fracture profiles that correspond to soft, hard and incompressible rock formations. For simplicity, the constitutive behaviour of the cohesive zone that obeys the elastic-softening was only considered as it is the case where the deference is expected to be larger. The fracture tip was chosen to be 3m away from wellbore. From figure (6.27) it is seen that the fracture corresponding to the soft rock formation is wider than the other two fractures. This observed small difference was expected and it is attributed to the fact that the

grain compressibility values that were chosen have a narrow span for a physical meaning and not extreme unrealistic values for the purpose of the simulation (Table 6.1).

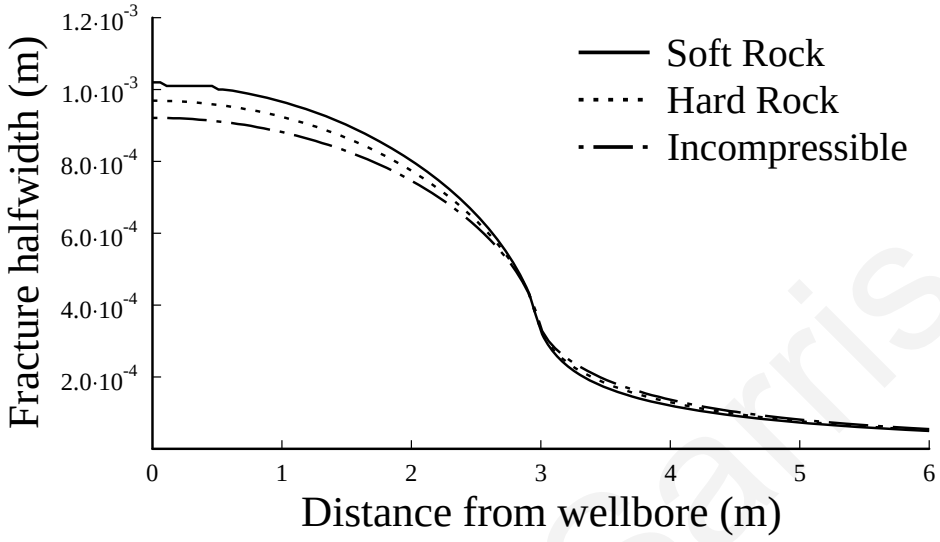

Figure 6.27: Comparison of porous compressible fractures for the elastic-softening case

Figure (6.28) shows the fluid pressures needed to propagate the fracture at the respective distance of 3m from wellbore. There is a small difference in the fluid pressures that are needed for propagating the fractures.

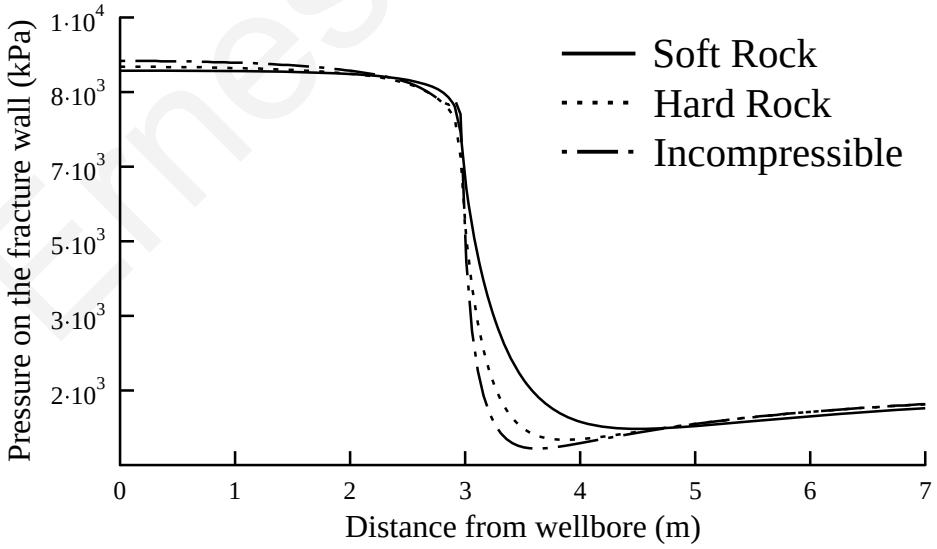

Figure 6.28: Comparison of fluid pressures in porous compressible fractures for the elastic-softening case

As mentioned before, this can be attributed to the small range of numerical values of compressibilities that were chosen to have a physical meaning. However, a closer examination in the area in front of the fracture tip reveals that there is a redistribution of pore pressure fields that affects the size of the cohesive zone caused by the local extra volumetric strain – (p_f / K_g) that is created by changing the bulk modulus of the solid grains.

Figure (6.29) presents the net pressures for all three cases examined. It is observed that the net pressure profiles for the three cases are descending as the fracture propagates away from the wellbore and reaches an almost steady net pressure few meters away from the wellbore. The difference in the net propagation pressures needed to propagate the fractures, as expected, is small. However, some difference is observed in the area near the wellbore in the case of the soft rock formation as the size of the cohesive zone that is created by the fracture propagation is larger.

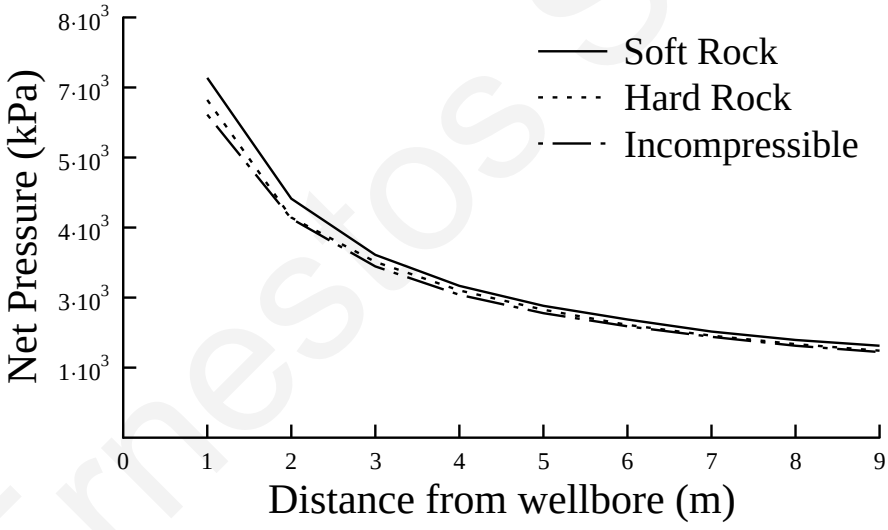

Figure 6.29: Comparison of net pressures in porous compressible fractures for the elastic-softening case

Figure (6.30) presents the cohesive stresses ahead of the visual fracture tip. The cohesive stresses correspond to the case where the fractures where left to propagate at 3m distance from wellbore and to be consistent with figures (6.27) and (6.28). As mentioned before, in soft grain formations larger sizes of cohesive zones are created than in the cases of the hard and incompressible grain formations.

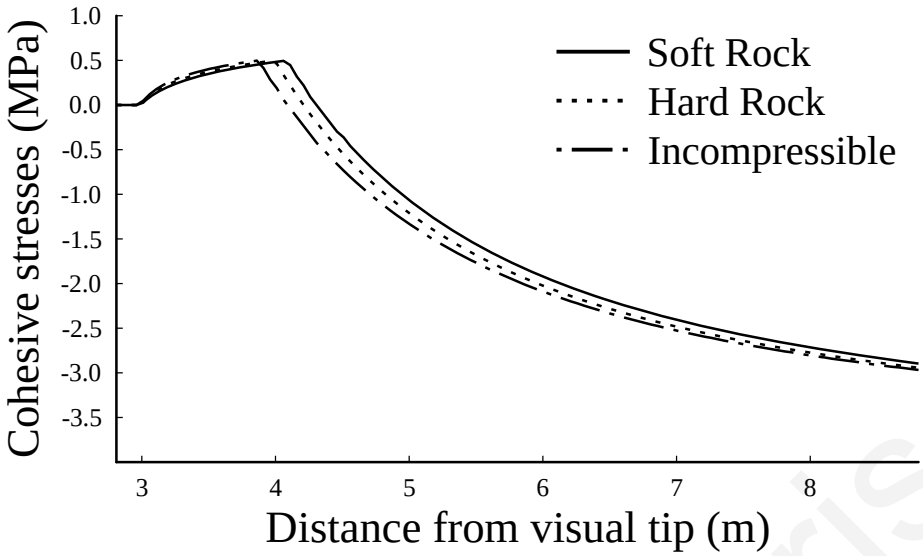

Figure 6.30: Comparison of cohesive stresses in porous compressible fractures for the elastic-softening case

Discussing the above results for the cohesive stresses, it is found that the fracture propagation in soft grain formations creates larger sizes of cohesive zones than in the hard and incompressible rock formations as a result of the extra local volumetric strain in the near tip area $-\left(p_f / K_g\right)$ that is created by changing the bulk modulus of the solid grains.

6.8 Conclusions

In this chapter, we investigated the parameters that influence the fluid driven fracture in impermeable and permeable formation under plane strain conditions and constitutive mode-I cohesive zone. These parameters include the fluid viscosity, the formation permeability, propagation velocity, obtained through the injection rate, and finally the formation compressibility. These parameters form the basis for interpreting and predicting the fracturing behavior in terms of fracture dimensions and pressures needed to propagate a fracture. The main conclusions are summarized as follows:

- Wider fracture profile is created when propagating a fluid driven fracture in poroelastic formation. The net pressures are larger and the size of the created cohesive zone is consistently larger in the case of permeable medium compared to the impermeable medium.

- Wider fracture profiles are created when propagating fluid driven fractures with highly viscous fluids in impermeable formations. The fluid pressures are larger and non uniform. Furthermore, the size of the process zone is significantly larger.
- For a fluid driven fracture propagating with highly viscous fluids in permeable formations similar results are obtained. Wider fractures are created when fracturing the formation with highly viscous fluids. The fluid pressures are large with a non uniform distribution. The size of the process zone is significantly larger. Furthermore, leak off is significantly minimized in the case of a propagating fracture with highly viscous fluids.
- It is found that the fluid pressures and the fracture apertures are larger in the case of a high permeability formation whereas in the low permeability formations narrow fracture profiles are created and the pressure needed to fracture the formation is lower. However, larger process zone is created as a result of the fracture process in the formation.
- Wider fracture profiles are obtained with high injection rates that correspond to fast propagation and narrower fractures in the case of low injection rate or slow propagation though the differences in the propagation pressure is relatively small. This result is attributed to the developed back-stress in the body of the fracture in the latter case.
- The influence of the grain compressibility has a limited effect on fluid pressures and fracture dimensions and process zone.
- From these findings, the additional mechanism of fluid flow diffusion from the fracture and the size of the cohesive zones were taken into account in the hydraulic fracture modelling and a physical model was proposed to partly explain the differences in the net-pressures between field measurements and model predictions.

7. Numerical Simulation in Cohesive Poroelastoplastic Continuum

7.1 Preamble

In this chapter, an attempt is made to investigate the importance of the parameters that affect the plastic zone development and hydraulic fracturing characteristics in inelastic saturated porous media. In order to achieve this task, the investigation of the main parameters that influence the propagation of a fluid driven fracture in a poroelastoplastic media will be performed. These parameters include the cohesive zone, propagation velocity, stress anisotropy and the formation pore pressure field. The fracture is driven in a permeable porous domain under plane strain conditions and rock strength parameters that correspond to weak formation by pumping of an incompressible viscous Newtonian fluid at the fracture inlet. Rock deformation is modeled with the Mohr-Coulomb yield criterion and an associative flow rule suitable for cohesive and frictional dilatants materials such as rocks. Fluid flow in the fracture is modeled by lubrication theory and the movement of the pore fluid in the surrounding medium is assumed to obey the Darcy law and is of the same nature as the formation fluid. The cohesive zone approach is used as the fracture propagation criterion. The problem is solved numerically to compute the solution for the fracture length, the fracture opening and propagation pressure as a function of the time and distance from the wellbore.

This chapter aims at understanding the behavior of the fluid driven fractures in inelastic porous media. It is expected that the plastic yielding and associated rock dilation in an inelastic saturated porous continuum is significantly affected by some of the main parameters that influence the fracture propagation. Furthermore, the diffusion process that was found to be a major mechanism in hydraulic fracture operations it is expected to further influence the plastic yielding and as a consequence the fracture dimensions and propagation pressures. These results may explain partially the discrepancies in net-pressures between field measurements and conventional model predictions.

7.2 Plane Strain Fluid Driven Fracture in Inelastic Continuum

The interaction between a pore fluid and the elastic skeleton of a porous material was first developed by Biot (1941) and may be considered to be a special case of the theory of interacting continua or of the theory of mixtures. Since then the theory of poroelasticity was established. The assumption of linear elastic behavior and Darcy flow behavior of the porous skeleton that will remain unaltered during loading of a poroelastic material is recognized as a limitation of the classical theory. A natural extension to the classical theory is to introduce concepts of elasto-plasticity to account for irreversible effects in the behavior of the porous skeleton. Such extension is capable to give rise to alterations in the elasticity and fluid flow behavior as a result from the generation of micro-cracks and micro-voids in the porous continuum in an average sense.

The use of porous plastic models is very common in many disciplines of engineering. In petroleum geomechanics, the coupling between the deformation of the solid skeleton and the motion of the pore fluid is thought to be of primary importance. The materials constituting the solid skeleton and the fluid can be different from one application to another. In petroleum geomechanics the solid skeleton may consist of sand grains or porous rocks and the fluid that moves through the solid may be any type of rheological fluid such as Newtonian or Power law. When the skeleton exhibits inelastic phenomena, such as development of permanent strains, damage and failure may occur. The comprehension of these non linear mechanisms and the parameters affecting them is of fundamental importance in hydraulic fracturing operations as it may explain the discrepancies in net-pressures between field measurements and conventional model predictions.

When a fracture is driven in a saturated porous media, the newly created surface of the fracture alters the stress field surrounding the body of the fracture and induces pore pressure change which affects the effective stresses and the development of the plastic zones in the near tip area of the fracture. Furthermore, the fluid driven problem in an inelastic saturated porous media further complicates the analysis as the diffusion of the fracturing fluid through the solid skeleton introduces some rate-dependency in the overall solution. Thus it is necessary to develop an appropriate numerical model to further investigate the coupling of pore pressure diffusion with deformation that follows a plastic yield criterion. In this chapter a single phase system is considered

where the "no drainage" assumption is considered which corresponds to the condition that any volume change in the solid skeleton would correspond to a pore fluid volume change. This is translated that the porous solids and the fracture fluid are assumed to be incompressible. This is a valid assumption since usually the bulk modulus of the fracture fluid is significantly higher than the bulk modulus of the dry skeleton.

7.2.1 Coupling the physical mechanisms and inelastic rock deformation

The physical process of the fluid driven fracture involves the pumping of a viscous fluid that pressurizes the fracture surfaces which deform. Increasing the pressurization, critical loading conditions will be reached ahead of the tip splitting the rock and driving hydraulically the fracture. Thus, this process reveals that there is a strong coupling between a) the moving fracturing fluid, b) the rock deformation which is inelastic, c) the pore fluid diffusion of the porous continuum and d) the fracture propagation. Depending on the formation properties, in-situ stresses and pumping parameters, the fracture may propagate for more than hundred meters.

In this research work the objective is to investigate the main parameters influencing the development of plastic zones in a porous-plastic rock under fully saturated conditions. Fluid loss which is also considered is allowed from the fracture walls (permeable walls) into the rock through diffusion. This leak-off is treated as unidirectional (1-D) and the scope is to investigate any effects associated with the coupled processes such as changes in the deformation due to diffusion of pore pressure or flows and pressures induced by mechanical deformation.

Plastic deformation in rocks and other materials is a function of the material parameters and loading conditions. Due to high stress concentration near the tip area of the fluid driven fracture, in weak rocks solutions from LEFM cannot be used to analyze the fracture process. Therefore it is necessary to incorporate plasticity and poroelastoplasticity to properly describe the irreversible deformation due to excessive shear stresses around the fracture tip.

For the inelastic response of the porous medium, the material model which has been adopted in the numerical calculations is formulated in the spirit of the Mohr-Coulomb plasticity with associated flow rule. Mohr-Coulomb criterion assumes that failure is controlled by the maximum shear stress which depends on the normal stress. Plastic behavior is characterized by an irreversible straining which can only be sustained once a threshold level is reached. Let f be the yield function, the effective

stresses, σ_1 be the major and σ_3 be the minor principle stress, then the Mohr-Coulomb criterion for non porous conditions is given by (Papamichos & Charalampakis 2004):

$$f = \frac{1}{2}(\sigma_1 - \sigma_3) + \frac{1}{2}(\sigma_1 + \sigma_3)\sin\varphi - c.cos\varphi \tag{7.1}$$

where c is the material cohesion and φ is the material friction angle. The sign convention adopted here is according to classical theory of mechanics i.e. compression is negative. The Mohr-Coulomb criterion, unlike the Drucker-Prager criterion, assumes that failure is independent of the value of the intermediate principal stress. Failure of typical rock-like and soil-like materials may include a small dependence on the intermediate principle stress. At this point it is considered that the Mohr-Coulomb criterion is sufficiently accurate.

Having established the yield criterion is now necessary to define a relationship for the post yielding behavior of the material. Plastic strains are derived from a plastic potential function which has similar form as the yield function. In the case of associated flow rule the plastic potential function g is identical to the as follows (Papamichos & Charalampakis 2004):

$$g = \frac{1}{2}(\sigma_1 - \sigma_3) + \frac{1}{2}(\sigma_1 + \sigma_3)\sin\psi \tag{7.2}$$

where ψ is the dilation angle. The dilation angle ψ as well as the material friction angle φ could be both functions of the plastic strain history in hardening models. It should be noted that the considered associated flow rule returns maximum plastic dissipation only for elastic-perfectly plastic materials and might not give maximum plastic dissipation for many types of hardening materials. However, this rule is found to closely capture the true behavior for a variety of materials.

The only extra parameters that are needed to model the inelastic behavior of the porous continuum are the material cohesion c, the material friction angle φ and the dilation angle ψ, that controls the volumetric change due to yielding and dilation of the material. In order to keep the parameters to a minimum, we have assumed associative plasticity theory which justifies the equivalence of the material friction angle with the dilation angle. Furthermore, in the hydraulic fracturing problem, the initial in-situ mean pressure in the near area of the fracture tip decreases during

propagation and under such conditions it is reasonable to assume an associative behaviour (Papanastasiou, 1999). Additionally, Papanastasiou and Thiercelin (1993) showed that the solution for non-associative material lies between the solution of elastic and associative material therefore the elastic solution and the associative solution presents the two bounds for the non-associative case.

7.2.2 Inelasticity in the process region

The inelastic processes in the cohesive region were discussed by Shet & Chandra (2002). According to their work, the position of the cohesive fracture tip is taken to coincide with the peak traction in the cohesive zone law. This selection facilitates a part of the cohesive energy to be dissipated in the forward region of the fracture while the rest of the energy is to be dissipated in the wake region. The conditions prevailing in the process zone will vary according to the type of material, geometric and loading conditions. Fracture growth is generally promoted by dissipation resulting from microstructural damage mechanisms in the forward region, both in the bounding material and the cohesive zone, while fracture advancement is impeded by other dissipation mechanisms. However, both physical processes consume energy, part of it being dissipated into the material and the rest into the fracture within the cohesive zone.

In this work, to accurately describe the fracture process in weak rocks, we model the plastic yielding that may occur in the surrounding the fracture and tip area which interacts with the mode I cohesive zone ahead of the tip. This is interpreted that in the fracture toughness dominated regime of a fluid driven fracture, the energy dissipation will include the inelastic processes taking place in the whole process zone. The various energy dissipation quantities are described by the conservation of energy (first law of thermodynamics) and have been detailed analyzed in section (2.3.3). Furthermore, when inelastic irreversible deformation takes place, it is expected that the influence of dilation and yielding would become important. The determination of the exact location of the plastic zone boundaries is an extremely difficult task to obtain and this depends on the material model and the loading conditions (Papanastasiou & Atkinson 2000). However, in the numerical computations performed in this work the locations of the plastic zone boundaries is part of the numerical solution which can determine the fracture growth, the amount of external

work expended, the recoverable elastic work, the plastic work and other dissipation works.

7.2.3 Plane strain inelastic fluid driven fractures

Modelling the propagation of hydraulic fractures is usually carried out prior to fracturing in order to optimize the treatment. A recent survey on net pressures indicated that these pressures predicted by conventional simulators fail to predict field observations. This difference between field and numerical models is even higher in weak formations (Van Dam et al., 2002). Several hypotheses have been proposed in order to explain the discrepancy. Among the most consistent with observations are: (1) high friction losses in constriction within a fracture and (2) effective fracture toughness effects which are related with micro cracking in the process zone or plasticity in the fracture tip area (Papanastasiou 1997). Two main approaches have been proposed to deal with the problem. The first approach is the dilation hypothesis which claims that the rock dilation behind the advancing fracture would constrain the opening which leads to sharp pressure gradients (Cleary et al., 1991). The second approach claims that the value of the fracture toughness is underestimated in the laboratory thus in the field is would be expected to be significantly larger (Shlyapobersky 1985). The high value of fracture toughness can be attributed to scale effects, to the influence of the insitu stress field, micro-cracking in the process zone or in plastic yielding in the fracture tip area.

The first results of works on the influence of inelastic rock behaviour were presented by Papanastasiou & Thiercelin (1993) and Papanastasiou (1997). It was showed that plastic yielding results in a shorted and wider fracture than the elastic fracture and that the wider openings of the elastoplastic fractures result in smaller fluid lag regions than the elastic fractures. The pressure from a smaller fluid lag region partially compensates the dissipated energy in the plastic zones. The difference strongly depends on the size of the plastic zones. The size of the plastic zones increases with the contrast of the insitu stresses and it is strongly influenced by the strength of the rock, the effective Young modulus and the pumping parameters (fluid viscosity and propagation velocity).

A physical model has been proposed by Papanastasiou (1997) for explaining the elevated net pressures. In his work the classical plane strain geometry (figure 7.1) was analyzed because it is the simplest way to appropriately describe the behaviour

near the fracture tip. The main processes in his physical model are: (1) the viscous fluid flow in the fracture, (2) the elastoplastic deformation caused by the stress concentration due to insitu stresses and the action of fluid pressures and, (3) fracture propagation into the rock formation. Fluid leak off was not taken into consideration under the assumption that it is minimized by fluid additives forming a filter cake on the fracture walls. The inelastic deformation that is analyzed by his model depends on rock properties and loading stresses. Furthermore, it is created in the area near the tip due to excessive stress concentration. This stress concentration creates high shear stresses around the fracture tip and plasticity theory is utilized to describe accurately the irreversible deformation from the shear stresses.

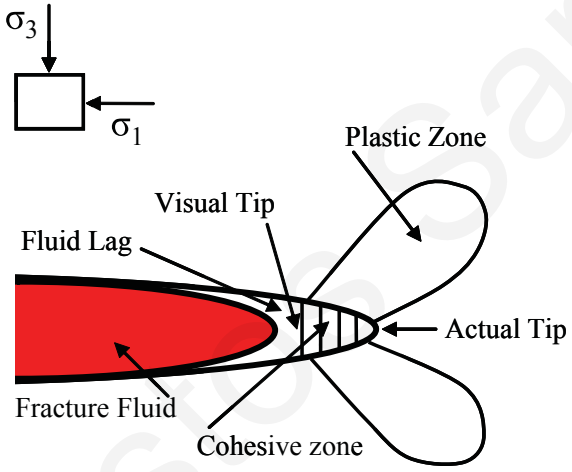

Figure 7.1: Geometry of a plane strain fracture driven in inelastic media

For a propagating fracture, Papanastasiou (1997) found that the plastic zones unload elastically behind the advancing fracture and the new area near the current tip deforms plastically. Summarizing, the rock mass remote from the fracture may deform elastically, whereas the area near the body of the fracture is initially elastic then deforms plastically and finally unloads elastically after the fracture has advanced. Under such conditions he managed to propagate the fracture under non proportional loading. Furthermore, he found that higher energy is needed for propagating the elastoplastic fractures because plastic yielding softens the material surrounding the tip. This reduces the level of stress in the direction of propagation providing an effective shielding resulting in an increase of the effective fracture toughness which is directly related to the plastic zones thus demanding higher net pressure to propagate the fractures.

7.2.4 Poroelastoplastic fracture propagation assumptions

The problem of hydraulic fracturing mechanical response is complicated by the elastic-plastic deformation coupled with the diffusion of the pore fluid. Solution of the fluid driven problem in an inelastic permeable formation under fluid saturated conditions requires numerical modelling. The numerical model presented in this chapter is an extension of the previous poroelastic model and presents some special limitations. The analysis is performed under the following assumptions:

- The fracture propagates in a permeable solid under fluid-saturated conditions displaying an elastic perfectly plastic material behavior.
- Fracture growth is considered under plane strain conditions and Mode-I loading conditions.
- The orientation of the fracture tip with respect to the insitu stress is such that, plastic yielding takes place in the plane of deformation. Reason being that in a deep rock formation where the vertical stress is usually the maximum, conditions of in plane deformation are met near the fracture front which propagates vertically.
- The effective stress is assumed to obey the Mohr-Coulomb yield criterion that adequately describes the pressure-sensitive behaviour of rock which exhibit dilatancy (increase in porosity) when sheared.
- The yielding mechanism used is associated with frictional sliding, either along particles or micro-cracks.
- Associative flow rule with perfect plastic hardening is adopted which returns maximum plastic dissipation (i.e worse case scenario).
- The fracture fluid front coincides with the fracture tip (i.e. no fluid lag is modeled).
- The propagation velocity is adjusted with the injection rate applied as boundary condition.
- Variation (evolution) of the pore pressure field in the permeable rock (i.e. the coupling between inelastic deformation and pore fluid) is such as it is accounted for by diffusion theory (Crank 1970).
- Pore pressure associated with leak-off from the fracturing fluid, behind the fracture walls is able to influence the circulation of pore fluid (i.e. the fracture wall behind the process zone is treated as permeable).

- Even though the cake building property has been assigned, it was set to correspond to the porous domain permeability so as to reach accurate conclusions about the influence of the diffusion process on the fracture analysis.
- The flow of fluid within the fracture is treated with the lubrication theory and the exchange of pore fluids between the fracture and the porous continuum is allowed.
- The fracture fluid and pore fluid are of the same nature, incompressible and Newtonian.
- The movement of pore fluids in the porous medium (continuity) is treated within the framework of Darcy law.
- The process zone includes the plastic yielding of the material and the cohesive zone.

The main objective is to calculate the fracture dimensions, the fluid pressures as a function of the parameters characterizing the fluid and the rock. Leak off from the fracture into the formation and pore fluid diffusion may change the effective stresses in the formation and hence the size of the plastic zones thus partially explaining the unexpected elevated net pressures that are encountered in the field.

7.3 Fluid-Driven Fractures in Permeable Inelastic Porous and Fluid-Saturated Cohesive Formations

In conventional rock mechanics, failure of rock formations is analyzed for dry domains (i.e. no pore pressure acting in the system). However, the usual assumption when analyzing failure of rocks in poromechanical systems is that the rock is saturated. Since the formations in petroleum related rock mechanics are generally saturated, this assumption is quite valid and it is important to investigate how the saturation affects the failure process. It is known that failure is governed by the effective stresses. In this case the failure criterion must be modified to account the fluid pressure constrain. By definition, the effective stresses are obtained by subtracting the fluid pressure from the total stress. Furthermore, the Biot coefficient must also be taken into account. In doing so, the failure criterion for a formation with pore fluid pressure is obtained by introducing the modified effective stress into the dry form of the failure criterion. In this work failure is formed in the spirit of Mohr-Coulomb theory and the equation describing failure in porous conditions is modified as (Fjaer et al., 1996):

$$\sigma_1 - \alpha p_f = 2c\frac{\cos\varphi}{1-\sin\varphi} + \left(\sigma_3 - \alpha p_f\right)\frac{1+\sin\varphi}{1-\sin\varphi} \tag{7.3}$$

Where σ_1 is the maximum insitu stress, σ_3 is the maximum insitu stress, α is the Biot coefficient, p_f is the pore pressure acting in the system, c is the material cohesion and φ is the material friction angle. In this section, an attempt is made to understand the physical consequences of the modified Mohr-Coulomb failure criterion in hydraulic fracturing. Furthermore, the works of Sarris & Papanastasiou (2010) and Papanastasiou and Thiercelin (1993) are extended in order to evaluate the influence of the plastic zones on the fracture and pressure behavior under poroelastoplastic conditions. The yielding mechanism used in the present work is associated with frictional sliding, either along particles or micro-cracks (i.e. no pore collapse or cap yield criterion used in this work). As mentioned earlier, the calculations were carried out in Abaqus, a nonlinear finite element code suit of programs. The usual 4-node, plane strain, isoparametric elements were used to model the domain and 6-node cohesive elements to model the fluid flow in the fracture and the fracturing process. Both types of elements, additionally from their u, v translation D.O.F, are equipped with a pore pressure D.O.F to account for the fluid diffusion in the porous domain. The two additional nodes in the cohesive elements, positioned in their center, are used to simulate the fluid flow during the propagation.

In this section the results from the analysis of the fluid driven problem in a poroelastoplastic solid to demonstrate the fully coupled solution are presented. These parameters include the rock properties, the pumping parameters, the in-situ stress field and the initial conditions. The only extra parameters that are needed to consider porous deformation and propagation of the poroelastoplastic fracture is the pore pressure of the domain requiring an extra degree of freedom at the nodes of the plane strain elements. Additional material parameters are the cohesion c, and friction angle φ. The numerical values of the used parameters are presented in Table (7.1).

For avoiding any confusion, the total stress field was applied in the analysis. After the first investigation described in Chapter 6, the chosen constitutive cohesive law is the elastic-softening ($k_n = 5$) curve which is considered the case where the cohesive zone that is created is the largest. Previous research works that examined the influence of the cohesive zone in hydraulic fracturing were published in Sarris and Papanastasiou (2010). The properties of the cohesive zone are also summarized in

Table (7.1). These properties include the uniaxial tensile strength, the fracture energy which is the area under the traction-separation curve calculated to meet an equivalent fracture toughness of 1 MPa.m$^{1/2}$, the permeability of the elements and the initial loading slope of the first branch of the cohesive constitutive law.

Table 7.1: Input parameters and material properties used in the computations

Variable	Value
Elastic Rock Properties	
Young modulus, **E** (MPa)	16200
Poisson ratio, **ν**	0.3
Inelastic Rock Properties	
Material cohesion, **c** (MPa)	1.515
Material friction angle, $\boldsymbol{\varphi^0}$	28
Material dilation angle, $\boldsymbol{\psi^0}$	28
Cohesive zone properties	
Constitutive thickness	1
Anti plane thickness	1
Maximum Traction, $\boldsymbol{\sigma_t}$ (MPa)	0.5
Cohesive stiffness, $\boldsymbol{K_n}$ (MPa)	81E+3 / 162E+3 / 324E+3
Cohesive energy, $\boldsymbol{J_{IC} = G_{IC}}$ (kPa.m)	0.112
Permeability coefficients *qt* (m/sec)	2.421E-10
Pumping Parameters	
Viscosity, **μ** (kPa.sec)	0.0001
Injection rate, **q** (m3/sec.m)	50E-6 / 500E-6 / 5000E-6
Domain permeability, **k** (m/sec)	2.421E-10
In-Situ Stress Field (Effective stresses)	
Maximum, $\boldsymbol{\sigma_1}$ (MPa)	14
Intermediate, $\boldsymbol{\sigma_2}$ (MPa)	9
Minimum, $\boldsymbol{\sigma_3}$ (MPa)	3.7
Initial Conditions	
Void ratio, **e**	0.333
Initial gap (perforation) - (m)	0.1
Pore pressure (MPa)	0.85 / 1.85 / 2.85

For studying the influence of the plastic zones in hydraulic fracturing, a number of parametric studies have been performed. These studies include a) mesh dependency

check, b) the influence of the cohesive constitutive law, c) the influence of the fluid flow parameters which is the product of the viscosity of the fluid and propagation velocity (i.e $\mu.v$) according to Equation (2.3), d) the influence of the formation pore pressure, e) the influence of the in-situ anisotropic stress field according to Equation (2.1) and finally f) the reduction of the wetted poroelastoplastic problem to the non-wetted porous elastoplastic problem (i.e fluid driven fracture in rock formations with limit dry pressure).

According to Papanastasiou (1999), the analysis of the fluid driven fracture propagating in non porous formation with a yield criterion to capture plastic yielding and dilation effects requires fine mesh near the tip to capture the strong gradients. Papanastasiou (1999) incorporated a re-meshing algorithm to deal with this requirement. However, in the present work no special remeshing algorithm was used as the mesh that was constructed was sufficiently fine along the predefine path of the fracture.

Before the decision to proceed with the computations without a remeshing algorithm, a mesh dependency check was performed. We have build models with reducing the mesh size above the predefined path of the fracture. For simplicity we present a comparison between a fine mesh (solid line) and the mesh that has been used throughout the numerical computations only (dashed line). For the case of the fine mesh, about 350,000 elements were constructed in the 30 x 30 m geometrical domain that presents 1,169,554 d.o.f. For the case of the coarse mesh, about 15,000 elements were constructed for the same geometric domain that presents 49,686 d.o.f. The above numbers show that the fine mesh has 20 times larger d.o.f than the coarse mesh, therefore, is expected to be much more computationally intensive.

Figure (7.2) presents a comparison of the fracture profiles between the fine and the coarse mesh. The fracture was left to reach 6 m in length in both cases. For the fracture to propagate up to 6 m in length with the coarse mesh, only 7 hours was needed while for the fracture driven with the fine mesh, 6 complete days was needed. The computations were performed in a workstation with 4 processors and a total 8 Gb of memory. From figure (7.2) it is seen that the fracture profiles that were created with the finer mesh are larger than the fracture profiles that are created with the coarse mesh. This suggests that the mesh dependency problem is also present in the case of a fracture driven in a porous formation. However, a closer examination of the fracture profile at 5 m shows that a 2.2 % difference exists only in the fracture profiles. Figure

(7.3) presents the fluid pressures needed to propagate the fractures with a fine and a coarse mesh. It is seen that the influence of the mesh dependency has a limited effect on the fluid pressures. A closer examination of the fluid pressures at 5 m shows that a 0.09 % difference exists only in the fluid profiles. Taking into account the time needed to complete the computations, the analyses were chosen to be performed with the coarser mesh.

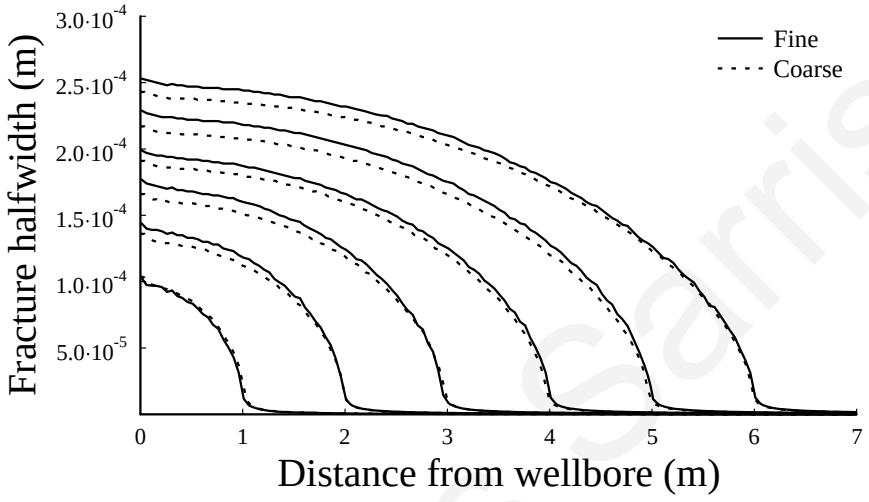

Figure 7.2: Comparison of fracture profiles between coarse and fine mesh in a poroelastoplastic analysis

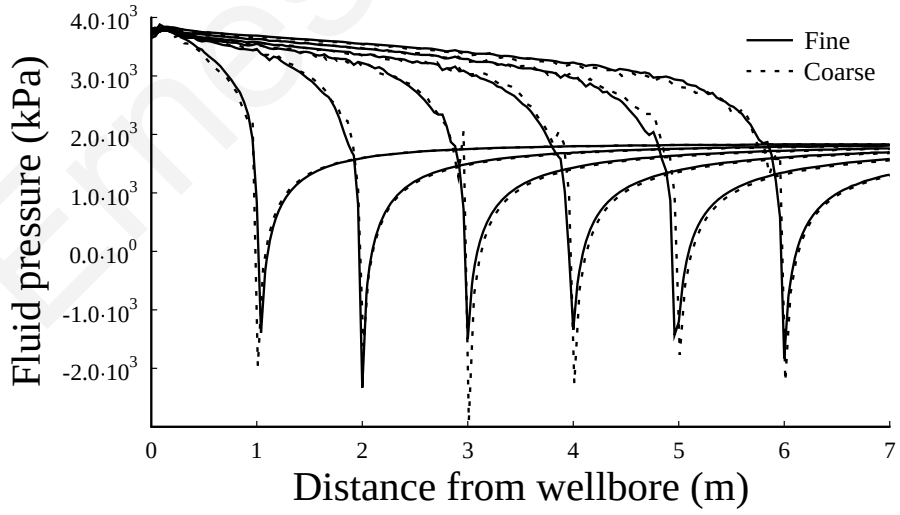

Figure 7.3: Comparison of fluid pressures between coarse and fine mesh in a poroelastoplastic analysis

Figure (7.4) shows the obtained half width of fractures propagating in a poroelastoplastic domain for cases of different loading slopes of the constitutive relation after the fracture propagated to reach a length of 2m.

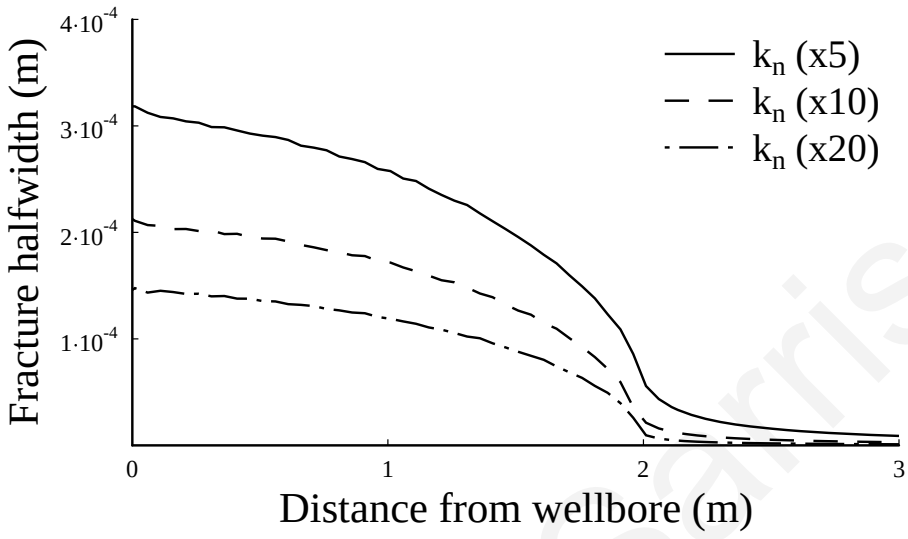

Figure 7.4: Fracture profiles for different values of the loading slope of the constitutive cohesive zone law

The reason for examining the fractures at 2m is to investigate any effects associated with near wellbore fractures. Indeed, it is assumed that in the poroelastoplastic hydraulic fractures, the process zone includes the generated plastic zones. We see that the calculated width of the propagating fracture that corresponds to the elastic softening case (k_n x 5) is much larger than the calculated width of the rigid-softening which corresponds to (k_n x 20). Furthermore, the cusping of the fracture profile in the cohesive zone is larger in the case of (k_n x 5). This large cusping is explained by the fact that in the elastic-softening case, the cohesive tractions are effective in resisting the fracture growth leading to more open fractures and larger plastic zones.

Figure (7.5) shows the corresponding pressure profile in the fractures when the visual tip has reached the distance of 2m. The fluid front position is found to be where the fluid pressure changes sign. It was assumed in these computations that the fluid reaches the fracture visual tip. From the fluid pressure profile it is evident that the fractures that correspond to the case of (k_n x 5) demand higher pressures to propagate. Another important feature of this figure is that the pore pressure field that is observed in front of the visual tip is significantly influenced by the fracture process. This is

explained by two reasons. First, this behavior is explained by the local volumetric strain that is caused by material yielding and secondly by the fact that the fracture in this case presents larger cohesive zone which include the plastic zones.

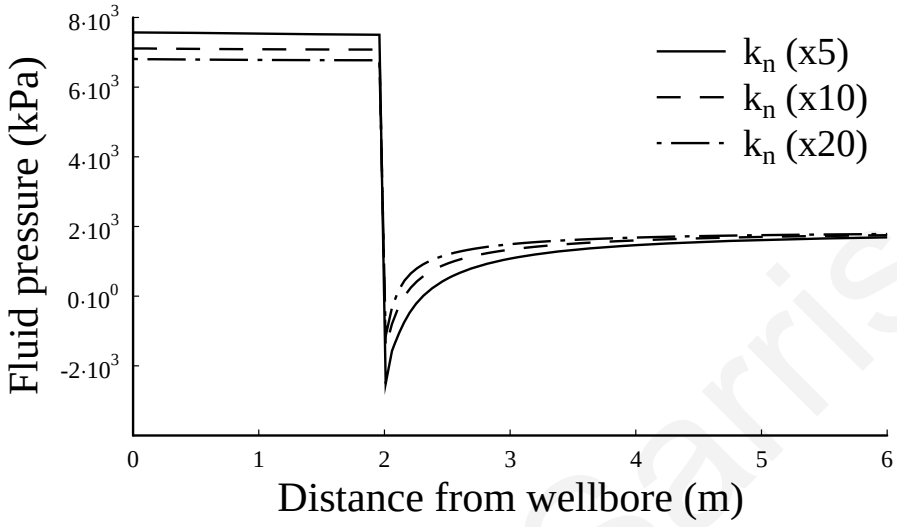

Figure 7.5: Fluid pressures in the fractures for different values of the loading slope of the constitutive cohesive law

Figure (7.6) shows the net breakdown pressure of the formation and the net propagation pressure. From figure (7.6) it is seen that the propagation pressure near wellbore is significantly larger in the case of (k_n x 5) and tends asymptotically to a constant value after some propagation distance away from wellbore. The pressures during early times of injection are initially increasing for some propagation steps until the stress field affecting the cohesive zone which includes the plastic zones is fully developed. It is also observed that near wellbore the pressures present the most significant difference. After the first few propagation steps the pressures tend to decrease to a steady state value. This can be explained by the fact that the effect of the process zone in the poroelastoplastic continuum is highly significant near wellbore but as the fractures propagate away from the wellbore, this effect becomes weaker because the size of the process zone becomes negligible compared to the fracture dimensions. The difference in the pressures that are needed to extend the fracture that are observed far from the wellbore is attributed to the energy required to fracture the formation and into any inelastic effects (i.e. material yielding due to frictional sliding).

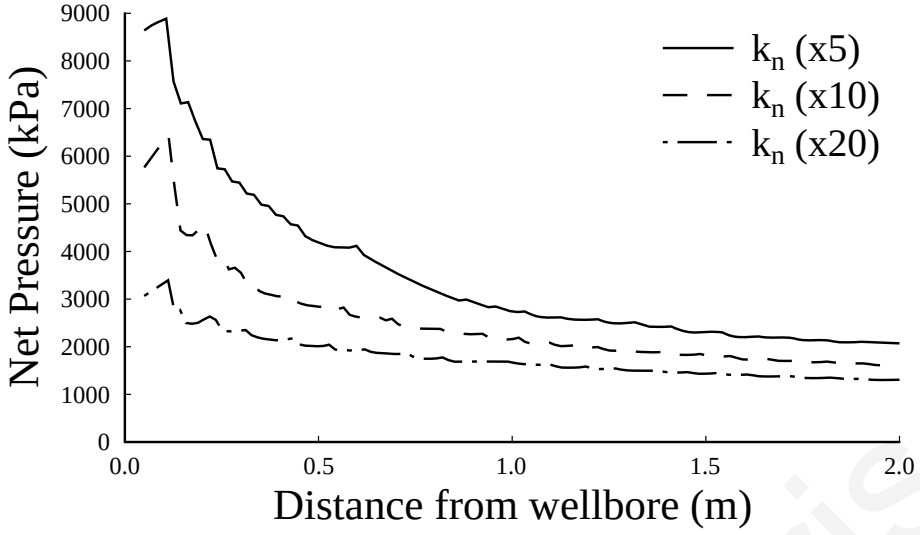

Figure 7.6: Net pressures vs. fracture length for different values of the loading slope of the cohesive zone law

A small discrepancy exists in the physical meaning of the fracture toughness dominated regime (K-dominant) between the poroelastic and the poroelastoplastic solutions. The physical meaning of the fracture toughness dominated regime in the poroelastic cases is that the Effective Fracture Toughness (EFT) increases and significant amount of energy is expended in fracturing the material. The effective fracture toughness is calculated from the J-integral approach which successfully assumes this K-dominant region ahead of the fracture tip. In this region ahead of the fracture tip the stress and displacement fields are a function of the loads and the fracture length. Therefore, the fracture toughness dominated regime in the poroelastoplastic fracture can only exist when the inelastic region can be contained within an angular region surrounding the fracture tip which means small scale yielding (Kanninen & Popelar 1985; Papanastasiou 1999). In the poroelastoplastic case if plastic yielding is large, the condition of the fracture toughness dominated regime may lose its meaning.

At this point the basic assumption of the cohesive zone that it is localized in a narrow band ahead of the fracture tip may still valid as the plastic yielding (plastic zones) of the material interacts with the more localized deformation in the cohesive zone. This means that the plot of the cohesive stresses versus distance from visual tip will not be representative for the size of the process zone which includes the surrounding plastic zones. In order to obtain a measure of the process zone, the energy that is dissipated due to plastic yielding is calculated.

Figure (7.7) presents a measure of the plastic zones that are generated (plastic energy dissipation) in the numerical model versus propagation time. As it was described in section (2.3.3), the energy that is dissipated due to plasticity is calculated for the entire numerical model which is the second term that arises in the internal energy balance of the poroelastoplastic system as:

$$E_p = \int_0^t \left(\int_V \sigma : \dot{\varepsilon}^{pl} dV \right) dt \tag{7.4}$$

Figure (7.7) shows that larger plastic zones are created and higher energy is dissipated for the case of (k_n x 5).

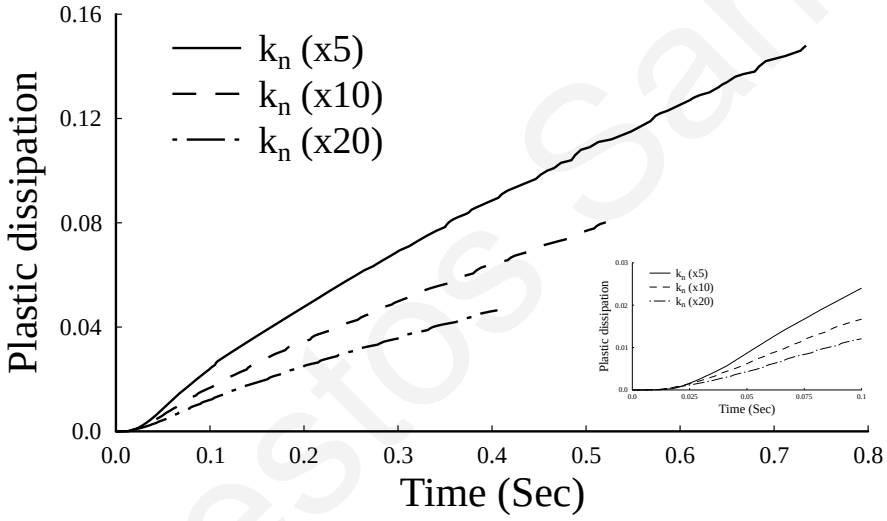

Figure 7.7: Plastic dissipation vs time for different values of the loading slope of the cohesive zone law (length at 2m)

For early times of injection the energy is exponentially dissipated (small plot at lower end) as a result of the development phase of the process zone which includes the plastic zones and the cohesive zone. Once the process zone is fully developed the dissipated energy follows a linear variation with propagation. In other words, while the fracture gains in length, more plastic yielding is accumulated in the numerical model. It is also seen that more time is needed to propagate the fracture to the same extend (i.e. 2m) for the case of (kn x 5) due to the larger volume of the created fracture.

As mentioned earlier, the analytic determination of the exact location of the plastic zone boundaries is an extremely difficult task to obtain. In the computations

presented in this section the plastic zone boundaries are computed numerically and are exactly determined as a part of the solution. For the two extreme cases of propagating poroelastoplastic fractures in soft (k_n x 5) and hard (k_n x 20) rock formations, the contours of plastic equivalent strains were plotted in figures (7.8) and (7.9) respectively. The definition of the equivalent plastic strain for the Mohr-Coulomb failure criterion is given by:

$$\bar{\boldsymbol{\varepsilon}}^{pl} = \int \frac{1}{c} \boldsymbol{\sigma} : d\,\boldsymbol{\varepsilon}^{pl} \tag{7.5}$$

where c is the cohesion yield stress.

Both figures (7.8) and (7.9) are plotted after the fractures have been left to propagate up to 2m length (i.e. L = 2 m). In order to obtain comparable results, the plastic strain scale was set to the same value for both numerical models (PEEQ = 2.5e-4). The equivalent plastic strain contours show that the plastic zones are larger in the case of a propagating fracture in soft rock formation. Furthermore, the strain contours extend in significant distance from the fracture surfaces into the formation. For a short fracture this plastic zone is relatively large but it relatively decreases as the fracture propagates longer. High intensity yielding is observed near the tip and residual plastic strain accumulates near the fracture walls after material unloading behind the advancing tip as the fracture propagates. Furthermore, as expected in the area near the wellbore the high intensity yielding zone is even larger. As the fracture propagates the plastic yielding reaches steady state conditions. Another important observation is that yielding takes place for fractures longer that the initial length that is imposed in the numerical models in order to achieve a well-posed initial solution. This remark explains the "signature" that it is observed in the fracture profiles. This behavior is in agreement with the previous results presented in figures (7.4) - (7.7) suggesting that larger plastic zones result in larger pressures to extend the fractures and the fracture profiles that are created are wider.

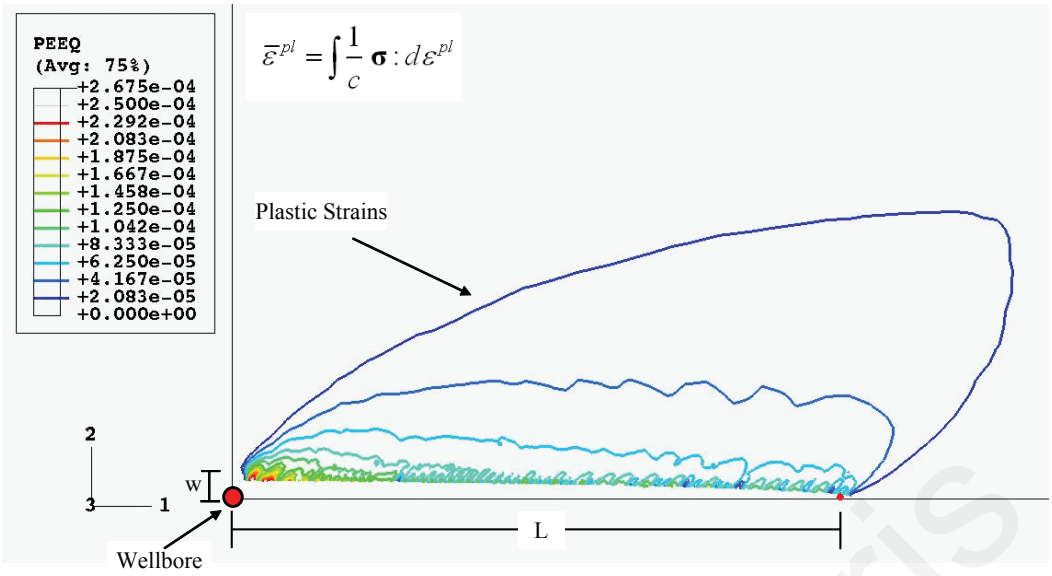

Figure 7.8: Plastic equivalent strains for kn (x 5) at 2m

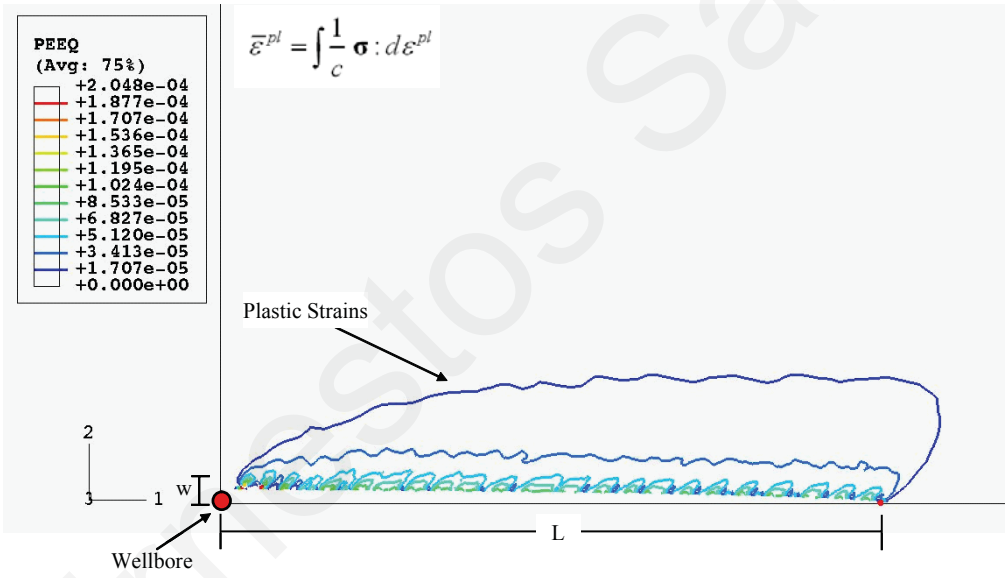

Figure 7.9: Plastic equivalent strains for kn (x 20) at 2m

The poroelastoplastic numerical models presented in this chapter are an extension of the inelastic models of the works of Papanastasiou & Thiercelin (1993) and Papanastasiou (1997; 1999). In these computations, the fracture walls behind the propagating fracture tips are treated as permeable with permeability equal to domain permeability with value of 2.5 mD. This means that no filter cake building mechanism is considered in order to keep the parameters affecting the problem to a minimum.

The next figures (7.10) and (7.11) are contour plots of the pore pressure fields for the two cases of propagating poroelastoplastic fractures in soft (k_n x 5) and hard (k_n x 20) rock formations respectively. Both figures (7.10) and (7.11) are plotted after

the fractures were propagated up to 2m length (i.e L = 2 m). In order to obtain comparable results, the pore pressure scale was set to the same value for both numerical models (POR = 6.8 e+3 kPa). It is evident that the pore pressure field is affected by the plastic yielding. In both cases there exists a highly negative regime of pore pressure ahead of the fracture tip which turns highly positive just after a small distance from the fracture tip towards the wellbore. It is reminded that the domain is fully saturated and the fluid rheology of the fracturing fluid and formation fluid are of the same nature (incompressible Newtonian). The negative sign suggests the presence of the cohesive and dilatant regions which enforce suction (negative values of fluid pressures) in the area of the fracture tip. In such case the negative sign implies that fluid is pulled towards the fracture tip which acts as a sink and suction takes place. Just after the suction the fluid returns to the porous domain. The positive sign suggests that the fluid is directed away from the fracture walls. In other words, negative sign implies that flux is directed towards the tip and positive sign implies that flux is directed away from the fracture. This conclusion is in agreement with the works of Radi et al., (2002) and Loret & Prevost (1991). Furthermore, we observed that the fluid has diffused to a larger distance which corresponds to the case of the fracture propagating in soft rock formation. As the magnitude of the negative sign is larger near the tip area, and by keeping the time scale equal in both models, this would imply that the flux of pore fluid towards the tip is higher. This increased flux which is sucked into the fracture it immediately returns to the porous domain and the diffusion process increases. This means that the plastic dilation increases the flux towards the fracture tips and the diffusion process is enhanced. The conclusion that plastic dilation triggers the flux towards the fracture tip is very similar to that of strain localization. It is known that shear bands which are zones of high shearing and dilatancy, attract pore fluids (Loret & Prevost 1991). At this point is important to mention that we do not model changes of permeability with deformation of the porous continuum. Here only the diffusion process is investigated.

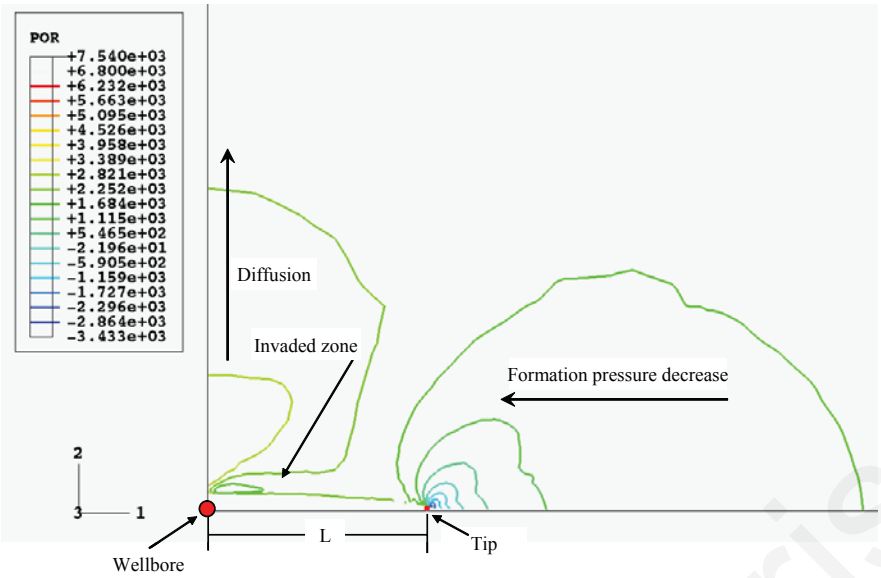

Figure 7.10: Pore pressure field solution for kn (x 5) at 2m

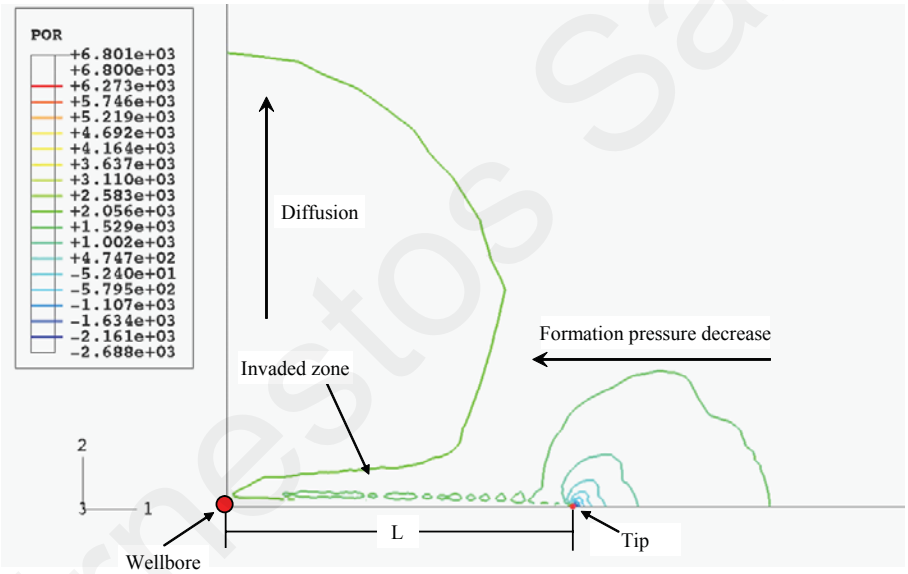

Figure 7.11: Pore pressure field solution for kn (x 20) at 2m

Summarizing the above results, we found that wider poroelastoplastic profiles are created when the fracture is driven in soft porous formations and the resulting large cusping of the fracture profile is explained by the cohesive tractions that are effective in resisting the fracture growth leading to larger plastic zones which means larger process zones. These large plastic zones and the cohesive zone demand higher pressures to propagate the fracture which are explained by the local volumetric strain that is caused by material yielding and by the large cohesive zone. The process zone in the poroelastoplastic continuum is highly significant for short fractures near

wellbore. Plastic dilation increases the flux towards the fracture tips and the diffusion process is enhanced.

7.4 Influence of Stress Anisotropy in Fluid-Driven Fractures in Poroelastoplastic Cohesive Formations

In the previous section it was demonstrated that the influence of dilatancy and yielding are significant parameters that affect the fracture dimensions and pressures needed to propagate the fractures. Furthermore, the dilatancy and plastic yielding are highly important if significant plastic deformation takes place. Due to the complexity of the porous models and loading conditions, the size the plastic zones is important for the fracture dimensions and fluid pressures. Therefore, the scaling of these plastic zones is important for understanding the problem. As it was mentioned in section (2.3.1) scaling of the plastic zones with the most important parameters that affect their size is attempted next.

The next step of this research work is to investigate the influence of the stress field in a poroelastoplastic continuum, according to Equation (2.1), which scales the plastic zone development through the insitu stress deviator (σ_1 - σ_3). At this point it is considered of paramount importance to impose the correct stress field acting in the correct directions. Figure (7.12) presents the orientation of the fracture tips with respect to the insitu stresses. It is generally accepted that the fracture always propagates perpendicular to the minimum insitu stress σ_3. In the first case shown in figure (7.12) the insitu stress field is such that plastic yielding takes place in the plane of deformation. This case it happens when the maximum insitu stress is acting perpendicular to the plane strain deformation. In the opposite case, the maximum insitu stress is in plane strain deformation. In a deep rock formation the vertical stress is usually the maximum and the conditions of in plane deformation are met near the fracture front which propagates vertically whereas the conditions of the out of plane deformation are encountered near a fracture front which propagates horizontally.

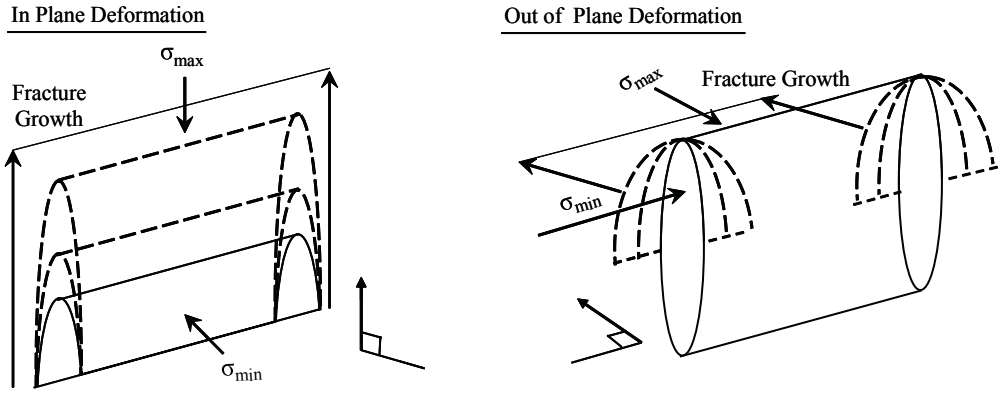

Figure 7.12: Deformation planes

Furthermore, the material model that has been utilized is the Mohr-Coulomb which neglects the influence of the intermediate insitu stress σ_2. To overcome any misleading results due to the influence of the intermediate insitu stress, in the numerical models the influence of the intermediate insitu stress is relaxed by setting it to be equivalent with the minimum insitu stress σ_3. This applied stress field will produce in plane deformation and it is assured that the fracture will propagate vertically and the plane strain model is still applicable in this case.

In this discussion, the in plane deformation was analyzed and it is emphasized that the plastic zone scaling depends strongly on the stress deviator parameter (σ_1 - σ_3). Figure (7.13) presents the Mohr circle of the insitu stress field. The increase of the maximum insitu stress σ_1 will result in an increase of the stress deviator. The aforementioned stress situation is met in deep rocks where the stress deviator in tectonic formations is significant.

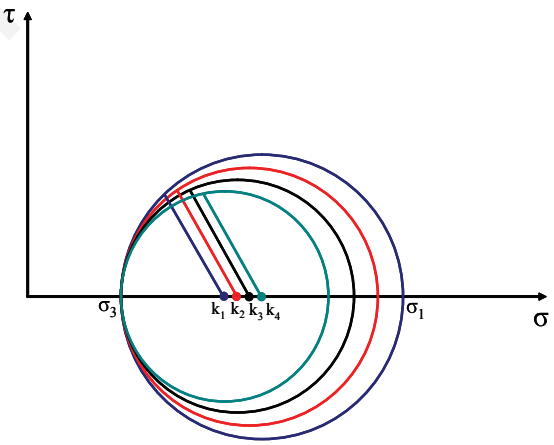

Figure 7.13: Physical meaning of the stress deviator

The problem of the plastic zone scaling is reduced in the investigation of the increase or decrease of the stress deviator as it is the stress parameter that mainly controls the plastic zones. In the first parametric investigation that has been conducted, the minimum insitu stress σ_3 was kept constant and the maximum insitu stress σ_1 was changed. By doing so the influence of the transition from isotropic to highly anisotropic stress field on the plastic zone development is achieved. Furthermore, it is ensured that the closure stress will be kept the same and any increase in the fracture dimensions will be attributed to the inelastic processes. For the purposes of the analysis five stress ratios σ_1/σ_3 have been created to accurately capture the transition from isotropic to highly anisotropic stress field cases. The values of these ratios namely are, R1, R3.25, R3.5, R3.8 and R4.05. R1 represents the isotropic while the R4.05 represents the highly anisotropic case. Table (7.2) shows the effective stress field that was considered to ensure in plane deformation. It is noted that in the numerical models, the total stress field is calculated and applied accordingly.

Table 7.2: In plane deformation anisotropic stress field (increase stress deviator)

Effective Stress Field			
σ_1 (MPa)	σ_3 (MPa)	σ_2 (MPa)	Stress Ratio
3.7	3.7	3.7	R (1)
12	3.7	3.7	R (3.25)
13	3.7	3.7	R (3.5)
14	3.7	3.7	R (3.8)
15	3.7	3.7	R (4.05)

As it was found in the previous investigation, the numerical model with the elastic-softening constitutive behaviour generates larger plastic zones. For this reason only the elastic-softening case (weak formation) is consider further in the investigation of the other main parameters. Figure (7.14) presents the fracture profile versus distance from wellbore. For comparison reasons the fractures were left to propagate up to 3m enough distance to reach accurate conclusions.

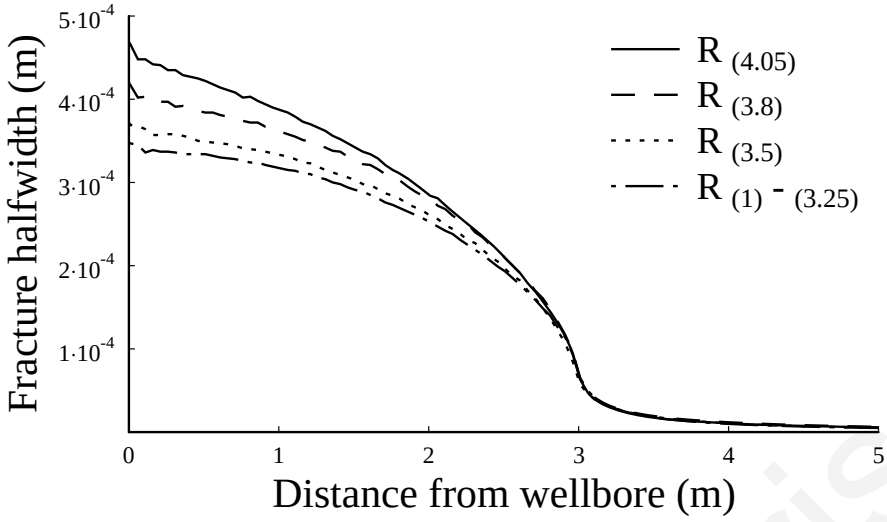

Figure 7.14: Fracture profiles for in plane deformation anisotropic stress ratios

We see that the fractures that correspond to the stress ratio R1 (isotropic) to R3.25 (anisotropic) present no difference and hence only the R1 (isotropic) case is plotted in this figure. In examining the other fractures that correspond to the other stress ratios we see that larger fractures are created when the propagation takes place in a highly anisotropic stress field.

Figure (7.15) presents the net pressures versus distance from wellbore. In this figure (7.15) both the part of the curve that corresponds to the initiation of the fracture and the part of the curve that corresponds to the extension of the fracture are included. As expected, higher initiation pressures are needed to initiate the fracture propagation in a highly anisotropic stress field. We emphasize here that no wellbore stress concentration is modelled in these studies. It is also observed that for early times of injection, up to a few propagation steps, the process zone appears to have a small effect. This effect diminishes completely after a certain propagation distance.

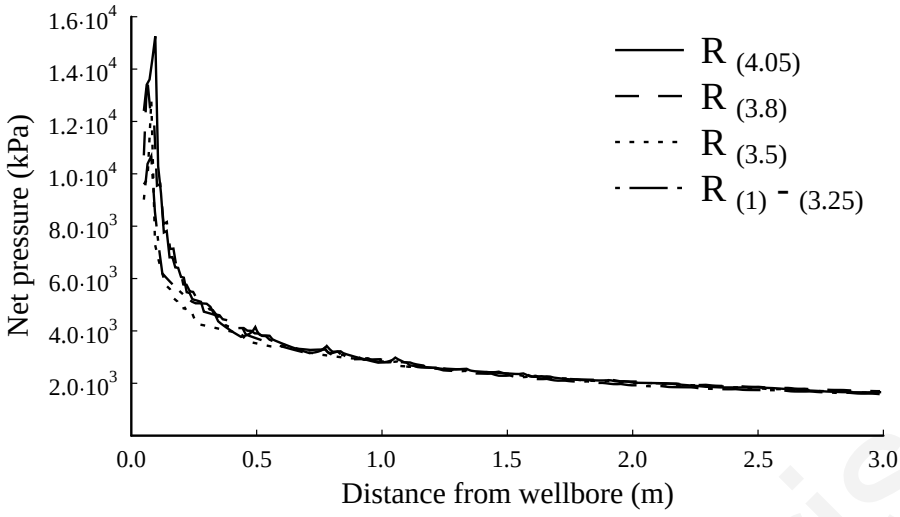

Figure 7.15: Net pressures for in plane deformation anisotropic stress ratios

Figure (7.16) shows the measure of the plastic dissipation versus propagation time. The results were plotted after the fracture propagated up to 3m. We see that almost negligible plastic zones are created when the fracture propagates in an isotropic stress field (R1). The fracture in this case behaves essentially as poroelastic. Larger plastic zones are created and more time is needed to propagate the fractures in a highly anisotropic stress field (R4.05) because of the larger fracture volume that is created.

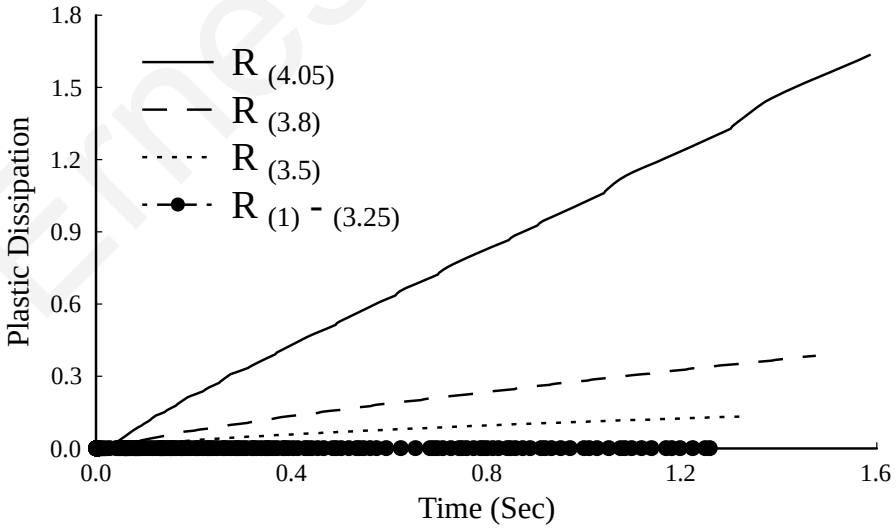

Figure 7.16: Plastic dissipation vs. time for in plane deformation anisotropic stress ratios

In the second investigation we examined the influence of the minimum insitu stress field. For the purposes of the analysis we carried out computations for three different input parameters. The names of these three models which represent the numerical values of the minimum insitu total stress that has been considered in the numerical computations are, S3 (5.55), S3 (7.55) and S3 (10.55). The initial pore pressure was constant p_0= 1.85 MPa. Table (7.3) shows the effective stress field that was considered to ensure in plane deformation. It is noted that in the numerical models, the total stress field is calculated and applied accordingly.

Table 7.3: In plane deformation anisotropic stress field (decrease stress deviator)

Effective Stress Field			
σ_1 (MPa)	σ_3 (MPa)	σ_2 (MPa)	Name
14	3.7	9	S3 (5.55)
14	5.7	9	S3 (7.55)
14	9	9	S3 (10.85)

Figure (7.17) presents the fracture profile versus distance from wellbore. For comparison reasons the fractures were left to propagate up to 3m enough distance to reach accurate conclusions.

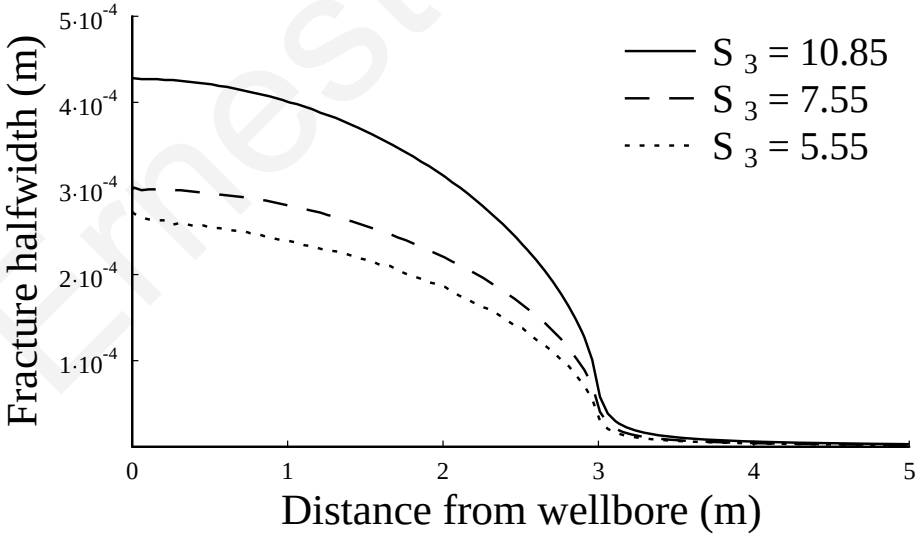

Figure 7.17: Fracture profiles for in plane deformation with different minimum insitu stress

The fracture that corresponds to the minimum insitu stress S3 (10.85) is significantly wider than the other two cases S3 (5.55) and S3 (7.55) despite the stress deviator is smaller in the first case. It seems that the wider fracture in the case of

S3 (10.85) is not due to plastic yielding but due to higher closure stress which affects the cohesive zone. The influence of the closure stress appears also on the pressures profiles in the fracture in Figure (7.18). The fracture tip is at the point where the pressure profile changes sign. As expected, higher pressures are needed to propagate the fracture when the minimum insitu stress is significantly larger. Ahead of the fracture tip is also seen that the pressure profile tends to the pore pressure value that was considered as the initial condition.

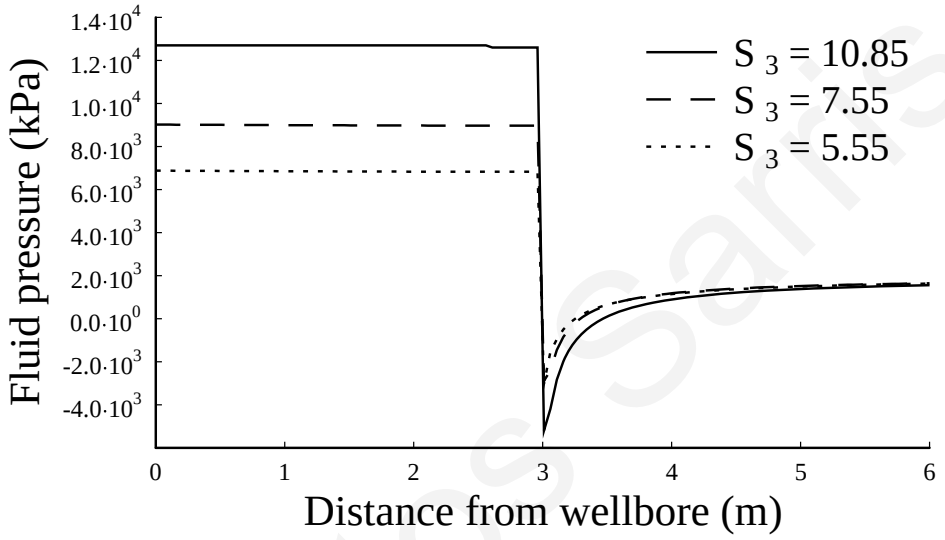

Figure 7.18: Pressure profiles for in plane deformation with different minimum insitu stress

Figure (7.19) presents the net pressures versus time at wellbore after the fracture has reached 3 m length. Higher breakdown pressures are needed to initiate the fracture propagation in the case of high closures stress due to the development of the larger cohesive zone rather than plastic zones. For early times of injection up to a few propagation steps and in an area near wellbore, the cohesive zone appears to have significant influence. With increasing fracture length the influence of the cohesive zone tends to diminish asymptotically. It is observed that larger times are needed to propagate the fracture when the minimum insitu stress is higher, S3 (10.85), and this is explained by the large volume of the fracture that is created.

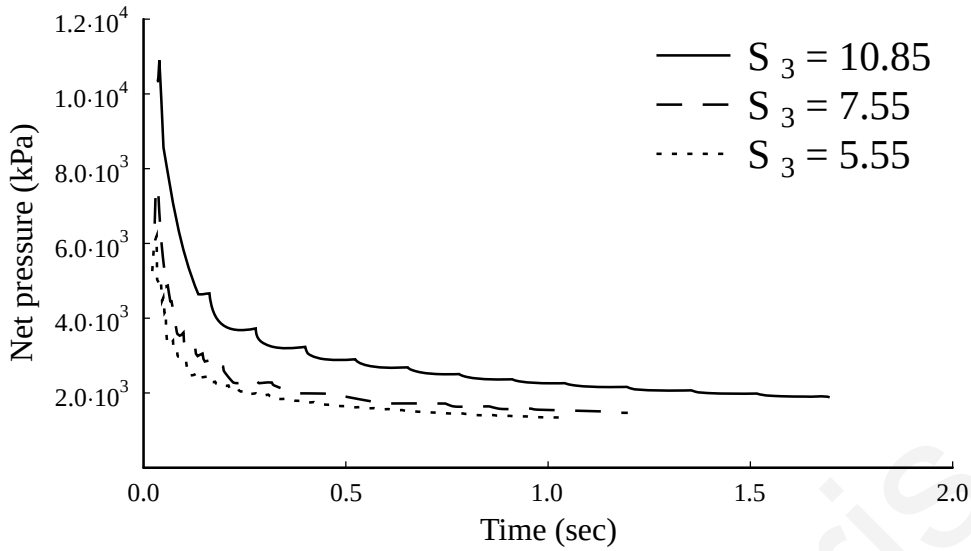

Figure 7.19: Net pressures for in plane deformation with different minimum insitu stress

Figure (7.20) shows the measure of the plastic dissipation versus time for the respective fractures of figure (7.17). As was interpreted earlier these results confirm that negligible plastic zones are created for all the stress situations S3 (10.85), S3 (5.55) and S3 (7.55). Additionally, the shape of the curves suggests that some plastic yielding may occur at the initiation phase and from that point and further the accumulated plastic strain remains constant suggesting no plastic dissipation. This leads to the conclusion that all the fractures created under these stress conditions behave as poroelastic and no significant plastic yielding is observed.

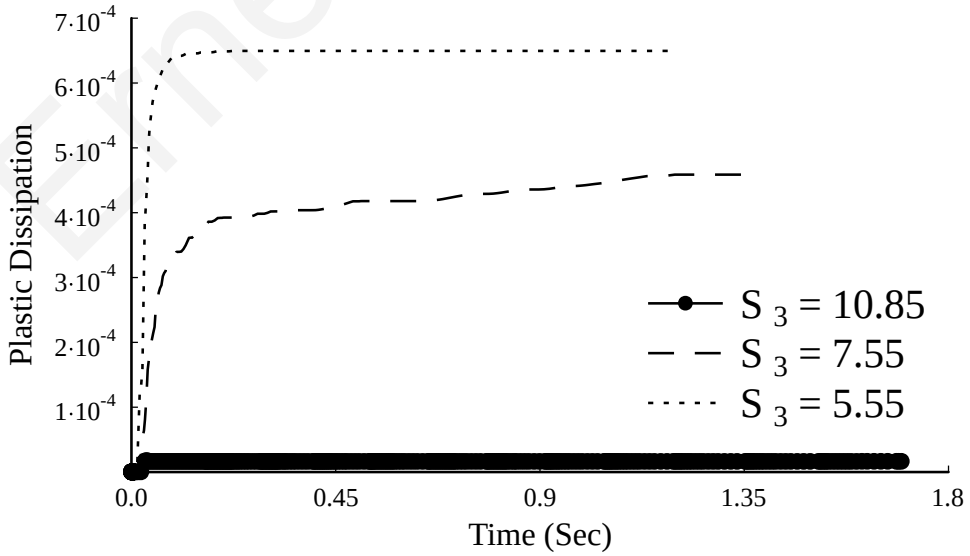

Figure 7.20: Plastic dissipation vs. time for in plane deformation with different minimum insitu stress

It is known that the Mohr-Coulomb yield criterion does not take into account the intermediate stress. A further analysis with a failure criterion such as the Drucker-Prager which takes into account the intermediate insitu stress would result in a more detailed description of the problem.

7.5 The influence of Propagation Velocity in Poroelastoplastic Cohesive Formations

This section is concerned with the investigation of the propagation velocity on the obtained plastic zones in a poroelastoplastic weak formation. In order to perform this investigation, a small parametric analysis has been conducted to study the influence of the second term ($\mu.v$) in equation (2.3). In this equation (2.3), the first term (E'^2/σ_T^3) represents the material properties while the second term ($\mu.v$) represents the fracture fluid properties. Therefore, equation (2.3) scales the plastic zones according to the specific material parameters through the fluid loading (N/m) inside the fracture.

In this study the investigation is focused on the influence of the fracture fluid velocity v, only in the loading term ($\mu.v$). Advance mathematical analysis of the fluid driven problem has showed that the fracture process is bounded in the parametric space by the fracture toughness dominated regime and the viscosity dominated regime for early times whereas for large times the fracture process is also dominated from the fluid losses (Detournay 2004; Adachi 2001). For the purposes of this work, any interactions with the viscosity dominated regime are avoided by keeping the fluid viscosity μ, at a low value and the influence of the fluid velocity v on the plastic zone development is parametrically investigated. We showed in the previous chapter that the viscosity dominated fluid driven fractures results in a non uniform pressure distribution and wider fracture profiles. However for the purposes of this analysis it is considered adequate to investigate the propagation velocity only and the investigation of the influence of the viscosity dominant mechanism is left for future work. Other research works of Zuorong et al. (2010) are dedicated to the numerical solution of the fracture process in the viscosity dominated regime in a porous elastic medium. The computational results that will be presented correspond to the elastic-softening constitutive law (k_n x 5). A constant flow rate with three different flow rates Q50, Q500 and Q5000 will be applied at the fracture inlet. The flow rate Q50 corresponds to the case where the fracture propagates extremely slowly where as the flow rate

Q5000 is the case where the fracture propagates fast. Fluid leak off from the fracture into the formation is taken into consideration assuming no fluid additives are used to form the filter cake on the fracture walls. Leak off from the fracture into the formation as well as pore pressure diffusion may change the effective stresses in the formation and hence the size of the plastic zones. Once again the fractures were left to propagate up to 3m.

Figure (7.21) shows the fracture profile versus distance from wellbore for the three different flow rates mentioned above. We see that wider fractures are created near the bulk of the fracture when the fractures are driven with high flow rate.

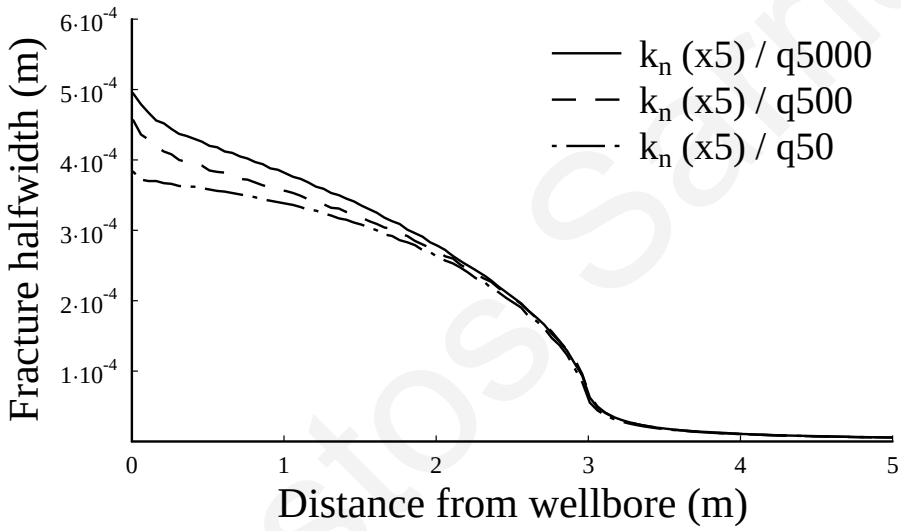

Figure 7.21: Fracture profile for different flow rates

Figure (7.22) presents the corresponding fluid pressures inside the fracture versus distance from wellbore for the three cases of propagation velocity examined. It seems that the flow rates are such that small differences create in the fluid pressure profile. This is mainly due to the value of permeability (2.5 mD) that was considered in the numerical models. As a result of the permeability value, the viscosity value and the injection rates the fracture fluid does no have the time to diffuse freely in the porous domain and reaches the visual tip in a nearly constant value profile.

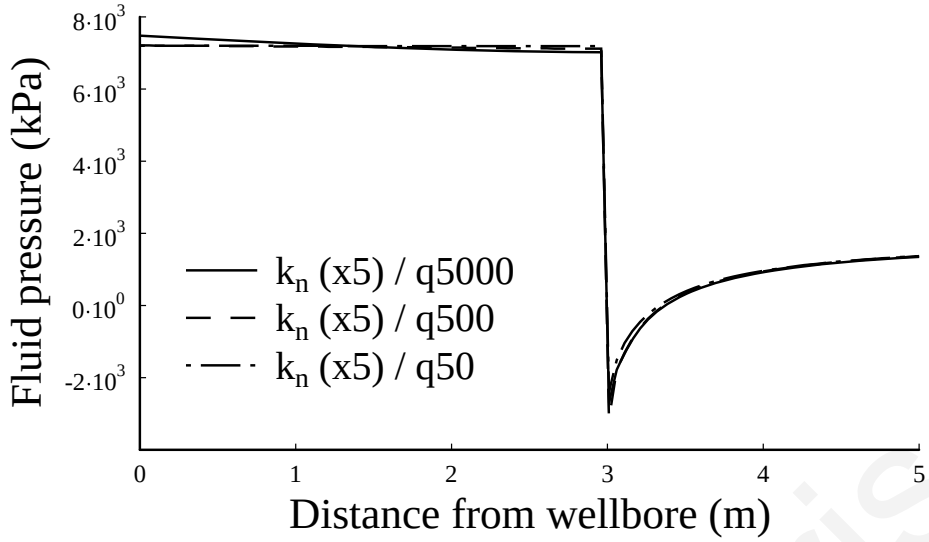

Figure 7.22: Fluid pressures for different flow rates

In Figure (7.23) the net pressures are plotted for the first 1.5 sec of injection to investigate the process zone initial development. From Figure (7.23) it is showed that the fracture that was created with the high flow rate (Q5000) reaches the length of 3m almost instantly. Such fast fracture propagation is almost impossible to apply in field treatments where the propagation velocity is approximately two orders of magnitude less. Moreover, if the fracture is left to propagate longer, lower net pressures would have been required to propagate the fracture. The other two cases of slow (Q50) and intermediate (Q500) propagation acquire much higher net pressures to propagate short fractures for the same injection time.

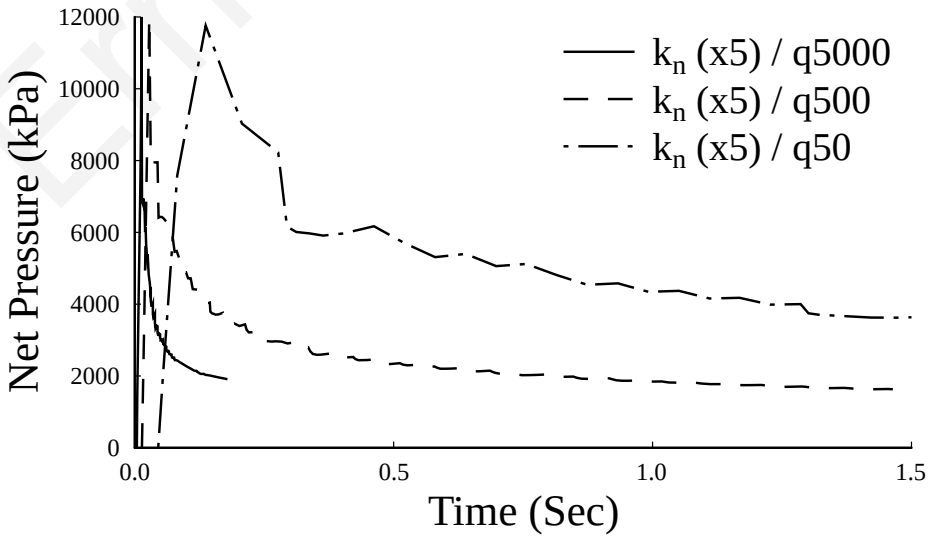

Figure 7.23: Net pressures of different flow rates

Figure (7.24) shows the plastic dissipation versus time for all three cases of propagation velocity. The final point on the curves show the time needed from the fractures to reach 3m in length. For the final fracture length this figure shows no significant difference in the plastic dissipation. This means that the plastic zones which are created have nearly the same length and intensity as the fractures in all three cases were loaded by almost the same pressure profile.

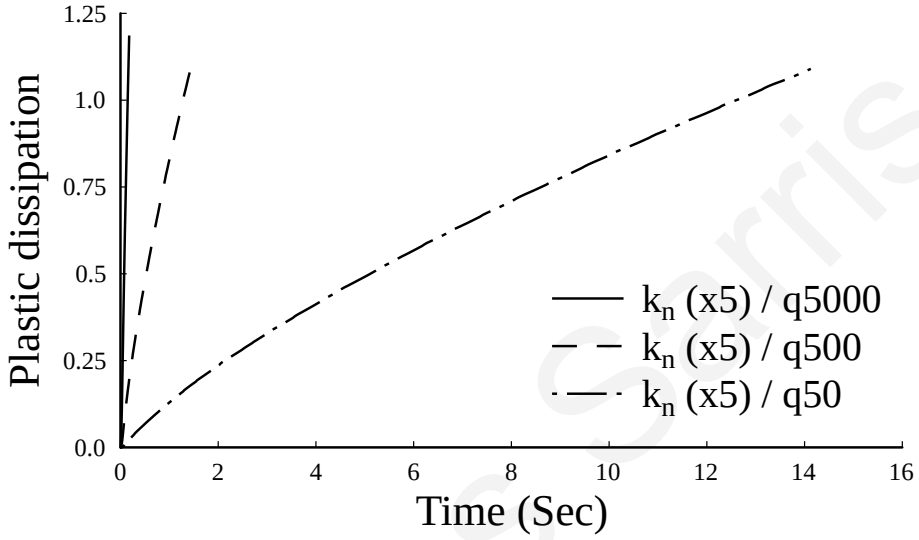

Figure 7.24: Plastic dissipation for different flow rates

The results found in this analysis suggest that from the reduction of the propagation velocity through the small flow rate applied at the fracture inlet, the pore pressure in the domain increases with the diffusion process. The poroelastoplastic model creates then back stresses which result in narrower fractures especially in the bulk of the fracture. We expect that in the case of high flow rate the diffusion effect on the fracture process can be minimized and larger plastic zones will be created. Moreover, it is found that the fluid loading that is created from the term ($\mu.v$) of equation (2.3) has an inverse influence with the pore pressure of the porous domain. In other words as the propagation velocity decreases, more fracture fluid invades the porous domain resulting in an increase of pore pressure surrounding the fracture walls thus creating back stresses on the fracture

7.6 The Influence of Pore Pressure of Propagating Fluid-Driven Fractures in Poroelastoplastic Cohesive Formations

In all the previous investigations presented in this chapter, the parameters that are relevant to equations (2.1) and (2.3) were based on previous publications by Papanastasiou and Thiercelin (1993) and Papanastasiou, (1999). The results found in this study with the poroelastoplastic model are consistent with observations from other related publications. Furthermore, we will examine in this section, how the fracture dimensions and fluid pressures depend on the initial pore pressure field. This study can be done with two different types of analysis, a) with the application of the same effective stress and different pore pressure and b) with the application of the same total stress and different pore pressure. In the first set of numerical models three different values of pore pressures have been applied to correspond to low, intermediate and high formation pressure. For simplicity the cases are called pp 0.85, pp 1.85 and pp 2.85 respectively. The numerical values represent the value of pore pressure that was used in MPa. These values of pore pressures were added to the effective stresses and the total stress field applied as initial stresses and as loading at the boundary. Furthermore, the numerical values of the pore pressure field were also applied as initial condition. The computations were carried out with the elastic-softening (k_n x 5) constitutive behaviour which corresponds to soft rock formations. The flow rate that was imposed at the fracture inlet was constant and corresponds to the Q500 case described before.

Figure (7.25) shows the fracture profiles versus distance from wellbore after all three fractures were propagated up to 3m. We see that significantly wider fracture profiles are created in the case of the fracture driven in a high pressure formation. This outlines the importance of the fluid movement and pressurization in the porous continuum.

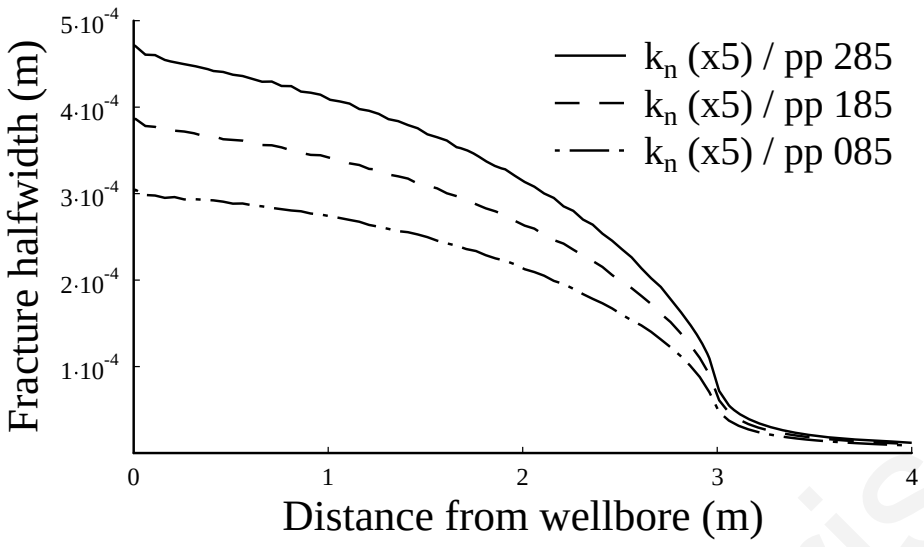

Figure 7.25: Fracture profiles for different values of pore pressures and total stress fields

Figure (7.26) shows the corresponding fluid pressure profiles for the three cases. We see that higher fluid pressure is needed to split and propagate the fractures in the high pressure formation. The visual fracture tip is found to be where the fluid pressure changes sign. Ahead of the three visual fracture tips the pressure tends to the imposed far-field initial condition values.

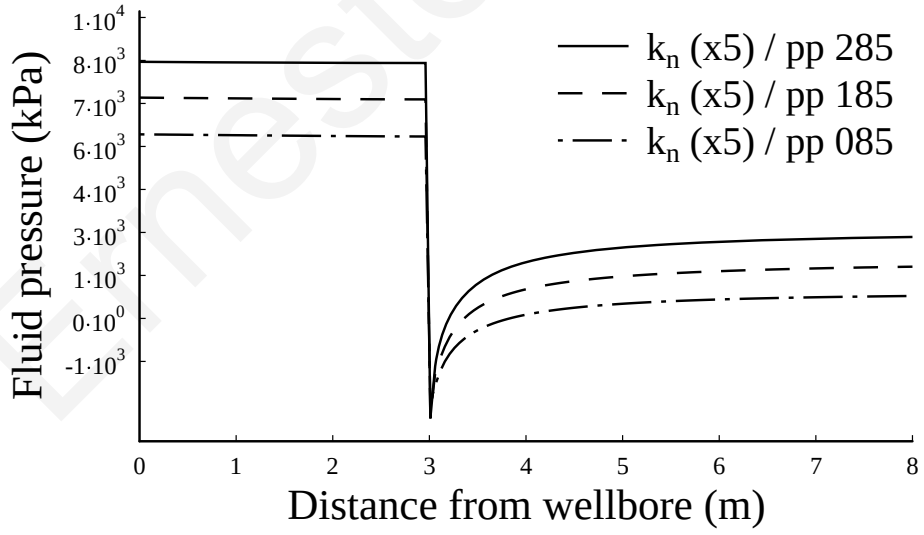

Figure 7.26: Fluid pressures for different values of pore pressures and total stress fields

Figure (7.26) shows that for a long fracture the difference in the pressure for the three cases is equal with the difference in the initial pore field. For short fractures the difference in the pressure is larger in the case of high formation pressure due to larger

plastic zone which is created in the high pressure formation. This finding is also shown in figure (7.27) which presents the net pressures versus distance from wellbore. The net-pressure is defined as the pressure in the fracture minus the remote total stress. It is evident that higher net- pressures are needed to propagate the short fractures in high pressure formations. The difference in the three cases decays to zero as the plastic zones scaled with the fracture length become negligible.

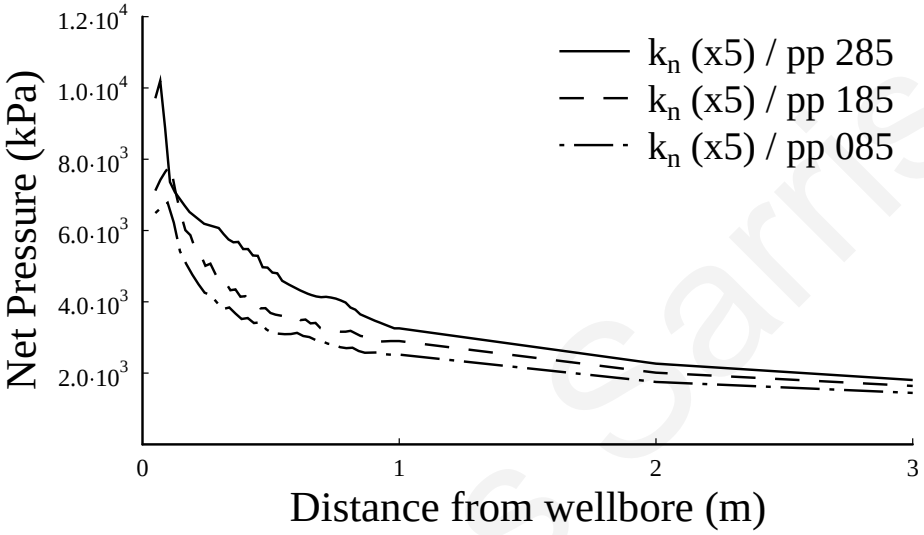

Figure 7.27: Net pressures of different values of pore pressures and total stress fields

Figure (7.28) presents the measure of plastic dissipation versus propagation time for all three numerical models. The last point of each curve corresponds to the time for reaching fracture length of 3m. It is evident that larger plastic zones are created in the case of the fracture driven in high pressurize formations. Furthermore, more time is needed for the fracture to reach 3m length in the high pressure case, of pp 2.85, mainly due to larger fracture volume that is created.

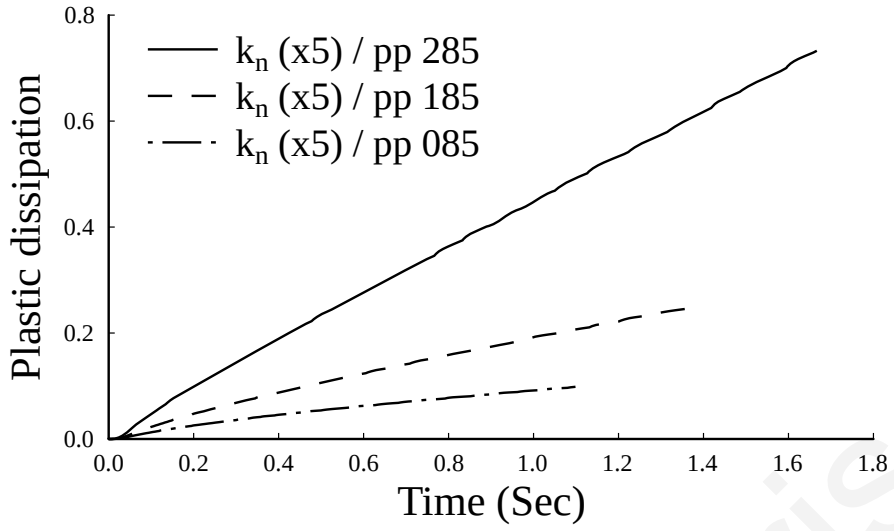

Figure 7.28: Plastic dissipation for different values of pore pressures and total stress fields

From the above analysis it is concluded that the process zone which includes the plastic zone length *Lp* is proportional to the initial pore pressure field. In other words, when a fluid driven fracture is created in a stress field with the same effective stresses but higher pressure formation, the created plastic zone will be larger. Furthermore, development of the plastic zones will result in wider fracture profiles and higher net pressures to propagate a fracture. The importance of the plastic zone which is scaled with the fracture length is diminishing as the fracture gets longer.

7.7 Poroelastoplastic Fluid-Driven Fractures at the limit of a Dry Formation

As emphasized in the previous section (7.6), the influence of the formation pore pressurize can be studied with two different loading cases, with the same effective stress as in section 7.6 or with the same total stress presented in this section. Analyzing the problem with the same total stress field it is ensured that the closure stress remains the same. We assumed that the values of the insitu stresses presented in Table (7.1) are for total stresses and only the pore pressure is varied. In each case the effective stresses are determined by subtracting the varying pore pressure from the constant total insitu stresses. Furthermore, we obtain the limiting case of a dry formation by setting the pore pressure equal to zero.

Figure (7.29) presents the fracture profile for all three cases examined after the fractures were propagated up to 4m. Figure (7.29) shows that fracture is narrower in

the bulk of the fracture in the case of low pressure formation as the limiting case of a dry formation. This result is attributed to the back-stresses which tend to close the fracture near the fracture inlet where the diffusion is greater in the case of a low pressure formation.

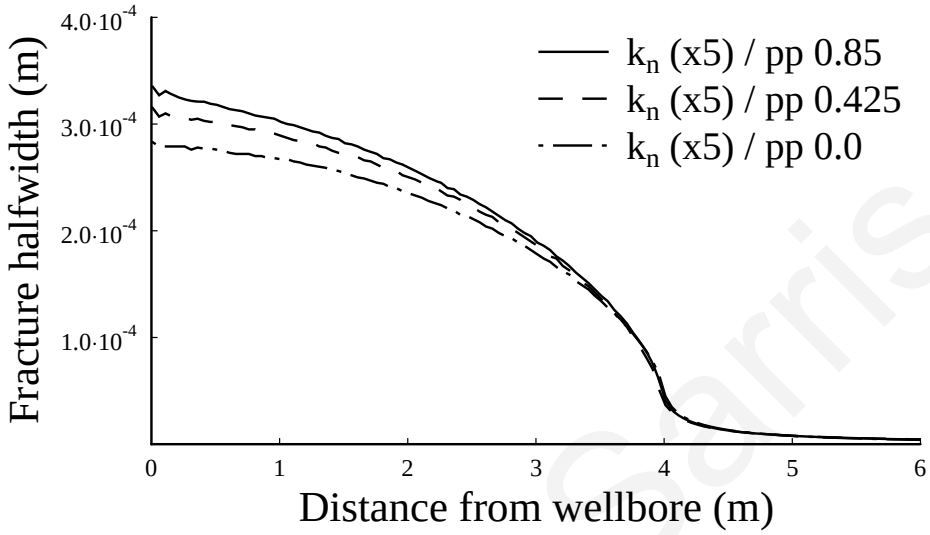

Figure 7.29: Fracture profiles for different values of pore pressures with effective stress field

Figure (7.30) presents the corresponding to the above case fluid pressure profiles. It appears that the fracture pressures needed to propagate all fractures are the same. We remind the reader that the closure stress which corresponds to the total stress was kept the same in this computation. The pressures in front of the visual fracture tip tend to the numerical value of the pore pressures that has been considered as initial conditions.

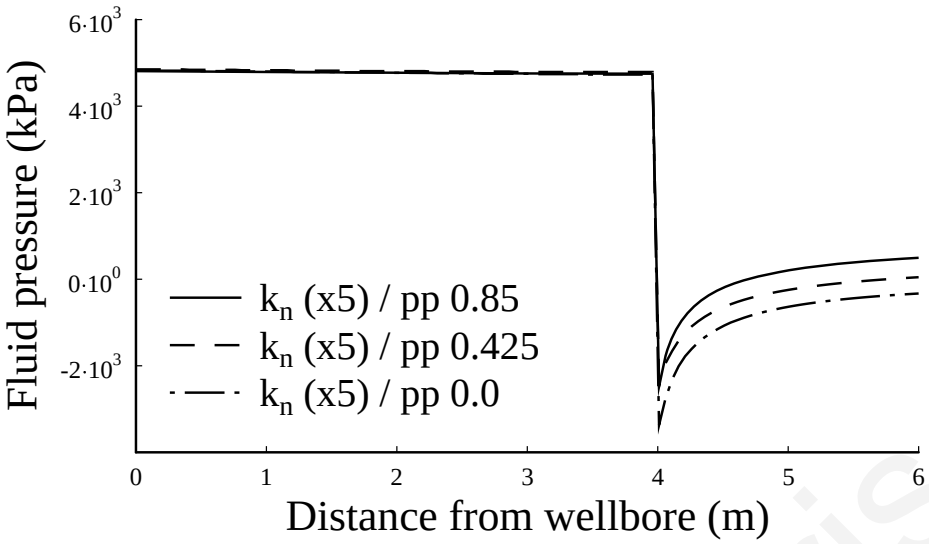

Figure 7.30: Fluid pressures for different values of pore pressures with effective stress field

Figure (7.31) shows the net pressures versus distance from wellbore for all cases examined.

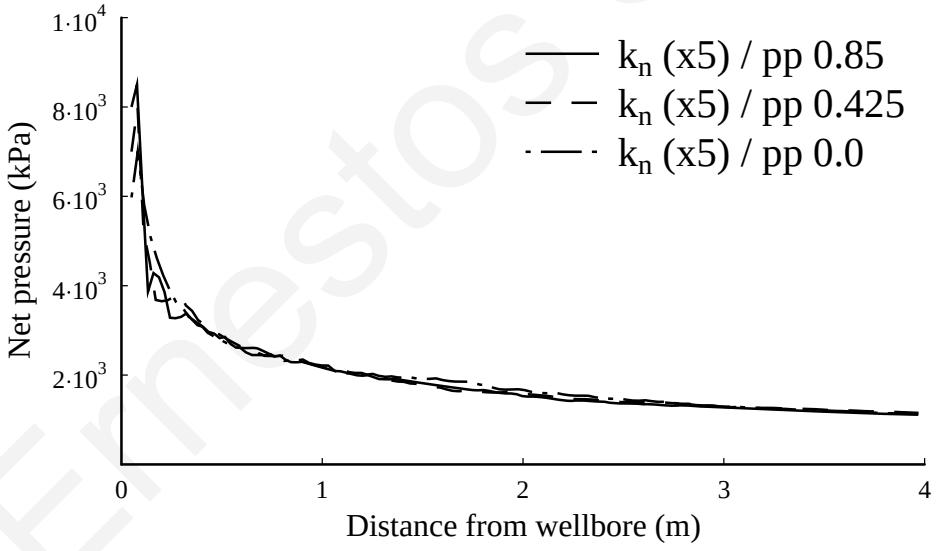

Figure 7.31: Net pressures for different values of pore pressures with effective stress field

As in all poroelastoplastic cases examined in this chapter the net pressures increase as a result of the plastic zone development and after a peak point the pressures descent to a constant value of the net pressure capable of overcoming the minimum insitu stress and propagating the fractures. The main reason behind the absent of any apparent difference in the net pressures is that the combination of the total stress and the small values of the formation pressure is not capable of creating

large plastic zones that will influence the net pressures. The only difference in the results is in the width profile near the inlet of the fracture which is interpreted to be caused by the back-stresses.

Figure (7.32) shows the measure of plastic dissipation versus time for all the cases examined. The total time required by each fracture to reach 4m was plotted. The plot has two y-axis with a common x-axis figure. The first two cases of zero (pp 0.0) and intermediate (pp 0.425) formation pressures present small plastic zone development whereas for the case of high formation pressure (pp 0.85), the plastic dissipation changes two orders of magnitude measured in the second y-axis.

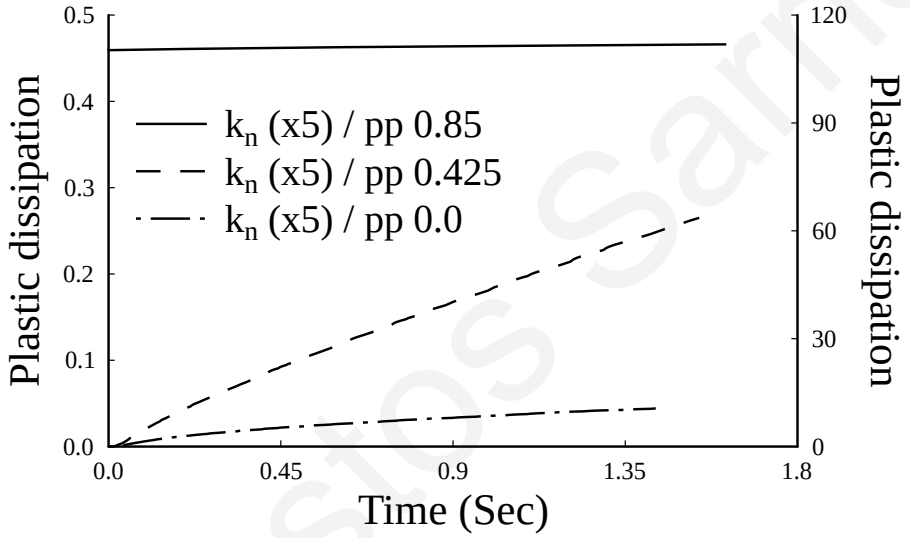

Figure 7.32: Plastic dissipation for different values of pore pressures with effective stress field

The first two cases behave essentially as all the other poroelastoplastic fractures examined in this work with comparable values of plastic dissipation whereas the high pressurization case (pp 0.85) shows constant plastic dissipation before fracture propagation. This paradoxical constantly high value of plastic dissipation leads to the conclusion that with the application of the stress field and the pore pressure value 0.85 MPa as initial condition, a state of initial yielding is created for the entire porous domain (i.e. yielding conditions have been reached before the injection step).

From the above numerical analysis it is concluded that a fracture which is driven in a dry porous elastoplastic continuum will have narrower fracture profile as a result of the smaller process zone which includes the plastic zones and as a result of larger back-stresses near the inlet of the fracture. In other words, fractures which are driven in high pressurize formations will have wider fracture profiles and higher net

pressures will be needed to propagate them mainly due to larger process zone. In both types of analysis (with total and effective stress fields) the plastic zone development is proportional to the pore pressure field. This can be explained from the Mohr circle of the stress state. With the introduction of pore pressure, the Mohr circle is displaced towards the yield criterion generating larger yielding conditions which eventually results in larger process zone. This in its turn will demand higher pressures to overcome the plastic yielding which shields the tip leading to wider fractures and larger propagation time to reach the same fracture length.

7.8 Comparison between porous and non porous models

The main focus of this work was to explain at least partially the discrepancy between field observations and predictions by classical hydraulic fracturing simulators in terms of the net pressure needed to propagate the fracture.

According to other related research works, this difference is attributed into two main hypotheses. The first hypothesis is that the high observed net pressure is related to a sharp drop of the fluid pressure (Detournay, 1998) and to the existence of a dry region near the fracture tip of the fracture (Garagash, 2006). The second hypothesis implies that the non linear deformation of the rock might have a strong influence in hydraulic fracturing (Papanastasiou, 1997). In this research work, the first hypothesis was dealt with the incorporation of the cohesive zone model as the fracture propagation criterion to ensure that the stresses in the vicinity of the fracture tip will remain finite and the second hypothesis was investigated by assuming the Mohr-Coulomb yield criterion to deal with plastic yielding with associated dilation. Computations were performed for a fracture driven in porous and non porous cohesive formations.

Figure (7.33) presents the fracture opening at wellbore versus time for a) a fracture driven in a non porous elastic formation, b) of a fracture driven in a poroelastic formation and c) of a fracture driven in a poroelastoplastic formation. All three fractures were left to propagate up to 3 m in length. The fracture that is driven in the non porous elastic formation corresponds to the case of a classical hydraulic fracturing simulator while the fractures that are driven in poroelastic and poroelastoplastic formations correspond to the cases that have been investigated with the advanced model of this study

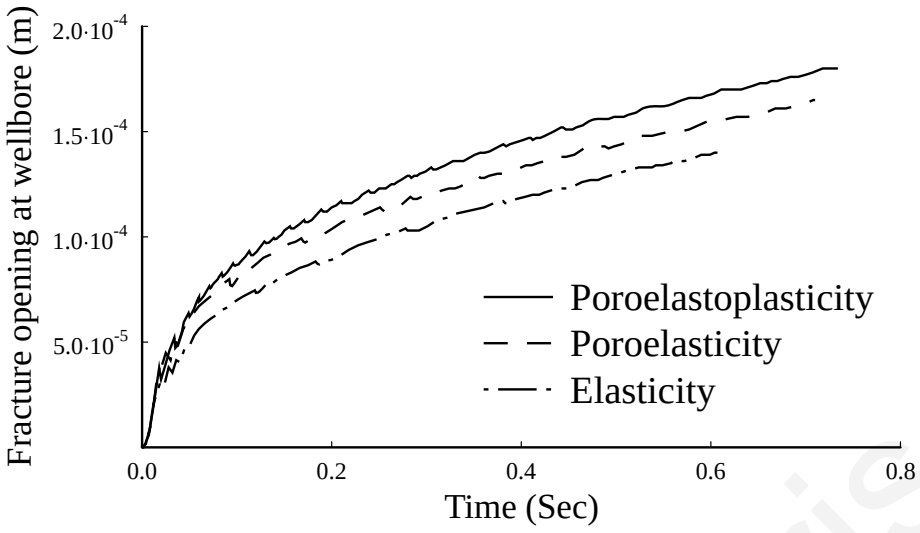

Figure 7.33: Fracture opening at wellbore to explain model-field discrepancies

From figure (7.33) it is seen that the fracture that is driven in a poroelastoplastic formation is wider than the fracture that is driven in both, poroelastic and non porous elastic formations. This is explained by the action of the process zone that includes plastic yielding and cohesive zone as well as due to the influence of the formation pressure and diffusion. A more detail examination of the fracture opening at wellbore it is seen that under the specific set of material data that have been used for the computations, the fracture that is driven in a poroelastic formation is *15.2 % wider* than the fracture driven in non porous elastic. Furthermore, the fracture that is driven in a poroelastoplastic formation is *22.25 % wider* than the fracture driven in non porous elastic.

Figure (7.34) presents the pressure at wellbore versus time needed to propagate the respective fractures of figure (7.33). It is seen that the pressure needed to propagate the fracture in a poroelastoplastic formation is significantly larger than the pressure needed to propagate the fracture in both, poroelastic and non porous elastic formations. This is explained again by the importance of the process zone that includes plastic yielding and cohesive zone as well the interaction with the formation pressure and diffusion.

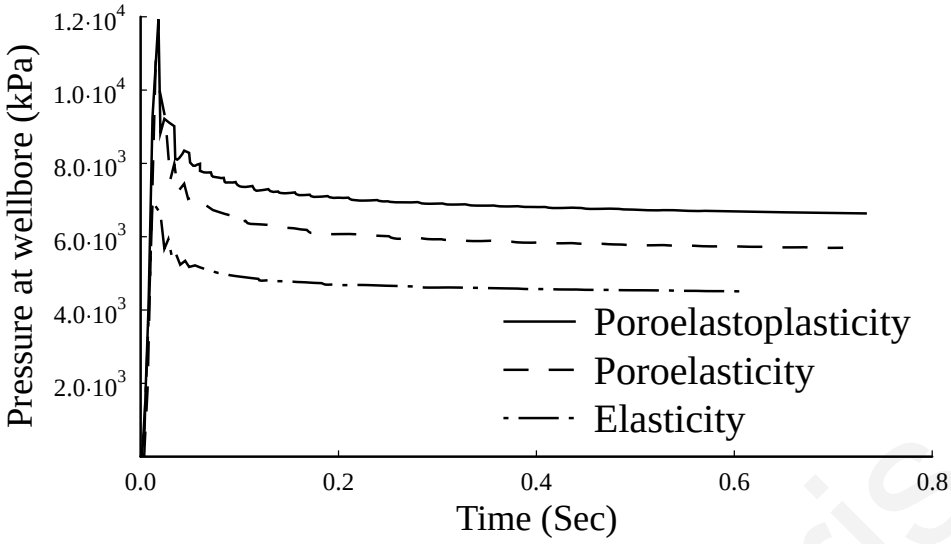

Figure 7.34: Pressure at wellbore to explain model-field discrepancies

A more detail examination of the pressure at wellbore for the specific set of material data that have been used for the computations, reveals that the pressure needed to propagate the fracture in a poroelastic formation is *20.9 % higher* than the pressure needed to propagate the fracture in non porous elastic formation. Furthermore, the pressure needed to propagate the fracture in a poroelastoplastic formation is *31.8 % higher* than the pressure needed to propagate the fracture in a non porous elastic. These results are in agreement with the motivation of this work to explain the discrepancy between classical models and field observations.

7.9 Conclusions

In this chapter we analyze the main parameters that influence the development of the process zone in fluid driven fractures in poroelastoplastic domain. These parameters include the cohesive zone characteristics, propagation velocity, the insitu stress anisotropy and the formation pore pressure. The objective was to explain, at least partially, the elevated pressures that are needed to propagate the fractures in the field and they are not accurately predicted by the conventional models. For this reason, a set of fully coupled models for the fluid-flow in the fracture, the rock deformation and the fracturing process were computed with the finite element method. The fractures were driven in a permeable porous elastoplastic domain under plane strain conditions that correspond to weak formation by pumping an incompressible viscous fluid at the fracture inlet. Rock deformation is modeled with the Mohr-Coulomb criterion suitable

for cohesive and frictional materials such as rocks assuming associative flow rule. Fluid flow in the fracture was modeled by lubrication theory and the movement of the pore fluid in the surrounding medium is assumed to obey the Darcy law and is of the same nature (Newtonian) as with the fracturing fluid. The cohesive zone approach is used as the fracture propagation criterion. The numerical computations include the solution for the fracture length, the fracture opening and propagation pressure and the plastic dissipation as a function of the time and distance from the wellbore. The conclusions of this work are the following:

- From the analysis conducted, it is found that propagation with an elastic-softening cohesive model, instead of rigid-softening, results in larger plastic zones that results in higher propagation pressure and wider fractures.
- The energy that is dissipated for creating the plastic zones increases abruptly at the first propagation steps and then increase linearly with the fracture length indicating that the plastic zone size had reached a steady state. In the poroelastoplastic continuum the cohesive and dilatant regions near the tip enforce suction. This pore fluid flux is even greater in the case of a fluid driven fracture in weak rock formation suggesting that plastic dilation increases the fluid flux. The insitu anisotropic stress field creates larger plastic zones leading to wider fracture profiles and higher propagation pressures. These obtained computations are a direct result of the large stress deviator that was considered in this case. When fracture propagation takes place in isotropic or in small stress deviator field the formation behaves essentially as poroelastic.
- It was demonstrated that with the reduction of the propagation velocity through the applied flow rate at the fracture inlet, the pore pressure in the domain increases significantly as the diffusion process in the poroelastoplastic model creates back stresses (through suction) and the fractures that are created are narrower. When the fracture is driven with high propagation velocity the fluid loading on the fracture wall becomes non uniform. From this behavior it is evident that the fluid losses can be minimized by applying an appropriate fluid rheology and pumping schedule that will result in a proper propagation velocity to avoid the diffusion process.

- Fluid driven fractures in high pressure formations results in wider fractures and higher propagation pressures as a consequence of the larger plastic zone development.

- The resulting process zone development which includes the plastic zones in poroelastoplastic media under fluid saturated conditions is an important parameter which explains partially the unexpected high fluid pressures observed in hydraulic fracturing field operations. It is concluded that the net pressures needed to propagate the fracture in highly pressurized formations are proportional to the plastic zone development $p_{net} \propto L_P$. Fractures which are driven in dry formations have narrower fracture profiles near the inlet as a result of the action of created back-stresses. Equation (2.1) which describes the scaling of the plastic zone with the stress field in dry rocks is modified to take into account the formation pressure. The following equation is proposed to scale the plastic zones according to the deviator stress in a poroelastoplastic pressurized rock formations:

$$Lp \propto \frac{\sigma_1 - \sigma_3}{\sigma_1 + \sigma_2 + \sigma_3 - 3P} \tag{7.5}$$

- Summarizing all the above results and extending the work of the previous chapter, the following stages for explaining the physical processes for a fluid driven fracture propagating in poroelastoplastic rock formation (figure 7.31) is proposed for explaining the elevated net pressures observed between field treatments and conventional numerical simulators.

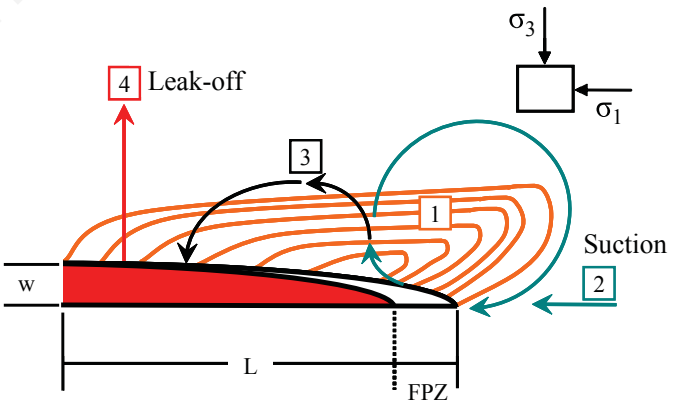

Figure 7.35: Different stages of the processes affecting the net pressures for propagating a fluid driven fracture in poroelastoplastic rock formation under saturated conditions

- After creating large pressure gradients at wellbore from pumping fracture fluid, the formation breaks down and significant plastic yielding takes place in the process (element 1). Plastic yielding and associated dilation creates under pressure which triggers pore fluid flux towards the fracture tip and suction takes place in the fracture process zone (element 2). The fluid flux enhanced due to the material yielding which is a similar behaviour to strain localization and circulates from the near area of the tip and is expelled immediately behind the fracture tip where the fluid front coincides with the visual tip. Pore fluid must necessarily be returning to the porous rock as it would otherwise cause an increase of the process zone and this would cause the propagating fracture to retard. With the immediate returning of the pore fluid to the porous continuum it is diffusing behind the advancing fracture and it is stored above the fracture walls (element 3). As the fracture propagation evolves, fracture fluid losses become significant and the fluid is largely invading the formation (element 4) and together with the pore fluid storage (element 3) are enhancing the diffusion process in the porous formation causing significant back stresses on the fracture walls. These mechanisms are causing the net pressures to increase in order to overcome both the confining insitu stress and the fluid storage that is created from material yielding, the pore fluid suction and the leak off process. These stages of the physical model described here explain at some extend the discrepancy between the highly elevated net pressures that are encountered in the field and conventional numerical simulators.

8. Conclusions

8.1 Preamble

In this chapter, we summarize the main conclusions and contributions. In addition, we make recommendations for future work and list possible extensions of the numerical simulations of the present research work.

8.2 Synthesis

The main objective of this research was to investigate the discrepancy between classical hydraulic fracturing simulators, which often underestimate the measured down-hole pressures, and field observations. For this purpose, a series of numerical simulations have been conducted based on advanced theories like poroelasticity and poroelastoplasticity.

We formulated the mathematical problem incorporating fundamentals and principles from the fields of geomechanics, fluid mechanics, fracture mechanics and poromechanics. We model hydraulic fracturing assuming plane strain fracture geometry and we model the cohesive zone as the fracture propagation criterion.

Based on the analysis of the physical problem, a model that governs the fluid driven problem was build and solved numerically with the finite element code Abaqus. These equations are coupled and non linear. The deformation of the porous continuum is obtained by the derivation of the equilibrium equation for the porous media in a descritized weak form. The constitutive behavior of the porous continuum is model through the effective stress principle. Fluid flow (movement) in the porous domain is governed by a continuity equation that describes the flow of the wetting fluid incorporating the Darcy law. Fluid flow inside the fracture is derived via the lubrication model which is represented by a diffusion equation that includes fluid infiltration from the fracture into the surrounding medium. The inelastic behavior of the porous continuum is described by the tangent stiffness matrix of the material which is required in the equilibrium equations. The inelastic tangent stiffness matrix is obtained by the yield criterion.

The fully coupled numerical computations of the fluid driven fracture propagating in an impermeable elastic rock formation were used to demonstrate the

model validation by comparing them with analytic solutions readily available for the literature and with other related numerical results.

Extending the fracture analysis with cohesive zone approach, two types of cohesive zone models were utilized to study the process zone in hydraulic fracturing treatments. These were the bilinear and exponential constitutive cohesive zone laws and they were used to analyze their influence on the fracture process zone in impermeable and permeable fluid driven fractures. They were used to compute numerically the fracture dimensions and fluid pressures in elastic and poroelastic media.

We studied fracture propagation in a cohesive poroelastic formation and examined the parameters that influence the fluid driven fracture in permeable formations under plane strain conditions and constitutive mode-I cohesive process zone. These parameters include the fluid viscosity, the formation permeability, injection rate and finally the formation compressibility.

Besides the main purpose of this research which was to explain the discrepancy between simulators and field observations, we extent the knowledge of fracturing in permeable inelastic domains. To accomplish this task, we derived the scaling of the plastic zones in inelastic porous continuum in anisotropic stress fields and in the presence of pore fluid pressure using the modified for porous media, Mohr-Coulomb failure criterion. Furthermore, inelastic behavior in the process zone and in the surrounding porous medium was studied through the energy that is dissipated in the hydraulic fracturing process.

8.3 Main Contributions

The main contributions obtained in the course of this research are summarized as follows:

- The first part of this research was devoted in the analysis of the influence of the cohesive zone characteristics on the modeling of hydraulic fracturing technique. The objective was to explain, at least partially, the elevated pressures that are needed to propagate the fractures in the field and they are not correctly predicted by the conventional models. In order to keep the model parameters to a minimum, rigid-softening and elastic-softening cohesive relations were considered to represent the splitting process of the rock near the fracture tip. A set of fully

coupled models for the fluid-flow in the fracture, the rock deformation and the fracturing process were implemented and solved numerically with the finite element code Abaqus. From the analysis conducted, it is found that for propagating a fracture with an elastic-softening cohesive model (weak formations) higher pressure is needed and the created fracture is wider compared to the case of a rigid-softening cohesive model (hard formations). These results are due to the larger process zone obtained with the elastic-softening model. Furthermore, it was shown that the exact form of the softening branch of the cohesive model has no significant influence on the obtained results. It was found that the existence of the confining stresses increases the size of the process zone and results in wider fractures and higher propagation pressures. The changes in the pore pressure during fracturing, increase further the size of the process zone which in turn increase the propagation pressures and the dimensions of the created fractures.

- Hydraulic fracturing in a poroelastic cohesive rock formation was studied numerically in the second part of this research. Again the objective was to further investigate the elevated pressures that are needed to propagate the fractures in the field as compared to conventional model predictions. It was found that the fluid pressures and the fracture apertures are larger in the case of a high permeability formation. The influence of the grain compressibility has a limited effect on fluid pressures and fracture dimensions. Wider fracture profiles are obtained with high injection rates that correspond to fast propagation and narrower fractures in the case of low injection rate or slow propagation though the differences in the propagation pressure is relatively small. This result is attributed to the developed back-stress in the body of the fracture in the latter case. These findings suggest that the additional mechanism of fluid flow diffusion from the fracture and the size of the cohesive zones must be taken into account in hydraulic fracture modelling as they may explain differences in the net-pressures between field measurements and model predictions and as a result of the above analysis a physical model is proposed.
- In the final part of this research work, the main parameters influencing the plastic zone development on the modeling of fluid driven fractures in poroelastoplastic domain was studied. These parameters include the cohesive zone characteristics, propagation velocity, stress anisotropy and the formation pressure field. The

fractures were driven in a permeable porous elastoplastic domain under plane strain conditions that correspond to a weak formation. Rock deformation is modeled with the Mohr-Coulomb criterion suitable for cohesive and frictional materials such as rocks assuming associative flow rule. From the analysis conducted, it was found that for propagating a fracture with an elastic-softening cohesive model (weak formation), higher pressure is needed, the created fracture is wider compared to the case of a rigid-softening cohesive model (hard formation) and significantly larger plastic zones are created. These results are due to the larger process zone which includes the plastic zone. Furthermore, it was found that the insitu anisotropic stress field creates larger plastic zones leading to wider fracture profiles. When the stress deviator is small the fracture essentially behaves as poroelastic. It was demonstrated that if the fracture is driven with high propagation velocity the fluid loading becomes non uniform. It was shown that when the fracture is driven with small propagation velocity, the fracture fluid diffusion dominates the process and back stresses are created on the fracture profile. Finally, it is found that the fractures propagating in high pressurized formations results in wider fractures and higher propagation pressures as a consequence of the larger plastic zone development. It has been shown that plastic yielding triggers pore fluid flux towards the propagating fracture enhancing the diffusion behind the fracture walls thus larger net pressures are needed to extend the fracture and the resulting fracture apertures are wider with larger volumes. The finding of this research may explain partially the discrepancies in net-pressures between field measurements and conventional model predictions.

8.4 Future Work

Based on the results obtained from this research, the following topics are suggested as future work on the same problem:

- From the results obtained in the poroelastic simulations it has been shown that fluid driven fractures behave completely in a different manner when the fracture is simulated in a viscosity dominated environment. Analysis of a viscosity dominated fluid driven fracture in inelastic porous media is not yet fully understood or studied.

- From the analysis of the fluid driven fractures in weak elastic and inelastic porous formations it has been shown that the stress and pore pressures fields surrounding the fractures changes as a result of the fracturing process. Analysis of the closure in porous elastic and inelastic weak formations will be helpful in estimating the risk of formation failure and stability of proppant after fracturing which is still an open question that is not fully understood.
- Hydraulic fracturing in weak formations could be influenced by the intermediate stress to an unknown degree. It is expected that an analysis with a failure criterion that takes into account the intermediate stress in the failure procedure and non linear yield criterions will produce interesting results.

References

Abaqus (2006). Version 6.6 Manuals.

Abe, H., T. Mura, and L. Keer, (1976). "Growth rate of a penny-shaped crack in hydraulic fracturing of rocks". *Journal of Geophysical Research,* vol. 81, pp. 5335-5340.

Abou-Sayed, A.S., (1978). "An experimental technique for measuring the fracture toughness of rocks under downhole stress conditions". *VDI-Berichte*, vol. 313, pp. 819-824.

Adachi, J., (2001). *Fluid-driven fracture in permeable rock*. Ph.D. thesis, University of Minnesota, MN.

Adachi, J., and E. Detournay, (2008). "Plane strain propagation of a hydraulic fracture in permeable rock". *Engineering Fracture Mechanics,* vol. 75, pp. 4666-4694.

Adachi, J., E. Siebrits, A. Peirce, and J. Desroches, (2007). "Computer simulation of hydraulic fractures". *International Journal of Rock Mechanics and Mining Sciences*, vol. 44, pp. 739-757.

Advani, S., J.L.J. Torok, and S. Choudhry, (1987). "Explicit time-dependent solutions and numerical evaluations for penny-shaped hydraulic fracture models". *Journal of Geophysical Research,* vol. 92 (B8), pp. 8049–8055.

Advani, S., T. Lee, and J. Lee, (1990). "Three dimensional modelling of hydraulic fractures in layered media: Finite element formulations". *ASME Journal of Energy Resources Technology,* vol. 112, pp. 1-18.

Advani, S.H., T.S. Lee, R.H. Dean, C.K. Pak, and J.M. Avasthi, (1997). "Consequences of fluid lag in three-dimensional hydraulic fractures". *International Journal of Numerical and Analytical Methods*, vol. 21, pp. 229-240.

Alfano, G., and M.A. Crisfield, (2001). "Finite element interface models for the delamination analysis of laminated composites: mechanical and computational issues". *International Journal for Numerical Methods in Engineering,* vol. 50, pp. 1701-1736.

Amrutharaj, G.S., K.Y. Lam, and B. Cotterell, (1995). "Fracture process zone concept and delamination of composite laminates". *Theoretical and Applied Fracture Mechanics,* vol. 24, pp. 57-64.

Anderson, T.L., (2005). *Fracture mechanics. Fundamentals and Applications.* (3rd ed.), CRC Press, Taylor and Francis, UK.

Atkinson, C., and R.V. Craster, (1991). "Plane strain fracture in poroelastic media". *Procedures of Royal Society of London*, vol. 434, pp. 605-633.

Barenblatt, G.I., (1959). "The formation of equilibrium cracks during brittle fracture: general ideas and hypothesis, axially symmetric cracks". *Applied Mathematical Mechanics*, vol. 23, pp. 622-636.

Barenblatt, G.I., (1962). "The mathematical theory of equilibrium cracks in brittle fracture". *Advances in Applied Mechanics,* vol. 7, pp. 55-129.

Batchelor, G.K., (1967). *An Introduction to Fluid Dynamics.* Cambridge University Press, U.K.

Bear, J., (1972). *Dynamics of Fluids in Porous Media.* Dover Publications, N.Y., U.S.

Benzeggagh, M.L., and M. Kenane, (1996). "Measurement of mixed-mode delamination fracture toughness of unidirectional glass/epoxy composites with mixed-mode bending apparatus". *Composites Science and Technology,* vol. 56, pp. 439-449.

Berryman, J.G., (1992). "Effective stress for transport properties of inhomogeneous porous rock". *Journal of Geophysical Research,* vol. 97, (B12), pp. 17409-17429.

Berryman, J.G., (1993). "Effective-stress rules for pore-fluid transport in rocks containing two minerals". *International Journal of Rock Mechanics, Mining Sciences and Geomechanical Abstracts,* vol. 30 (7), pp. 1165-1168.

Bigoni, D., and E. Radi, (1993). "Mode I crack propagation in elastic-plastic pressure-sensitive materials". *International Journal of Solids and Structures,* vol. 30, pp. 899-919.

Biot, M.A., (1941). "General theory of three dimensional consolidation". *Journal of Applied Physics,* vol. 12, pp. 155-164.

Biot, M.A., L. Masse, and W.L. Medlin, (1986). "A Two-Dimensional Theory of Fracture Propagation". *SPE Production Engineering,* vol. 1, pp. 17-30.

Bohloli, B. and C.J. de Pater, (2006). "Experimental study on hydraulic fracturing of soft rocks: influence of fluid rheology and confining stress". *Journal of Petroleum Science and Engineering,* vol. 53, pp. 1-12.

Boone, J.T, and A.R, Ingraffea, (1990). "A numerical procedure for simulation of hydraulically driven fracture propagation in poroelastic media". *International Journal for Numerical and Analytical Methods in Geomechanics,* vol. 14, pp. 27-47.

Boone, T.J., P.A. Wawrzynek, and A.R. Ingraffea, (1986). "Simulation of fracture process in rock with application to hydrofracturing". *International journal of Rock Mechanics, Mining Sciences and Geomechanical Abstracts,* vol. 23, pp. 255-265.

Bruno, M.S., and F.M. Nagakawa, (1991). "Pore pressure Influence on Tensile Fracture Propagation in Sedimentary Rock". *International journal of Rock Mechanics, Mining Sciences and Geomechanical Abstracts*, vol. 28, pp. 261-273.

Bunger, A.P., E. Detournay, D.I. Garagash, and A.P. Peirce, (2007). "Numerical Simulation of Hydraulic Fracturing in the Viscosity-Dominated Regime". SPE Hydraulic Fracturing Technology Conference, (SPE 106115-MS), 29-31 January 2007, College Station, Texas, U.S.A.

Camacho, G.T., and M. Ortiz, (1996). "Computational modelling of impact damage in brittle materials". *International Journal of Solids and Structures,* vol. 33, pp. 2899-2938.

Camanho, P.P., and C.G. Davila, (2002). "Mixed-mode decohesion finite elements for the simulation of delamination in composite materials". NASA/TM-2002-211737.

Carbonell, R., (1996). *Self-similar solution of a fluid-driven fracture.* Ph.D. Thesis, University of Minnesota, Mineapolis, U.S.

Carter, E., (1957). *Optimum fluid characteristics for fracture extension.* In. G. Huward and C. Fast (Eds.). Drilling and Production Practices, American Petroleum Institute, Tulsa OK.

Chandra N., H. Li, C. Shet, and H. Ghonem, (2002). "Some issues in the application of cohesive zone models for metal-ceramic interfaces". *International Journal of Solids and Structures*, vol. 39, pp. 2827-2855.

Cheng, A.H-D., Y. Abousleiman, and J.C. Roegiers, (1993). "Review of some poroelastic effects in rock mechanics". *International journal of Rock Mechanics, Mining Sciences and Geomechanical Abstracts,* vol. 30, pp. 1119-1126.

Cleary, M.P., C.A. Wright, and T.B. Wright, (1991). "Experimental and modeling evidence for major changes in hydraulic fracturing design and field procedures". Proceedings SPE Gas Technology Symposium, Houston.

Clifton, R., and A. Abou-Sayed, (1981). "A variational approach to the prediction of the three-dimensional geometry of hydraulic fractures". In Proc. SPE/DOE Low Permeability Reservoir Symposium, Denver. Society of Petroleum Engineers, (SPE 9879).

Crank, J. (1970). *The mathematics of diffusion.* Oxford University Press, New York.

Craster, R.V., and C. Atkinson, (1994). "Crack problems in a poroelastic medium: an asymptotic approach". *Philosophical Transactions, Royal Society of London, Series A,* vol. 346, pp. 387-428.

De Borst, R., (2001). "Some recent issues in computational failure mechanics". *International Journal for Numerical Methods in Engineering,* vol. 52, pp. 63-95.

De Borst, R., (2003). "Numerical aspect of cohesive zone models". *Engineering Fracture Mechanics*, vol. 70, pp. 1943-1961.

De Pater, C.J., L. Weijers, M. Savic, K.H.A.A. Wolf, P.J. van de Hoek, and D.T. Barr, (1994). "Experimental Study of Nonlinear Effects in Hydraulic Fracture Propagation". *SPE Production Engineering,* vol. 9, pp. 239-246.

Desroches, J., and M. Thiercelin, (1993). "Modelling the Propagation and Closure of Micro-Hydraulic Fractures". *International Journal of Rock Mechanics, Mining Sciences and Geomechanics Abstracts,* vol. 30, pp. 1231-1243.

Desroches, J., B. Lenoach, P. Papanastasiou, and M. Thiercelin, (1994). "On the Modelling of Near Tip Processes in Hydraulic Fractures". *International Journal of Rock Mechanics, Mining Sciences and Geomechanics Abstracts,* vol. 30, No. 7, pp. 1127-1134.

Detournay, E., (1998). "Fluid and solid singularities at the tip of a fluid-driven fracture". Proceedings IUTAM Symposium on Non-Linear Singularities in Deformation and Flow (Eds. Durban D. and J.R.A. Pearson), Dordrecht, Kluwer Academic Publishers.

Detournay, E., (2004). "Propagation regimes of fluid driven fractures in impermeable rocks". *International journal of Geomechanics,* vol. 1, pp 1-11.

Detournay, E., A.H-D. Cheng, and J. McLennan, (1990). "A poroelastic PKN hydraulic fracture model based on an explicit moving mesh algorithm". *ASME Journal of Energy Resources Technology,* vol. 112, pp. 224-230.

Detournay, E., and A.H. Cheng, (1988). "Poroelastic response of a borehole in a non-hydrostatic stress field". *International Journal of Rock Mechanics, Mining Sciences and Geomechanics Abstracts,* vol. 25, pp. 171-182.

Detournay, E., and A.H-D. Cheng, (1993). *Fundamentals of poroelasticity.* Comprehensive Rock Engineering: Principles, Practice and Projects, J.A. Hudson, ed., Pergamon Press, Oxford, UK.

Detournay, E., and D. Garagash, (2003). "The near-tip region of a fluid-driven fracture in a permeable elastic solid". *Journal of Fluid Mechanics,* vol. 494, pp. 1-32.

Detournay, E., J.D. McLennan, and J.C. Roegiers, (1986). "Poroelastic concepts explain some of the hydraulic fracturing mechanisms". (SPE 15262), SPE Unconventional Gas Technology Symposium, Louisville (KY).

Dong, Y., (2010). *Hydraulic fracture containment in sand.* Ph.D. thesis, Delft University of Technology, Delft, The Netherlands.

Dong, Y., and C.J. de Pater, (2001). "Numerical implementation of displacement discontinuity method and its application in hydraulic fracturing". *Computer Methods in Applied Mechanics and Engineering,* vol. 191, pp. 745-760.

Dugdale, D.S., (1960). "Yielding of steel sheets containing slits". *Journal of the Mechanics and Physics of Solids,* vol. 8, pp. 100-104.

Economides, M., and K. Nolte, (2000). *Reservoir Stimulation.* Wiley, Chichester, England.

Espinosa, H.D., and P.D. Zavattieri, (2003). "A grain level model for the study of failure initiation and evolution in polycrystalline brittle materials. Part I: Theory and numerical implementation". *Mechanics of Materials,* vol. 35, pp. 333-364.

Fjaer, E., R.M. Holt, P. Horsrud, A.M. Raaen, and R. Risnes, (1996). *Petroleum Related Rock Mechanics.* Developments in Petroleum Science. vol. 33, Elsevier, New York.

Garagash, D., (1998). *Near-Tip Processes of Fluid-Driven Fractures.* Ph.D Thesis, University of Minnesota, Minneapolis.

Garagash, D., (2000). "Hydraulic fracture propagation in elastic rock with large toughness". In J. Girard, M. Liebman, C. Breeds, and T. Doe (Eds.), Rock Around the Rim - Proc. 4th North American Rock Mechanics Symposium, Rotterdam, Balkema.

Garagash, D., (2006). "Propagation of plane-strain hydraulic fracture with a fluid lag: Early-time solution". *International Journal of Solids and Structures,* vol. 46, pp. 5811-5835.

Garagash, D., and E. Detournay, (2000). "The tip region of a fluid-driven fracture in an elastic medium". *ASME Journal of Applied Mechanics*, vol. 67, pp. 183-192.

Garagash, D.I., and E. Detournay, (2005). "Plane strain propagation of fluid driven fracture: small toughness solution". *ASME Journal of applied Mechanics, v*ol. 72, pp. 916-928.

Geertsma, J., (1957). "The effect of fluid pressure decline on volumetric changes in porous rock". *Petroleum Transactions: American Institute of Mining Engineers,* vol. 2, No.10, pp. 331-340.

Geertsma, J., and F. de Klerk, (1969). "A rapid method of predicting width and extent of hydraulic induced fractures". *Journal of Petroleum Technology,* (SPE 2458), vol. 246, pp. 1571- 1581.

Geubelle, P.H, and J.S. Baylor, (1998). "Impact induced delamination of composites: 2D simulation". *Composites Part B*, vol. 29B, pp. 589-602.

Griffith, A.A., (1920). "The phenomena of rupture and flow in solids". *Philosophical Transactions, Royal Society of London, Series A*, vol. 221, pp. 163-198.

Hillerborg, A., M. Modeer, and P.E. Petersson, (1976). "Analysis of crack formation and crack growth in concrete by means of fracture mechanics and finite elements". *Cement and Concrete Research,* vol. 6, pp. 773-782.

Hubbert, M.K., and D.G. Willis, (1957). "Mechanics of Hydraulic Fracturing". *Journal of Petroleum Technology,* vol. 9, pp. 153-168.

Hughes, T.J.R., and J. Winget, (1980). *Finite Rotation Effects in Numerical Integration of Rate Constitutive Equations Arising in Large-Deformation Analysis.* Short Communications, John Wiley & Sons, N.Y.

Hutchinson, J.W., (1968). "Singular behavior at the end of a tensile crack in a hardening material". *Journal of the Mechanics and Physics of Solids,* vol. 16, pp. 18-31.

Hutchinson, J.W., and A.G. Evans, (2000). "Mechanics of materials: Top-down approaches to fracture". *Acta Materialia*, vol. 48, pp. 125-135.

Ingraffea, A. and T. Boone, (1988). "Simulation of hydraulic fracture propagation in porous rock". In G. Swoboda (Ed.), Proc. 6th Int. Conf. on Numerical Methods in Geomechanics, Innsbruck, Rotterdam, Balkema.

Irwin, G.R., (1957). "Analysis of stresses and strains near the end of a crack traversing a plate". *Journal of Applied Mechanics,* vol. 24, pp. 361-364.

Jeffrey, R.G, A. Settari, K.W. Mills, X. Zhang, and E., Detournay, (2001). "Hydraulic fracturing to induce caving: fracture model development and comparison to field data". (Elsworth D, Tinucci J.P, Heasley K.A, eds.), Rock mechanics in the

national interest-proceedings of the 38th US rock mechanics symposium, Lisse, Balkema.

Kanninen, M.F., and C.H. Popelar, (1985). *Advanced fracture mechanics*. Oxford University Press.

Khristianovich, S.A., and Y.P. Zheltov, (1955). "Formation of Vertical Fractures by Means of Highly Viscous Liquid". Procedures of Fourth World Petroleum Congress, Rome.

Lecampion, B., and E. Detournay, (2007). "An implicit algorithm for the propagation of a hydraulic fracture with a fluid lag". *Computer Methods in Applied Mechanics and Engineering,* vol. 196, pp. 4863-4880.

Legarth, B., E. Huenges, and G. Zimmermann, (2005). "Hydraulic fracturing in sedimentary geothermal reservoir: results and implications". *International Journal of Rock Mechanics and Mining Sciences,* vol. 42, pp. 1028-1041.

Lenoach, B., (1995). "The crack tip solution for hydraulic fracturing in a permeable solid". *Journal of the Mechanics and Physics of Solids,* vol. 43, No. 7, pp. 1025-1043.

Li, H., and N. Chandra, (2003). "Analysis of crack growth and crack-tip plasticity in ductile material using cohesive zone models". *International Journal of Plasticity,* vol. 19, pp. 849-882.

Loret, B., and J.H. Prevost, (1991). "Dynamic strain localization in fluid-saturated porous media". *Journal of Engineering Mechanics,* vol. 117, pp. 907-922.

Mack, M., and R. Warpinski, (2000). *Mechanics of hydraulic fracturing*. In M. Economides and K. Nolte (Eds.), Reservoir Stimulation (3rd ed.), Chapter 6, Chichester UK: John Wiley & Sons.

Meng, H.Z., and K.E. Brown, (1987). "Coupling of production forecasting, fracture geometry requirements and treatment scheduling in the optimum hydraulic fracture design". (SPE 16435).

Mi, Y., M.A. Crisfield, G.A.O. Davis, and H.B. Helweg, (1998). "Progressive delamination using interface elements". *Journal of Composite Materials,* vol. 32, pp. 1246-1272.

Mokryakov, V., (2011). "Analytical solution for propagation of hydraulic fracture with Barenblatt cohesive tip zone". *International Journal of Fracture,* (accepted paper).

Mori, A., and M. Tamura, (1987). "Hydrofracturing pressure of cohesive soils", *Soils and Foundations, Japanese Society of Soil Mechanics and Foundation Engineering,* vol. 27, pp. 14-22.

Moschovidis, Z., R., Steiger, R., Peterson, N., Warpinski, C., Wright, Ed., Chesney, J., Hagan, A., Abou-Sayed, R., Keck, M., Frankl, S., Wolhart, B., McDaniel, A., Sinor, L., Miller, R., Beecher, J., Dudley, D., Zinno, and O. Akhmedov, (2000). "The Mounds drill-cuttings injection experiment: final results and conclusions". Proceedings of the IADC/SPE drilling conference, Richardson, Society of Petroleum Engineers, (SPE 59115).

Muller, W., (1986). "Brittle crack growth in rock". *Pure and Applied Geophysics*, vol. 124, pp. 694-709.

Murdoch, L.C., (1993). "Hydraulic fracturing of soil during laboratory experiments. Part 1. Methods and Observations". *Geotechnique*, vol. 43, pp. 255-265.

Murdoch, L.C, and W.W. Slack, (2002). "Forms of hydraulic fractures in shallow fine grained formations". *Journal of Geotechnical and Geoenvironmental Engineering,* vol. 128, pp. 479-487.

Muskhelishvilly, N.I., (1953). *Some Basic Problems of the Theory of Elasticity.* 4th Edition, J.R. Radok (trans.), Groningen, Netherlands, P. Noordhoff.

Needleman, A., (1987). "A continuum model for void nucleation by inclusion debonding". *ASME Journal of Applied Mechanics,* vol. 54, pp. 525-531.

Needleman, A., (1990). "An analysis of decohesion along an imperfect interface". *International Journal of Fracture,* vol. 42, pp. 21-40.

Nilson, R., (1988). "Similarity solutions for wedge-shaped hydraulic fracture driven into a permeable medium by a constant inlet pressure". *International Journal of Numerical and Analytical Methods in Geomechanics,* vol. 12, pp. 477-495.

Nordgren, R., (1972). "Propagation of vertical hydraulic fractures". *Journal of Petroleum Technology,* (SPE 3009), vol. 253, pp. 306-314.

Panah, A.K., and E. Yanagisawa, (1989). "Laboratory studies on hydraulic fracturing criteria in soil". *Soils and Foundations, Japanese Society of Soil Mechanics and Foundation Engineering,* vol. 29, pp. 14-22.

Papamichos, E., and N. Charalampakis, (2004). *Strength of Materials*. Tziolas publications, Thessaloniki. (in greek).

Papanastasiou, P., and C. Atkinson, (2000). "Representation of crack-tip plasticity in pressure sensitive geomaterials". *International Journal of Fracture,* vol. 102, pp. 271-286.

Papanastasiou, P., and M. Thiercelin, (1993). "Influence of inelastic rock behaviour in hydraulic fracturing". *International Journal of Rock Mechanics, Mining Sciences and Geomechanics Abstracts*, vol. 30, No. 7, pp. 1241-1247.

Papanastasiou, P., (1997). "The influence of plasticity in hydraulic fracturing". *International Journal of Fracture,* vol.84, pp. 61-79.

Papanastasiou, P., (1999). "An efficient algorithm for propagating fluid driven fractures". *Computational Mechanics,* vol. 24, pp. 258-267.

Papanastasiou, P., (1999b). "The effective fracture toughness in hydraulic fracturing". *International Journal of Fracture,* vol. 96, pp. 127-147.

Papanastasiou, P., and D., Durban, (2001). "Singular plastic fields in non-associative pressure sensitive solids". *International Journal of Solids and Structures,* vol. 38, pp. 1539-1550.

Perkins, T.K., and L.R. Kern, (1961). "Widths of Hydraulic Fractures". *Journal of Petroleum Technology,* vol. 13, pp. 937-949.

Radi E., D. Bigoni, and B. Loret, (2002). "Steady crack growth in elastic-plastic fluid saturated porous media". *International Journal of Plasticity,* vol. 18, pp. 345-358.

Rice, J., (1968). *Mathematical analysis in the mechanics of fracture.* In H. Liebowitz (Ed.), *Rapture, an Advanced Treatise,* vol. 11, Chapter 3, pp. 191-308, New York, Academic Press.

Rice, J.R., (1968), "A Path Independent Integral and the Approximate Analysis of Strain Concentration by Notches and Cracks". *Journal of Applied Mechanics*, vol. 35, pp. 379-386.

Rice, J.R., (1980). *The mechanics of earthquake rupture.* In: Physics of the earth's interior. Amsterdam, North-Holland Publishing Company.

Rice, J.R., and M.P. Cleary, (1976). "Some basic stress diffusion solutions for fluid-saturated elastic porous media with compressible constituents". *Review of Geophysics and Space Physics*, vol. 14, pp. 227-241.

Rice, J.R., and G.F. Rosengren, (1968). "Plane strain deformation near a crack tip in a power-law hardening material". *Journal of the Mechanics and Physics of Solids,* vol. 16, pp. 1-12.

Ritchie, R.O., (1999). "Mechanisms of fatique-crack propagation in ductile and brittle solids". *International Journal of Fracture,* vol. 100, pp. 53-83.

Roy, Y.A., and R.H. Dodds Jr., (2001). "Simulation of ductile crack growth in thin aluminium panels using 3-D surface cohesive elements". *International Journal of Fracture,* vol. 110, pp. 21-45.

Sarris, E., and P. Papanastasiou, (2010). "The influence of the cohesive process zone in hydraulic fracturing modelling". *International Journal of Fracture,* vol. 167, pp. 33-45.

Sarris, E., and P. Papanastasiou, (2011). "Modelling of hydraulic fracturing in a poroelastic cohesive formation". *International Journal of Geomechanics ASCE* (accepted paper).

Savitski, A., (2000). *Propagation of a Penny-Shaped Hydraulic Fracture in an Impermeable Rock.* Ph.D. Thesis, University of Minnesota, Minneapolis. U.S.

Savitski, A., and E. Detournay, (2001). "Propagation of a fluid-driven penny-shape fracture in an impermeable rock: Asymptotic solutions". *International Journal of Solids and Structures,* vol. 39, pp. 6311-6337.

Schellekens, J.C.J., and R. De Borst, (1993). "On the numerical integration of interface elements". *International Journal of Numerical Methods in Engineering,* vol. 36, pp. 43-66.

Schlangen, E., and J.G.M. van Mier, (1992). "Experimental and numerical analysis of micromechanisms of fracture of cement-based composites". *Cement and Concrete Composites,* vol. 14, pp. 105-118.

Schmitt, D.R., and M.D. Zoback, (1992). "Diminished pore pressure in low-porosity crystalline rock under tensional failure: apparent strengthening by dilatance". *Journal of Geophysical Research,* vol. 97, pp. 273-288.

Schreffler, B.A, S. Secchi, and L. Simoni, (2006). "On adaptive refinement techniques in multi-field problems including cohesive fracture". *Computer Methods in Applied Mechanics and Engineering,* vol. 195, pp. 444–461.

Settari, A., (1985). "A new general model of fluid loss in hydraulic fracturing". *Society of Petroleum Engineers Journal (SPE 11625)*, vol. 25, No. 4, pp. 491-501.

Shet, C., and N. Chandra, (2002). "Analysis of energy balance when using cohesive zone models to simulate fracture processes". *Journal of Engineering Materials and Technology,* vol. 124, pp. 440-450.

Shet, C., and N. Chandra, (2004). "Effect of the shape of T-δ cohesive zone curves on the fracture response". *Mechanics of Advanced Materials and Structures,* vol. 11, pp. 249-275.

Shlyapobersky, J., (1985). "Energy analysis of hydraulic fracturing." 26th U.S Symposium on Rock Mechanics, Rapid City, SD, USA.

Siebrits, E., and A. Peirce, (2002). "An effective multilayer planar 3D fracture growth algorithm using a fixed mesh approach". *International Journal for Numerical Methods in Engineering,* vol. 53, pp. 691-717.

Siebrits, E., and A. Peirce, (2000). "Hydraulic fracturing in laminated reservoirs". In R. Jeffrey and J. McLennan (Eds.). Proc. Workshop on Three-Dimensional and Advanced Hydraulic Fracture Modelling, Seattle.

Sinclair, G.B., (1996). "On the influence of cohesive stress-separation laws on elastic stress singularities". *Journal of Elasticity,* vol. 44, pp. 203-221.

Sneddon, I., and M. Lowengrub, (1969). *Crack problems in the classical theory of elasticity*. John Wiley and Sons, New York.

Sousa, J., B. Carter, and A. Ingraffea, (1993). "Numerical simulation of 3D hydraulic fracture using Newtonian and power-law fluids". *International Journal of Rock Mechanics and Mining Sciences,* vol. 30, No. 7, pp. 1265-1271.

Spence, D., and P. Sharp, (1985). "Self-similar solution for elasto-hydrodynamic cavity flow". *Proceedings of Royal Society of London, Series A.*, vol. 40, pp. 289-313.

Spence, D.A., and D.L., Turcotte, (1985). "Magma-driven propagation crack". *Journal of Geophysical Research,* vol. 90, pp. 575-580.

Terzaghi, K., (1925). "Structure and volume of voids of soils". In. Erdbaumechanik auf Bodenphysikalisher Grundlage, pp. 10-13. Translated by A. Casagrande.

Thiercelin, M.J., R.G. Jeffrey, and K. Ben-Naceur, (1987). "The influence on fracture toughness on the geometry of hydraulic fractures". (SPE 16431).

Tvergaard, V., and J.W. Hutchinson, (1992). "The relation between crack growth resistance and fracture process parameters in elastic-plastic solids". *Journal of the Mechanics and Physics of Solids,* vol. 40, pp. 1377-1397.

Valko P., and M.J. Economides, (1995). *Hydraulic fracture mechanics*. John Wiley and Sons, New York.

Van Dam, D.B., (1999). *The Influence of Inelastic Rock Behaviour on Hydraulic Fracture Geometry*. Ph.D. Thesis, Delft University of Technology, The Netherlands.

Van Dam, D.B., C.J. de Pater, and R. Romijn, (1997). "Experimental study of the impact of plastic rock deformation on hydraulic fracture geometry". *International Journal of Rock Mechanics and Mining Sciences,* vol. 34, No. 318, pp. 3-40.

Van Dam, D.B., P. Papanastasiou, and C.J. de Pater, (2002). "Impact of rock plasticity on hydraulic fracture propagation and closure". *SPE Production & Facilities,* vol. 17, No. 3, pp. 149-159.

Van Damme, L., E. Detournay, and A.H.D. Cheng, (1989). "A tow-dimensional poroelastic displacement discontinuity method for hydraulic fracture simulation". *International Journal for Numerical and Analytical Methods in Geomechanics,* vol. 13, pp. 215-224.

Van Den Hoek, P.J., J.T.M. Van Den Berg, and J. Shlyapobersky, (1993). "Theoretical and experimental investigation of rock dilatancy near the tip of a propagating hydraulic fracture". *International journal of Rock Mechanics, Mining Sciences and Geomechanical Abstracts,* vol. 30, pp. 1261-1264.

Van Vliet, M.R.A., (2000). *Size effect of concrete and rock under uniaxial tension*, Ph.D. Thesis, Delft University of Technology, Delft, The Netherlands.

Vardoulakis, I., and J. Sulem, (1995). *Bifurcation Analysis in Geomechanics.* Blackie Academic and Professional, U.K.

Wang C., P., Liu, R., Hu, and S. Xiutang, (1990). "Study of the Process Zone in Rock by Laser Speckle Interferometry". *International journal of Rock Mechanics, Mining Sciences and Geomechanical Abstracts,* vol. 27, No. 1, pp. 65-69.

Warpinski, N., Z. Moschovidis, C. Parker, and I. Abou-Sayed, (1994). "Comparison study of hydraulic fracturing models: Test case GRI-staged field experiment No. 3". *SPE Production & Facilities, (SPE 25890)*, vol. 9, No.1, pp. 7-16.

Wawersik, W.R., J.W. Rudnicki, P. Dove, J. Harris, J.M. Logan, L. Pyrak-Nolte, F.M. Jr Orr, P.J. Ortoleva, F. Richter, N.R. Warpinski , J.L. Wilson, and T.F. Wong, (2001). "Terrestrial sequestration of CO2: an assessment of research needs". *Advances in Geophysics.,* vol. 43, pp. 97-177.

Wells, A.A., (1961). "Unstable crack propagation in metals: cleavage and fast fracture". Proceedings of the Crack Propagation Symposium, vol. 1, paper 84, Cranfield, UK.

Whittaker, B.N., R.N. Singh, and G. Sun, (1992). *Rock Fracture Mechanics: Principles, Design, and Applications*. Elsevier, Amsterdam, The Netherlands.

Williams, B., (1970). "Fluid loss from hydraulically induced fractures". *Journal of Petroleum Technology,* vol. 22, No. 6, pp. 882-888.

Xu, X.P., and A. Needleman, (1993). "Void nucleation by inclusion debonding in a crystal matrix". *Modelling and Simulation in Materials Science and Engineering,* vol. 1, pp. 111-132.

Xu, X.P., and A. Needleman, (1994). "Numerical simulations of fast crack growth in brittle solids". *Journal of Mechanics and Physics of Solids*, vol. 42, pp. 1397-1434.

Yi, T., and J. Peden, (1994). "A comprehensive model of fluid loss in hydraulic fracturing". *SPE Production and Facilities, (SPE 25493)*, vol. *9,* No. 4, pp. 267-272.

Yuan, Y., (1997). *Simulation of Penny-Shaped Hydraulic Fracturing in Porous Media.* Ph.D. Thesis, University of Oklahoma, USA.

Zhang, X., E. Detournay, and R. Jeffrey, (2002). "Propagation of a penny-shape hydraulic fracture parallel to the free-surface of an elastic half-space". *International Journal of Fracture,* vol. 115, pp. 125-158.

Zhang, Z.X., S.Q. Kou, J. Yu, Y. Yu, L.G. Jiang and B.A. Lindqvist, (1999). "Effects of loading rate on rock fracture". *Int. J. Rock. Mech. Min. Sci. and Geomech. Abstr.,* vol. 36, No. 5, pp. 597-611.

Zimmerman, R.W., (1991). *Compressibility of sandstones.* Developments in Petroleum Science, vol. 29, Elsevier, New York.

Zuorong, C., A.P. Bunger, X. Zhang, and R.J. Jeffrey, (2009). "Cohesive zone finite element-based modeling of hydraulic fractures". *Acta Mechanica Solida Sinica,* vol. 22, pp. 443-452.

Zuorong C., (2010). "Finite element of Viscosity-Dominated Hydraulic fractures". 10th Hydraulic Fracturing Summit, Papanastasiou P., Bunger A., and Gordeliy E. (eds.), Limassol, Cyprus, 15-18 July.